

DEVELOPMENT OF A MEMS-BASED ACOUSTIC ENERGY HARVESTER

BY

STEPHEN BRIAN HOROWITZ

A DISSERTATION PRESENTED TO THE GRADUATE SCHOOL
OF THE UNIVERSITY OF FLORIDA IN PARTIAL FULFILLMENT
OF THE REQUIREMENTS FOR THE DEGREE OF
DOCTOR OF PHILOSOPHY

UNIVERSITY OF FLORIDA

2005

Copyright 2005

by

Stephen Brian Horowitz

I dedicate this dissertation to my wife, Megan. You're my sweetheart, my wife and my best friend. I love you more than words can say.

TABLE OF CONTENTS

	<u>Page</u>
LIST OF TABLES	vii
LIST OF FIGURES	viii
ABSTRACT	xiv
 CHAPTER	
1 INTRODUCTION	1
Acoustic Energy Harvester—Concept	1
Motivation	5
Background	6
Piezoelectricity	6
Piezoelectric Materials in MEMS	6
Materials and properties	7
Deposition methods	8
Piezoelectric integration with MEMS	9
Reduced-Order Modeling of Piezoelectric Materials	11
Energy Absorption/Vibration Damping and Energy Harvesting	13
Approach	14
2 THEORETICAL BACKGROUND	17
Overview—Energy Harvesting	17
Maximum Average Power Transfer	20
Electromechanical Transducers	23
Lumped Element Modeling	25
Helmholtz Resonator	29
Lumped Element Model	29
Equivalent Circuit	33
Piezoelectric Composite Plate	35
Piezoelectricity	36
Composite Plate Modeling	41
Lumped element model	41
Equivalent circuit	46
Case 1: Well below the short-circuit mechanical resonant frequency	50
Case 2: At the short-circuit mechanical resonant frequency	52
General expression vs. simplified cases	54

	Effects of including the radiation impedance.....	55
	Equivalent circuit parameters of piezoelectric composite circular plates	61
	Acoustic Energy Harvester Dynamic Behavior.....	68
	Acoustical Input Behavior.....	68
	Electrical Output Behavior.....	71
	Operation at an Optimal Frequency.....	76
	Device Configurations.....	79
3	FABRICATION AND PACKAGING.....	82
	Overview.....	82
	Process Flow.....	82
	Packaging.....	92
	Packaging Scheme.....	92
	Quarter-wave resonator package.....	92
	Sealed cavity package.....	94
	Chip to Package Mounting.....	94
	Poling.....	96
4	EXPERIMENTAL SETUP.....	98
	Parameters and How They are Obtained.....	98
	Experimental Setup Details.....	101
	Ferroelectric Measurements.....	101
	Electrically Actuated Response—Laser Scanning Vibrometer.....	102
	Acoustic Characterization – Plane Wave Tube.....	103
	Electrical Impedance Characterization.....	107
	Initial Deflection Measurements – Wyko Optical Profilometer.....	107
5	EXPERIMENTAL RESULTS AND DISCUSSION.....	108
	Ferroelectric Measurements.....	108
	Electrical Measurements.....	110
	Electrical Output Impedance.....	110
	Electrically Actuated Response—Laser Scanning Vibrometer.....	114
	Frequency response.....	114
	Linearity.....	124
	Acoustical Measurements.....	126
	Acoustically Actuated Frequency Response – Plane-Wave Tube.....	126
	Sealed cavity package.....	126
	Quarter-wave resonator package.....	127
	Acoustic Input Impedance Measurements – Plane-Wave Tube.....	130
	Quarter-Wave Resonator Package.....	133
	Initial Deflection Measurements – Wyko Optical Profilometer.....	134
	Energy Harvesting Measurements.....	138
	Optimal Resistance.....	138
	Optimal Energy Harvesting.....	139

6	ALTERNATIVE APPLICATION—PIEZOELECTRIC MICROPHONE	147
7	CONCLUSION AND FUTURE WORK.....	153
	Development Issues.....	154
	Future Work.....	156
APPENDIX		
A	MATLAB CODE	158
	lem.m	158
	eh_setup.m.....	163
	silicon_sweep.m.....	163
	platinum.m.....	163
	tio2.m.....	163
	piezo_sweep.m.....	164
	initialise.m.....	164
	totaldeflection_forP.m.....	164
	totaldeflection_forV.m.....	164
	initialdeflection.m.....	165
	formmatrix_CMFa.m.....	165
	frommatrix_dA.m.....	166
	abdpiezo.m.....	166
	constants1234.m.....	167
	solver1.m.....	168
B	DETAILED PROCESS FLOW.....	170
	Energy Harvester - Process Traveler.....	170
	Graphical Representation of Process Flow.....	172
	Mask Layouts.....	174
	Package Drawings.....	178
	LIST OF REFERENCES.....	180
	BIOGRAPHICAL SKETCH.....	195

LIST OF TABLES

<u>Table</u>	<u>page</u>
1-1: Typical material properties of select piezoelectric materials.	7
1-2: Selected thin film piezoelectric materials and corresponding properties as reported in the literature.....	10
2-1: Equivalent lumped elements in several common energy domains.....	28
2-2: Conjugate power variables.	29
2-3: General material properties used in modeling.....	55
2-4: PZT properties used in modeling.	55
2-5: Chosen device configurations for fabrication.....	81
3-1: Wafer bow measurements and the resulting calculated stress.....	86
3-2: Measured wafer mass and calculated density of PZT.	87
5-1: Summary of electrical impedance measurements.	113
5-2: Comparison of ferroelectric and dielectric properties of thin film PZT.....	113
5-3: Summary of electrically actuated frequency response measurements.	124
6-1: Summary of experimental results of microphone.	152

LIST OF FIGURES

<u>Figure</u>	<u>page</u>
1-1: Roadmap to Chapter 1.....	2
1-2: Schematic of overall energy harvesting concept.....	3
1-3: Conceptual schematic of the acoustic energy harvester.....	4
1-4: Basic LCR electrical circuit.....	4
2-1: Roadmap to Chapter 2.....	18
2-2: Thévenin equivalent circuit for purposes of maximizing power transfer.....	21
2-3: Diagram showing side view of a Helmholtz resonator and its mechanical equivalent of a mass-spring-damper system.....	29
2-4: Equivalent circuit representation of a Helmholtz resonator.....	34
2-5: Theoretical pressure amplification of a conventional Helmholtz resonator. (a) magnitude (b) phase.....	35
2-6: Cross-sectional and 3-D schematic of piezoelectric composite circular plate. (not to scale).....	36
2-7: Notation of axes used in piezoelectric transduction.....	37
2-8: Idealized perovskite crystal structure for PZT. a) centrosymmetric structure prior to poling. b) non-centrosymmetric structure after poling.....	38
2-9: Schematic of the poling process:.....	39
2-10: Polarization vs. electric field hysteresis loop.....	40
2-11: Electro-acoustic equivalent circuit representation with C_{eb} , C_{as} and ϕ	46
2-12: Electro-acoustic equivalent circuit representation with C_{ef} , C_{as} and ϕ'	47
2-13: Dynamic electro-acoustic equivalent circuit.....	48

2-14: Sensitivity vs. frequency for a piezoelectric composite circular plate.	55
2-15: Equivalent circuit of piezo-composite plate including the radiation impedance.	57
2-16: Equivalent circuit with resistive load.	60
2-17: Conceptual 3-D and cross-sectional schematic of the circular composite plate	62
2-18: Effective acoustic short-circuit compliance as a function of R_1/R_2 and t_p/t_s	63
2-19: Effective acoustic mass as a function of R_1/R_2 and t_p/t_s	64
2-20: Short-circuit resonant frequency as a function of R_1/R_2 and t_p/t_s	65
2-21: Electro-acoustic transduction coefficient as a function of R_1/R_2 and t_p/t_s	66
2-22: Electromechanical coupling coefficient, k , as a function of R_1/R_2 and t_p/t_s	67
2-23: Equivalent circuit for acoustic energy harvester with resistive load.	68
2-24: Magnitude of the acoustical input impedance for the piezoelectric composite diaphragm and in combination with the Helmholtz resonator	70
2-25: Magnitude and phase of the acoustical input power for an input acoustic pressure of $P = 94 \text{ dB}$	72
2-26: Electrical output impedance for the piezoelectric composite diaphragm by itself and in combination with the Helmholtz resonator.	73
2-27: Magnitude and phase of the output voltage for the piezoelectric composite diaphragm and in combination with the Helmholtz resonator.	74
2-28: Magnitude and phase of the electric output power delivered to the load resistor.	75
2-29: Magnitude and phase of the energy harvester efficiency.	76
2-30: Open-circuit voltage as a function of the applied acoustic pressure for the piezoelectric diaphragm by itself and packaged with a Helmholtz resonator.	77
2-31: Input and output power as a function of the load resistance placed across the electrodes of the piezoelectric material.	78
2-32: Input and output power as a function of the applied acoustic input pressure, while using an optimal load resistor.	79
3-1: Roadmap for Chapter 3.	83

3-2: Condensed process sequence in cross-section.	84
3-3: Early DRIE results showing significant sidewall damage.	88
3-4: SEM image showing black silicon at the base of a DRIE-etched trench.	89
3-5: SEM image of a successful DRIE etch through the thickness of a silicon wafer.	90
3-6: Illustration of a single diaphragm device..	91
3-7: Block layout illustrating numbering scheme for devices.	91
3-8: Wafer layout illustrating numbering scheme for blocks.	92
3-10: Quarter-wave resonator package consisting of acrylic plug, copper leads and vent channel.	93
3-11: Sealed cavity package.....	95
3-12: Optical photograph of a packaged energy harvester.	95
4-1: Roadmap for Chapter 4.	99
4-2: Experimental setup for impedance and power measurements.	104
4-3: Schematic of incident, reflected and input power.	106
5-1: Roadmap for Chapter 5.	108
5-2: Hysteresis loop for Device 1A-5-4 in a sealed cavity package. The device has a radius of $1200 \mu m$ and a central mass.	109
5-3: Measured parallel output capacitance, C_p vs. outer radius, R_2 overlaid with a theoretical capacitance curve based on the average extracted dielectric constant.	111
5-4: Parallel output resistance, R_p , vs. outer radius, R_2 , overlaid with a theoretical resistance curve based on the average measured conductivity.....	112
5-5: Device 1A-6-1, electrically actuated center deflection for the device with a radius of $900 \mu m$ and no central mass, packaged in the quarter-wave resonator package..	115
5-6: Device 1A-6-2, electrically actuated center deflection for the device with a radius of $900 \mu m$ and a central mass, packaged in the quarter-wave resonator package..	116
5-7: Device 1A-11-3, electrically actuated center deflection for the device with a radius of $1200 \mu m$ and no central mass, packaged in the quarter-wave resonator.....	117

5-8: Higher order mode image of Device 1A-11-3, taken using scanning laser vibrometer at 120.9 kHz.....	117
5-9: Device 1A-10-4, electrically actuated center deflection for the device with a radius of 1200 μm and a central mass, packaged in the quarter-wave resonator.	118
5-10: Device 1A-6-5, electrically actuated center deflection for the device with a radius of 1500 μm and no central mass, packaged in the quarter-wave resonator.....	119
5-11: Device 1A-10-6, electrically actuated center deflection for a device with a radius of 1500 μm and a central mass, packaged in the quarter-wave resonator package. .	120
5-12: Device 1A-3-7, electrically actuated center deflection for the device with a radius of 1800 μm and no central mass, packaged in the sealed-cavity package.....	121
5-13: Electrically actuated sensitivity at low frequency (well below resonance) ($R_1/R_2 = 0.95$).....	122
5-14: Summary of electrically actuated resonant frequencies.	122
5-15: Drop in resonant frequency due to the addition of the central mass.	123
5-16: Magnitude of the resonant center deflection versus driving voltage.....	125
5-17: Mechanical sensitivity at resonance versus driving voltage.....	126
5-18: Device 1A-5-4, magnitude and phase of the acoustically actuated frequency response in a sealed cavity package for the device with a radius of 1200 μm and a central mass.	128
5-19: Device 1A-10-4 in a quarter-wave resonator package. Magnitude and phase of the acoustically actuated frequency response for the device with a radius of 1200 μm and a central mass.	129
5-20: Device 1A-6-5 in a quarter-wave resonator package. Magnitude and phase of the acoustically actuated frequency response for the device with a radius of 1500 μm and no central mass.	130
5-21: Device 1A-10-2, Normalized acoustic impedance in a sealed cavity package for the device with a radius of 900 μm and a central mass.	131
5-22: Device 1A-5-4, Normalized acoustic impedance in a sealed cavity package for the device with a radius of 1200 μm and a central mass.	132
5-23: Device 1A-3-7, Normalized acoustic impedance in a sealed cavity package for the device with a radius of 1800 μm and no central mass.....	132

5-24: Device 1A-6-1, Normalized acoustic impedance in a quarter-wave resonator package for the device with a radius of 900 μm and no central mass.	133
5-25: Device 1A-11-3, Normalized acoustic impedance in a quarter-wave resonator package for the device with a radius of 1200 μm and no central mass.	134
5-26: Device 1A-11-3, Initial static deflection resulting from residual stresses for a device with a radius of 1200 μm and no central mass.	135
5-27: Device 1A-6-6, Initial static deflection resulting from residual stresses for a device with a radius of 1500 μm and a central mass.	136
5-28: Device 1A-3-7, Initial static deflection resulting from residual stresses for a device with a radius of 1800 μm and no central mass.	136
5-29: Device 1A-3-8, Initial static deflection resulting from residual stresses for a device with a radius of 1800 μm and a central mass.	137
5-30: Measured power delivered to a load as function of the load resistance for Device 1A-4-4 and Device 1A-3-8 as compared against theoretical values.	140
5-31: Measured output voltage across the load as a function of applied acoustic pressure and compared to theoretical values..	140
5-32: Measured power delivered to load as a function of applied acoustic pressure and compared to theoretical values.	141
5-33: Measured overall efficiency of each device overlaid with theoretical values for comparison.	142
5-34: Resonant frequency versus applied acoustic pressure, resulting from nonlinear response.	146
6-1: Linearity of the microphone device at 1 kHz	148
6-2: Frequency response spectrum in terms of magnitude and phase.	149
6-3: Noise floor spectrum of output voltage when no acoustic signal is applied, as well as noise floor due to measurement setup alone.	151
6-4: Electrically actuated frequency response of microphone device.	152
7-1: Roadmap to Chapter 7.	154
B-1: Step 1: Deposit Ti on SOI Wafer and oxidize to TiO_2	172
B-2: Step 2: Deposit Ti/Platinum(30nm/170nm) -Lift-Off w/ Mask (ElectrodeBot).....	172

B-3: Step 3: Spin PZT - 6 times to achieve desired thickness.....	172
B-4: Step 4: Deposit Platinum(180nm)-Lift-off w/ Mask (ElectrodeTop).....	172
B-5: Step 5: Wet Etch PZT using Pt as etch mask.....	173
B-6: Step 6.1: Spin thick photo resist on bottom (7um).....	173
B-7: Step 6.2: Pattern using mask (Cavity).....	173
B-8: Step 6.3: DRIE to BOX.....	173
B-9: Step 6.4: Ash Resist.....	173
B-10: Step 6.5: BOE backside to remove oxide.....	174
B-11: Backside metal mask.....	174
B-12: Bottom electrode mask.....	175
B-13: Top electrode mask.....	176
B-14: Cavity mask.....	177
B-15: Detailed schematic drawing of quarter wave resonator package and mounting....	178
B-16: Detailed schematic of sealed cavity package and mounting plate.....	179

Abstract of Dissertation Presented to the Graduate School
of the University of Florida in Partial Fulfillment of the
Requirements for the Degree of Doctor of Philosophy

DEVELOPMENT OF A MEMS-BASED ACOUSTIC ENERGY HARVESTER

By

Stephen Brian Horowitz

December 2005

Chair: Toshikazu Nishida

Cochair: Mark Sheplak

Major Department: Electrical and Computer Engineering

In this dissertation, I discuss the development of an electromechanical acoustic resonator for reclamation of energy using microelectromechanical systems (MEMS) technology. The MEMS device converts acoustical energy to electrical energy that can then either be stored for later use or utilized directly for a particular circuit application.

The work presented in this dissertation takes a first step towards that goal, by designing, fabricating and testing several electromechanical acoustic resonators of varying size. The resonators are fabricated using MEMS processing techniques on a silicon wafer. Each resonator consists of a 3 μm thick silicon diaphragm with a circular ring of piezoelectric material. The diaphragm transduces an acoustical pressure fluctuation into a mechanical deformation, while the piezoelectric material transduces that mechanical deformation into an electrical signal (charge or voltage).

CHAPTER 1 INTRODUCTION

The goal of my research was to utilize microelectromechanical systems (MEMS) based fabrication techniques to develop an electromechanical acoustic resonator for harvesting of acoustic energy. The MEMS device converts acoustical energy to electrical energy that can then either be stored or used directly for a particular circuit application. The relatively small geometries possible in MEMS make such a device useful for small, portable devices, where battery requirements are often difficult to meet. Additionally, the device is well suited to applications where wiring is difficult such as remote sensors or unwieldy as in the case of large arrays of devices requiring power.

This chapter begins with an overview of the acoustical to electrical energy reclamation process that is employed in this research. Following this, the motivation behind this research is presented. Then, an in-depth literature survey is presented to familiarize the reader with the technological and theoretical developments related to energy harvesting and piezoelectricity, followed by a short discussion of the technical approach that was employed. A graphical roadmap for this chapter is shown in Figure 1-1.

Acoustic Energy Harvester—Concept

The overall concept behind the energy harvester is illustrated in Figure 1-2. The main idea is to convert acoustic energy into a usable form of electrical energy. The figure illustrates a plane wave tube as the source of acoustic power. Some of the incident

acoustic power is reflected at the end of the tube; however, a portion is transmitted through to the energy harvester that is circled in Figure 1-2. The energy harvester performs the actual transduction of energy from the acoustical to the electrical energy domains. More details on this transduction technique will be provided later.

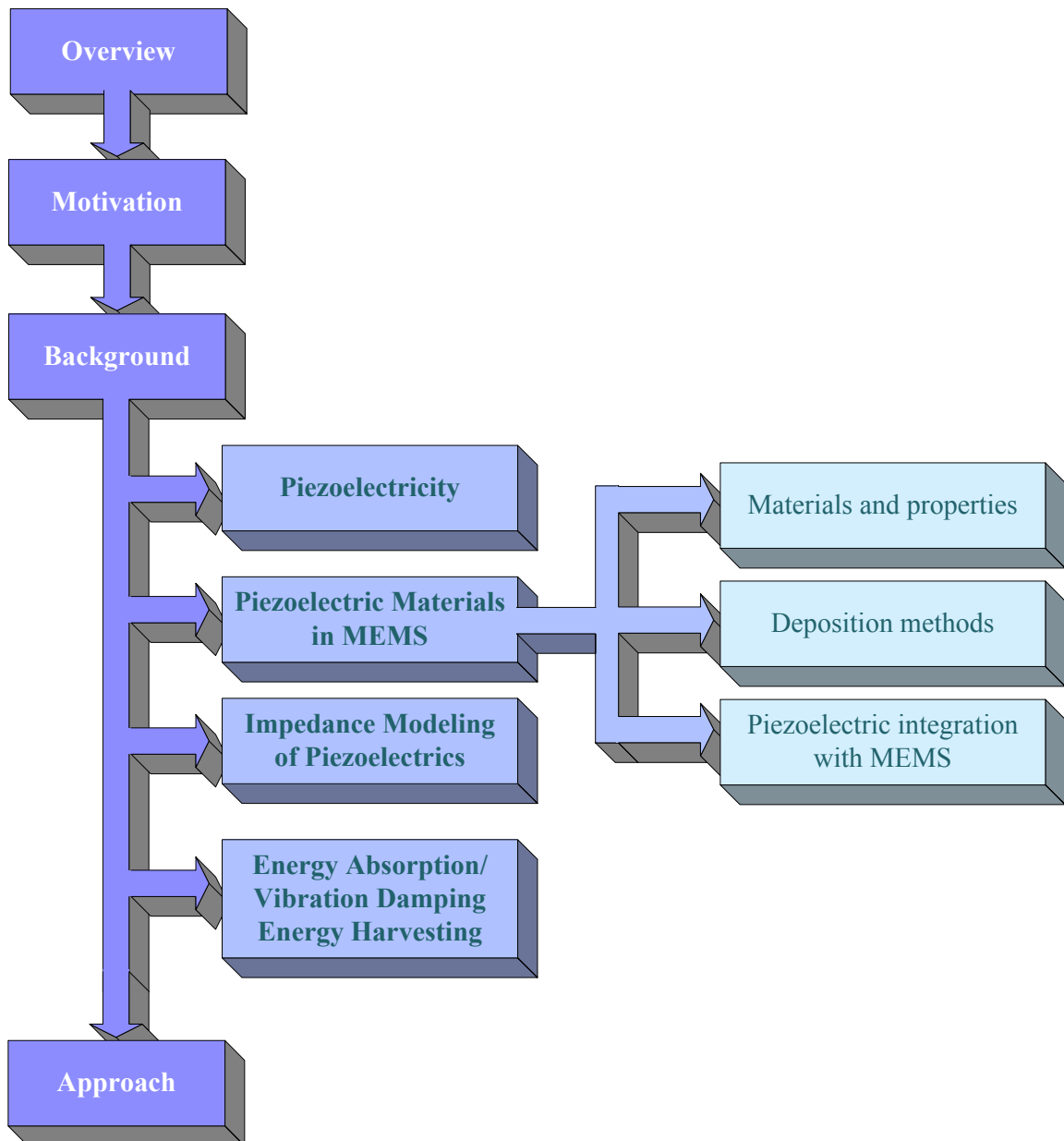


Figure 1-1: Roadmap to Chapter 1.

The electrical energy that exits the energy harvester has the same temporal form as the input acoustic signal, which we assume for now is sinusoidal. The sinusoidal signal is then routed to the energy harvesting circuitry that serves to rectify and condition the signal before sending it on to the end application. In the example illustrated in Figure 1-2, the end application is a battery that is charged by the output of the harvesting circuitry.

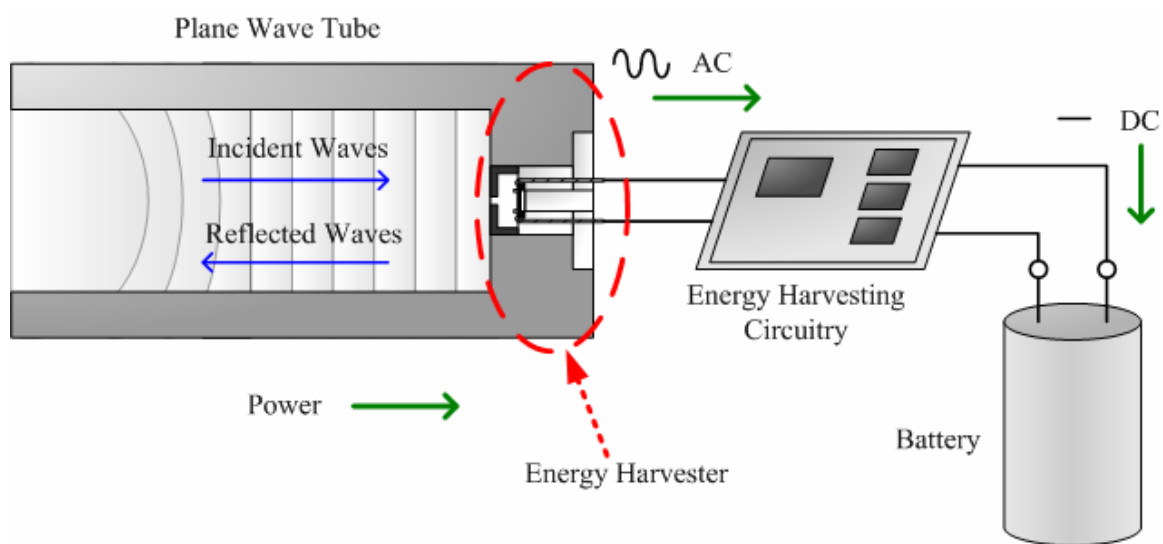


Figure 1-2: Schematic of overall energy harvesting concept.

A conceptual close-up schematic of the acoustic energy harvester is shown in Figure 1-3. This device consists of a Helmholtz resonator possessing a piezoelectric composite backplate. A Helmholtz resonator, which is a type of acoustic resonator, consists of a cavity connected to the environment through a small neck. When excited by an acoustic input, a single resonance is seen, whereby the acoustic pressure inside the cavity is amplified to a level much greater than the incident acoustic signal [1, 2].

The Helmholtz resonator is very similar to an LCR resonant circuit in electrical engineering, as shown in Figure 1-4. Both systems have a single degree-of-freedom, with a single resonant peak, whereby the amplitude of the forcing function is greatly

amplified. In the LCR circuit, the voltage is equivalent to the acoustic pressure. Both systems operate through the oscillation of energy between generalized potential and kinetic forms. In electrical systems this storage occurs via capacitors and inductors respectively. These electroacoustic analogies will be explained in more detail in Chapter 2.

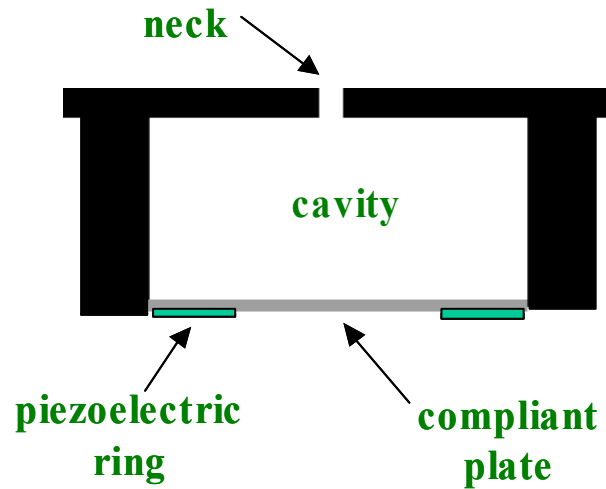


Figure 1-3: Conceptual schematic of the acoustic energy harvester.

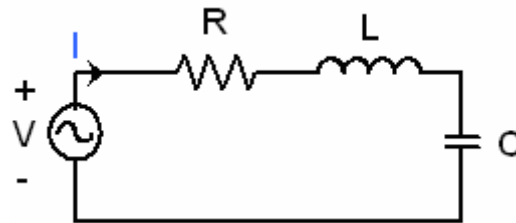


Figure 1-4: Basic LCR electrical circuit.

The large acoustic cavity pressure created by the resonance can then be exploited for energy reclamation by converting the acoustic energy to electrical energy. This conversion is performed by the piezoelectric composite plate. First, acoustical to mechanical transduction is accomplished via the compliant diaphragm, followed by mechanical to electrical transduction, due to the piezoelectric response of the composite, whereby a mechanical strain creates an electrical voltage.

The voltage that is created through the electromechanical transduction can be harvested by the energy harvester circuit, which is a necessary part of the energy harvesting process. The necessity arises due to the need to match impedances at interfaces. As will be derived in Chapter 2, the power transfer across an interface is maximized when the impedances on each side of the interface are complex conjugates of each other. This is often referred to as impedance matching. One role of the energy harvesting circuit is to provide an input impedance that matches the output impedance of the piezoelectric structure. Additionally, the harvesting circuit converts the form of the electrical energy to a more appropriate form for storage, such as converting from AC to DC.

In one implementation, a rectifying switched capacitor circuit is used to efficiently convert the AC signal to DC that is then stored across a low-loss capacitor [3]. Another possibility is based on the Kymissis circuit approach [4]. This approach utilizes passive storage elements for impedance matching coupled with a regulated output, for improved energy harvesting performance.

Motivation

Acoustic energy is commonly present in a variety of everyday situations. The motivation behind this research is to enable the reclamation of that energy that would otherwise be lost. Although the available acoustic energy may be small in many situations, the energy requirements for certain applications such as microsensing are also correspondingly small. The ability to reclaim acoustic energy and store it in a usable electrical form enables a novel means of supplying power to relatively low power devices.

Background

Piezoelectricity

In 1880, the brothers Pierre and Jacques Curie discovered that some crystals developed surface charges when compressed [5]. They furthermore found that these charges were proportional to the applied pressure. This phenomenon was later named “piezoelectricity” by Wilhelm Gottlieb Hankel, and is historically referred to as the direct piezoelectric effect [5]. Additionally, in these same crystals, a strain is produced under application of an electrical field. This is commonly referred to as the converse piezoelectric effect. The material constant relating strain and charge in a piezoelectric material is known as the piezoelectric charge modulus, d , and is typically quoted in units of pC/N or pm/V . In order for a material to be piezoelectric, it must have a non-centrosymmetric crystal structure.

It was not until 1921, that a useful application was developed for piezoelectricity. It came in the form of a quartz crystal oscillator that was developed by Walter Cady to provide good frequency stability for radio systems [5, 6]. Then, in 1947, the first commercial phonograph pickups based on barium titanate ($BaTiO_3$), a piezoelectric ceramic, were introduced [6]. Modern applications of piezoelectric materials now include high voltage ignition systems, piezoelectric motors, ink-jet printer heads, acoustic speakers, sonar, ultrasonic transducers, frequency filters, acoustic delay lines, electrical transformers, and a wide range of physical sensors, such as acoustic, force, pressure, and acceleration sensors [6].

Piezoelectric Materials in MEMS

A number of papers have been published on the use of piezoelectric and ferroelectric materials in MEMS [6, 7]. Piezoelectric materials commonly used include

zinc oxide (ZnO), aluminum nitride (AlN), and lead zirconate titanate (PZT). The choice of piezoelectric material depends on several selection factors including deposition methods, process complexity, integrated circuit (IC) compatibility, and material parameters.

Materials and properties

Of the three commonly used materials, PZT offers the largest piezoelectric modulus [6]. In comparison to PZT, AlN and ZnO have relatively weak piezoelectric coefficients and coupling factors, however they tend to have low dielectric constants and low dielectric losses, making them more attractive for certain applications [8]. A table of typical material properties is shown in Table 1-1 for comparison; however these properties are highly dependent on the deposition method, as will be described in more detail shortly.

Table 1-1: Typical material properties of select piezoelectric materials.

	d_{31}	d_{33}	$\epsilon_{33,r}$	E	ρ
	[pC/N]	[pC/N]		[GPa]	[kg/m ³]
PZT[6]	-130	290	1300	96	7.7
AlN[8]	n/a	3.4	10.5	330	3.26
ZnO[9-11]	-4.7	12	12.7	210	5.6

In Table 1-1, d_{31} is the piezoelectric coefficient relating electrical displacement in the ‘3’ direction (z-axis) to a mechanical stress in the ‘1’ direction (x-axis) and is the relevant coefficient for bending-mode transducers, whereas d_{33} relates the electrical displacement in the ‘3’ direction (z-axis) to a mechanical stress in that same direction. The coefficient, d_{33} , is thus the relevant coefficient for compression-mode transducers. Additionally, $\epsilon_{33,r}$, E , and ρ are the relative dielectric constant, Young’s modulus and mass density of the materials, respectively.

Of the three materials, only AlN is fully compatible with standard IC processing, eliminating the integration difficulties present with PZT and ZnO. PZT poses a particular integration challenge, as lead contamination is always a big concern; however, PZT has been integrated successfully into ferroelectric random-access memory (FRAM) [12-14], typically using sputtered platinum as a bottom electrode and diffusion barrier layer.

Deposition methods

Piezoelectric deposition techniques include various sputtering methods, photo-ablation [15], hydrothermal and chemical vapor deposition (CVD) techniques, and spin-on sol-gel processing. For deposition of PZT, three popular methods are sputtering, sol-gel and hydrothermal techniques. The earliest work used various forms of sputtering to deposit PZT [16-22] followed soon after by CVD [23]. Castellano and Feinstein [16] used an ion-beam sputtering technique to deposit PZT as did Trolrier-McKinstry et al., [22] while Sreenivas et al. [17] employed DC magnetron sputtering in their PZT deposition. Additionally, sputter deposition of PZT thin films was performed by Kawabata et al. [24] and Li et al. [25]. Dubois and Muralet [8] deposited PZT using two different methods. One method involved a sol-gel process and produced an average thickness of 900 *nm*. The other method used reactive sputtering and achieved a thickness of approximately 500 *nm*.

Hydrothermal deposition relies on a chemical reaction between a titanium bottom electrode and ionic solution under high temperature and pressure. Deposition of 10 μm thick PZT by hydrothermal techniques was performed by Kanda et al. [26] for use in a touch probe sensor. Additionally, Morita et al. [27-30] chose to deposit PZT by the hydrothermal method due to the relatively large thicknesses achievable and the self-alignment of the poling direction during deposition.

More recently, numerous researchers have utilized the sol-gel process for deposition of PZT [31-47]. In particular, Bahr et al. [31] used a sol-gel PZT process and investigated the reliability and piezoelectric properties of the resulting material. Using this process for various film thicknesses, the relative dielectric constant, $\epsilon_{33,r}$, varied between 700 and 1000 and delamination occurred for an indentation load of $1250 \mu N$ for a film sintered for 5 minutes. Higher loads were found to be achievable using longer sinter times. Bernstein et al. [32] and Xu et al. [33] used a sol-gel process to achieve crack-free PZT films with thicknesses of up to $12 \mu m$ that yielded piezoelectric properties close to the bulk values for PZT. A dielectric constant of 1400 and a piezoelectric coefficient, d_{33} , of $246 pC/N$ were reported on a $4 \mu m$ thick film. The PZT films were used on an array of membranes for acoustic imaging. Kunz et al. [37] report a piezoelectric coefficient, d_{31} , of $110 pC/N$ for a sol-gel deposited PZT film used in a triaxial accelerometer. Zurn et al. [48] report similar material properties for sol-gel deposited PZT on a microcantilever, including a d_{31} of $120 pC/N$ for a PZT film thickness of $0.5 \mu m$ deposited on a low-stress silicon nitride layer. A summary table of deposited thin film piezoelectric materials and their properties, as reported in the literature, is given in Table 1-2. In this table, e_{31} is a piezoelectric coefficient relating mechanical stress and an electric field, $\tan \delta$ is called the loss tangent and is a measure of the relative losses in the material, and σ_{res} is the residual stress in the material, while the other properties are as previously defined.

Piezoelectric integration with MEMS

Some of the earliest integration of piezoelectric materials with MEMS focused primarily on ZnO [49, 50] and AlN [49] as the piezoelectric material. More recently,

Devoe and Pisano [10] developed and characterized surface micromachined piezoelectric accelerometers that utilized thin films of ZnO for sensing. Deposition of the ZnO was performed using single-target RF sputtering and exhibited a piezoelectric coefficient of 2.3 pC/N . Also, Devoe [9] investigated micromechanical beam resonators that use ZnO and a three-mask fabrication process. The resonators are intended for use as electromechanical filters.

Table 1-2: Selected thin film piezoelectric materials and corresponding properties as reported in the literature.

Ref.	Material	Deposition Method	Properties							
			$\epsilon_{33,r}$	d_{31} $\left(\frac{\text{pC}}{\text{N}}\right)$	d_{33} $\left(\frac{\text{pm}}{\text{V}}\right)$	e_{31} $\left(\frac{\text{C}}{\text{m}^2}\right)$	E (GPa)	ρ $\left(\frac{\text{kg}}{\text{m}^3}\right)$	$\tan \delta$	σ_{res} (MPa)
[9, 10]	ZnO	RF Sputt.	12.7	2.3	--	--	161	5605	--	1...80
[11]	ZnO	Sputtered	--	--	--	--	210	5700	--	--
[8]	AlN	DC Sputt.	10.5	--	3.4	-1.02	--	--	0.002	-700
[8]	PZT (45/55)	React. Sputt.	900	--	55	-5.12	--	--	0.03	150
[8]	PZT (45/55)	Sol-Gel	1100	--	50	-8.28	--	--	0.03	70
[8]	PZT (53/47)	React. Sputt.	1300	--	70	-6.83	--	--	0.05	230
[26]	PZT	Hydrothermal	--	-34.2	--	-0.13	--	--	--	--
[31]	PZT (52/48)	React. Sputt.	700-1000	--	--	--	--	--	--	--
[32]	PZT	React. Sputt.	1400	--	246	--	--	--	0.03	--
[37]	PZT (53/47)	React. Sputt.	--	110	--	--	--	--	--	--
[42]	PZT	React. Sputt.	1100	--	--	--	--	--	--	--
[44, 45]	PZT (52/48)	React. Sputt.	800	--	-200	--	56	--	0.02	--
[48]	PZT	React. Sputt.	--	--	120	--	60	7600	--	--
[16]	PZT	IB Sputt.	125	--	--	--	--	--	--	--
[20, 21]	PZTWCd	RF Sputt.	60-460	--	30	--	--	--	--	--
[51]	PZT(X/1-X)	React. Sputt.	200-600	--	--	--	--	--	0.02	--

The integration of ZnO with micromachining was also investigated by Indermühle et al. [52], where it was used in an array of silicon micro cantilevers. The end application for the array was parallel atomic force microscopy. Another application of ZnO was performed by Han and Kim [11] in the fabrication of a micromachined piezoelectric ultrasonic transducer. They sputter deposited ZnO on Al, followed by a layer of parylene

for insulation. Dubois and Muralt [8] fabricated thin films of RF sputtered AlN and performed measurements of the effective transverse piezoelectric coefficient that yielded a value of 3.4 pm/V .

Reduced-Order Modeling of Piezoelectric Materials

The development of accurate, practical models of the piezoelectric transduction and associated structural interactions is critical to the design and behavioral prediction of piezoelectric based devices, particularly when micromachining is involved. For a micromachined device, considerable time and expense must be invested in the fabrication, and it is therefore desirable to have some ability to predict the device behavior before proceeding with fabrication.

Behavioral prediction can be accurately accomplished using complete analytical methods. However, these methods, which often involving partial differential equations, can often be unwieldy and physically unintuitive. Furthermore, this functional form is not readily conducive to a full systems level design that links the transducer to electronics. Similarly, finite element modeling (FEM) techniques are often used to predict system behavior, numerically. The results produced by this technique can very precisely follow the physical system; however, the physical insight that can be gleaned is limited. Additionally, it is very difficult to determine scaling behavior from FEM results. The scaling behavior, i.e., the change in the system performance as the entire system is scaled up or down, is a critical design issue in the creation of devices using micromachining technology. In order to facilitate a physics-based approach for design, a simplified, reduced-order model is necessary that accurately captures the geometric and

material dependencies. This reduced-order model uses lumped elements to represent the key components that dominate the device behavior.

In 1915, Butterworth [53] first showed that any mechanical oscillator, when driven by a periodic voltage across a capacitor, would have an equivalent electrical circuit consisting of a resistance, inductance and capacitance in series, and all in parallel with another capacitance. Working independently, the earliest equivalent circuit model specifically for piezoelectric materials was developed by Van Dyke in 1925 [54-56]. Later, Dye [57] proved that Van Dyke's circuit could be derived from Butterworth's theorem. Additionally, Mason [58, 59] and Cady [5] provided thorough reviews of the equivalent circuit model and associated equations for quartz oscillator applications. Finally, Fischer [60] extensively covered equivalent circuit models for electromechanical oscillators.

Significant research has been performed on the modeling of structures containing piezoelectric materials. [38, 41, 61-94] Cho et al. [61, 65] developed a five-port generalized equivalent circuit for a piezoelectric bimorph beam. The generalized circuit can be used under a variety of boundary conditions. In these papers, three boundary conditions are specifically analyzed – free, simply supported, and cantilevered. For these boundary conditions, the equivalent circuit was found to produce the exact expressions for the beam vibration. Other equivalent circuits were developed by Martin [68] for resonators with low Q values, Sheritt et al. [69] for thickness vibrators, Lin [67] for coupled ceramic disk resonators, and Chen et al. [68] for coupled resonant filters. Tilmans [94] also presented an equivalent circuit approach for modeling distributed parameter systems. Liang et al. [66] developed a generalized electromechanical

impedance model that was then used to address issues of energy conversion, power consumption, and dynamic response. The approach described can be used for any system for which the driving-point impedance can be found either analytically or experimentally. Additionally, van de Leur [91] provided a critical interpretation of equivalent circuit models obtained from impedance measurements, indicating that care must be taken in identifying individual components contributing to an impedance as resulting from particular structures in a given device. This can be further understood as an example of the non-uniqueness of equivalent circuit representations, i.e., more than one equivalent circuit can represent the same impedance. Additionally, Lesieutre and Davis [87] provided insight into the piezoelectric coupling coefficient, including a technique whereby an outside stress is applied to increase the effective device coupling coefficient beyond the coupling coefficient of the material itself.

Research into coupled resonators and their unique properties is a related and also relevant topic since the acoustic energy harvester involves mating the piezoelectric composite diaphragm to a Helmholtz resonator, resulting in a coupled resonant system. Fischer [60] provided an early treatment of coupled resonant systems. Chen et al., [72], Lin [71, 95], and Li et al. [96] also discuss modeling and design of coupled resonant systems. These papers address some of the issues involved in coupled resonators, including the shift in resonant frequencies away from their uncoupled values.

Energy Absorption/Vibration Damping and Energy Harvesting

The absorption of acoustical and mechanical energy via piezoelectric coupling is closely related to the harvesting of electrical energy from acoustical and mechanical energy sources. From the acoustical point of view, acoustical energy that is converted to the electrical domain and dissipated across a resistive load can be viewed as being

absorbed. From the electrical point of view, the incident acoustical energy can be viewed as an energy source that may theoretically be harvested and used immediately for electrical subsystems or stored for later use. Because of the related nature of these two fields, papers that address either of these fields are directly relevant to acoustic energy harvesting.

Some of the earliest work in piezoelectric vibration damping was performed by Hagood and von Flotow [97] who used resistive and inductive elements in various shunt networks designed to dissipate mechanical energy. A few years later, Hollkamp [98] discussed the use of resonant electrical shunt circuits for multi-modal vibration suppression. In addition, numerous other researchers have investigated piezoelectric means of vibration damping [99-108]. More recently, Caruso [109] discusses electrical shunt circuits for damping of vibrations, as does Wu et al. [110] for damping of panels on an F-15 aircraft.

Additionally, a number of papers directly address the issue of obtaining electrical energy from piezoelectric conversion of mechanical energy [3, 4, 111-117]. Early work in this area was performed by Lomenzo et al. [114] and Stein et al. [116]. Later, Kymissis' [4] and Smalser's [3] work focuses on the electrical circuitry necessary for storage of piezoelectrically generated energy, while Meninger [115] discusses energy harvesting from an electrostatic transducer. Goldfarb and Jones, [111] Giurgiutiu and Rogers [112, 113] and Zhou and Rogers [117] utilize impedance modeling of the piezoelectric and associated structure to analyze the ability to harvest energy.

Approach

The approach taken in this research is to divide the concept of an acoustical energy harvester into three distinct components as shown previously in Figure 1-2. The first

component consists of a piezoelectric composite diaphragm that is responsible for the acoustical to electrical transduction of energy. The second component, which is the packaging, serves as a means to improve the acoustical coupling to the environment. The third and final component is the electrical circuitry that takes the alternating current (AC) electrical signal from the piezoelectric diaphragm and converts it into a direct current (DC) output that can be stored for later use. The first two components of the energy harvester were developed in this research, while the conversion circuitry remains an ongoing research topic in our group [118-120]. Furthermore, a macroscale version of an acoustic energy harvester was previously developed [120] and, through miniaturization, led to the present MEMS-based energy harvester.

Chapter 2 presents a theoretical background on various aspects of this research including lumped element modeling of the complete system as well as individual components along with predictions of the dynamic behavior. Chapter 3 discusses the fabrication of the piezoelectric diaphragm and the packaging scheme employed. Following this, the experimental setup is provided in Chapter 4, including a discussion of the measurements that were taken. Then, in Chapter 5, the experimental results are presented. Chapter 6 addresses an alternate application that has been explored, while Chapter 7 presents the conclusions and a statement of the contributions to this research. Finally, Appendix A presents the Matlab program code for computing the diaphragm deflection and calculating the lumped element values, while Appendix B provides a detailed process flow, mask layout, and packaging design

The main contributions of this dissertation are as follows:

- Acoustic energy harvesting concept

- Comprehensive lumped element model (LEM) of the acoustic energy harvester
- First reported integration of thin-film PZT with SOI-based MEMS
- First aeroacoustic capable piezoelectric microphone.

CHAPTER 2 THEORETICAL BACKGROUND

This chapter focuses on the theory and modeling of the acoustic energy harvester and each of its components. The chapter begins with an overview of energy harvesting, followed by an introduction to lumped element modeling, by discussing both its utility and limitations. This is followed by the development of a lumped element model for a Helmholtz resonator and the corresponding equivalent circuit. Next, the modeling of piezoelectric composite circular plates is addressed. To achieve this, an equivalent circuit is presented and general equations are discussed. Then specific limiting cases are addressed that simplify the analysis. Finally, the overall dynamic behavior of the system is theoretically investigated, including the acoustical input and electrical output behavior. A graphical overview of this chapter is provided by the roadmap of Figure 2-1.

Overview—Energy Harvesting

The general concept behind energy harvesting is to convert energy from the environment that is in an otherwise unusable form into a more useful form. Often the form of energy that is most useful in modern applications is electrical energy, where it can be stored in a battery or used to power electrical circuitry. The initial form of energy can originate from any number of energy domains, such as optical, thermal, mechanical, acoustical, fluidic, chemical, and biological. Some form of transducer is then required to convert that energy to a usable form of electrical energy. Depending on the situation, that also may require passage of the energy through an intermediary energy domain..

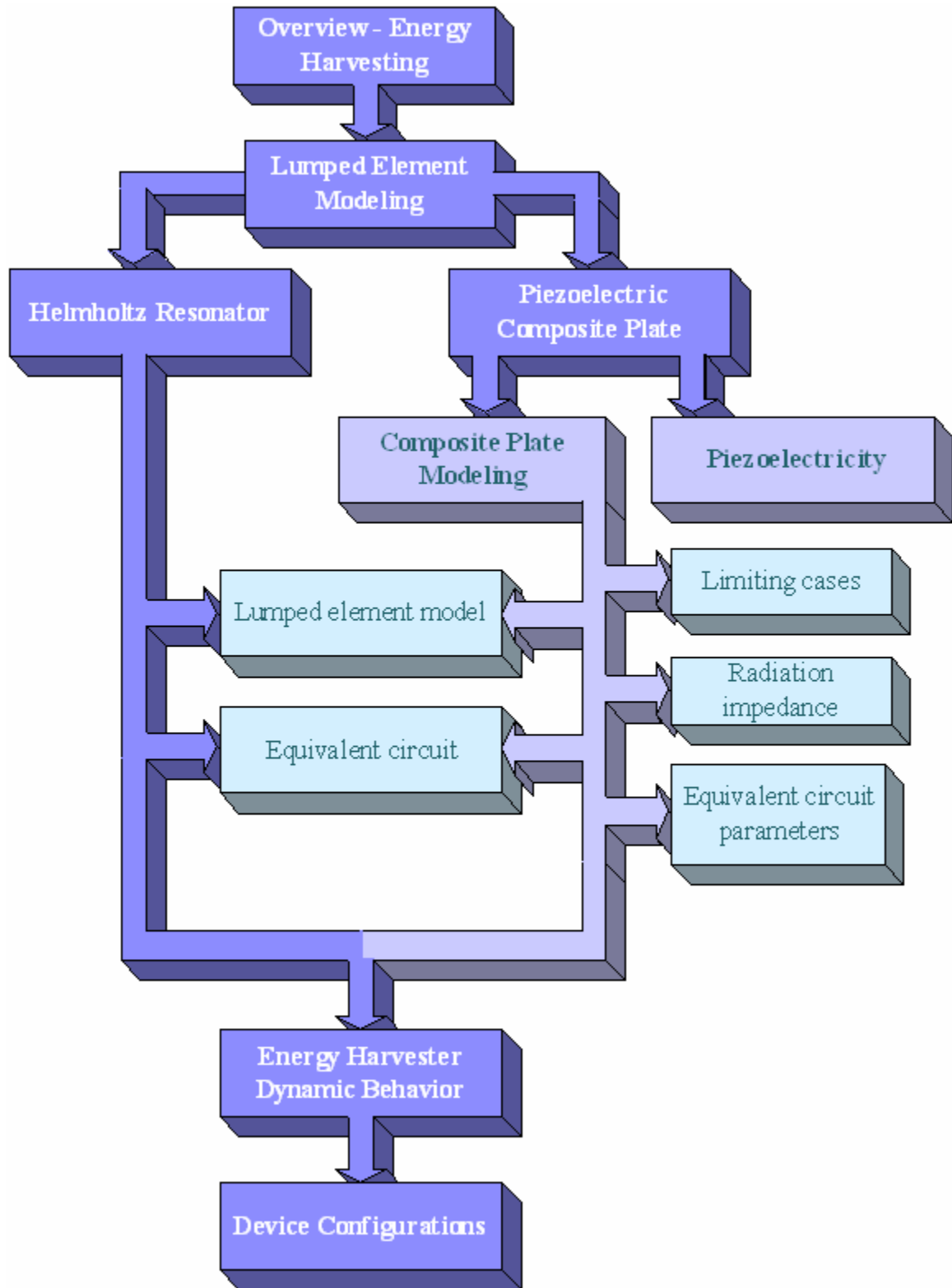


Figure 2-1: Roadmap to Chapter 2.

There are pros and cons to each of these different local energy sources [121]. Some energy sources such as solar power utilize the optical energy domain to achieve high power densities on the order of $15,000 \mu\text{W}/\text{cm}^2$ in direct sunlight. The main downside is that direct sunlight is not always available. Vibrational energy, on the other hand, offers power densities up to $250 \mu\text{W}/\text{cm}^2$. While this is considerably lower than solar energy, it is useful in places without sunlight but where high vibrational energy is available.

Acoustic energy, in a manner similar to vibrational energy, offers power densities on the order of $1 \mu\text{W}/\text{cm}^2$ for a 100 dB acoustic signal [121], or approximately $964,000 \mu\text{W}/\text{cm}^2$ at 160 dB . While most signals are typically much lower than 160 dB , there are applications where such high levels are present. Additionally, as with vibrational energy, acoustic energy, does not require the presence of sunlight.

Chemical energy sources are commonly employed today in the form of batteries and fuel cells. Batteries typically offer power densities in the range of $45 \mu\text{W}/\text{cm}^3$ for non-rechargeables, and $7 \mu\text{W}/\text{cm}^3$ for rechargeable lithium batteries [121]. Fuel cells employing methanol, on the other hand, offer power densities as high as $280 \mu\text{W}/\text{cm}^3$, leading to the current interest in fuel cell development [121]. Additionally, a micro-combustion engine that employs hydrocarbons as a fuel source realizes power densities of $333 \mu\text{W}/\text{cm}^3$ [122]. The downside to these types of chemical energy sources is the limited supply of energy. Used batteries must either be replaced or recharged and fuel cells require refueling for continual operation. By contrast, the scavenged energy sources, such as vibrational, solar, and acoustical do not theoretically have a limited supply of energy, given the right operating environment.

For the particular application considered in this dissertation, the initial energy is in the form of acoustical energy. In order to convert acoustical energy into electrical energy, a diaphragm based transducer is utilized. The diaphragm transducer utilizes the mechanical energy domain as an intermediary to transfer energy.

Maximum Average Power Transfer

Regardless of the route through which the energy passes, certain fundamental issues must be addressed in order to maximize the amount of energy that is harvested. Whenever a change in impedance is encountered by a traveling wave, a reflection of all or part of the energy in that wave occurs, while the remaining energy is transmitted. The procedure for maximizing the energy focuses on minimizing the reflected component and thus maximizing the transmitted component. This is achieved by matching the impedance along the route traveled by the energy. As long as the impedance at a given interface is matched, complete transmission of the energy will occur, regardless of whether or not the two sides of the interface are in the same energy domain. Often it is not possible to match an impedance exactly, due to external and physical constraints on the system, however it is generally still desirable to match the impedances as closely as possible in order to optimize for maximum energy within those constraints [2, 123].

Additionally, one must consider that power is a complex quantity. The total power, which is generally complex, is composed of real power and reactive power. The real power is the physical power that is delivered to the load, while the reactive power represents energy that is temporarily stored in the load, before it returns to the source. When designing an energy harvesting system, it is generally preferable to maximize the real power rather than the total power, as it is only the real power that is ultimately retained by the load.

It is useful to look at a Thévenin equivalent circuit, as shown in Figure 2-2, in order to determine the maximum achievable power transfer to a load [124]. Assuming sinusoidal voltage and current, the average real power delivered to the load is

$$\Pi_L = \frac{1}{2} V_L I_L \cos(\theta_{V_L} - \theta_{i_L}), \quad (2.1)$$

where V_L and I_L are the peak magnitudes of the voltage and current at the load, and θ_{V_L} and θ_{i_L} are the phase angles of the voltage and current respectively. This can be rewritten as

$$\Pi_L = \frac{1}{2} V_L I_L (pf), \quad (2.2)$$

where pf is the power factor, defined by the ratio of average power to apparent power and is given by

$$pf = \frac{\Pi_L}{V_{rms} I_{rms}}, \quad (2.3)$$

where V_{rms} and I_{rms} are the root-mean-square voltage and current, respectively.

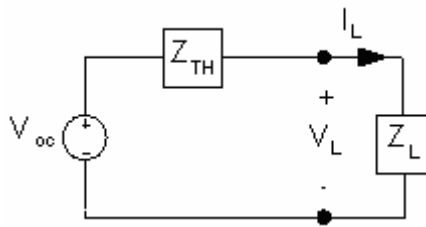


Figure 2-2: Thévenin equivalent circuit for purposes of maximizing power transfer.

Using basic circuit analysis, the load voltage and current can be expressed in terms of the open circuit voltage, V_{oc} , the Thévenin equivalent impedance Z_{TH} , and the load impedance, Z_L . The expressions are given as

$$V_L = \frac{V_{oc} Z_L}{Z_{TH} + Z_L} \quad (2.4)$$

and

$$I_L = \frac{V_{oc}}{Z_{TH} + Z_L}, \quad (2.5)$$

where the Thévenin equivalent impedance, $Z_{TH} = R_{TH} + jX_{TH}$, and the load impedance can be written as $Z_L = R_L + jX_L$. Plugging these expressions back into Eq. (2.4) and Eq. (2.5) and separating out the magnitude components yields

$$|V_L| = \frac{V_{oc} (R_L^2 + X_L^2)^{\frac{1}{2}}}{\left[(R_{TH} + R_L)^2 + (X_{TH} + X_L)^2 \right]^{\frac{1}{2}}} \quad (2.6)$$

and

$$|I_L| = \frac{V_{oc}}{\left[(R_{TH} + R_L)^2 + (X_{TH} + X_L)^2 \right]^{\frac{1}{2}}}. \quad (2.7)$$

The phase angle between the voltage and current can also be expressed as $\theta_{V_L} - \theta_{i_L} = \theta_{Z_L}$, where θ_{Z_L} is the phase angle of the impedance. The power factor can be defined as

$$pf = \cos \theta_{Z_L} = \frac{R_L}{(R_L^2 + X_L^2)^{\frac{1}{2}}}. \quad (2.8)$$

Plugging this expression into Eq. (2.1), together with Eq. (2.6) and Eq. (2.7) yields

$$\Pi_L = \frac{1}{2} \frac{V_{oc}^2 R_L}{(R_{TH} + R_L)^2 + (X_{TH} + X_L)^2}. \quad (2.9)$$

As, the quantity $(X_{TH} + X_L)$ is only in the denominator, any nonzero value reduces the overall power absorbed by the load, thus $X_L = -X_{TH}$ is optimal and reduces Eq. (2.9) to

$$\Pi_L = \frac{1}{2} \frac{V_{oc}^2 R_L}{(R_L + R_{TH})^2}. \quad (2.10)$$

This expression can be maximized by differentiating this expression with respect to R_L and equating the derivative to zero, yielding an optimal value of $R_L = R_{TH}$. The average power to the load can be maximized, then, by setting the load impedance to

$$Z_L = R_L + jX_L = R_{TH} - jX_{TH} = Z_{TH}^*, \quad (2.11)$$

where Z_{TH}^* is the complex conjugate of the Thévenin impedance. This derivation assumes total freedom in the choice of the load impedance.

Under the constraint of a purely resistive load, where $X_L = 0$, the equation given in Eq. (2.9) can be differentiated directly and set equal to zero with $X_L = 0$, in order to find the maximum average power transfer. This procedure yields an optimal value for the load resistance of

$$R_L = \sqrt{R_{TH}^2 + X_{TH}^2} = |Z_{TH}|, \quad (2.12)$$

under the constraint of a purely resistive load.

Electromechanical Transducers

A transducer can be broadly defined as an interface between any two energy domains, including optical, thermal, mechanical, electrical, acoustical, fluidic, chemical, and biological. Typically, transducers are broadly classified into two main categories: sensors and actuators. The breakdown among these classifications relates to the direction of information flow. Sensors are transducers that convert information from the environment into a form that is more easily analyzed, recorded or processed. Actuators, on the other hand, take information from this form and convert it into a form that more

readily interacts with the intended environment. Both types of transducers are mainly concerned with the way in which the information is utilized.

The classifications described above focus on the information aspect of a given signal that is encoded in either the effort or flow, but not their product. As such, these types of transducers are optimized for transmission of information in one direction or another. Besides information, a signal carries power. A third type of transducer exists that falls under neither category and can be best described as an energy harvester. The concept behind the energy harvester is to achieve an optimal amount of average power transfer between energy domains. Instead of optimizing sensitivity or dynamic range, an energy harvester is optimized for efficiency and maximum average power transfer.

Additionally, actuators and especially sensors are designed as linear devices in order to facilitate a straightforward relationship between input and output. The linear input-output relationship ensures that the problem of calculating their behavior is tractable, and is necessitated by the information contained in the signal. Energy harvesters, on the other hand, do not necessarily require a linear input-output relationship as only the power is of interest. Some details of the input may get lost in the nonlinear transduction, but only the power at the output is needed.

There are a wide range of transduction techniques available that couple the mechanical and electrical energy domains, including electrostatic, electrodynamic, piezoresistive and piezoelectric [1, 125]. Each technique offers various tradeoffs among performance, reliability, and material integration. Transducers can be separated into two types, direct and indirect, based on the way they interact with energy. Direct transducers, as the name implies, directly transduce energy between the two energy domains. Indirect

transducers, however, rely upon a second energy source that modulates the primary energy source as it passes through the transducer. The inherent nature of indirect transduction leads to a lower transduction efficiency as compared to direct transduction.

Electrodynamic transduction, a direct transduction mechanism, yields high coupling efficiencies. Additionally, this method uses no outside power source in order to operate. The transduction is essentially powered by the input signal itself. Despite these advantages, electrodynamic transduction suffers from difficulty in integrating the particular required materials, such as copper or magnetic materials, into a standard IC process line. Additionally, the necessary fabrication is often more complex than the other techniques discussed here.

Piezoelectric transduction requires no outside source of power other than the input signal, and offers a high sensitivity, with a potentially low noise floor. The main disadvantages are the difficulty in integrating the piezoelectric materials into a standard process flow, and the limited coupling efficiency due to indirect transduction of energy.

Lumped Element Modeling

The most accurate, complete, mathematical description of a physical system is a physics-based model, supported by an exact analytical expression for the system behavior. Why then are alternative modeling techniques commonly used? These alternative methods, such as lumped element modeling (LEM), and finite element modeling (FEM), excel in predicting system behavior in situations where an exact, analytical approach is unwieldy or impossible. Additionally, it is not uncommon to have an exact mathematical description of a system that allows for precise prediction of device behavior, but is so complex that it offers little in the way of physical insight into the

design and scaling system. Often, the exact solution is in a mathematical form that, while convenient for behavioral prediction, conceals the underlying physics.

Similarly, FEM techniques can accurately predict system behavior, in this case via a numerical approach. The results produced by this technique can very precisely follow the physical system; however, the physical insight that can be gleaned is limited. Furthermore, the results depend on the numerical mesh and convergence of the iterative calculations. In particular, it is very difficult and/or cumbersome to determine scaling behavior from FEM results. The scaling behavior, i.e. the change in the system performance as the entire system is scaled up or down, is a critical design issue in the creation of devices using micromachining technology.

In order to efficiently understand the physics behind a given systems response and also to fully appreciate the scaling laws for that system, it is necessary to employ LEM [1, 60]. The concept behind LEM is to reduce the complexity of an analytical or numerical expression by breaking down a given distributed system into discrete elements based on how the system interacts with energy [60, 126]. More specifically, the total energy going into any given system is divided among three distinct types of interactions: the storage of kinetic energy, the storage of potential energy, and the dissipation of energy. All systems are composed of these three energy processes.

In some systems, known as distributed systems, the storage of kinetic and potential energy occurs over a distributed region in space [90, 127]. To accurately represent these systems mathematically requires a partial differential equation, as spatial and temporal components are inherently coupled. Physically, the distribution occurs because the wavelength is on the order of the physical system or smaller. At different points along

the period of the wave, differing amounts of energy are split among the energy storage and dissipation mechanisms.

As the wavelength of the signal (e. g. acoustical, fluidic, mechanical, optical, etc....) gets larger, to where it is significantly larger than the length scale of interest, very little variation occurs in the distribution of energy as a function of space.

Mathematically, under these conditions, the spatial and temporal components can be decoupled, allowing for the use of ordinary differential equations to solve the problem, rather than partial differential equations. Physically, it means each energy storage or dissipation mechanism can be equated to the energy stored or dissipated in an equivalent element that is lumped to a chosen spatial location.

In various energy domains, the names for the types of lumped elements vary; however, the concept and mathematics remain the same. In lumped mechanical systems, kinetic energy is stored via mass, potential energy via the compliance of a spring (i.e. inverse of stiffness), and dissipation of energy through the losses of a damper. Similarly, in electrical systems, where lumped element systems are commonplace due to the extremely long wavelengths of electrical signals, kinetic energy is stored in the magnetic field of an inductor, while potential energy is stored in the charge across a capacitor. Additionally, dissipation of energy is modeled via the resistor. Finally, in lumped acoustical systems, the kinetic and potential energy is stored in an acoustical mass and acoustical compliance, respectively, while dissipation of energy is represented by an acoustic resistance. These elements are summarized in Table 2-1.

The commonplace nature of lumped elements in electrical systems has led, over the years, to a large growth in graphical and analytical techniques to solve large networks of

interconnected elements. These networks are most commonly represented using electrical circuit notation. A significant benefit of lumped element modeling is that in all of the energy domains, the lumped elements can be represented using an equivalent circuit form. Thus, masses can be represented using inductors, compliances using capacitors, and dissipative components using resistors. Once the complete equivalent circuit is constructed, standard circuit analysis techniques (e.g. Kirchoff's current and voltage laws) can be applied to find the solution of interest.

Table 2-1: Equivalent lumped elements in several common energy domains.

	Kinetic Energy Storage	Potential Energy Storage	Energy Dissipation
Acoustical	Acoustic Mass [kg/m^4]	Acoustic Compliance [m^3/Pa] or [m^5/N]	Acoustic Resistor [$m^4 s$]
Mechanical	Mass [kg] (pt mass)	Compliance [m/N] (spring)	Frictional Damper [$m \cdot s$]
Electrical	Inductance [H]	Capacitance [F]	Resistance [Ω]

Whenever dealing with more than one lumped element, the concept of power flow between the elements must be considered. If we define the power flow from element A to element B as Π_{AB} and the reverse as Π_{BA} , then the net power flow from A to B is

$$\Pi_{net} = \Pi_{AB} - \Pi_{BA}. \quad (2.13)$$

Now, since each of the power flows must be greater than or equal to zero, then they can each be written as the square of a real number, r_1 and r_2 [128]. The net power flow can then be rewritten as

$$\Pi_{net} = r_1^2 - r_2^2 = (r_1 + r_2)(r_1 - r_2). \quad (2.14)$$

It is therefore seen that the net power flow can be written as the product of two real numbers, which are referred to as conjugate power variables. Moreover, these quantities

are more specifically referred to as an effort, e , and a flow f , where the product $e \cdot f$ is the power. A table of conjugate power variables, divided into effort and flow, is given in Table 2-2 for a number of energy domains.

Table 2-2: Conjugate power variables .

Energy Domain	Effort	Flow
Mechanical translation	Force, F	Velocity, v
Fixed-axis rotation	Torque, τ	Angular velocity, ω
Electric circuits	Voltage, V	Current, I
Magnetic circuits	MMF, \mathfrak{M}	Flux rate, $\dot{\phi}$
Incompressible fluid flow	Pressure, P	Volumetric flow, Q
Thermal	Temperature, T	Entropy flow rate, \dot{S}

(after Senturia, pg 105 [128])

Helmholtz Resonator

Lumped Element Model

LEM was applied to the Helmholtz resonator in order to better understand the system [1, 125]. A schematic diagram of a Helmholtz resonator is shown below in Figure 2-3, where V is the cavity or bulb volume, l and $S = \pi a^2$ are the length and cross-sectional area of the neck, respectively, where a is the radius of the neck, P_1' is the incident acoustic pressure, and P_2' is the cavity acoustic pressure. Both P_1' and P_2' are considered to be functions of the radian frequency, ω .

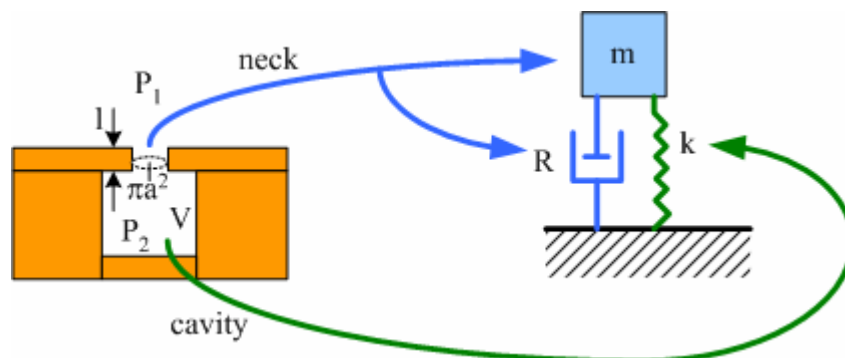


Figure 2-3: Diagram showing side view of a Helmholtz resonator and its mechanical equivalent of a mass-spring-damper system.

A conventional Helmholtz resonator can be lumped into three distinct elements. The neck of the resonator constitutes a pipe through which frictional losses are incurred. Additionally the air that is moving through the neck possesses a finite mass and thus kinetic energy. Therefore the neck has both dissipative and inertial components. The air in the cavity is compressible and stores potential energy, and is therefore modeled as a compliance.

The acoustic compliance of the cavity and effective mass of the neck can be derived from first principles. [129] As mass flows into the bulb, the volume, V , remains constant, assuming the walls are rigid, and so the pressure must rise, by conservation of mass.

$$\frac{dM}{dt} = V \frac{d\rho(t)}{dt} \equiv Q\rho_o \rightarrow \text{mass flow rate} \left[\frac{\text{kg}}{\text{s}} \right], \quad (2.15)$$

where M is the mass in the bulb, ρ_o is the mean density of the air, and $Q = u(\pi a^2)$ is the volumetric flow rate or volume velocity, where u is the velocity. If the disturbance is harmonic and isentropic then

$$P'_2 = c_o^2 \rho_o = \frac{c_o^2 Q \rho_o}{j\omega V}, \quad (2.16)$$

where c_o is the isentropic speed of sound of the medium and $j = \sqrt{-1}$.

The linearized momentum equation for a lossless medium is given by

$$\rho_o \frac{\partial u}{\partial t} = -\nabla P', \quad (2.17)$$

where P' is the acoustic pressure. Assuming a linear pressure gradient yields

$$P'_1 - P'_2 = \rho_o \frac{\partial u}{\partial t} l, \quad (2.18)$$

where l is the length of the neck. Substituting for P_2' yields the following equation.

$$P_1' = \frac{Q\rho_0c_0^2}{j\omega V} + \frac{j\omega Q\rho_0l}{S}. \quad (2.19)$$

Factoring Q , this can be rewritten as

$$P_1' = Q \left(\frac{1}{j\omega C_{ac}} + j\omega M_{aN} \right), \quad (2.20)$$

where the effective acoustic compliance, C_{ac} , of the cavity is

$$C_{ac} = \frac{V}{\rho_0c_0^2} \left[\frac{m^3}{Pa} \right], \quad (2.21)$$

and effective acoustic mass, M_{aN} , of the air in the neck is given by

$$M_{aN} = \frac{\rho_0l}{S} \left[\frac{kg}{m^4} \right]. \quad (2.22)$$

The notation for the lumped elements has been determined through the use of three components. First, the primary variable name is determined by the element type. Next, the first subscript represents, the energy domain in which the element has been defined, where the subscript 'a' represents the acoustic energy domain, 'e' represents the electrical energy domain, and 'm' represents the mechanical energy domain. The final subscript, which has been capitalized for easier reading, represents the actual structure that is represented at least in part by the lumped element. In this instance, 'C' represents, the cavity, while 'N' stands for the resonator neck. Later, a compliant diaphragm will be introduced that will be represented by a 'D' subscript. The expressions above do not account for any viscous damping effects that occur in the Helmholtz resonator neck. The

viscous damping represents a resistance, whose value can be approximated from pressure driven, laminar pipe flow as

$$R_{aN} = \frac{8\pi\mu l}{S^2} \left[\frac{kg}{m^4 s} \right], \quad (2.23)$$

where μ is the dynamic viscosity of the air. Furthermore, the viscous damping produces a non-uniform axial velocity profile in the neck that ultimately leads to an additional factor of 4/3 in the expression for the effective acoustic mass [130]. The corrected effective mass is then given as

$$M_{aN} = \frac{4\rho_o l}{3S} \left[\frac{kg}{m^4} \right]. \quad (2.24)$$

Additionally, the effective resistance and mass of the neck are, in fact, non-linear and frequency dependent due to turbulence and entrance/exit effects, [131] however for simplicity in modeling, these are not considered here.

The expression for cavity compliance given by Eq. (2.21) can be compared to an approximation based on the exact expression for the impedance in a short closed tube [2].

The exact expression is given by

$$Z_{in} = \frac{-j\rho_o c_o}{\pi a^2} \cot(kl), \quad (2.25)$$

where $k = \frac{\omega}{c_o}$ is the wavenumber. Using a Maclaurin series expansion of the cotangent

function yields

$$\cot(kl) = \frac{1}{kl} - \frac{1}{3}kl - \frac{1}{45}(kl)^3 - \dots \quad (2.26)$$

For $kl \ll 1$, the impedance can be approximated by keeping only the first couple of terms in the expansion, yielding

$$Z_{in} = \frac{\rho_o c_o}{jkl\pi a^2} + j \frac{kl\rho_o c_o}{3\pi a^2} = \frac{\rho_o c_o^2}{j\omega V} + j\omega \frac{\rho_o V}{3(\pi a^2)^2}. \quad (2.27)$$

From this expression, we once again see that

$$C_{ac} = \frac{V}{\rho_o c_o^2} \left[\frac{m^3}{Pa} \right]. \quad (2.28)$$

We now also have an additional mass term, given by

$$M_{ac} = \frac{\rho_o V}{3(\pi a^2)^2} \left[\frac{kg}{m^4} \right], \quad (2.29)$$

which is equal to one-third the acoustic mass of the cavity. This correction term is small for $kl \ll 1$ but becomes more prominent as kl increases. At $kl = 1$, the correction term is 33.3% of the primary term, while at $kl = 0.1$ the correction term is only 0.33% of the primary term.

Equivalent Circuit

To create an equivalent circuit model for the Helmholtz resonator, knowledge of how to connect these lumped elements is needed. Connection rules between elements are defined based on whether an effort-type variable or a flow-type variable is shared between them [132]. Whenever an effort variable, such as force, voltage or pressure, is shared between two or more elements, those elements are connected in parallel in the equivalent circuit. Conversely, whenever a common flow (i.e., velocity, current, or volume velocity) is shared between elements, those elements are connected in series. These connection rules are used to obtain the equivalent circuit representation for the Helmholtz resonator, as shown in Figure 2-4. The connection rules, as given, are assuming that what is known as an impedance analogy is employed. If an admittance

analogy were used instead, then the connection rules would be reversed from what is described above.

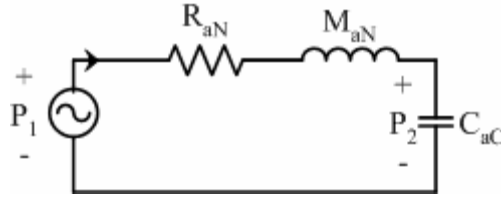


Figure 2-4: Equivalent circuit representation of a Helmholtz resonator.

The frequency response function P_2/P_1 , represents the pressure amplification of the resonator. It is the ratio of cavity pressure to incident pressure, and is given by

$$\frac{P_2}{P_1} = \frac{1}{R_{aN} + sM_{aN} + \frac{1}{sC_{aC}}}, \quad (2.30)$$

where $s = j\omega$.

From an analysis of the above circuit, a single resonant peak is expected in this frequency response function, when the sum of the reactances is zero, and is given by

$$f_{res} = \frac{1}{2\pi\sqrt{M_{aN}C_{aC}}} \text{ [Hz]}. \quad (2.31)$$

At the resonant frequency, the pressure amplification reaches a value of

$$PA_{res} = \frac{M_{aN}}{R_{aN}} (2\pi f_{res}). \quad (2.32)$$

This is shown in Figure 2-5, for an arbitrary Helmholtz resonator having a neck length and diameter of 3.18 mm and 4.72 mm, respectively, and a cavity volume of 1950 mm³. The single peak in the pressure amplification frequency response represents the single degree of freedom present in the system.

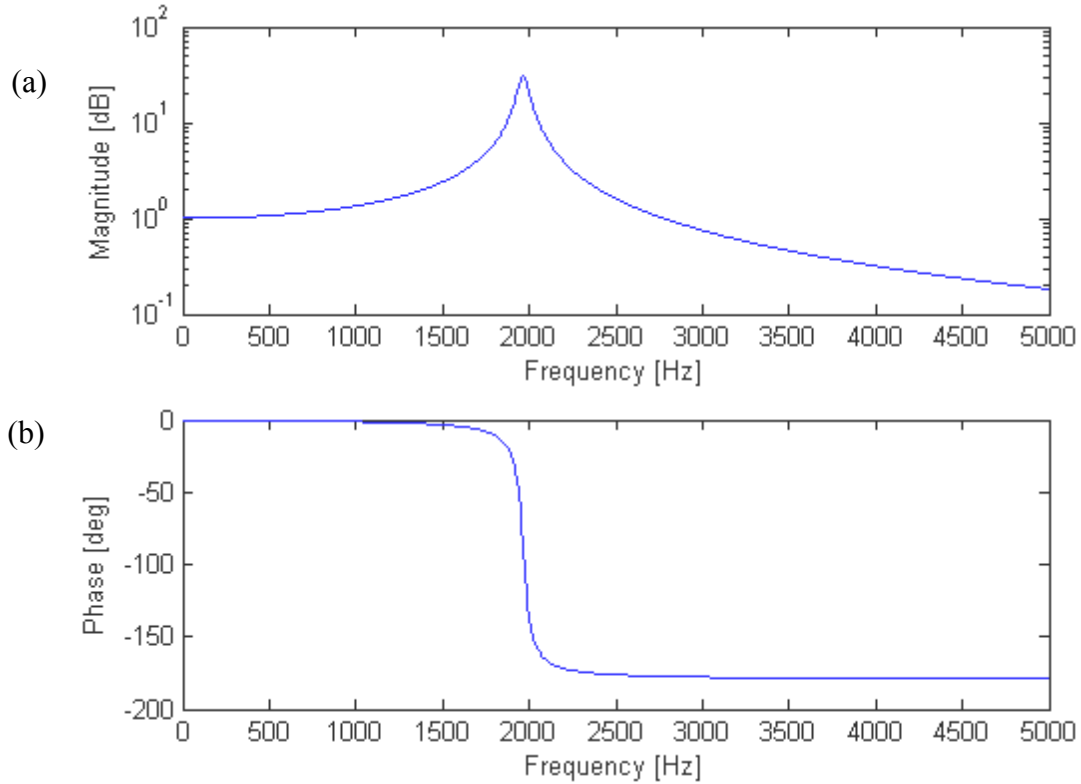


Figure 2-5: Theoretical pressure amplification of a conventional Helmholtz resonator. (a) magnitude (b) phase.

Piezoelectric Composite Plate

On the back wall of the Helmholtz resonator, a piezoelectric diaphragm can be placed such that the acoustic pressure in the cavity can be exploited to cause a deflection of the plate and ultimately an electrical signal via piezoelectric transduction. The piezoelectric composite plate, consisting of a circular layer of silicon and an annular ring of PZT, is shown in cross-section in Figure 2-6, where E is the Young's modulus, ν is Poisson's ratio and ρ is the density of the silicon and PZT as indicated by the subscript. Additionally, t_s is the thickness, and R_2 is the outer radius of the silicon, while for the PZT, t_p is the thickness, ε is the relative permittivity, d_{31} is the transduction coefficient for a voltage applied across the piezoelectric causing a displacement in the radial

direction, and σ_p is the residual stress. A region of high stress exists in a circular plate near the clamped boundary during deflection of the plate. By placing the PZT in this region, the electromechanical coupling is increased due to the stress concentration. In addition, the annular structure facilitates the connection of electrodes and bond pads, as the metal lines can be run from the bond pads to the outer radius of the annular structure and therefore do not have to be placed across the surface of the diaphragm.

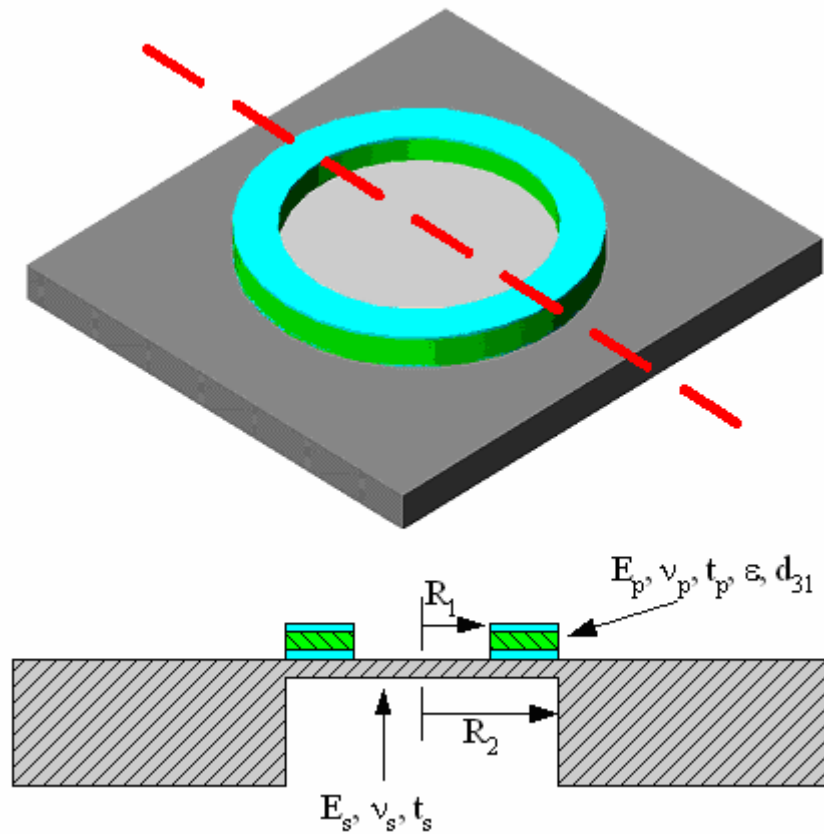


Figure 2-6: Cross-sectional and 3-D schematic of piezoelectric composite circular plate. (not to scale)

Piezoelectricity

Mathematically, the linear piezoelectric effect is expressed as [133]

$$S_{ij} = s_{ijkl}^E T_{kl} + d_{kij} E_k \quad (2.33)$$

and

$$D_i = d_{ikl}T_{kl} + \varepsilon_{ik}^T E_k, \quad (2.34)$$

where S_{ij} is the mechanical strain, s_{ijkl}^E is the elastic compliance (m^2/N) at constant electric field, T_{kl} is the mechanical stress (N/m^2), and d_{kij} is the piezoelectric coefficient (C/N or m/V), D_i is the electric displacement (C/m^2), ε_{ik}^T is the electric permittivity at constant stress (F/m), and E_k is the electric field (V/m) [133]. These equations can also be rewritten using a reduced notation convention, by replacing ij or kl by p or q where i, j, k , and l can only have values of 1,2,or 3 while p and q can have any value between 1 and 6. Using this notation, the resulting equations are

$$S_p = s_{pq}^E T_q + d_{kp} E_k \quad (2.35)$$

and

$$D_i = d_{iq} T_q + \varepsilon_{ik}^T E_k. \quad (2.36)$$

The subscripts in the reduced notation equations refer to the component of each variable in a specified direction as defined by Figure 2-7. For example, d_{31} is the piezoelectric coefficient relating electrical displacement in the '3' direction (z-axis) to a mechanical stress in the '1' direction (x-axis). From Eq. (2.33), it is also seen to relate a mechanical strain in the '3' direction (x-axis) with an electric field in the '1' direction.

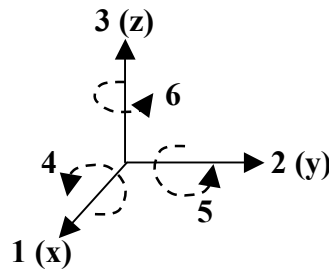


Figure 2-7: Notation of axes used in piezoelectric transduction.

One class of materials, ferroelectrics, exhibits the property that the direction of their polar axis can be changed through application of an external electric field [5, 6, 134]. The polar axis is the direction along which a polar molecule exhibits an internal electric field. When the external electric field is then removed, the polar axis remains in an altered direction. This process that causes a long term rotation of the polar axis is commonly referred to as “poling”. All ferroelectric materials are also piezoelectric, however they are not naturally piezoelectrically active, as the crystal structure is centrosymmetric, as in Figure 2-8a. PZT is a typical example of a ferroelectric material, and has a perovskite crystal structure as shown in Figure 2-8. By applying an external electric field to rotate the polar axis, a non-centrosymmetric crystal structure is created and the ferroelectric material becomes piezoelectrically active, as in Figure 2-8b. Additionally, as a piezoelectrically active material is brought close to its Curie temperature, it loses its piezoelectric properties as the dipoles relax to their unpoled state.

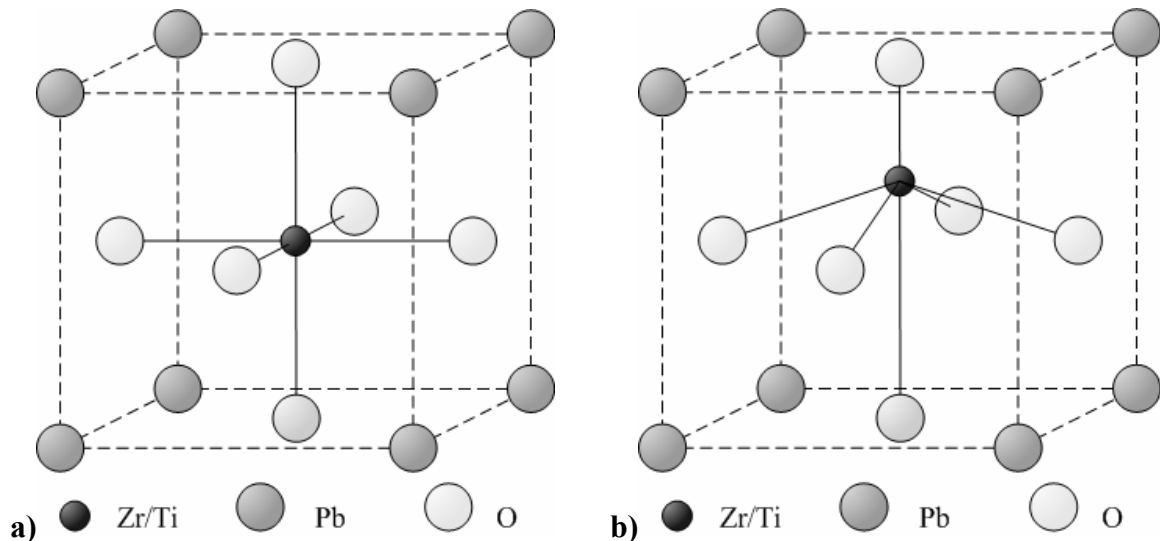


Figure 2-8: Idealized perovskite crystal structure for PZT. a) centrosymmetric structure prior to poling. b) non-centrosymmetric structure after poling.

A piezoelectric ceramic, such as PZT, consists of individual domains. The polarization within each domain is in the same direction; however, the polarization direction varies randomly from domain to domain, leading to a net polarization of zero. This is illustrated in Figure 2-9(a), for the unpoled material. After poling the material with a sufficiently high electric field, the dipoles are rotated so that the polarization of each domain is in the same general direction, as defined by the poling direction, as is illustrated in Figure 2-9(b). Raising the temperature during poling enhances the polarization and resulting piezoelectric properties, as the dipoles rotate more readily at higher temperatures [6].

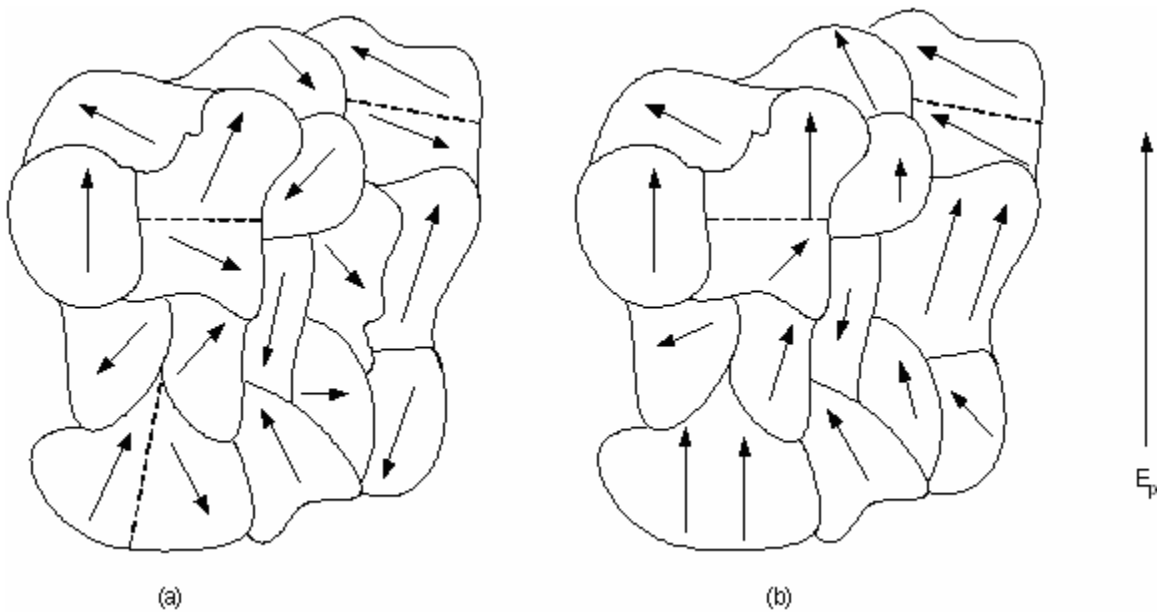


Figure 2-9: Schematic of the poling process: a) An unpoled piezoelectric material, where the polarization in each domain is randomly oriented. B) The same material, after poling, where the domains are now polarized mostly along the direction of the applied field. (after Setter, pg 6 [6])

An additional property of ferroelectric materials is the double-valued nature of their response to an electrical excitation, resulting in a hysteretic behavior. Hysteresis is a property of systems that do not react instantly to an applied force and may not return to

their original state when the force is removed. In ferroelectrics, when an electric field via a voltage is applied, a polarization is incurred. Upon removal of the voltage, the polarization decreases but does not return to zero. The result is a remanent polarization, P_r . If the voltage is swept up and down, the result will be what is known as a hysteresis loop, shown in Figure 2-10.

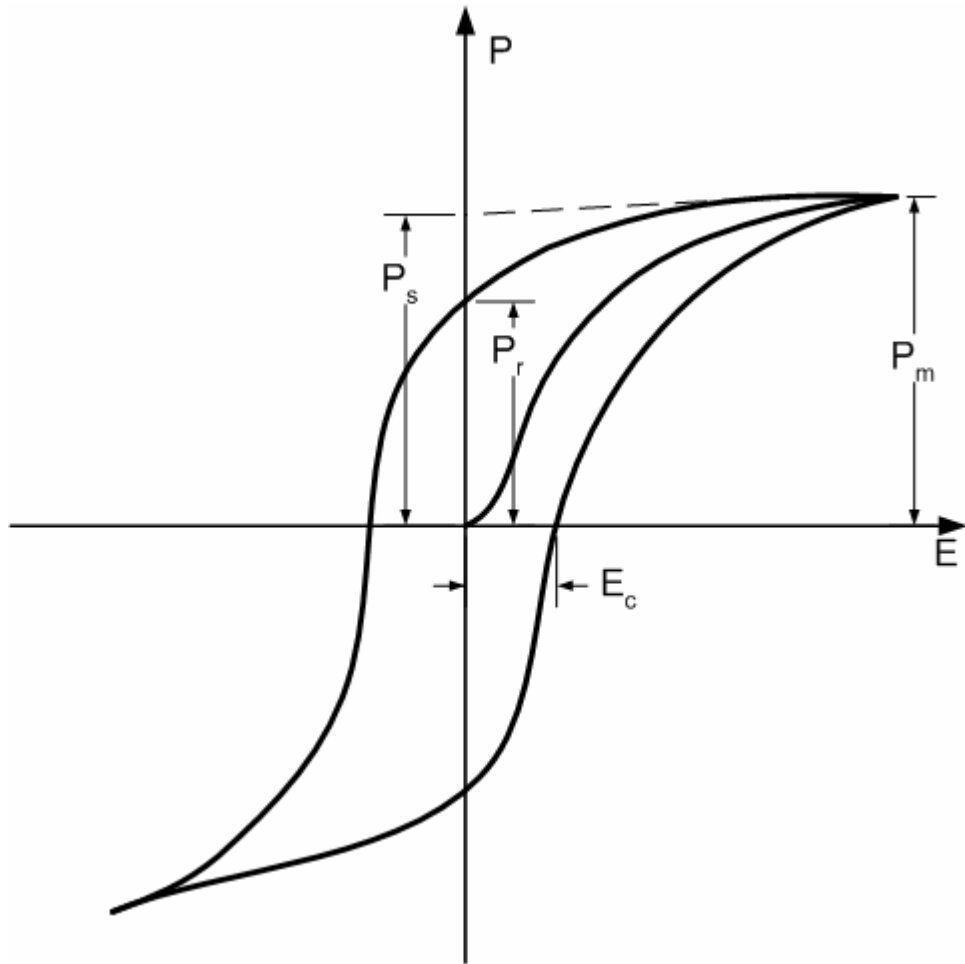


Figure 2-10: Polarization vs. electric field hysteresis loop (after Xu, pg 10 [134]).

The graph is displayed here as polarization, P , typically given in $[\mu\text{C}/\text{cm}^2]$, versus applied electric field, E , although other variations do exist. There are four figures of merit shown in the illustration. P_m is the maximum polarization measured, while P_r is

the remanent polarization (i.e. the polarization which remains when the field is returned to zero). Furthermore, P_s is known as the spontaneous polarization and is defined as the straight line extrapolation of the line defined by the upper saturation region. Finally, the coercive field, E_c , represents the magnitude of the field required to cancel out the remanent polarization.

Composite Plate Modeling

In order to accurately model this structure, the material properties of each of the layers were considered. These include the mechanical properties of the layers such as Young's Modulus, E , and Poisson's ratio, ν and the dielectric constant, ϵ , and piezoelectric coefficient, d_{31} , of the PZT. The subscript p or s indicates the layer as PZT or silicon respectively. Furthermore, the geometry of the structure is accounted for in the values for inner PZT radius, R_1 , outer PZT radius, R_2 , PZT thickness, t_p , and silicon thickness, t_s .

Lumped element model

A pressure applied to the plate creates a deflection of the plate, resulting in a stress in the piezoelectric layer. The stress deforms the piezoelectric layer, creating an electrical charge on the electrodes, thus generating a voltage across the piezoelectric layer. Although the stress and charge are distributed over a finite region of the plate, it is useful to first look at one-dimensional (1-D) piezoelectric transduction. This 1-D analysis can then be extended to incorporate effective lumped element values that are calculated from the actual distributed case.

In the 1-D piezoelectric transduction, the piezoelectric material displaces longitudinally due to the application of a force, F , and/or a voltage, V , applied in the

thickness direction. Additionally, a charge, q , is generated by the application of the same force and/or voltage. The constitutive equations, Eq. (2.33) and Eq. (2.34), can be extended to this situation by modifying their form.

When looking at the resulting strain and electric displacement in the '3' direction, for an applied stress and electric field in the same direction, the equations reduce to

$$S_{33} = s_{33}^E T + d_{33} E \quad (2.37)$$

and

$$D_{33} = d_{33} T + \epsilon_{33}^T E, \quad (2.38)$$

Then this set of equations can be converted by multiplying both sides by the thickness of the piezoelectric material.

$$\begin{aligned} t(S_{33} = s_{33}^E T + d_{33} E) \\ tS = s_{33}^E tT + d_{33} tE \end{aligned} \quad (2.39)$$

Now, the mechanical compliance of a material under compression in the thickness direction can be defined as

$$C_m = \frac{s_{33}^E t}{A}, \quad (2.40)$$

where t is the thickness, and A is the area over which the force is applied. Additionally, for a constant electric field, E ,

$$E = \frac{V}{t}. \quad (2.41)$$

Substituting (2.40) into second part of (2.39) yields,

$$x = C_m AT + d_{33} V \quad (2.42)$$

Finally, the stress, T , when applied over the area, A , can be equated to a force, F , given by

$$F = TA, \quad (2.43)$$

leading to the final equation given by

$$x = C_m F + d_{33} V. \quad (2.44)$$

A similar procedure can then be performed on Eq. (2.38), by multiplying both sides by the area, and making similar substitutions as before, giving

$$A(D_{33} = d_{33}T + \epsilon_{33}^T E), \quad (2.45)$$

$$q = d_{33}F + \epsilon_{33}^T AE, \quad (2.46)$$

$$q = d_{33}F + \frac{\epsilon_{33}^T A}{t} V, \quad (2.47)$$

so

$$q = d_{33}F + C_{ef} V. \quad (2.48)$$

Thus a pair of equations can be written describing the 1-D piezoelectric transduction, and is given by

$$\begin{bmatrix} x \\ q \end{bmatrix} = \begin{bmatrix} C_{ms} & d_{33} \\ d_{33} & C_{ef} \end{bmatrix} \begin{bmatrix} F \\ V \end{bmatrix}. \quad (2.49)$$

In this pair of equations, C_{ms} , the mechanical compliance when a short is placed across the electrodes of the piezoelectric, is defined as

$$C_{ms} = \frac{x|_{V \rightarrow 0}}{F}, \quad (2.50)$$

while C_{ef} , the electrical capacitance when the piezoelectric is free to move, is defined by

$$C_{ef} = \frac{q|_{F \rightarrow 0}}{V} = \frac{\epsilon_{33}^T A_p}{t_p}, \quad (2.51)$$

where q is the resulting charge from the applied voltage V , ϵ_{33} is the electrical permittivity in the thickness direction, A_p is the area of the piezoelectric, and t_p is the thickness of the piezoelectric. Furthermore, d_{33} is the piezoelectric coefficient relating the displacement in the thickness direction for an applied voltage in the same direction, when no mechanical force is applied across the piezoelectric, defined by

$$d_{33} = \frac{x|_{F=0}}{V}. \quad (2.52)$$

For the case of the piezoelectric composite plate that is presented here, though, there is a distributed, nonuniform deflection across the plate. In order to apply the 1-D model developed above to this situation, it is necessary to lump the actual distributed deflection to a single point and compute effective values by equating the energy in the distributed system to the energy in a corresponding lumped component. The 1-D electromechanical transduction described above can then be extended to relate the acoustical and electrical energy domains by integrating over the areas and switching to acoustic conjugate power values, as well as incorporating time-harmonic signals [64]. The time-harmonic, electroacoustical equivalent of Eq. (2.49) is given by

$$\begin{bmatrix} I \\ Q \end{bmatrix} = \begin{bmatrix} j\omega C_{ef} & j\omega d_A \\ j\omega d_A & j\omega C_{as} \end{bmatrix} \begin{bmatrix} V \\ P \end{bmatrix} \begin{bmatrix} A \\ m^3/s \end{bmatrix}, \quad (2.53)$$

where P is the acoustic pressure, Q is the volume velocity of the plate, I is the electrical current. Furthermore, d_A is the piezoelectric coefficient relating the volumetric displacement to the applied voltage, when pressure equals zero, and defined by

$$d_A = \frac{\Delta Vol}{V} \Big|_{P \rightarrow 0} = \frac{\int_0^{R_2} w(r) \Big|_{P \rightarrow 0} 2\pi r dr}{V} \left[\frac{m^3}{V} \right], \quad (2.54)$$

where $w(r)$ is the deflection as a function of the radial position, R_2 is the radius of the plate and ΔVol is the volumetric displacement defined by

$$\Delta Vol = \int_0^{R_2} 2\pi r w(r) dr \left[m^3 \right]. \quad (2.55)$$

Additionally, C_{as} , the acoustical compliance when a short circuit is placed across the piezoelectric, is defined by

$$C_{as} = \frac{\Delta Vol}{P} \Big|_{V \rightarrow 0} = \frac{\int_0^{R_2} w(r) \Big|_{V \rightarrow 0} 2\pi r dr}{P} \left[\frac{m^3}{Pa} \right]. \quad (2.56)$$

From two-port network theory, a generalized electro-acoustic, reciprocal, two-port network can be written as

$$\begin{bmatrix} I \\ Q \end{bmatrix} = \begin{bmatrix} Y_{ef} & G \\ G & Y_{as} \end{bmatrix} \begin{bmatrix} V \\ P \end{bmatrix}, \quad (2.57)$$

where Y_{ef} is the electrical admittance when the acoustic terminal is free to move (i.e. no pressure exists, $P = 0$), Y_{as} is the acoustical admittance when the electrical terminal is shorted (i.e. no voltage exists, $V = 0$), and G is the electro-acoustic transduction admittance, given both by the ratio of current, I , to pressure, P , when $V = 0$, and the ratio of volume-velocity, Q , to voltage, V , when $P = 0$. Comparing Eq. (2.53) and Eq. (2.57), it can be seen that

$$G = j\omega d_A, \quad (2.58)$$

$$Y_{ef} = j\omega C_{ef}, \quad (2.59)$$

and

$$Y_{as} = j\omega C_{as}. \quad (2.60)$$

Equivalent circuit

Using Eq. (2.57), an equivalent electro-acoustic circuit can be drawn, as shown in Figure 2-11, where C_{eb} , the electrical capacitance when the plate is blocked from moving is given by

$$C_{eb} = C_{ef}(1-k^2) [F], \quad (2.61)$$

the transduction factor, ϕ , is given as

$$\phi = \frac{-G}{Y_{as}} = \frac{-j\omega d_A}{j\omega C_{as}} = \frac{-d_A}{C_{as}} \left[\frac{Pa}{V} \right], \quad (2.62)$$

and the coupling factor, k , is given by

$$k = \sqrt{\frac{G^2}{Y_{ef}Y_{as}}} = \sqrt{\frac{d_A^2}{C_{ef}C_{as}}}. \quad (2.63)$$

Physically, the coupling factor, k , represents the fraction of energy that is coupled between the acoustical and electrical energy domains. It is seen here to be a function of the piezoelectric coefficient, d_A , which represents coupled energy and the two elements which store potential energy associated with the transduction, C_{ef} and C_{as} . The coupling factor is therefore related to the ratio of the coupled energy to the stored energy.

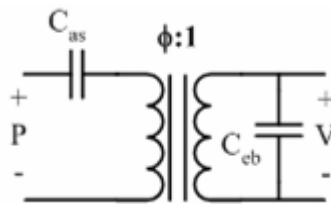


Figure 2-11: Electro-acoustic equivalent circuit representation with C_{eb} , C_{as} and ϕ .

An alternative equivalent circuit can also be drawn, as shown in Figure 2-12. The alternative circuit is simply another representation for the same physical process.

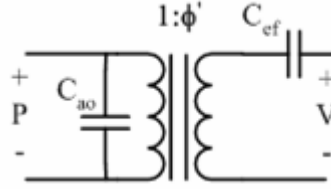


Figure 2-12: Electro-acoustic equivalent circuit representation with C_{ef} , C_{ao} and ϕ' .

In Figure 2-12, C_{ao} represents the acoustic compliance when an open-circuit is placed across the piezoelectric, and is given by,

$$C_{ao} = C_{as} (1 - k^2) \left[\frac{m^3}{Pa} \right]. \quad (2.64)$$

Additionally, the transduction factor, ϕ' , is given by

$$\phi' = \frac{-G}{Y_{ef}} = \frac{-j\omega d_A}{j\omega C_{ef}} = \frac{-d_A}{C_{ef}} \left[\frac{V}{Pa} \right]. \quad (2.65)$$

The two circuits above represent the transduction under static conditions, thus they do not take into account the dynamics of the system (i.e. mass). At frequencies greater than zero, a mass must be added to the equivalent circuit. As the mass stores kinetic energy, it is represented by its electrical equivalent, which is an inductor. Furthermore, this mass must be in series with the compliance, as both experience the same motion (i.e. displacement or velocity). The acoustic mass, M_{ad} , is determined by equating the lumped kinetic energy of a point mass moving with the center velocity to the total kinetic energy of the vibrating diaphragm and is therefore given by ,

$$M_{ad} = 2\pi \int_0^{R_2} \rho_A \left(\frac{w(r)|_{V=0}}{\Delta V|_{V=0}} \right)^2 r dr \quad (2.66)$$

where ρ_A is the areal density of the piezoelectric composite plate defined by,

$$\rho_A = \int_{z_1}^{z_2} \rho dz \quad [kg/m^2], \quad (2.67)$$

where ρ is the density of the corresponding layer.

In addition to the above mentioned elements, it is also necessary to include an additional element that represents the dielectric losses that are incurred during transduction, yielding the circuit shown in Figure 2-13. Generally this is expressed through a term known as the loss tangent, also known as the dielectric loss factor. Represented by the ratio of the parallel reactance to the parallel resistance in the dielectric, the loss tangent is formally given by

$$\tan \delta = \frac{X_p}{R_p} = \frac{1}{2\pi f C_p R_p}, \quad (2.68)$$

where R_p is a resistor in parallel with a capacitance, C_p , and f is the frequency at which R_p and C_p were measured. The loss tangent is also equal to the inverse of the quality factor, Q .

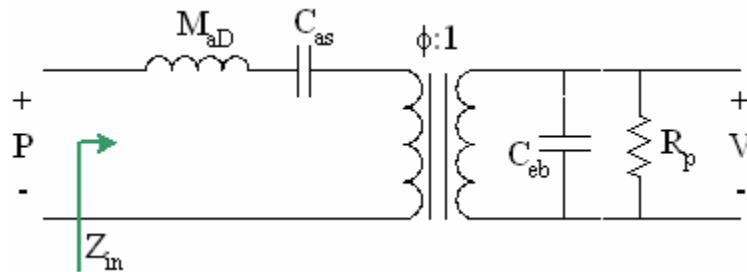


Figure 2-13: Dynamic electro-acoustic equivalent circuit.

In this circuit, M_{ad} represents the acoustic mass of the diaphragm. The input impedance from the acoustical side is then given by

$$Z_m = sM_{ad} + \frac{1}{sC_{as}} + \phi^2 \frac{R_p}{1 + sC_{eb}R_p}. \quad (2.69)$$

By voltage division we get

$$V\phi = P \frac{\phi^2 \frac{R_p}{1 + sC_{eb}R_p}}{Z_{in}} = P \frac{\phi^2 \frac{R_p}{1 + sC_{eb}R_p}}{sM_{aD} + \frac{1}{sC_{as}} + \phi^2 \frac{R_p}{1 + sC_{eb}R_p}}, \quad (2.70)$$

which, after rearranging yields,

$$\frac{V}{P} = s\phi C_{as} R_p \frac{1}{s^3 M_{aD} C_{as} C_{eb} R_p + s^2 M_{aD} C_{as} + sR_p (C_{eb} + \phi^2 C_{as}) + 1}. \quad (2.71)$$

This is the general expression for the open-circuit sensitivity of the circular composite piezoelectric plate. From a physical standpoint it is also useful to look at certain conditions that allow for additional insight. The presence of the dielectric loss resistance, R_p , complicates some of the underlying behaviors of the device, by adding an additional R-C time constant. Looking at a situation in which this parallel loss resistance is infinite (i.e. $R_p \rightarrow \infty$), the above expression can be reduced to

$$\frac{V}{P} = \phi \frac{C_{as}}{C_{eb}} \frac{1}{s^2 M_{aD} C_{as} + \phi^2 \frac{C_{as}}{C_{eb}} + 1}. \quad (2.72)$$

Several important things can be gleaned from this expression. First of all, the equation describes the behavior of a second order system, with a primary resonance occurring when the denominator goes to zero at

$$\omega_{res} = \sqrt{\frac{1 + \phi^2 \frac{C_{as}}{C_{eb}}}{M_{aD} C_{as}}}. \quad (2.73)$$

From this expression, the resonance is seen to depend on the ratio $\phi^2 C_{as} / C_{eb}$ in addition to the standard dependence on the product $M_{aD} C_{as}$. If $\phi = 0$, this reduces to a

simple plate. For $\phi \neq 0$, electrical energy is stored across the piezoelectric, resulting in a stiffer device possessing a larger ω_{res} .

The full expression that includes the dielectric loss, given by Eq. (2.71), is the general expression for the sensitivity of the circular composite piezoelectric plate. It can be further simplified for two important cases:

1. Well below the short-circuit mechanical resonant frequency (compliance dominated)
2. At the short-circuit mechanical resonant frequency (resistance dominated)

Case 1: Well below the short-circuit mechanical resonant frequency

When a short is placed across C_{eb} , it is equivalent to assigning $R_p \rightarrow 0$. Physically, this implies that no electrical energy storage is allowed, as the voltage across the capacitor, C_{eb} , must be zero. The expression for the short-circuit mechanical resonant frequency is given by

$$\omega_{res_{sc}} = \sqrt{\frac{1}{M_{ad}C_{as}}}, \quad (2.74)$$

which is the same resonant frequency as described above when $\phi = 0$. Note that both cases describe a situation where no electrical energy is stored. The general expression for sensitivity can then be rewritten in terms of $\omega_{res_{sc}}$ as

$$\frac{V}{P} = j\omega\phi C_{as}R_p \frac{1}{j\omega \left(\frac{j\omega}{\omega_{res_{sc}}}\right)^2 C_{eb}R_p + \left(\frac{j\omega}{\omega_{res_{sc}}}\right)^2 + j\omega R_p (C_{eb} + \phi^2 C_{as}) + 1}. \quad (2.75)$$

Well below resonance, we have

$$\left| \left(\frac{j\omega}{\omega_{res_{sc}}} \right)^2 \right| \ll 1. \quad (2.76)$$

This term can then be dropped from the expression, yielding

$$\frac{V}{P} \cong j\omega\phi \frac{C_{as}}{C_{eb}} \frac{1}{j\omega \left(1 + \phi^2 \frac{C_{as}}{C_{eb}} \right) + \frac{1}{R_p C_{eb}}}. \quad (2.77)$$

To simplify this further, the transduction factor, ϕ , can be written in terms of the effective piezoelectric modulus, d_A , by recalling Eq. (2.62), yielding

$$\begin{aligned} \frac{V}{P} &\cong \frac{-j\omega d_A}{C_{as}} \frac{C_{as}}{C_{eb}} \frac{1}{j\omega \left(1 + \left(\frac{-d_A}{C_{as}} \right)^2 \frac{C_{as}}{C_{eb}} \right) + \frac{1}{R_p C_{eb}}} \\ &\cong \frac{-d_A}{C_{eb}} \frac{1}{\left(1 + \frac{d_A^2}{C_{as} C_{eb}} \right) + \frac{1}{j\omega R_p C_{eb}}}. \end{aligned} \quad (2.78)$$

Furthermore, the blocked electrical capacitance, C_{eb} , can be written in terms of the free electrical capacitance, C_{ef} and the coupling coefficient, k , using Eq. (2.61) and Eq.

(2.63) to yield the an expression for sensitivity, given by

$$\begin{aligned} \frac{V}{P} &\cong \frac{-d_A}{C_{eb}} \frac{1}{\left(1 + \frac{d_A^2}{C_{as} C_{eb}} \right) + \frac{1}{j\omega R_p C_{eb}}}, \\ &\cong \frac{-d_A}{C_{eb}} \frac{1}{\left(1 + \frac{d_A^2}{C_{as} C_{ef} (1-k^2)} \right) + \frac{1}{j\omega R_p C_{ef} (1-k^2)}}, \\ &\cong \frac{-d_A}{C_{eb}} \frac{1}{\left(1 + \frac{k^2}{(1-k^2)} \right) + \frac{1}{j\omega R_p C_{ef} (1-k^2)}}, \end{aligned} \quad (2.79)$$

which can be simplified further to yield

$$\begin{aligned}
\frac{V}{P} &\cong \frac{-d_A}{C_{eb}} \frac{1}{\frac{1}{(1-k^2)} + \frac{1}{j\omega R_p C_{ef} (1-k^2)}}, \\
&\cong \frac{-d_A}{C_{eb} \frac{1}{(1-k^2)} + \frac{1}{j\omega R_p}}, \\
&\cong \frac{-d_A}{C_{ef} + \frac{1}{j\omega R_p}}, \\
&\cong \frac{\phi'}{1 + \frac{1}{j\omega C_{ef} R_p}}.
\end{aligned} \tag{2.80}$$

Now under the condition of a high value for the loss resistor, R_p , Eq. (2.80) can be reduced approximately to

$$\frac{V}{P} \cong \frac{-d_A}{C_{ef}} \tag{2.81}$$

This corresponds to the alternative transduction coefficient, ϕ' , given by

$$\phi' = \frac{-d_A}{C_{ef}}, \tag{2.82}$$

and thus under the conditions of a high loss resistor and operation well below $\omega_{res_{sc}}$, the sensitivity can be given by

$$\frac{V}{P} \cong \phi'. \tag{2.83}$$

Case 2: At the short-circuit mechanical resonant frequency

The general expression for sensitivity is once again given by

$$\frac{V}{P} = j\omega\phi C_{as} R_p \frac{1}{j\omega \left(\frac{j\omega}{\omega_{res_{sc}}} \right)^2 C_{eb} R_p + \left(\frac{j\omega}{\omega_{res_{sc}}} \right)^2 + j\omega R_p (C_{eb} + \phi^2 C_{as}) + 1}. \tag{2.84}$$

Now, since we are only considering the system at the short-circuit resonance, where

$\omega = \omega_{res_{sc}}$, we have

$$\left(\frac{j\omega}{\omega_{res_{sc}}} \right)^2 = -1, \quad (2.85)$$

yielding an exact expression for the sensitivity as

$$\frac{V}{P} = j\omega\phi C_{as} R_p \frac{1}{-j\omega C_{eb} R_p - 1 + j\omega R_p (C_{eb} + \phi^2 C_{as}) + 1} = \frac{1}{\phi}. \quad (2.86)$$

We therefore find that the sensitivity at resonance reduces to

$$\frac{V}{P} = \frac{1}{\phi} = \frac{\phi'}{k^2}, \quad (2.87)$$

as

$$k^2 = \phi\phi'. \quad (2.88)$$

This can be understood from the equivalent circuit of Figure 2-13. At $\omega = \omega_{res_{sc}}$, the impedance of the mass is canceled by the impedance of the compliance, permitting a direct transduction of energy from the acoustic to electrical energy domain. Note that $\omega_{res_{sc}}$ exists whether or not $R_p = 0$, therefore Eq. (2.86) is always valid whenever $\omega = \omega_{res_{sc}}$. In other words, Eq. (2.86) holds whenever the operating frequency coincides with the frequency that is defined by the short-circuit resonance, but makes no requirement for an actual short-circuit load.

As the load across C_{eb} is increased, the resonance frequency will shift towards the open-circuit resonance. Recalling Eq. (2.64), the open and short-circuit acoustic compliances are related by the coupling factor and define the limits of the resonant frequency as all resistive loads fall somewhere between open and short-circuit. The

larger the coupling factor, then the larger the range between open and short-circuit resonant frequencies.

General expression vs. simplified cases

Figure 2-14 plots the open-circuit and near short-circuit sensitivity versus frequency overlaid with the values of ϕ' and $1/\phi$. The material properties used in calculating these results are shown in Table 2-3 and Table 2-4. Notice that below resonance, the general open-circuit sensitivity expression asymptotes to the value of ϕ' . Additionally, notice that the general expression reaches the value of $1/\phi$ at a frequency below where the peak amplitude occurs. This is because $1/\phi$ is the simplified expression for the sensitivity at the short-circuit mechanical resonant frequency, whereas the general expression represents the open-circuit frequency response. Thus the peak amplitude occurs at the open-circuit resonant frequency. The frequency at which the general expression for sensitivity reaches the value of $1/\phi$ coincides with the short-circuit resonant frequency, as expected. Also note that this short-circuit sensitivity calculation was performed with an almost-short circuit condition, primarily to illustrate the effect on the resonant frequency. To achieve the almost-short circuit condition a resistive load of $1\ \Omega$ was used as the value is much less than the impedance due to C_{eb} . One final feature of the frequency response is the low frequency rolloff that is visible in the open circuit case. This rolloff is due to the dielectric loss resistor, R_p , and the resulting time constant due to the combination of that resistor and the electrical capacitance, as evidenced in Eq. (2.80) for the low frequency regime.

Table 2-3: General material properties used in modeling.

Material	E [GPa]	ν	ρ [kg/m ³]	t [μ m]
Silicon	150	0.27	2300	3
Platinum	170	0.38	21440	0.170
TiO ₂	283	0.28	2150	0.100

[135, 136]

Table 2-4: PZT properties used in modeling.

E_p [GPa]	ν_p	ρ_p [kg/m ³]	ε	d_{31} [pm/V]	$\tan \delta$	σ_p [MPa]
30	0.3	7600	1000	-50	0.02	30

[9, 10, 16, 31]

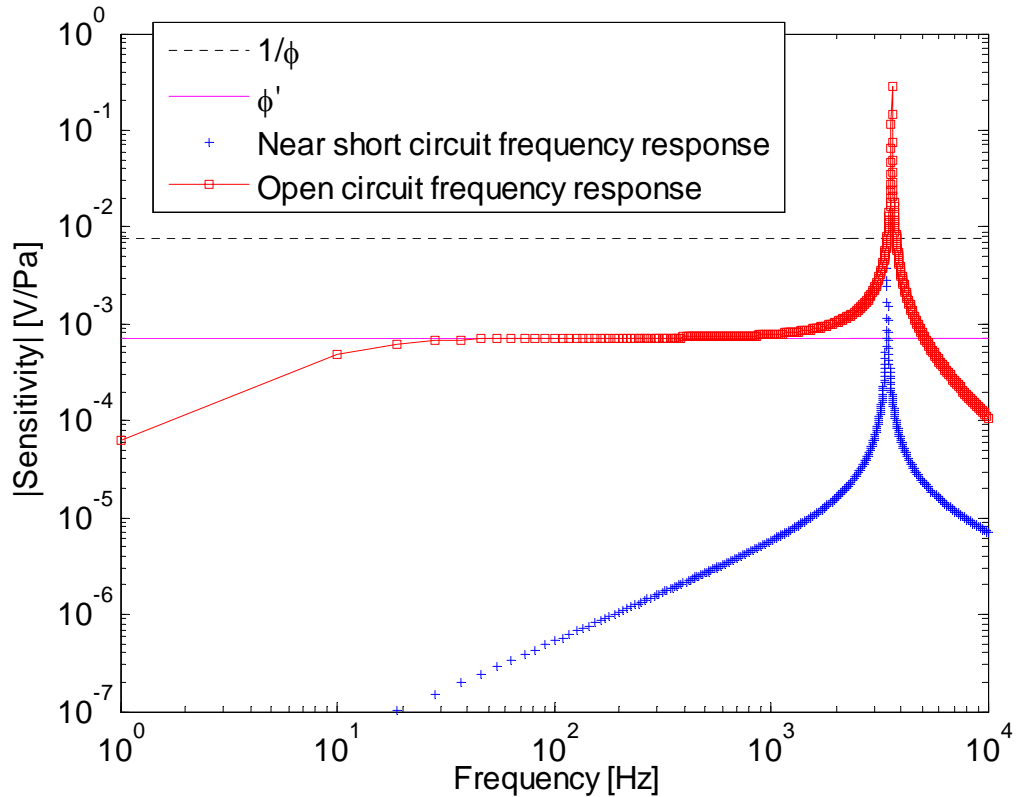


Figure 2-14: Sensitivity vs. frequency for a piezoelectric composite circular plate.

Effects of including the radiation impedance

Since the clamped circular plate is vibrating in a medium, the radiation impedance of the plate must be taken into account, and consists of a radiation mass and radiation resistance. The radiation mass accounts for the inertial mass of the fluid that is vibrating in unison with the plate, while the radiation resistance accounts for the acoustic radiation

of energy away from the plate. In addition to the radiation resistance, energy is lost via structural radiation to the supports. The radiation resistance and radiation mass is determined to first-order by approximating the backplate as a piston in an infinite baffle, as given by Blackstock [2] in terms of specific acoustic impedance, Z_p , as

$$Z_p = \rho_o c_o \left[1 - \frac{2J_1(2ka)}{2ka} + j \frac{2K_1(2ka)}{2ka} \right] = \rho_o c_o [R_1(2ka) + jX_1(2ka)], \quad (2.89)$$

where $R_1(2ka)$ and $X_1(2ka)$ indicate that they are functions of $2ka$, $a = R_2$ is the radius of the piston, J_1 is a Bessel function of the first kind of order one, and K_1 is a first-order Struve function. The Maclaurin expansions of Eq. (2.89) are also given by [2] as

$$R_1 = \frac{(ka)^2}{1 \cdot 2} - \frac{(ka)^4}{1 \cdot 2^2 \cdot 3} + \frac{(ka)^6}{1 \cdot 2^2 \cdot 3^2 \cdot 4} \dots \quad (2.90)$$

and

$$X_1 = \frac{4}{\pi} \left[\frac{2ka}{3} - \frac{(2ka)^3}{3^2 \cdot 5} + \frac{(2ka)^5}{3^2 \cdot 5^2 \cdot 7} \dots \right]. \quad (2.91)$$

For small values of ka , where $ka \ll 1$, the resistance and reactance can be approximated by keeping only the first terms of Eq. (2.90) and Eq. (2.91).

The radiation impedance as given in Eq. (2.89) is in terms of specific acoustic impedance. This is converted to an acoustic impedance via the effective area, A_{eff} , of the piezoelectric plate. As the circular composite diaphragm does not deflect uniformly over the entire surface (i.e. the deflection is a function of radial distance), the volume displaced by the deflection of the diaphragm is less than that of a circular piston of the same area. The effective area, A_{eff} , is therefore defined to represent the equivalent area that a circular piston with uniform deflection would need to have to create the same

volumetric displacement as the composite diaphragm. This is necessitated by the need to maintain continuity of volume velocity across the interface between the mechanical and acoustical domains. It can be calculated by integrating the distributed deflection of the diaphragm over the entire surface and then dividing by the center deflection of the diaphragm. By using the center deflection as the reference value, the distributed deflection is then considered to be lumped to the center. For an axisymmetric deflection, such as would occur for the fundamental mode, the effective area is given by

$$A_{eff} = \frac{\int w(r) 2\pi r dr}{w(0)} \quad [m^2]. \quad (2.92)$$

The radiation resistance can then be approximated, for low values of ka as

$$R_{aDrad} \cong \frac{(ka)^2 \rho_o c}{2A_{eff}}, ka \ll 1 \quad \left[\frac{kg}{m^4 s} \right], \quad (2.93)$$

while the radiation mass is approximated as

$$M_{aDrad} \cong \frac{8ka \rho_o c}{3\pi \omega A_{eff}}, ka \ll 1 \quad \left[\frac{kg}{m^4} \right]. \quad (2.94)$$

These two elements add in series to create a radiation impedance, Z_{rad} , that is defined by

$$Z_{aDrad} = R_{aDrad} + sM_{aDrad}. \quad (2.95)$$

The equivalent circuit of the composite plate including the radiation impedance is shown in Figure 2-15.

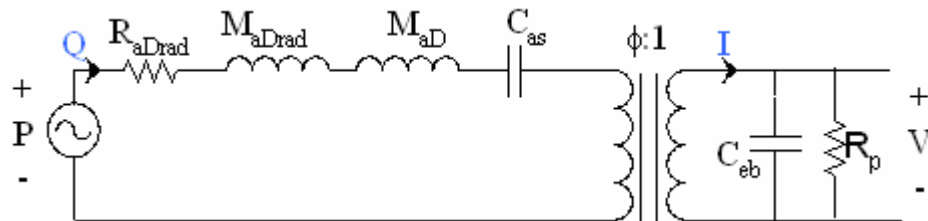


Figure 2-15: Equivalent circuit of piezo-composite plate including the radiation impedance.

When the radiation impedance of the diaphragm is added to the equivalent circuit, the analysis becomes only slightly more complex. The acoustical input impedance, Z_{in} , defined as P/Q , can be represented in terms of the equivalent circuit parameters, and is now given by

$$Z_{in} = sM_{aD} + sM_{aDrad} + R_{aDrad} + \frac{1}{sC_{as}} + \phi^2 \frac{R_p}{1 + sC_{eb}R_p}. \quad (2.96)$$

Then, the general expression for sensitivity is now given via the voltage divider method as

$$V\phi = P \frac{\phi^2 \frac{R_p}{1 + sC_{eb}R_p}}{Z_{in}} = P \frac{\phi^2 \frac{R_p}{1 + sC_{eb}R_p}}{sM_{aD} + sM_{aDrad} + R_{aDrad} + \frac{1}{sC_{as}} + \phi^2 \frac{R_p}{1 + sC_{eb}R_p}} \quad (2.97)$$

or

$$\frac{V}{P} = \frac{\phi \frac{R_p}{1 + sC_{eb}R_p}}{sM_{aD} + sM_{aDrad} + R_{aDrad} + \frac{1}{sC_{as}} + \phi^2 \frac{R_p}{1 + sC_{eb}R_p}} \quad (2.98)$$

From Figure 2-15, it can be seen that the radiation mass, M_{aDrad} , adds directly to the acoustical mass of the plate, M_{aD} , as is evidenced in Eq. (2.97), while R_{aDrad} provides damping to this second-order system. Note that here, the acoustical resistance, R_{aDrad} , damps the resonance, while the electrical resistance, R_p , leads to a low frequency rolloff. The different effects arise because R_{aDrad} is in series with the reactive elements, C_{as} and

M_{ad} , while R_p is in parallel with the capacitance, C_{eb} . The general expression for the undamped resonance frequency is now given by

$$\omega_{res} = \sqrt{\frac{\phi^2 \frac{C_{as}}{C_{eb}} + 1}{(M_{ad} + M_{aDrad}) C_{as}}}. \quad (2.99)$$

When a short is placed across C_{eb} , it is effectively removed. This is mathematically equivalent to assigning $C_{eb} \rightarrow \infty$, as the impedance of a capacitor is inversely proportional to the capacitance. The short-circuit resonance frequency then reduces to

$$\omega_{res_{sc}} = \frac{1}{\sqrt{(M_{ad} + M_{aDrad}) C_{as}}}. \quad (2.100)$$

Upon comparison with Eq. (2.74), it can be seen that the short-circuit resonance frequency has now been shifted downward by the radiation mass, as is also the case with the open-circuit resonance frequency. At the radial frequency of the short-circuit resonance, the short-circuit input impedance reduces to

$$Z_{in} = R_{aDrad}, \quad (2.101)$$

because C_{eb} and R_p are effectively removed by the short-circuit. The volume velocity, Q , is then given by

$$Q = \frac{P}{R_{aDrad}}. \quad (2.102)$$

Via the piezoelectric transduction, the current, I , in the piezoelectric material, is then given by

$$I = Q\phi = \frac{\phi P}{R_{aDrad}}. \quad (2.103)$$

The output voltage in this case, however, remains at zero due to the short circuit placed across the output capacitance. To achieve real power at the output, a finite resistive load is necessary. Adding a resistive load, R_{load} , across the output yields the equivalent circuit shown in Figure 2-16.

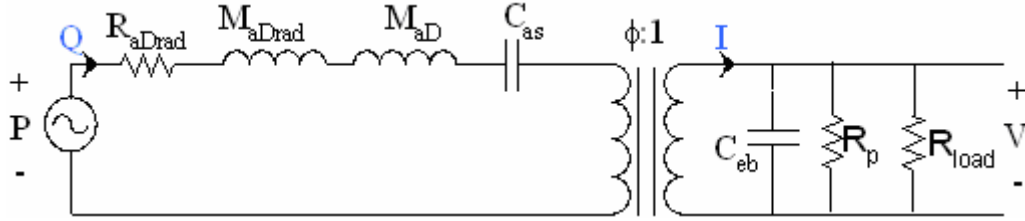


Figure 2-16: Equivalent circuit with resistive load.

The input impedance, Z_{in} , is then given by

$$Z_{in} = s(M_{aD} + M_{aDrad}) + R_{aDrad} + \frac{1}{sC_{as}} + \phi^2 \frac{R_{load} R_p}{R_{load} + R_p + R_{load} R_p s C_{eb}}. \quad (2.104)$$

Now, if we choose R_{load} such that $R_{load} \ll 1/sC_{eb}$ and $R_{load} \ll R_p$, then the parallel combination of these three elements can be approximated with just R_{load} . In addition, the resonant frequency will be very close to the short-circuit resonant frequency. At this frequency, the input impedance reduces to

$$Z_{in} = R_{aDrad} + \phi^2 R_{load}, \quad (2.105)$$

and the volume velocity, Q , is given by

$$Q = \frac{P}{Z_{in}} = \frac{P}{R_{aDrad} + \phi^2 R_{load}}. \quad (2.106)$$

Through piezoelectric transduction, a current, I , is created in the piezoelectric given by

$$I = Q\phi = \frac{P\phi}{R_{aDrad} + \phi^2 R_{load}}. \quad (2.107)$$

As the resistance, R_{load} , is much less than $1/sC_{eb}$, most of the current goes through it, leading to a voltage drop given by

$$V = IR_{load} = \frac{P\phi R_{load}}{R_{aDrad} + \phi^2 R_{load}}. \quad (2.108)$$

Thus the power absorbed by the load resistance is purely real and is given by

$$\text{Re}\{\Pi\} = \text{Re}\{IV\} = \frac{P^2 \phi^2 R_{load}}{(R_{aDrad} + \phi^2 R_{load})^2}. \quad (2.109)$$

An optimal solution to this equation is found by setting

$$\frac{d\Pi}{dR_{load}} = 0 = -P^2 \phi^2 \frac{(-R_{aDrad} + \phi^2 R_{load})}{(R_{aDrad} + \phi^2 R_{load})^3}. \quad (2.110)$$

Solving for the optimal load resistance yields

$$R_{load} = \frac{R_{aDrad}}{\phi^2}, \quad (2.111)$$

which is just the impedance matching condition at the interface. Note that is for the special case of $R_{load} \ll 1/sC_{eb}$, $R_{load} \ll R_p$ and operation at resonance.

Equivalent circuit parameters of piezoelectric composite circular plates

In order to obtain the equivalent circuit parameters, an analytical model was developed for the piezoelectric composite circular plate by Wang et al. [62, 63]. Using this approach, analytical modeling was accomplished by dividing the problem of Figure 2-6 into two portions, an inner circular plate, surrounded by an annular composite ring with matching boundary conditions at the interface, as shown in Figure 2-17. The boundary conditions consist of equal moments and forces at the interface as well as equal slope and transverse displacement. After solving for the deflection in each region, the deflection equation for each region can then be combined [62, 63].

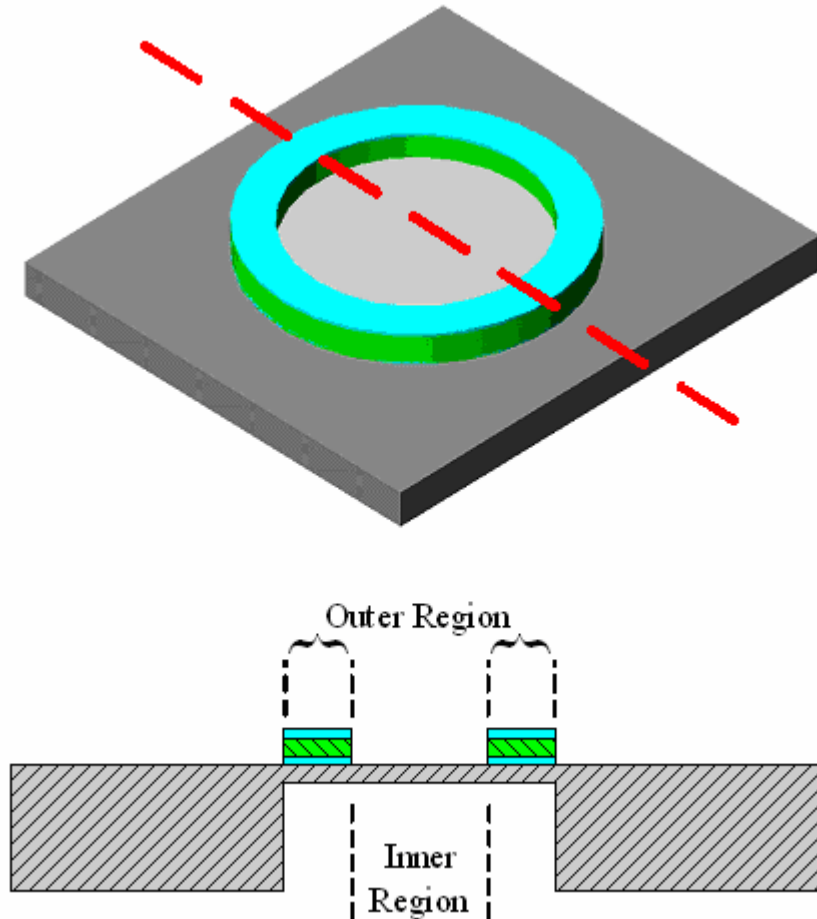


Figure 2-17: Conceptual 3-D and cross-sectional schematic of the circular composite plate. (Not to scale.)

The deflection equation can then be utilized to determine the potential and kinetic energy stored in the plate, leading to expressions for the acoustic compliance and mass of the composite plate. Similarly, expressions can be found for the electro-acoustic transduction coefficient and the blocked electrical capacitance. Using the parameters shown in Table 2-3 and Table 2-4, plots were obtained for the lumped elements as a function of both R_1/R_2 and t_p/t_s . As many of the material parameters for PZT are highly dependent on actual processing conditions and techniques, typical values were chosen as a ‘best guess’ estimate [8, 12-14, 16-48]. The effective acoustic short-circuit

compliance and mass are functions of both R_1/R_2 and t_p/t_s and are shown in Figure 2-18 and Figure 2-19, respectively.

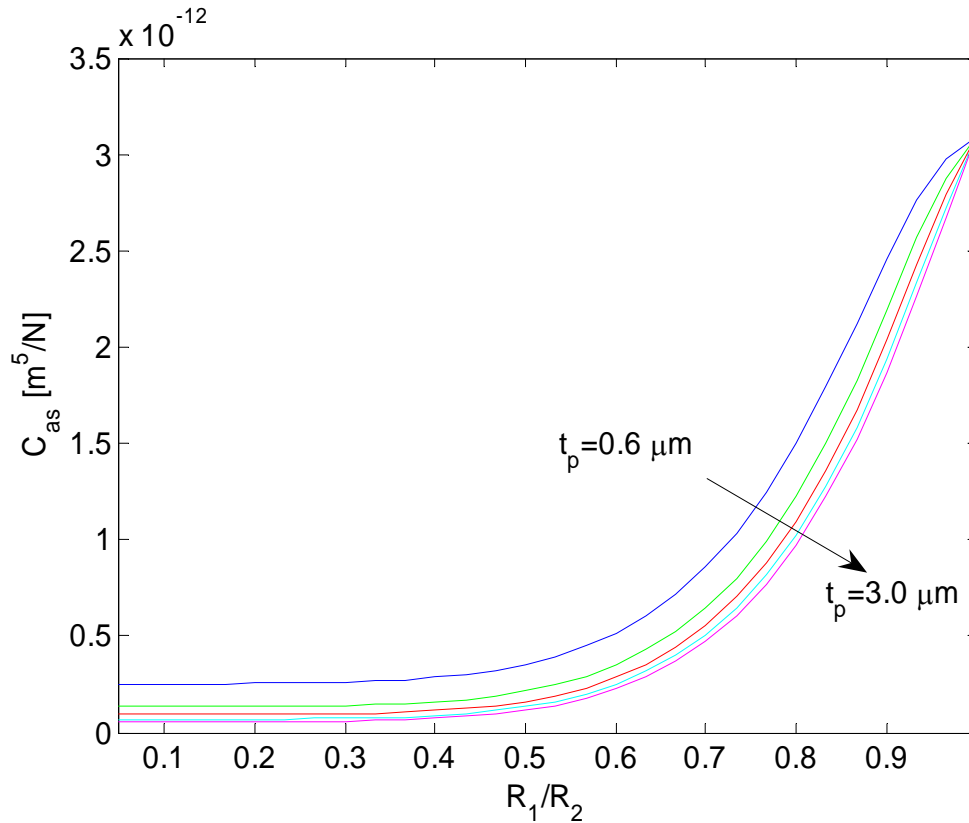


Figure 2-18: Effective acoustic short-circuit compliance as a function of R_1/R_2 and t_p/t_s . For these calculations, $t_s = 3\mu\text{m}$ and $R_2 = 2\text{mm}$, while the piezoelectric layer has thicknesses of $t_p = 0.6, 1.2, 1.8, 2.4, 3.0 [\mu\text{m}]$.

The acoustic compliance is found to increase with increasing R_1/R_2 and decrease with increasing t_p/t_s , however, the acoustic mass is found to generally decrease with R_1/R_2 and increase with t_p/t_s . It is also useful to look at the physical limits and effects of R_1/R_2 . As $R_1/R_2 \rightarrow 0$, the piezoelectric ring covers the entire surface of the diaphragm and the compliance is at a relative minimum for a given thickness, while the mass is at relative maximum. Furthermore, note that the acoustic mass is most sensitive

to changes in the piezoelectric layer thickness under this condition. Meanwhile, as $R_1/R_2 \rightarrow 1$, the piezoelectric ring would have infinitesimal width and so would be essentially nonexistent. Under this condition, the piezoelectric layer thickness has no effect on the compliance, as would be expected.

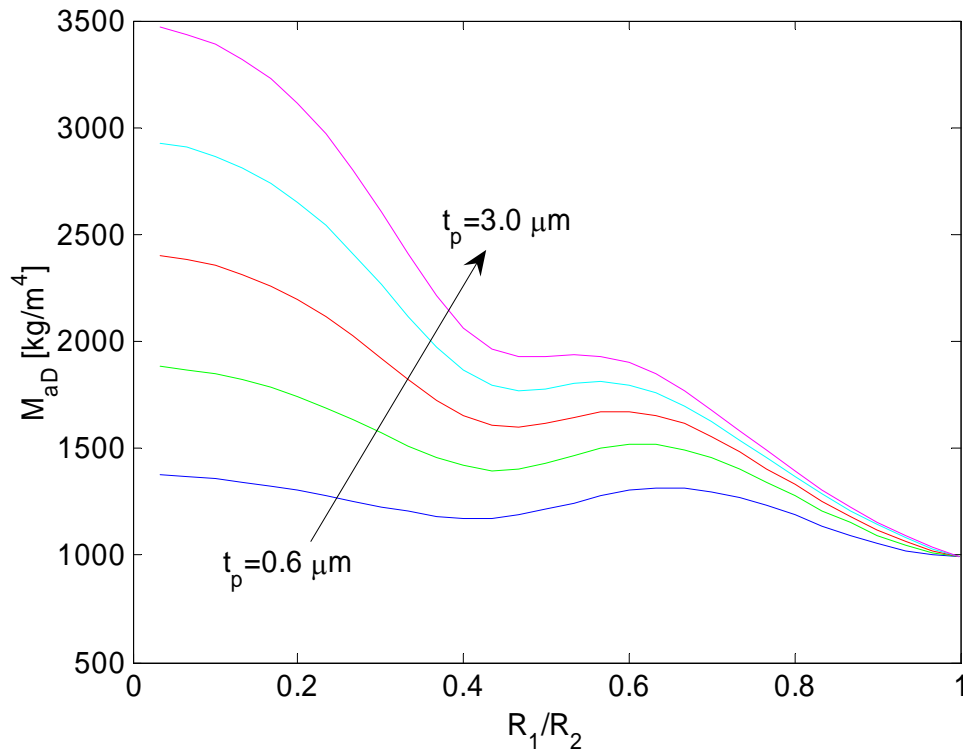


Figure 2-19: Effective acoustic mass as a function of R_1/R_2 and t_p/t_s . For these calculations, $t_s = 3\mu\text{m}$ and $R_2 = 2\text{mm}$, while the piezoelectric layer has thicknesses of $t_p = 0.6, 1.2, 1.8, 2.4, 3.0 [\mu\text{m}]$.

Shown in Figure 2-20 is a graph of the resonant frequency as a function of both R_1/R_2 and t_p/t_s . From this figure, it can be seen that the resonant frequency increases as the thickness of the piezoelectric layer increases or generally as the inner radius of the piezoelectric layer decreases. The resonant frequency trend with respect to thickness arises because the effective acoustic mass is found to increase with the thickness while the effective acoustic compliance decreased, but by a much larger amount. Again, it

should be noted that at the limit of $R_1/R_2 \rightarrow 1$, the resonant frequency is no longer affected by the thickness of the piezoelectric layer. Also, for a given t_p , there is a maximum resonant frequency at $R_1/R_2 \sim 0.4$.

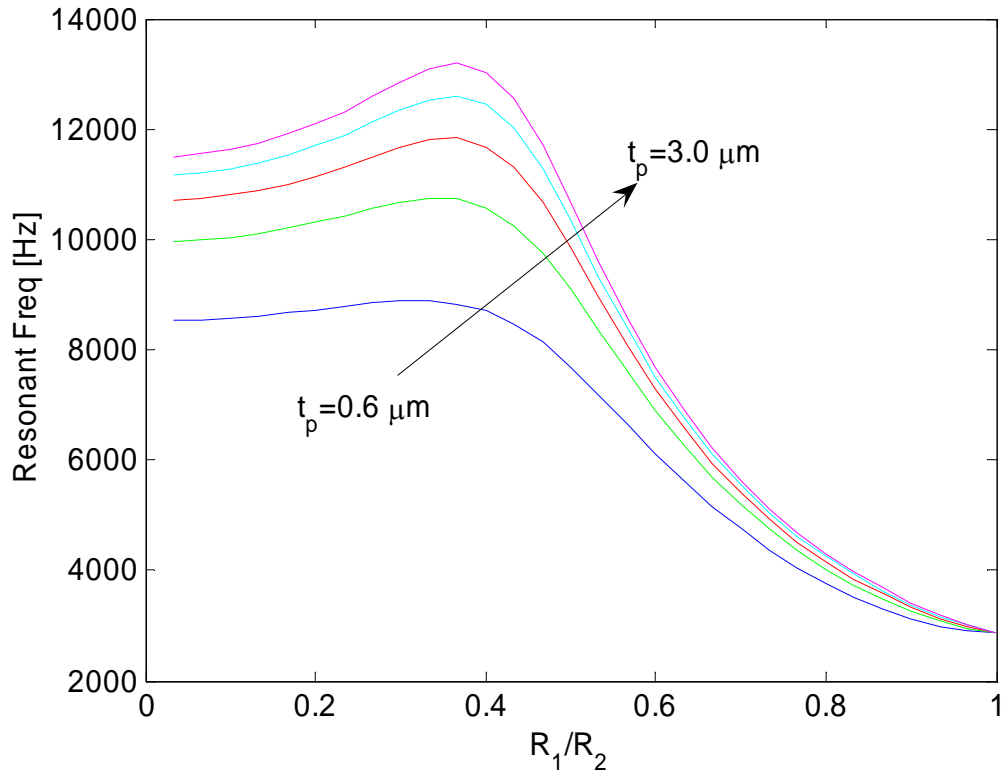


Figure 2-20: Short-circuit resonant frequency as a function of R_1/R_2 and t_p/t_s . For these calculations, $t_s = 3\mu m$ and $R_2 = 2mm$, while the piezoelectric layer has thicknesses of $t_p = 0.6, 1.2, 1.8, 2.4, 3.0 [\mu m]$.

The electro-acoustic transduction coefficient, ϕ , was also found as function of these relative dimensions, and is shown in Figure 2-21. The transduction coefficient represents the conversion of the voltage across the piezoelectric to the acoustic pressure produced by the resulting motion of the composite plate. It should be noted that the transduction coefficient is negative, implying a 180° phase shift between pressure and voltage, as

computed relative to an assumed poling direction. As can be seen in Figure 2-21, a maximal magnitude occurs when R_1/R_2 is around 0.45.

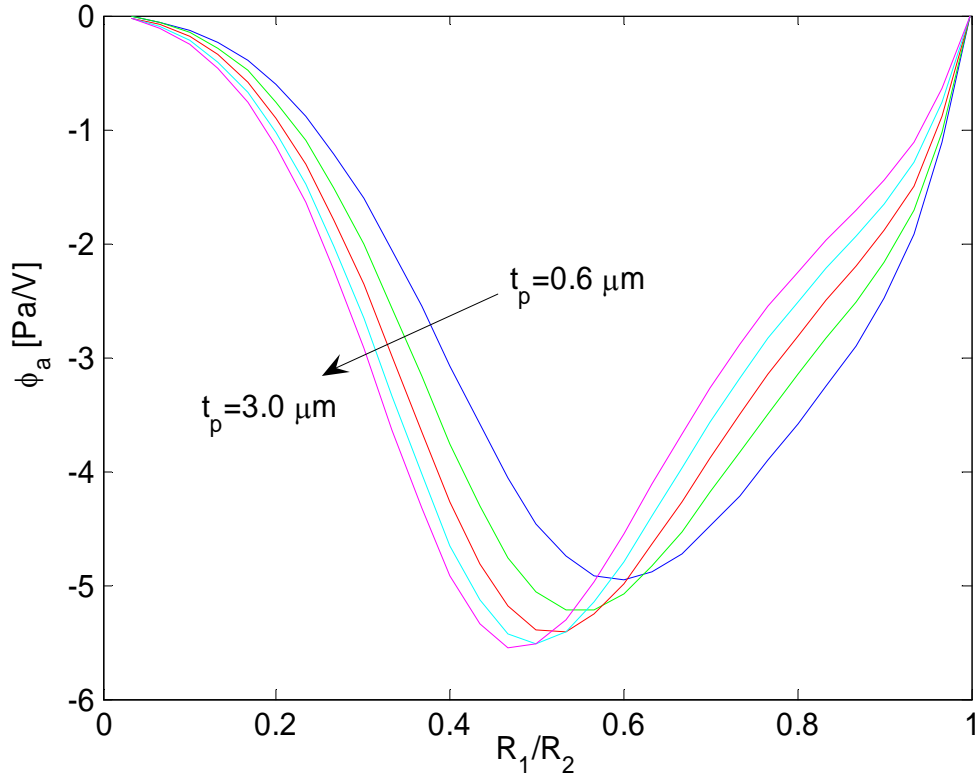


Figure 2-21: Electro-acoustic transduction coefficient as a function of R_1/R_2 and t_p/t_s . For these calculations, $t_s = 3\mu\text{m}$ and $R_2 = 2\text{mm}$, while the piezoelectric layer has thicknesses of $t_p = 0.6, 1.2, 1.8, 2.4, 3.0 [\mu\text{m}]$.

Additionally, the magnitude of the transduction coefficient increases with increasing piezoelectric thickness. Looking at the limit as $R_1/R_2 \rightarrow 1$, the transduction is seen to decrease to zero, as would be expected of a structure with no piezoelectric material. Furthermore, as $R_1/R_2 \rightarrow 0$ and the piezoelectric material covers the entire diaphragm, the transduction factor is seen to go to zero as well. Physically, this results from cancellations between different regions of the diaphragm that are undergoing opposite polarities of stress, such that the net electric displacement (charge) is zero.

Another parameter of interest is the coupling coefficient, k . It is defined as the ratio of energy converted by the transducer to the energy supplied to the transducer, thus providing a measure of the coupling. For the purposes of harvesting energy, this parameter is more important than the transduction coefficient as the primary interest is in maximizing the coupled energy, rather than maximizing only the output voltage. A plot of k as a function of R_1/R_2 and t_p/t_s is shown in Figure 2-22.

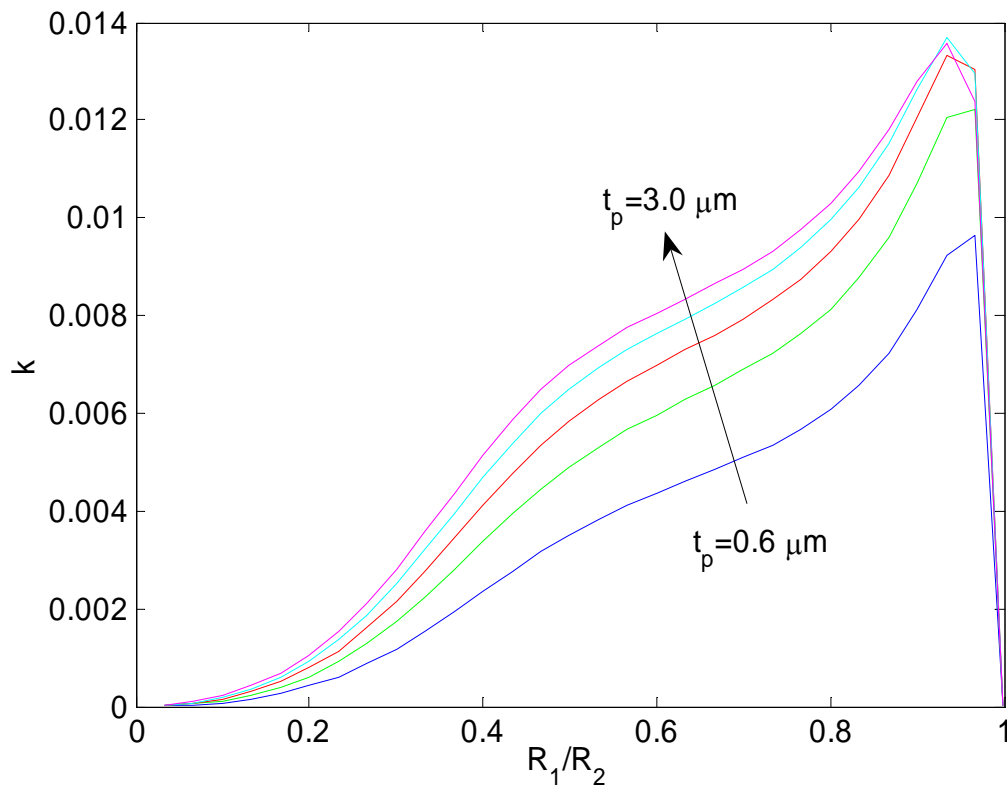


Figure 2-22: Electromechanical coupling coefficient, k , as a function of R_1/R_2 and t_p/t_s . For these calculations, $t_s = 3\mu\text{m}$ and $R_2 = 2\text{mm}$, while the piezoelectric layer has thicknesses of $t_p = 0.6, 1.2, 1.8, 2.4, 3.0 [\mu\text{m}]$.

From the figure, the maximum k of 0.013 is obtained for an R_1/R_2 ratio of 0.95 and a t_p/t_s ratio of unity. Physically, the increasing trend in k as R_1/R_2 increases, arises from the stress distribution within the diaphragm. There is a stress concentration near the clamped boundary of the diaphragm that provides for a high level of coupling. By

concentrating the piezoelectric material in this high stress region, the averaged coupling factor over the ring will be higher than a piezoelectric ring that is spread over a larger area.

Acoustic Energy Harvester Dynamic Behavior

When the piezoelectric diaphragm is mounted in the wall of a Helmholtz resonator, the equivalent circuit for the diaphragm (Figure 2-16) is combined with that of the Helmholtz resonator (Figure 2-4). By using the same lumped element connection rules previously described, the complete circuit can be obtained, as shown in Figure 2-23.

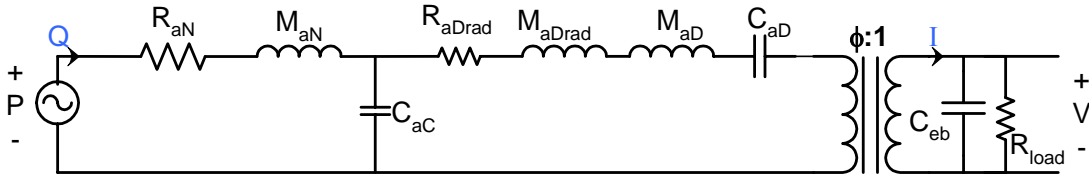


Figure 2-23: Equivalent circuit for acoustic energy harvester with resistive load.

Notice that the equivalent circuit for the diaphragm is in parallel with the cavity compliance, C_{aC} . This occurs because the pressure in the cavity is responsible both for compressing the air in the cavity as well as deflecting the diaphragm, i.e. the cavity and the diaphragm both see the same pressure. Additionally, it is assumed that $R_{load} \ll R_p$ and therefore the parallel combination can be approximated as $R_{load} // R_p \cong R_{load}$.

Acoustical Input Behavior

An expression for the acoustical input impedance can be obtained from the equivalent circuit and is given by

$$Z_{in} = R_{aN} + sM_{aN} + \frac{\frac{1}{sC_{aC}} \left(s(M_{aD} + M_{aDrad}) + \frac{1}{sC_{aD}} + R_{aDrad} + \frac{\phi^2 R_{load}}{1 + R_{load} sC_{eb}} \right)}{\frac{1}{sC_{aC}} + s(M_{aD} + M_{aDrad}) + \frac{1}{sC_{aD}} + R_{aDrad} + \frac{\phi^2 R_{load}}{1 + R_{load} sC_{eb}}}. \quad (2.112)$$

From this equation, it can be seen that the total input impedance is simply the impedance of the Helmholtz resonator neck in series with a parallel combination of the Helmholtz resonator cavity impedance and the piezoelectric composite diaphragm impedance with a resistive load attached.

Many energy harvesting devices with varying geometries were designed for this dissertation, but for illustrative purposes, I will only explore the behavior of one, which serves as a typical example. More explicitly, eight different devices were designed and created to give a range in performance, but to illustrate the qualitative and typical behavior of the devices, only a single “representative” device was plotted for the remainder of this chapter. A plot of the acoustical input impedance versus frequency is shown in Figure 2-24 for the piezoelectric composite diaphragm, both with and without the Helmholtz resonator, to elucidate the behavior of the individual components. For this plot and those that follow, the Helmholtz resonator has a neck length of $L = 3.18 \text{ mm}$, and a radius of $R_n = 2.36 \text{ mm}$ along with a cavity volume of $V_{cav} = 1950 \text{ mm}^3$, in addition to a diaphragm with a thickness of $t_{si} = 3 \text{ }\mu\text{m}$ and a outer and inner radius of $R_2 = 1.95 \text{ mm}$ and $R_1 = 1.85 \text{ mm}$, respectively. These dimensions were chosen as typical values in the range of what was expected of the final device and package design. From this plot, it can be seen that, by itself, the piezoelectric composite diaphragm has a single resonance near 3.6 kHz , where the impedance reaches a local minimum. When combined with the Helmholtz resonator, two minima are seen. The lower resonance that occurs near 1.8 kHz is dominated by the Helmholtz resonator that has an uncoupled resonance of 2 kHz , as evidenced by the peak in Figure 2-5. The upper resonance at 3.9 kHz is

dominated by the piezoelectric composite diaphragm. Additionally, an antiresonance, where the impedance reaches a local maxima, occurs between the two resonances.

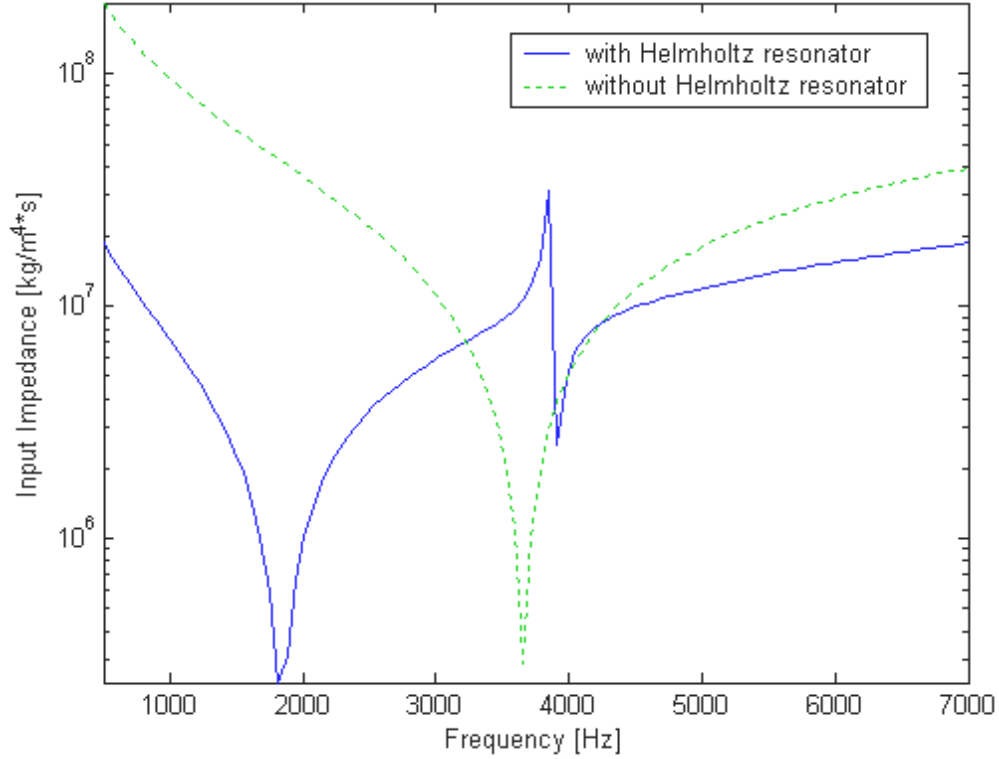


Figure 2-24: Magnitude of the acoustical input impedance for the piezoelectric composite diaphragm and in combination with the Helmholtz resonator. ($L = 3.18 \text{ mm}$, $R_n = 2.36 \text{ mm}$, $V_{cav} = 1950 \text{ mm}^3$, $t_{si} = 3 \text{ }\mu\text{m}$, $R_2 = 1.95 \text{ mm}$, $R_1 = 1.85 \text{ mm}$)

The acoustical input power can be obtained from the input acoustic pressure, P , and is given by

$$\text{Re}\{\Pi_{in}\} = \frac{P^2}{\text{Re}\{Z_{in}\}}. \quad (2.113)$$

The input acoustic pressure, P , is measured inside the plane-wave tube near the end-face of the tube. The microphone that measures this pressure is placed as close as possible ($\sim 1/16''$) to the end-face so that it serves as a measure of the pressure that is incident on the energy harvesting device. In the case of the device that includes a Helmholtz

resonator, the incident pressure is the pressure incident upon the resonator neck, while for the diaphragm only device, it is the pressure incident upon the face of the diaphragm.

A plot of the magnitude and phase of the input power is shown in Figure 2-25.

This plot assumes an ideal acoustic source, i.e. that the applied acoustic pressure is constant and independent of the input impedance. In reality, this is not the case, and the applied acoustic pressure will vary as a function of frequency due to a frequency dependent impedance as seen by the speaker. The important point to take away from this plot, however, is that there are frequencies at which the input power will be maximized. These frequencies occur when the input impedance is minimized thus allowing for maximum power flow from an ideal source. These do not necessarily correspond to frequencies where the output power is maximized, as will be shown in the next section.

Electrical Output Behavior

The electrical output impedance can be found in a similar manner and is given by

$$Z_{out} = R_{load} // \frac{1}{sC_{eb}} // \left[\frac{1}{\phi^2} \left(s(M_{aD} + M_{aDrad}) + \frac{1}{sC_{aD}} + R_{aDrad} + \frac{1}{sC_{aC}} // (R_{aN} + M_{aN}) \right) \right]. \quad (2.114)$$

Expanding this equation out yields the full expression for the output impedance, given by

$$Z_{out} = \frac{(R_{load}) \frac{1}{sC_{eb}} \left[\frac{1}{\phi^2} \left(s(M_{aD} + M_{aDrad}) + \frac{1}{sC_{aD}} + R_{aDrad} + \frac{\frac{1}{sC_{aC}}(R_{aN} + M_{aN})}{\frac{1}{sC_{aC}} + R_{aN} + M_{aN}} \right) \right]}{(R_{load}) \frac{1}{sC_{eb}} + \left(R_{load} + \frac{1}{sC_{eb}} \right) \frac{1}{\phi^2} \left(s(M_{aD} + M_{aDrad}) + \frac{1}{sC_{aD}} + R_{aDrad} + \frac{\frac{1}{sC_{aC}}(R_{aN} + M_{aN})}{\frac{1}{sC_{aC}} + R_{aN} + M_{aN}} \right)}. \quad (2.115)$$

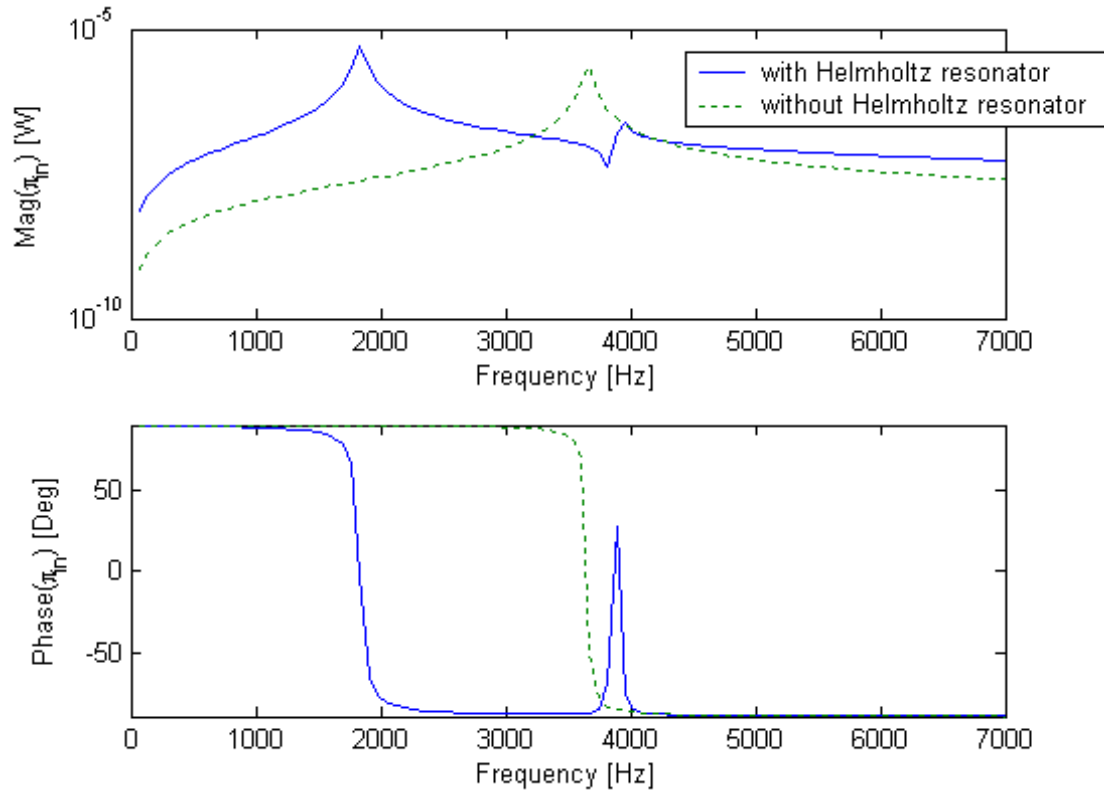


Figure 2-25: Magnitude and phase of the acoustical input power for an input acoustic pressure of $P = 94 \text{ dB}$. ($L = 3.18 \text{ mm}$, $R_n = 2.36 \text{ mm}$, $V_{cav} = 1950 \text{ mm}^3$, $t_{si} = 3 \text{ }\mu\text{m}$, $R_2 = 1.95 \text{ mm}$, $R_1 = 1.85 \text{ mm}$)

A graphical plot of the electrical output impedance is shown in Figure 2-26 in terms of real and imaginary components. The solid curve in the figure corresponds to the expression given by Eq. (2.115), while the dotted curve represents the impedance of the piezoelectric composite diaphragm by itself. Notice that only the real component shows any significant difference between the two cases. Physically, this is due to the “poor” coupling that is typical of indirect transducers. The result is that acoustical components have minimal effect on the electrical impedance.

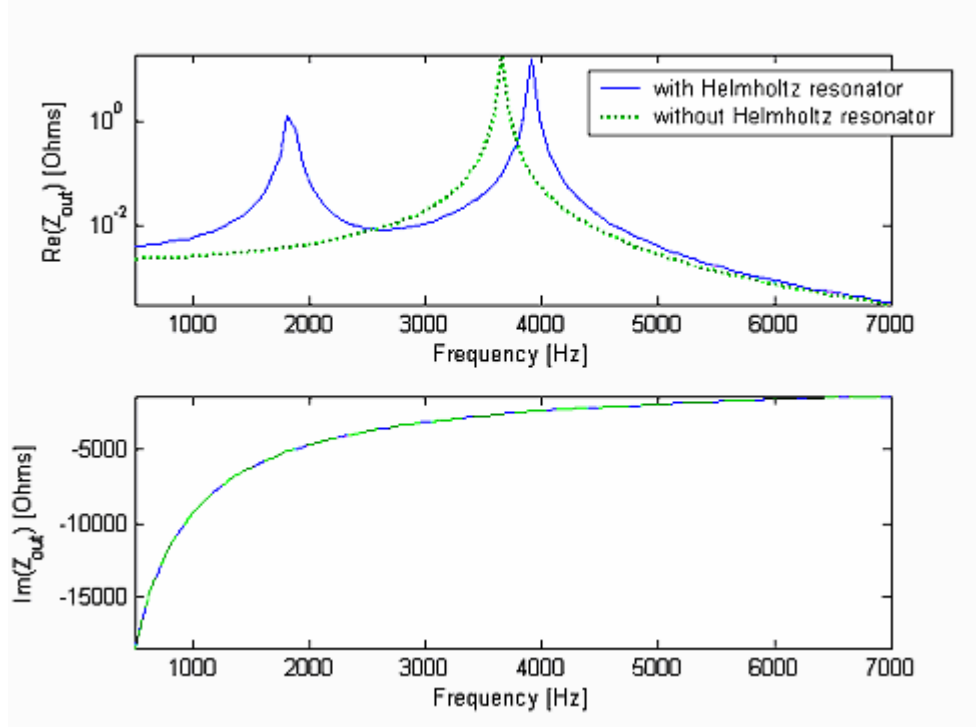


Figure 2-26: Electrical output impedance for the piezoelectric composite diaphragm by itself and in combination with the Helmholtz resonator. ($L = 3.18 \text{ mm}$, $R_n = 2.36 \text{ mm}$, $V_{cav} = 1950 \text{ mm}^3$, $t_{si} = 3 \text{ }\mu\text{m}$, $R_2 = 1.95 \text{ mm}$, $R_1 = 1.85 \text{ mm}$)

The output voltage can easily be found from the equivalent circuit to be

$$V = \left[\frac{(P\phi) \frac{1}{sC_{eb}} R_{load}}{\frac{1}{sC_{eb}} + R_{load}} \right] \cdot \left[\left(\frac{R_{aN} + sM_{aN}}{1} + 1 \right) \left(s(M_{aD} + M_{aDrad}) + \frac{1}{sC_{aD}} + R_{aDrad} + \frac{\phi^2 R_{load}}{1 + R_{load} C_{eb}} \right) + R_{aN} + sM_{aN} \right] \quad (2.116)$$

The output voltage is displayed graphically in Figure 2-27 for the piezoelectric composite diaphragm by itself and in combination with the Helmholtz resonator. For both cases, the magnitude has a similar shape to the output impedance, although a few differences remain. In the output impedance curve, the second resonant peak is higher than the first, whereas for the output voltage curve shown below, the first resonant peak

is higher than the second. The voltage curve shown was computed for a load resistance, R_{load} , equal to the electrical output resistance at the diaphragm resonance frequency, and an input acoustic pressure of 1 Pa.

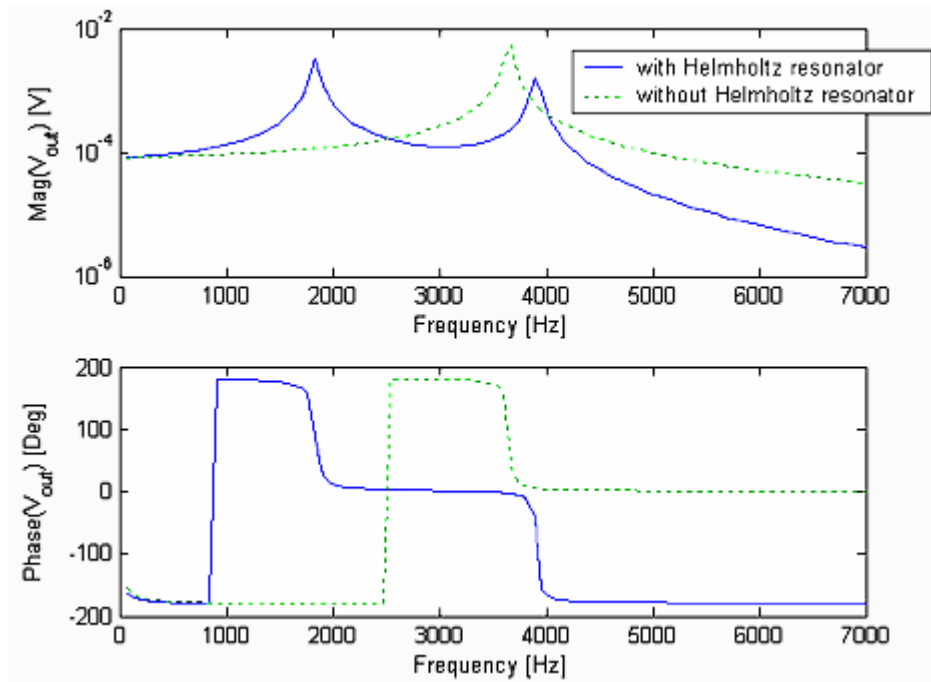


Figure 2-27: Magnitude and phase of the output voltage for the piezoelectric composite diaphragm and in combination with the Helmholtz resonator. ($L = 3.18 \text{ mm}$, $R_n = 2.36 \text{ mm}$, $V_{cav} = 1950 \text{ mm}^3$, $t_{st} = 3 \text{ }\mu\text{m}$, $R_2 = 1.95 \text{ mm}$, $R_1 = 1.85 \text{ mm}$, $P = 94 \text{ dB}^1$)

The electrical power delivered to the resistive load, R_{load} , can be found from

$$\text{Re}\{\Pi_{out}\} = \frac{V^2}{R_{load}}. \quad (2.117)$$

A plot of the electrical output power delivered to the resistive load is shown in Figure 2-28 for the piezoelectric composite diaphragm by itself and in combination with the Helmholtz resonator, for the case of an incident acoustic pressure of 1 Pa.

¹ dB re 20 μPa throughout this document.

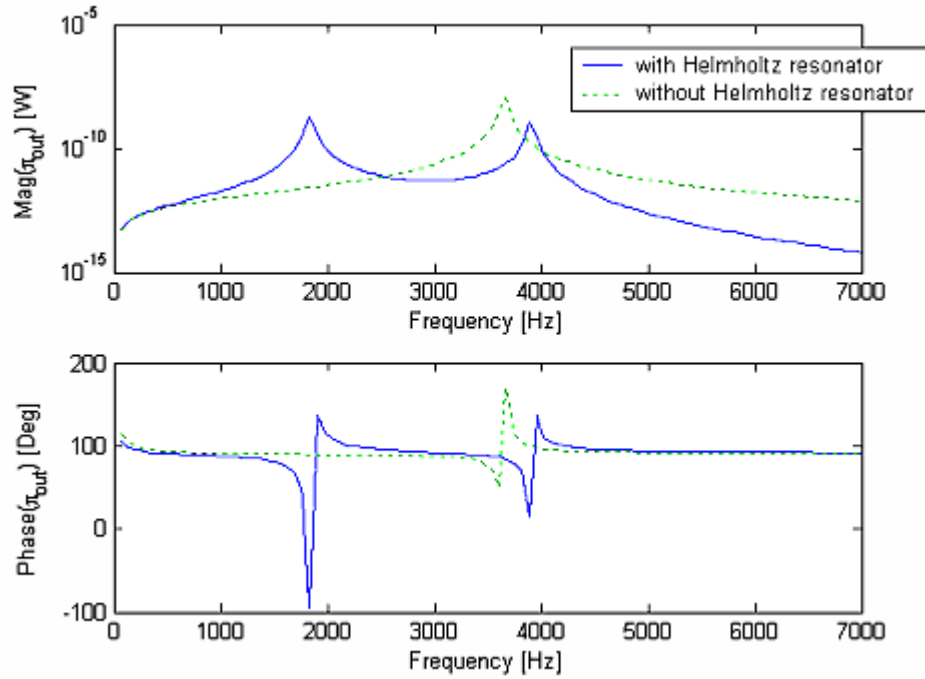


Figure 2-28: Magnitude and phase of the electric output power delivered to the load resistor. ($L = 3.18 \text{ mm}$, $R_n = 2.36 \text{ mm}$, $V_{cav} = 1950 \text{ mm}^3$, $t_{si} = 3 \text{ }\mu\text{m}$, $R_2 = 1.95 \text{ mm}$, $R_2 = 1.85 \text{ mm}$, $P = 94 \text{ dB}$)

The overall power conversion efficiency, Γ , can then be found as the ratio of output electrical power to input acoustical power, given by

$$\text{Re}\{\Gamma\} = \frac{\text{Re}\{\Pi_{out}\}}{\text{Re}\{\Pi_{in}\}}. \quad (2.118)$$

The magnitude and phase of the efficiency is shown in Figure 2-29 for the piezoelectric diaphragm by itself and in combination with the Helmholtz resonator. As seen in the plot, the efficiency of the composite diaphragm reaches a peak at the diaphragm resonance, while the efficiency of the coupled system reaches a peak at the second resonance, which is dominated by the diaphragm resonance. It is important to note that the peak magnitude is similar both with and without the Helmholtz resonator, suggesting that little benefit is gained through the use of the Helmholtz resonator, as this

Helmholtz resonator was not optimally designed for impedance matching. This need not always be the case, as the relative benefits of impedance matching are somewhat offset in varying amounts by the increased resistive losses due to the Helmholtz resonator. The benefits can thus be enhanced by maintaining the improved impedance matching while minimizing the additional losses. A perfect impedance match between the plane wave tube and the Helmholtz resonator would improve the efficiency by approximately 40% over the values shown in the figure. This value is estimated based on comparison to a Helmholtz resonator that is perfectly impedance matched to the plane-wave tube.

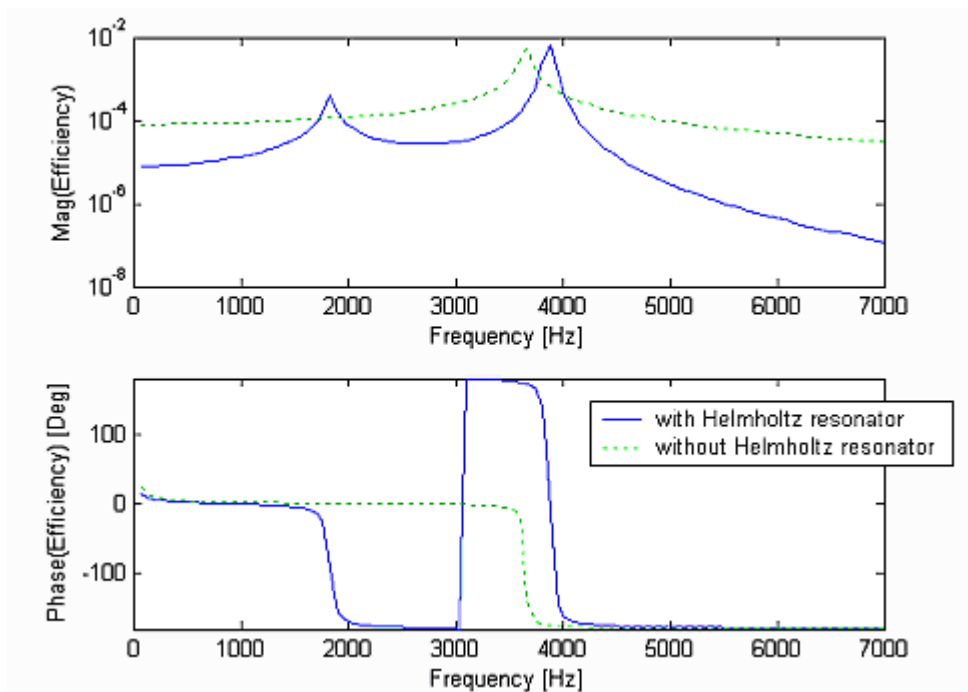


Figure 2-29: Magnitude and phase of the energy harvester efficiency. ($L = 3.18 \text{ mm}$, $R_n = 2.36 \text{ mm}$, $V_{cav} = 1950 \text{ mm}^3$, $t_{si} = 3 \text{ }\mu\text{m}$, $R_2 = 1.95 \text{ mm}$, $R_2 = 1.85 \text{ mm}$, $P = 94 \text{ dB}$)

Operation at an Optimal Frequency

To get a better feel for these devices in their intended application as harvesters of energy, it helps to look at the theoretical behavior for a single frequency. For the purposes of illustration, a device with the geometry of Device 8, as given by Table 2-5 on

page 81 was used and the frequency at which the efficiency is maximized was chosen. This optimal frequency is different between the diaphragm mounted on the Helmholtz resonator and the diaphragm strictly by itself. For the diaphragm mounted on the Helmholtz resonator, a sinusoidal signal at 1966 Hz was applied, while for the diaphragm mounted by itself, a sinusoidal signal at 13.11 kHz was used. For both cases, the signal was swept over a range of acoustic pressures while the open circuit output voltage was determined. A plot of the open circuit voltage versus acoustic pressure for both cases is shown in Figure 2-30.

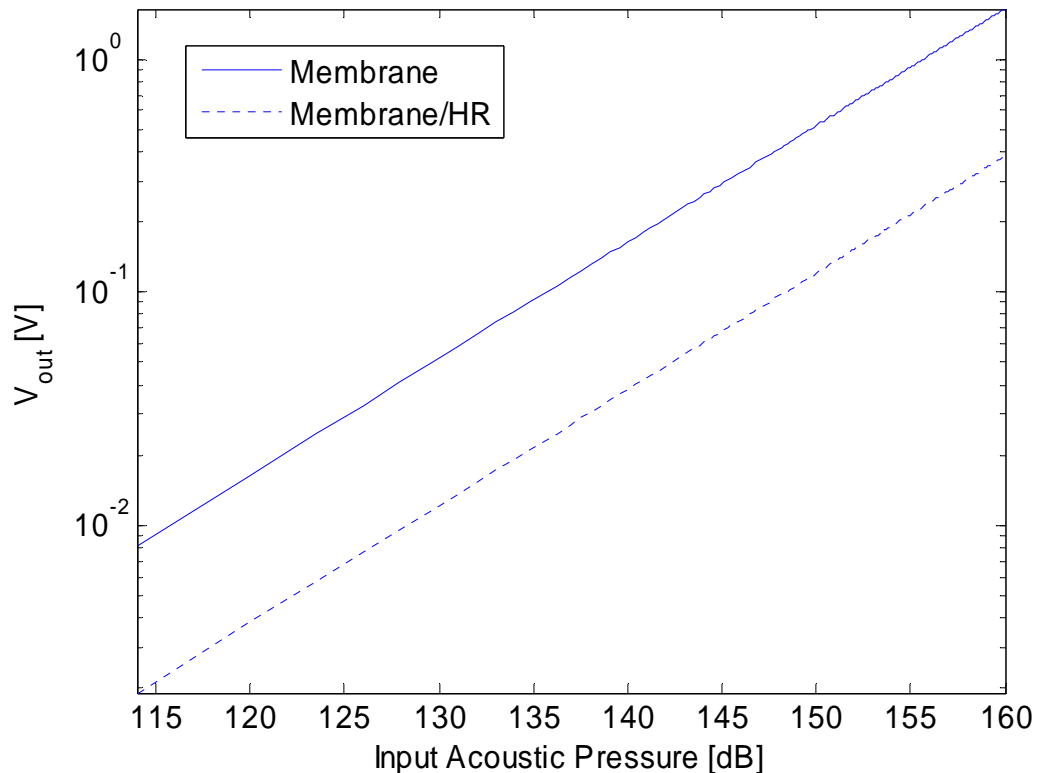


Figure 2-30: Open-circuit voltage as a function of the applied acoustic pressure for the piezoelectric diaphragm by itself and packaged with a Helmholtz resonator. (Device = 8 from Table 2-5, $f_{HR}=1966\text{ Hz}$, $f_{mem}=13.11\text{ kHz}$)

Note the steadily increasing output voltage as the acoustic pressure increases, as would be expected for a linear system such as this. This model, however, does not take into account any nonlinearities that may occur at high acoustic levels. Such

nonlinearities may include, but are not limited to, piezoelectric saturation effects on the output voltage and large deflection effects on the diaphragm compliance, in addition to acoustic nonlinearities introduced by the Helmholtz resonator orifice at high amplitudes. These nonlinearities will act to limit the maximum voltage in a real world application.

Operating at these same optimal frequencies, a load resistor was placed across the output terminals and the power was determined through that resistor. Repeating this over a range of load resistances yields the plot shown in Figure 2-31. Note that while the input power remains constant, the output power has a peak at a particular load resistance. This corresponds to the optimal resistance as given by Eq. (2.12). The input and output power using an optimal load are also shown on this graph and are indicated by an 'x' for both the diaphragm with the Helmholtz resonator and without.

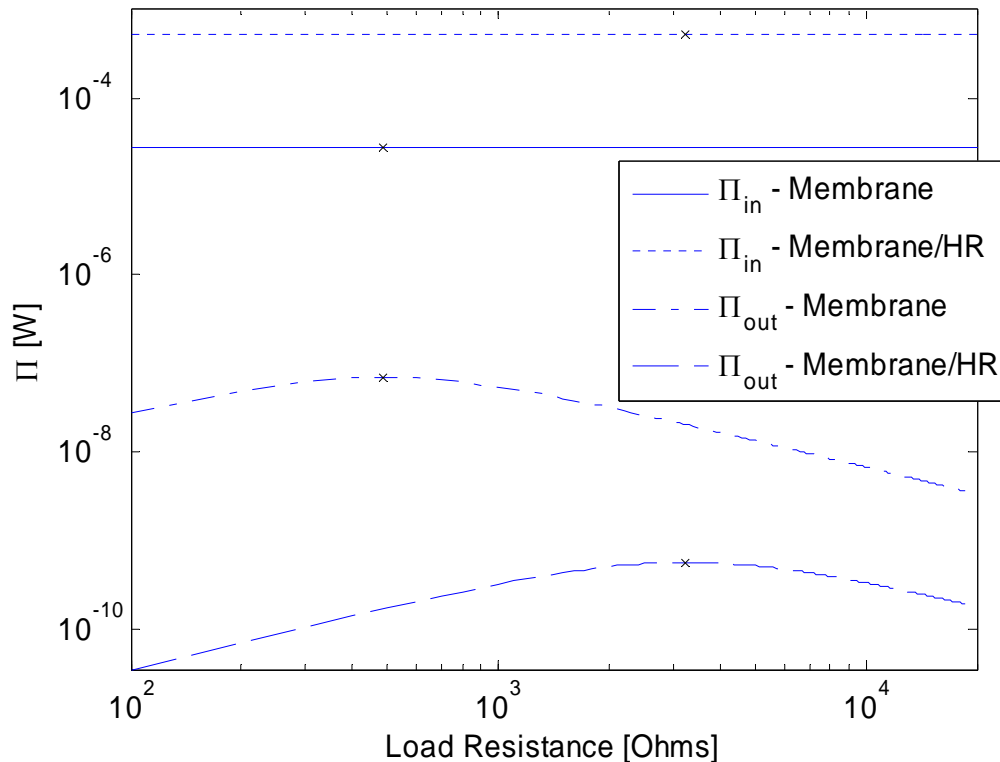


Figure 2-31: Input and output power as a function of the load resistance. Shown for the piezoelectric diaphragm by itself and packaged with a Helmholtz resonator. (Device = 8 from Table 2-5, $f_{HR} = 1966 \text{ Hz}$, $f_{mem} = 13.11 \text{ kHz}$, and $P = 114 \text{ dB}$)

Using the optimal values for the load resistance in each case, the input power and output power was determined as a function of the applied acoustic input pressure, and is shown in Figure 2-32. Once again, it is important to note that nonlinear effects are not included in the model used to calculate the output power.

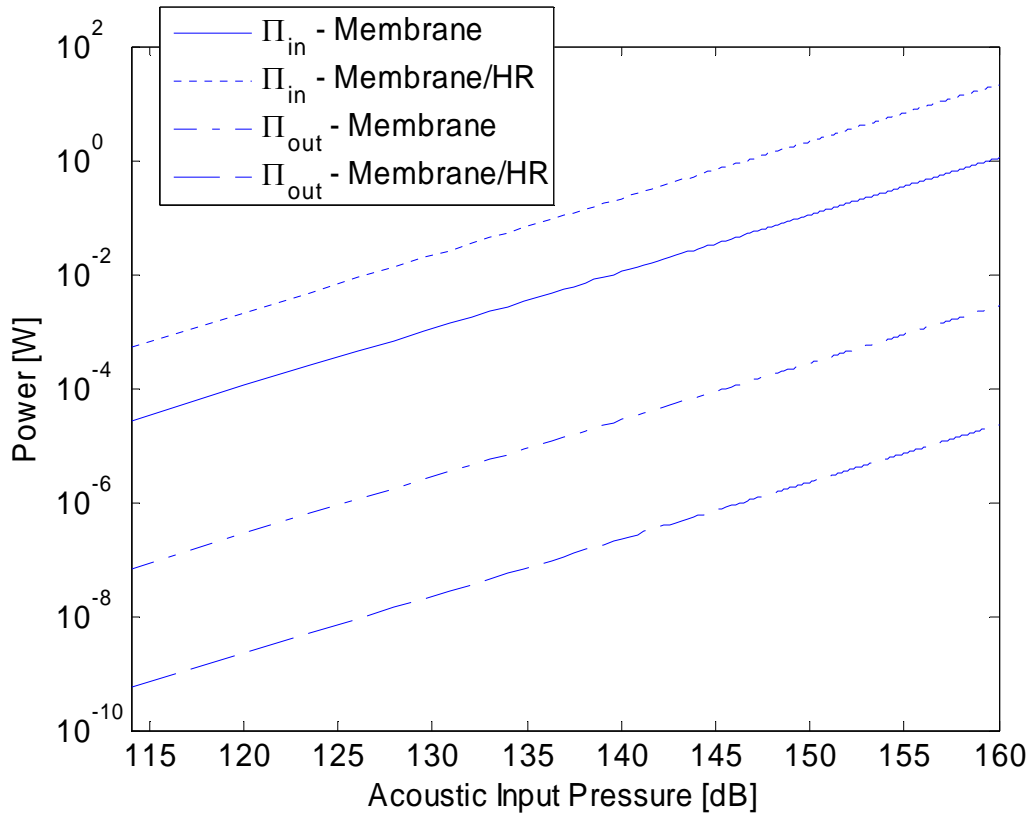


Figure 2-32: Input and output power as a function of the applied acoustic input pressure, while using an optimal load resistor. (Device = 8 from Table 2-5, $f_{HR} = 1966$ Hz, $f_{mem} = 13.11$ kHz, $R_{load,Mem} = 486 \Omega$, $R_{load,Mem/HR} = 3242 \Omega$)

Device Configurations

The devices were designed based on the theoretical plots, along with estimates of the output power based on the lumped element model. Eight configurations were chosen based on their resonant frequency and maximum power before the onset of nonlinear behavior. The criteria for choosing the designs were to keep the resonant frequencies

inside of the testable range, below 6.4 kHz , while maximizing the power. Four outer radii, R_2 , were chosen, consisting of 0.9 , 1.2 , 1.5 , and 1.8 mm , while the inner radii were all chosen to be 0.95 times their outer counterpart. The second four configurations had the same dimensions as the first four, with the addition of a central pillar of silicon designed to act as a rigid mass. It should be noted that the addition of the central mass invalidates the structural model that was used, however, the model is still expected to provide some guidance over the behavior of these particular devices as well. The central mass was added in order to reduce the resonant frequency of the diaphragms. It was fixed at 0.2 times the outer radius of each diaphragm. This value was chosen such that the central mass was located primarily over a region of the diaphragm that experiences little stress. By restricting the mass to this region, only a minimal increase in the diaphragm stiffness was expected, while the mass of the diaphragm could be greatly increased, thereby lowering the resonant frequency. The addition of this central pillar was predicted to lower the resonant frequency of each device by an average of 57.76% . Additionally, the diaphragm thickness was chosen to be $3 \text{ }\mu\text{m}$. Only one thickness for the diaphragm was chosen as all the devices were going to be made on the same wafer.

The chosen device configurations are summarized in Table 2-5. Overall, the geometries were chosen as to create a proof of concept set of devices. Manual parameter adjustment was performed in order to improve performance, however, strong constraints were placed on the geometry in order to ensure fabrication ability and improve the chances of first-run success. Also listed in the table are the predicted resonant frequencies and maximum power before the onset of nonlinearities. Note that this does not define an upper limit for the output power but merely provides a figure of merit upon

which to compare devices. Also, for the purposes of predicting the behavior of these specific devices and comparing them to experimental data, the lumped element parameters were computed using the equations from Chapter 2 and the Matlab code given in Appendix A. The calculated parameters are given in Table 2-6.

Table 2-5: Chosen device configurations for fabrication.

Device	t_{si} [μm]	t_p [μm]	R_2 [μm]	R_1 [μm]	R_{mass} [μm]	f_{res} [kHz]	Pow_{out} [nW]
1	3	0.5	900	830	0	65.68	15.56
2	3	0.5	900	830	180	28.08	36.12
3	3	0.5	1200	1115	0	48.14	1.73
4	3	0.5	1200	1115	240	20.37	3.99
5	3	0.5	1500	1400	0	38.01	0.302
6	3	0.5	1500	1400	300	15.98	0.667
7	3	0.5	1800	1685	0	31.41	0.070
8	3	0.5	1800	1685	360	13.15	0.162

Table 2-6: Lumped element parameters used for theoretical models.

Device	ϕ [$\frac{Pa}{V}$]	ϕ' [$\frac{V}{Pa}$]	k	d_A [$\frac{m^3}{V}$]	C_{aD} [$\frac{m^3}{Pa}$]	M_{aD} [$\frac{kg}{m^4}$]	M_{aDmass} [$\frac{kg}{m^4}$]	C_{eb} [nF]
1	-1.81	-5.80E-07	0.001	1.01E-14	5.58E-15	5663.3	0	17.4
2	-1.81	-5.80E-07	0.001	1.01E-14	5.58E-15	5663.3	19649	17.4
3	-9.29	-7.16E-06	0.008	1.93E-13	2.07E-14	2602.5	0	26.9
4	-9.29	-7.16E-06	0.008	1.93E-13	2.07E-14	2602.5	11052	26.9
5	-12.93	-1.94E-05	0.016	7.43E-13	5.74E-14	1521.8	0	38.2
6	-12.93	-1.94E-05	0.016	7.43E-13	5.74E-14	1521.8	7073.6	38.2
7	-16.92	-4.71E-05	0.028	2.42E-12	1.43E-13	1009.8	0	51.3
8	-16.92	-4.71E-05	0.028	2.42E-12	1.43E-13	1009.8	4912.2	51.3

CHAPTER 3 FABRICATION AND PACKAGING

Overview

This chapter focuses on the device fabrication and process flow, as well as the device packaging design and implementation. First, a detailed discussion of the process flow is presented, including fabrication methods, equipment, and recipes. This is followed by an overview of the packaging schemes that were employed. The packages were designed to flush mount the device in order to expose the diaphragm directly to the acoustic input, thereby enabling direct measurement of the diaphragm parameters. Two variations in package design were employed, namely a quarter-wave resonator package and a sealed cavity package. A graphical overview of this chapter is provided by the roadmap of Figure 3-1.

Process Flow

The devices were batch fabricated on 4” silicon-on-insulator (SOI) wafers. The process sequence is given in detail in Appendix B. All of the processing steps up through the deposition of the top electrode were performed at Sandia National Laboratories. The remainder of the steps were formed at the University of Florida, with the exception of the PZT etch step which was performed at the Army Research Laboratory.

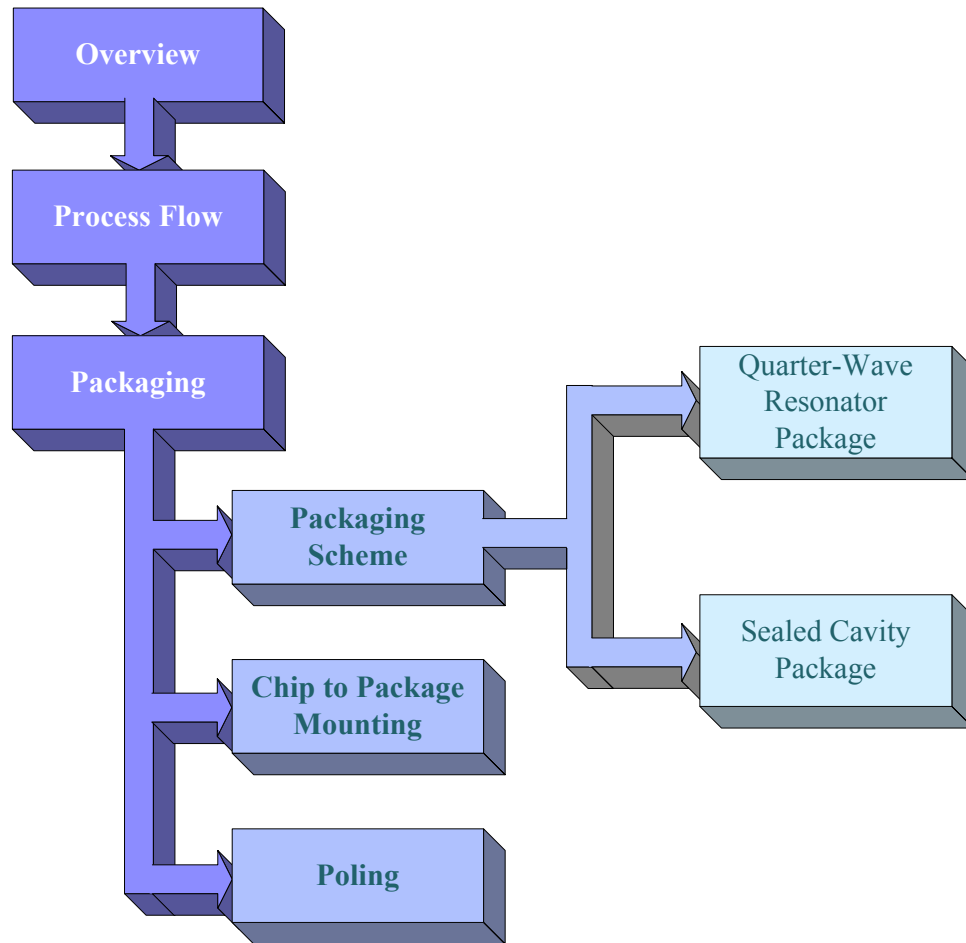


Figure 3-1: Roadmap for Chapter 3.

A diaphragm thickness of $3\ \mu\text{m}$ was desired in order to achieve a testable resonant frequency and therefore required a top silicon thickness in that range, as the top silicon layer of the SOI wafer ultimately forms the bulk of the diaphragm. Unfortunately, the only available SOI wafers contained a top silicon layer of $12\ \mu\text{m}$ thickness. In order to reduce this thickness, a timed KOH (Potassium Hydroxide) etch [137] was performed, however a residue was left behind on most of the wafers, that was difficult to remove. The composition of the residue was not identifiable, however a 1 minute dip in 10% Nitric acid, followed by a 2:1 Piranha etch for 5 minutes had no noticeable effect.

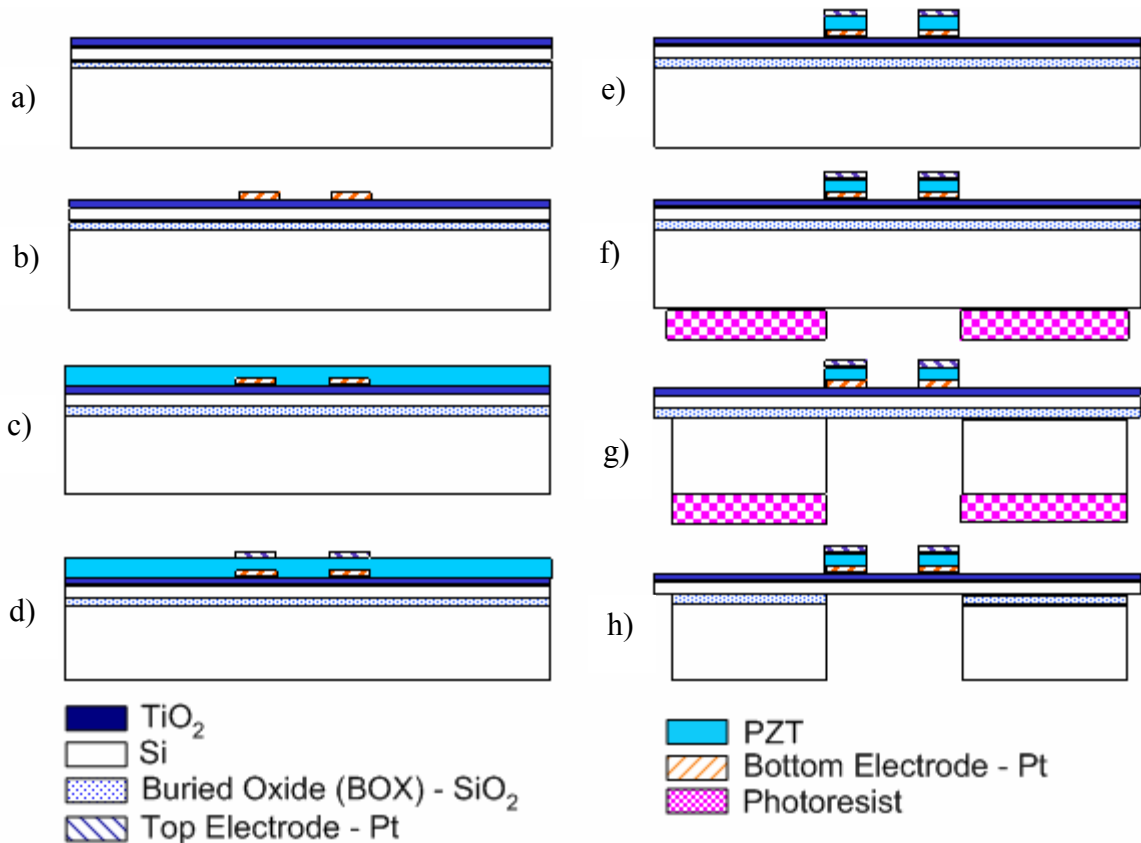


Figure 3-2: Condensed process sequence in cross-section. a) Deposit 100 nm of Ti on SOI Wafer and oxidize to form TiO_2 . b) Deposit Ti/Pt (40/180 nm) and liftoff with “ElectrodeBot” mask. c) Spin coat PZT 52/48 solution & pyrolyze (6 layers for 400 nm total). d) Deposit Pt (180 nm) and liftoff with “ElectrodeTop” mask. e) Wet Etch PZT in 3:1:1 of $(\text{NH}_4)\text{HF}_2/\text{HCl}/\text{DI}$ water. f) Spin & pattern thick photoresist on bottom with “Cavity” mask. g) DRIE (deep reactive ion etch) to buried oxide layer. h) Ash resist and BOE (buffered oxide etch) backside to remove to buried oxide layer.

Two of the original KOH-etched wafers were replaced with two new wafers that were etched in an HNA bath to avoid the residue issue [138]. The advantage of the HNA etch was a smooth, mirror finished surface to the wafer with no visible residue. The disadvantage was a less consistent etch rate than the KOH procedure. For comparison the HNA etch had an average etch rate of $2.6 \mu\text{m}/\text{min}$ with a standard deviation of $0.33 \mu\text{m}/\text{min}$, while the KOH etch had an etch rate of $1.69 \mu\text{m}/\text{min}$ with a standard deviation of $0.03 \mu\text{m}/\text{min}$.

Following the wafer thinning, the process flow proceeded as given by Figure 3-2. The first step was to deposit a 100 *nm* thick layer of Ti, and oxidize in a tube furnace to create a TiO₂ layer that serves as a diffusion barrier for the PZT [139-142] as shown in Figure 3-2a.

A liftoff process was then used to pattern the bottom electrodes with 40 *nm* of Ti followed by 180 *nm* of Pt as shown in Figure 3-2b. The Ti layer served as an adhesion layer in this step. The next step was the deposition of a previously mixed 52/48 sol-gel solution of PZT [139, 143, 144] as shown in Figure 3-2c. The solution was spin-cast at 2500 RPM for 30 sec, then pyrolyzed at 350 °C in air for 2 *min* on a hot plate. Repeating the spin and pyrolyze step 6 times yielded a total PZT thickness of approximately 400 *nm*. The wafers were then furnace annealed at 650 °C for 30 *min* to achieve a perovskite phase of PZT that has the most attractive piezoelectric properties.

Wafer bow measurements were performed after deposition and oxidation of the TiO₂ as well as after annealing of the PZT. By recording the wafer curvature in terms of radius or bow, the stress in the layers can be determined [145-147]. Table 3-1 shows the results and calculations from these measurements for all of the fabricated wafers. Stress levels were first calculated for the combination of TiO₂ and backside SiO₂ that was formed during the titanium oxidation step. Then the stress contribution from the TiO₂ was calculated. Finally, using the wafer curvature measurements after deposition and annealing of the PZT, the stress in the PZT layer was calculated.

In order to calculate the stress from the wafer curvature, a relationship known as Stoney's equation [145-147] was used and is given by

$$\sigma_f = \frac{E_s h_s^3}{6(1-\nu_s) R h_f^2 \left(1 + \frac{h_s}{h_f}\right)} \quad (3.1)$$

where $1/R$ is the curvature, h_s, h_f is the substrate and film thickness respectively, E_s is Young's modulus of the substrate and ν_s is Poisson's ratio of the substrate.

Table 3-1: Wafer bow measurements and the resulting calculated stress.

Wafer #	Initial		After TiO ₂ Dep. + Ox.			TiO ₂ + SiO ₂	TiO ₂	After PZT		PZT
	Radius [m]	Bow [μ m]	Radius [m]	Bow [μ m]	Stress [MPa]	Stress [MPa]	Stress [MPa]	Radius [m]	Bow [μ m]	Stress [MPa]
1	-43.8	18.51	-137.8	6.15	1367.1	844.7	1217.0	-149.9	5.65	12.8
1A	-40.1	20.5	-103.2	8.4	1335.3	1239.7	1809.6	-1144	1.52	176.3
2	-38.9	20.45	-99.0	8.03	1371.1	848.8	1223.1	-1338	0.72	187.3
3	-60.8	13.05	-291.4	3.12	1140.6	678.6	967.9	n/a	n/a	n/a
4	-44.2	18.24	-121.2	6.93	1259.8	772.9	1109.4	279.3	-2.82	249.9
5A	-63.7	12.84	-717.3	1.48	1254.5	776.3	1114.5	156.3	-4.74	159.4
6	-43.0	18.86	-109.3	7.6	1235.4	769.5	1104.2	809.9	-0.77	214.5
7	-44.3	18.3	-106.1	7.84	1154.2	714.8	1022.2	662.9	-1.27	233.5

Before the above equation can be used to find the stress in the TiO₂ layer, the thickness of the SiO₂ layer that was formed during the oxidation step must be determined. For silicon oxidation, the relationship between oxide thickness and oxidation time is approximated by [148]

$$t_{ox}^2 + A t_{ox} = B(t + \tau), \quad (3.2)$$

where A and B are coefficients which depend on material properties and operating conditions, t_{ox} is the total oxide thickness, t is the oxidation time, and τ is a time shift due to an initial oxide thickness. For short oxidation times, where $t \ll A^2/4B$, this equation reduces to

$$t_{ox} \cong \frac{B}{A}(t + \tau). \quad (3.3)$$

For <100> silicon oxidized in dry O₂ at 650°C, $B/A \approx 0.0001[\mu\text{m}/\text{hr}]$, and $B \approx 0.0001[\mu\text{m}^2/\text{hr}]$. Under these conditions, the approximation of short oxidation times holds, as the total oxidation time was 30 min, yielding an oxide thickness of approximately 50 nm. This thickness was then utilized in Stoney's equation to help determine the contribution due to each of the layers.

In addition to wafer bow measurements, the density of the PZT was calculated by measuring the mass of the wafers both before and after deposition. The results of these measurements are shown in Table 3-2.

Table 3-2: Measured wafer mass and calculated density of PZT.

Wafer	Mass [g]		PZT Density
	Pre-PZT	Post-PZT	$[\text{kg}/\text{m}^3]$
1A	9.752	9.7734	10217
2	9.4816	9.5129	9963
4	9.5049	9.5369	10185
5A	9.7445	9.7616	8164
6	9.556	9.5771	10074
7	9.5565	9.5764	9501
Avg.			9684

Following the PZT deposition, the top electrodes were deposited and patterned in a liftoff process similar to the bottom electrodes as shown in Figure 3-2d. The top electrodes also served as a hard etch mask for etching the PZT. The PZT was etched using a 3:1:1 solution of ammonium bifluoride ((NH₄)HF₂), hydrochloric acid (HCl), and deionized water as shown in Figure 3-2e. The etchant leaves a residue that then must be removed with a dilute nitric acid and hydrogen peroxide solution.

The next step was to deposit a thick photoresist on the backside, and pattern the backside release etch as shown in Figure 3-2f. Then the silicon wafer is backside etched using a deep reactive ion etch (DRIE) process, also known as a Bosch etch [148-152] as

shown in Figure 3-2g. This is a plasma-based etch process that alternates between a plasma etch, and a polymer deposition. The polymer is easily removed from the bottom of the etch holes during the ensuing etch cycle, but serves to significantly slow down any lateral etching, leading to high-aspect ratio etching. The ratio of etch time to passivation time during each cycle, along with a number of other process parameters, greatly affects the resulting etch quality. Shown in Figure 3-3 is a scanning electron micrograph (SEM) image of the sidewall of one of the test devices after an early stage, through-wafer, DRIE test, prior to working out the optimal parameters. In this figure, significant erosion of the sidewall can be seen, in the form of both pitting and undercutting. For comparison, the upper right region of the image shows what a smooth silicon sidewall looks like. The damage shown here is a result of an etch-to-passivation ratio that is too high. The passivation layer is then insufficient to protect the sidewalls during the entire etch cycle.

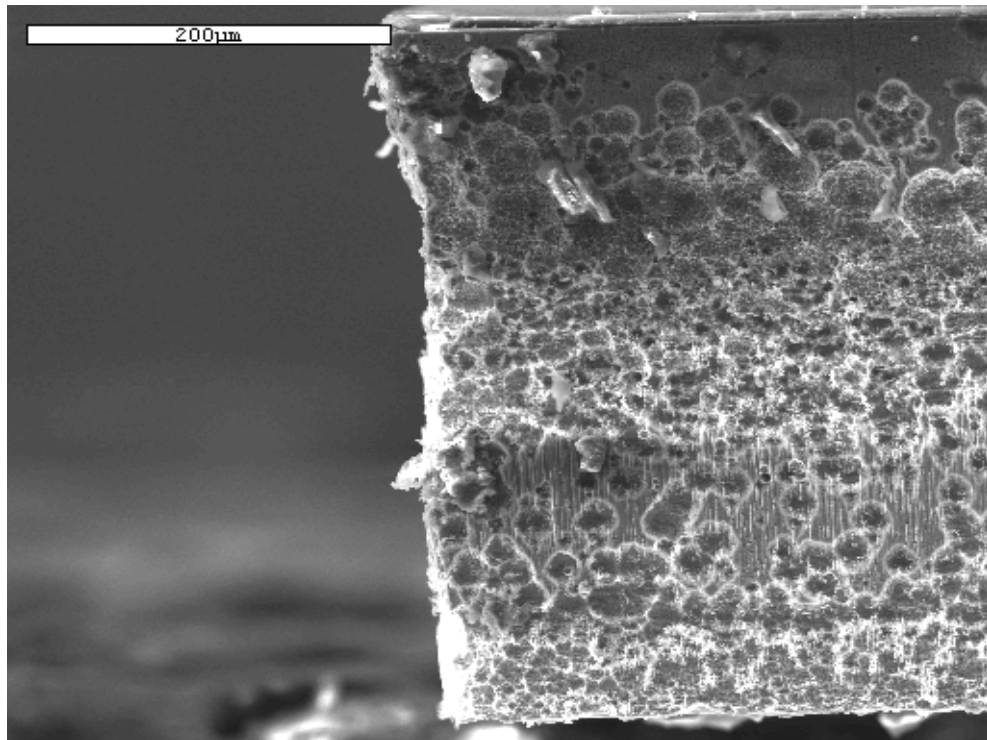


Figure 3-3: Early DRIE results showing significant sidewall damage.

A different problem occurs when the etch-to-passivation ratio is too low. In this instance, some portions of the passivation layer are not removed from the bottom of the etch holes during the etch cycle, leading to a micromasking effect and the ultimate formation of what is known as “silicon grass” or “black silicon” [153]. This was also encountered during the early trial stages of our DRIE attempts. Shown in Figure 3-4 is an SEM image showing the formation of black silicon at the base of a trench.

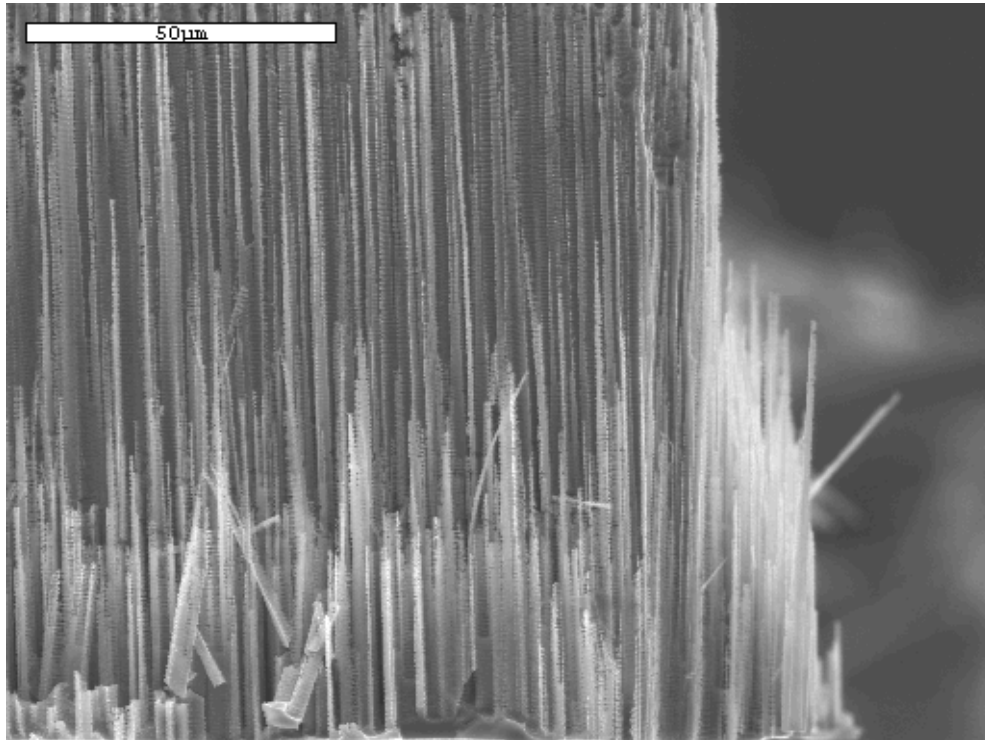


Figure 3-4: SEM image showing black silicon at the base of a DRIE-etched trench.

Finally, after adjustment of the various process parameters a successful DRIE was performed through the thickness of the silicon wafer. This is shown in Figure 3-5. Notice, a nearly vertical sidewall was achieved with little cratering and erosion, leaving a smooth surface with the exception of the large debris particle.

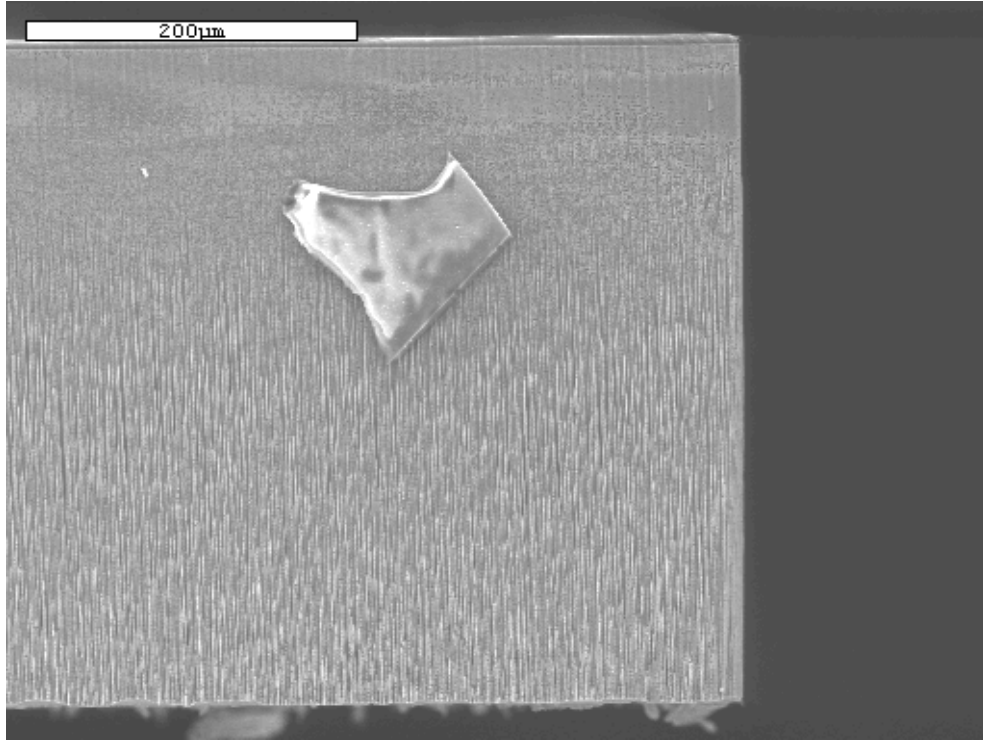


Figure 3-5: SEM image of a successful DRIE etch through the thickness of a wafer.

Once the DRIE recipe was worked out, the DRIE process was used here to etch through the bulk of the silicon wafer, stopping on the buried oxide layer, leaving a thin diaphragm as well as creating channels that served to later separate the wafer.

Additionally, the central pillar that serves as the point mass was created in this process by masking the central portion of the diaphragm backside. Following the DRIE, the photoresist was stripped from the backside. A composite top view schematic and cross-section of the device are shown in Figure 3-6. The devices were arranged on the wafer in blocks as shown in Figure 3-7. Each block consists of the eight device configurations. The blocks were then arranged on the wafer as shown in Figure 3-8. The blocks were arranged across the wafer such that the wafer would maintain structural stability after the DRIE release of the die within the blocks. A photograph of a completed energy harvester chip taken under a microscope with a 1.25x lens is shown in Figure 3-6c.

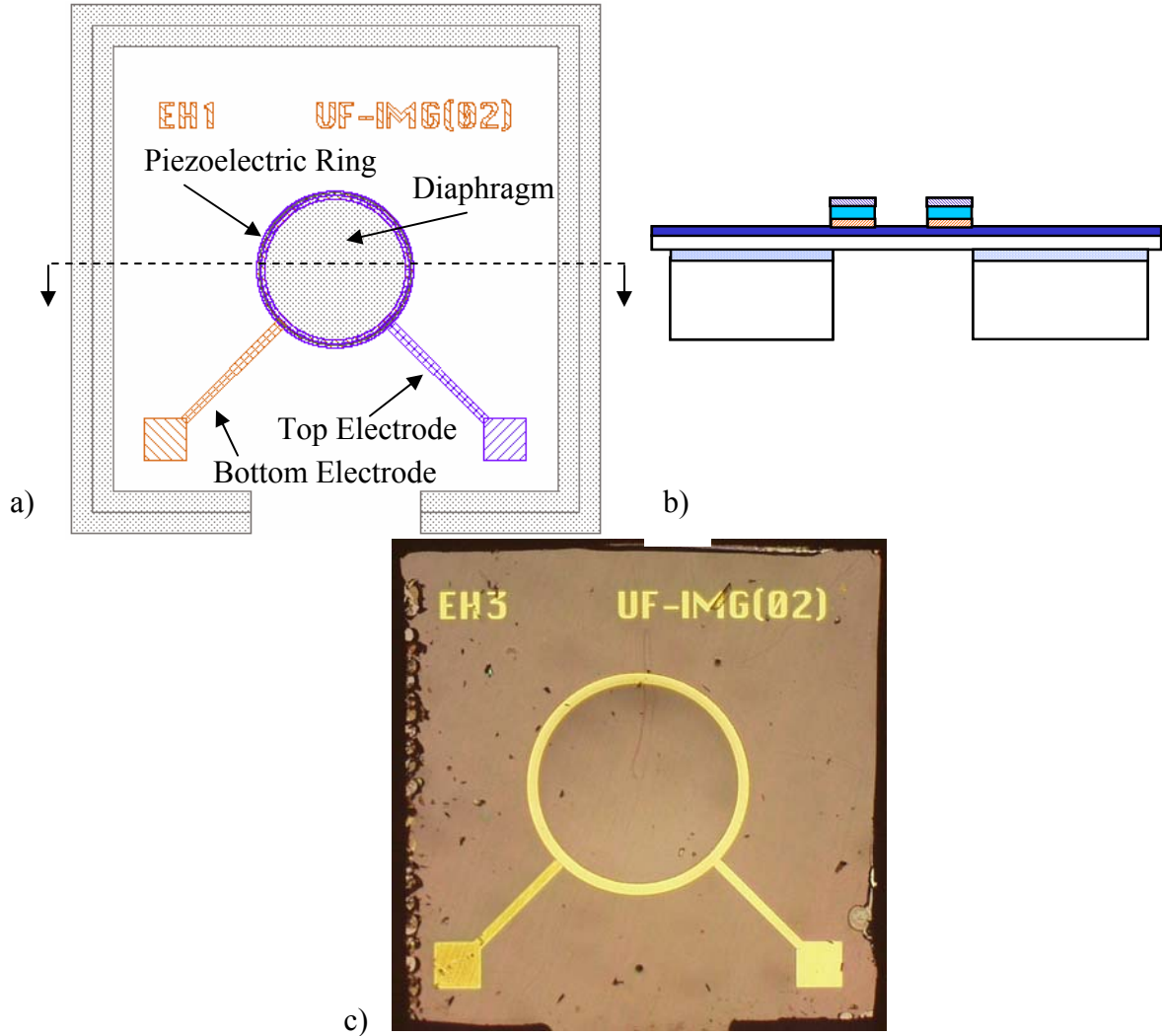


Figure 3-6: Illustration of a single diaphragm device. a) Composite top view schematic of single diaphragm device showing ring shaped electrodes, with bottom electrode extending to lower left and top electrode extending to lower right. Also shown is the die separation channel around the perimeter. b) Completed cross-section showing the Pt/PZT/Pt sandwich. c) Optical photograph of a completed device, taken under a microscope with a 1.25x magnification.

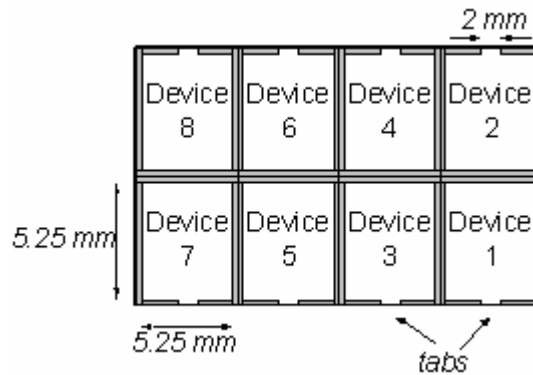


Figure 3-7: Block layout illustrating numbering scheme for devices, per Table 2-5.

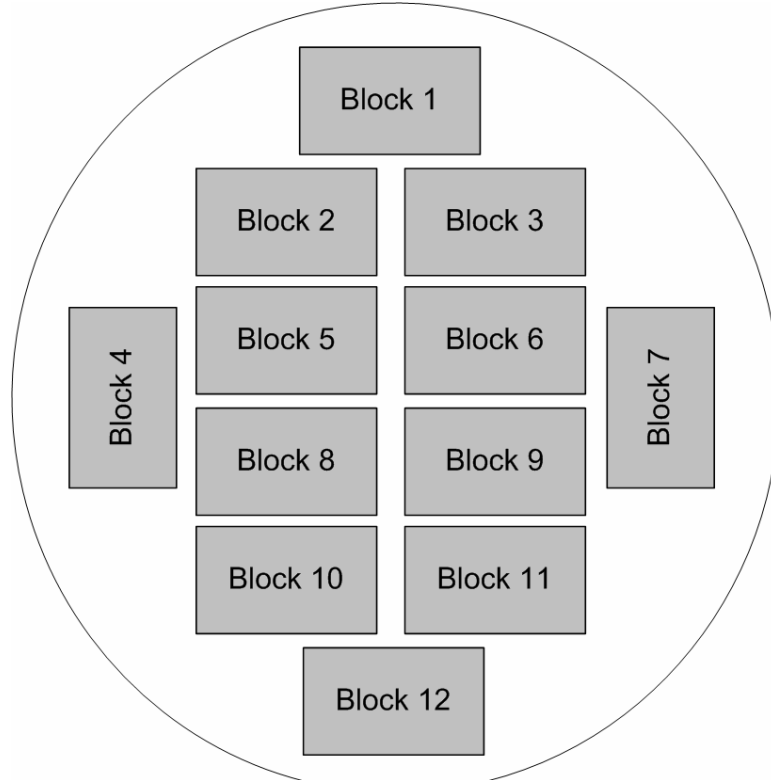


Figure 3-8: Wafer layout illustrating numbering scheme for blocks.

Packaging

Following the processing steps listed above, each die was separated from the wafer by scribing across the small tab holding each die and cleaving at the scribe line. Then each die was mounted in a Lucite package, described next, and bonded to a pair of electrical leads. The devices to be tested inside of an acoustic plane wave tube were packaged accordingly so that a tight seal was created with the plane wave tube while allowing external electrical access to the devices.

Packaging Scheme

Quarter-wave resonator package

In order to provide a convenient package for measurement of the diaphragm parameters, an acrylic plug for the acoustic waveguide was designed and constructed.

The plug allows for flush mounting of the device on the topside, and acoustic venting on the backside to prevent a cavity stiffening effect. The cavity stiffening effect describes an overall lowering of sensitivity due to the low compliance (i.e. high stiffness) of a small cavity (Eq. (2.21)). This however introduced a quarter-wave resonance effect that will be demonstrated in the experimental results. Additionally, two, 18 gauge, copper wires are embedded in the plug to allow for electrical connection to the electrodes of the piezoelectric ring. A schematic of the package is shown in Figure 3-9.

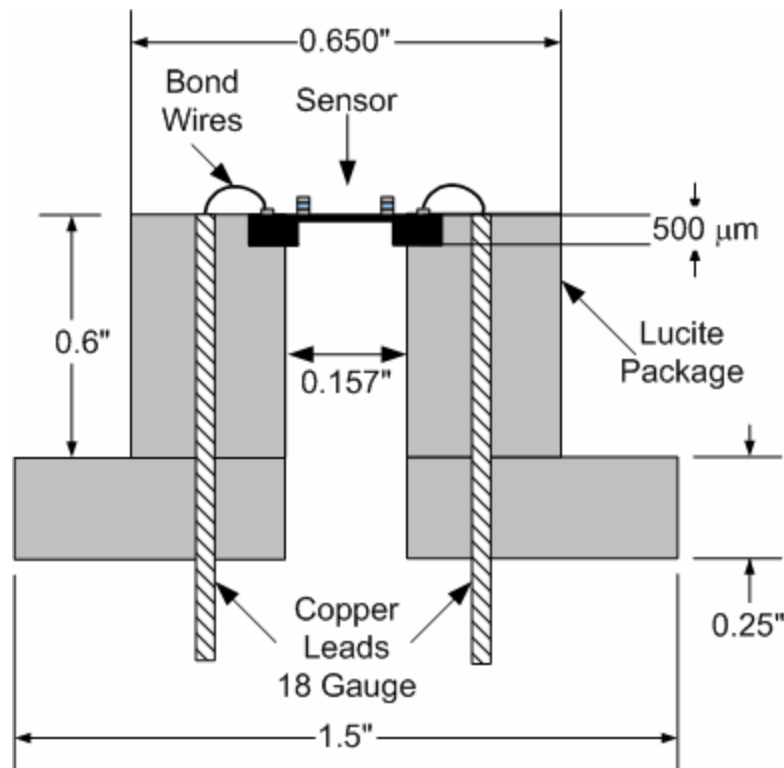


Figure 3-9: Quarter-wave resonator package consisting of acrylic plug, copper leads and vent channel.

The quarter-wave resonance effect arises because of the impedance mismatch that occurs at the interface between the backside vent channel and the environment on the exterior of the package. An acoustic wave that is traveling down the channel is reflected upon encountering the open end of the channel. This sets up a standing wave within the

channel. Both the pressure, P , and velocity, U , exhibit this spatial pattern, and the ratio of P/U , which is the impedance, Z , shows a spatial dependency as well.

Mathematically, the impedance at a distance x along the length of the channel can be written as

$$Z(x) = jZ_o \tan(kx), \quad (3.4)$$

where Z_o is the specific acoustic impedance of the medium. When the distance, x , is equal to $\frac{1}{4}$ of the wavelength, this equation reduces to

$$Z\left(\frac{\lambda}{4}\right) = jZ_o \tan\left(k \frac{\lambda}{4}\right) = jZ_o \tan\left(\frac{2\pi f}{c} \frac{c}{4f}\right) = 0 \quad (3.5)$$

Thus, the impedance goes to zero at frequency-position combinations where $x = \lambda/4$. This zero impedance allows for large velocity responses for small pressure inputs, i. e. a resonance. Similarly, there are frequency-position combinations where the impedance becomes infinite. In practice, various losses serve to limit the impedance from becoming exactly zero or infinity.

Sealed cavity package

This package was designed so that the parameters of the piezoelectric composite diaphragm could be measured independently of effects due to the quarter-wave resonator. The design is identical to the quarter-wave resonator except the vent channel is sealed. A cross-sectional schematic of the sealed cavity package is given in Figure 3-10 and a corresponding optical photograph of the device and package is shown in Figure 3-11.

Chip to Package Mounting

The chip was flush mounted within the provided recess in the package, and epoxy bonded to the package to provide an airtight seal. The electrical connections to the

package leads were accomplished via short lengths of flattened bare wire that were bonded using two-part, silver epoxy (Epotek™ H20E) on the chip bond pads as well as to the copper pads on the package. The silver epoxy was then cured at 90° C for one and a half hours. A relatively low temperature, long curing time recipe was chosen so as to remain below the glass transition temperature of the Lucite, which occurs at 100° C.

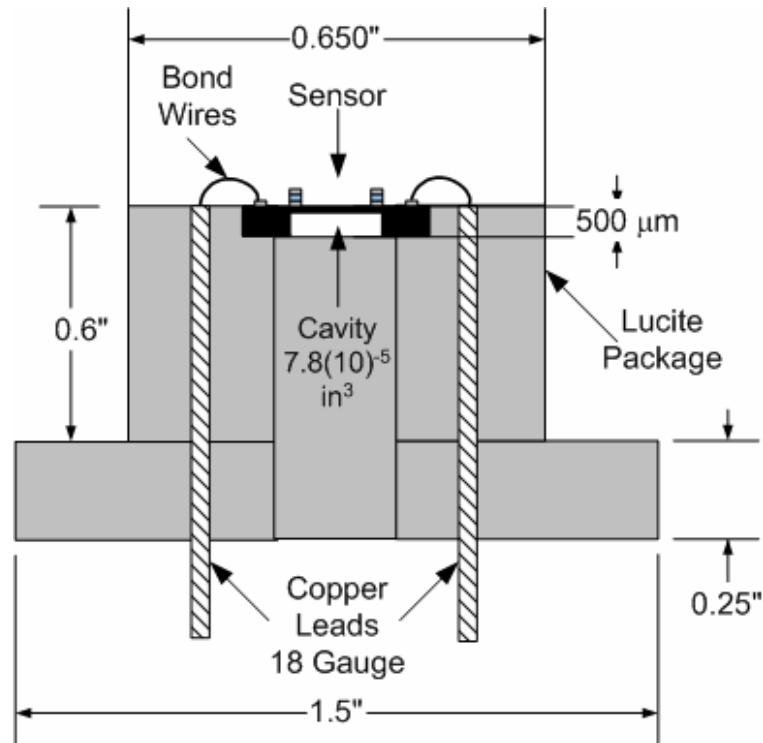


Figure 3-10: Sealed cavity package.

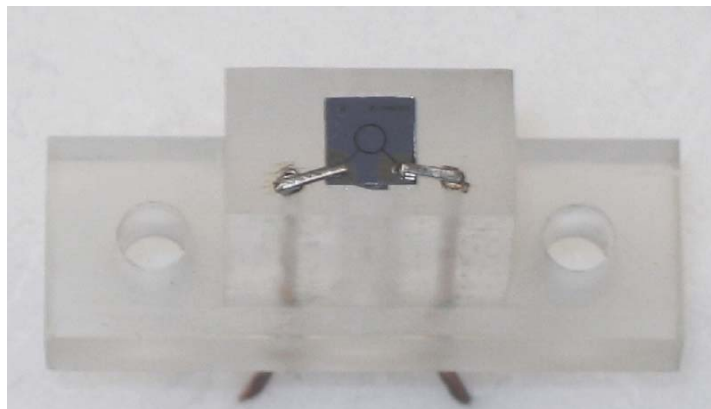


Figure 3-11: Optical photograph of a packaged energy harvester.

The silver epoxy method, as outlined above, was used because of problems encountered when trying to wire bond from the package to the die. The problems were believed to have arisen from overhanging top electrode metal on the individual die. The liftoff step that produced the top electrode was found to have left “stringers” around the edges of the electrode. These “stringers” were the result of performing a liftoff using positive resist, as the positive sidewall slope of the resist does not allow for a clean break in the metal deposition, thereby leading to tearing during the liftoff portion of this step.

The overhanging metal was found to cause short-circuits on all of the devices of several wafers. On two of the wafers, no short-circuits were evident initially; however, after wire bonding, all devices would then exhibit a short-circuit. It was concluded that the vibrations and impact of the wire bonding tool were causing the overhanging top electrode to fall into contact with the bottom electrode directly beneath it. This problem was avoided by utilizing a more gentle approach to bonding, namely silver epoxy. The entire issue, however, could be avoided in the future by using a negative resist and an image reversal mask to create a negative sloping photoresist sidewall for this liftoff step.

Poling

Following the completion of the packaging steps, the devices were poled so as to align the domains along the poling axis. It should be noted that the devices were found to exhibit a small amount of piezoelectric behavior prior to poling. This is believed to be due to a partially pre-aligned structure resulting from the deposition process.

Poling was accomplished by applying an electric field across the device for a specified amount of time. The devices were poled at room temperature at $20 \text{ V}/\mu\text{m}$ that corresponds to an applied voltage of 5.34 V for the given device thickness. This poling

field was held for 10 *min* . A typical maximum polarization of $16.9 \mu\text{C}/\text{cm}^2$ was achieved with a remanent polarization of $6.26 \mu\text{C}/\text{cm}^2$. More details of this measurement are provided in Chapter 5.

Typically, poling is accomplished at higher temperatures for improved piezoelectric properties [8, 145], although Bernstein et al [28] reported acceptable poling results at room temperature. While it was desirable to try a higher temperature poling procedure, temperature constraints caused by the glass transition temperature of the acrylic package prohibited the use of temperatures above $100 \text{ }^\circ\text{C}$.

Prior the successful poling of the devices, several other variations of the poling method were tested. For instance, initially, $10 \text{ V}/\mu\text{m}$ was utilized as a poling field, however piezoelectric properties were found to be relatively unchanged from the unpoled state. Additionally, higher electric fields were tested, above $20 \text{ V}/\mu\text{m}$, however this consistently led to the development of a short-circuit in the device. The short was believed to be a result of the many stringers that overhung from the top electrode layer down to the bottom electrode. At sufficiently high voltages, the force of attraction between these stringers and the bottom electrode is hypothesized to pull them into contact.

CHAPTER 4 EXPERIMENTAL SETUP

This chapter discusses the various setups for the experimental work. A series of measurements were performed to experimentally determine the various parameters of the piezoelectric composite diaphragm. This allows for further analysis and verification of the models. The measurements were performed using four different experimental setups. First, the electrical output impedance of each device was measured using an impedance meter. Then an electrically actuated response was measured using a scanning laser vibrometer (LV), to determine a voltage driven frequency response and corresponding mode shapes. Following this, an acoustically actuated response was measured using an acoustic plane wave tube. This was used to determine a pressure driven frequency response, input and output power, output voltage and efficiency. Finally, the static mode shapes were measured using an optical profilometer to determine the initial deflection due to residual stresses. A graphical overview of this chapter is provided by the roadmap of Figure 4-1.

Parameters and How They are Obtained

A structured methodology was developed for obtaining all of the desired measurement parameters for the composite plate. Using a predefined set of experiments and a few relations between various parameters, a method was derived for obtaining each of the parameters.

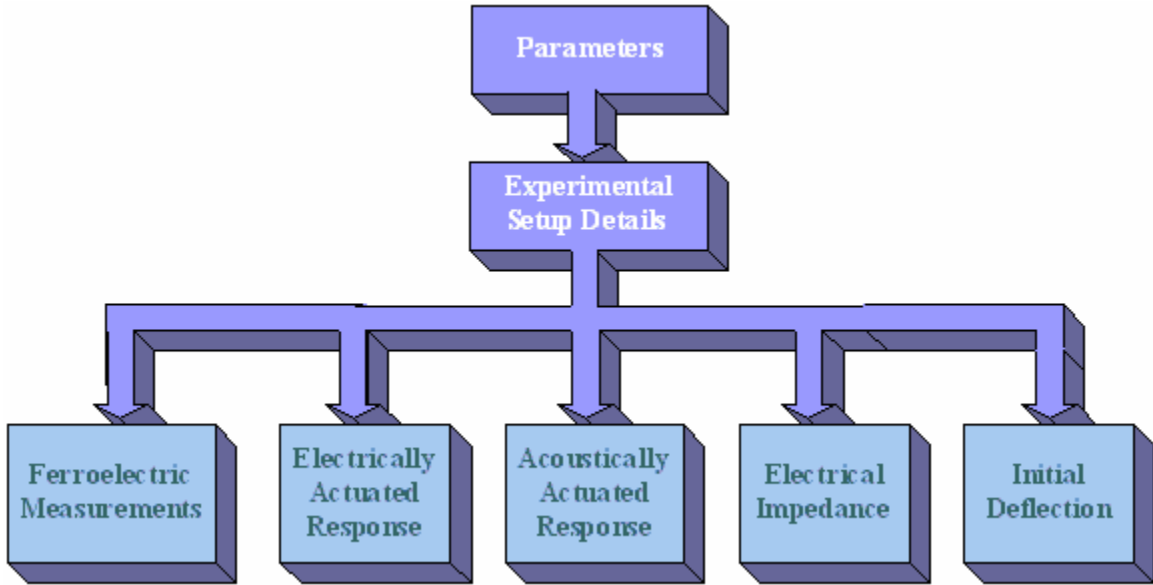


Figure 4-1: Roadmap for Chapter 4.

The series electrical output capacitance, C_s , and resistance, R_s , can be experimentally obtained through use of an impedance meter. This measurement needs to be performed after poling the device, as the poling procedure can affect the capacitance. The measured value can then be compared to theory, given by $C_s = \epsilon A/d$ if totally free, (Eq. (2.51)) and $C_s = (\epsilon A/d)(1 - k^2)$ if totally blocked, (Eq. (2.61)). Now in the case of the energy harvesters, $k \ll 1$ so that the free and blocked cases are approximately equal. For the series resistance, the theoretical value can be obtained from a predicted loss tangent for the material.

The resonant frequency of the devices can be obtained through use of an acoustic plane-wave tube (PWT) that is used to excite the diaphragm acoustically, while the output voltage from the device is measured. The measured frequency can then be compared to a theoretical value that is based on the lumped element model for C_{ad} and

M_{ad} .

There are four readily definable sensitivities of interest for the energy harvester. Two of these sensitivities are defined at resonance, while the other two represent static sensitivities. $Sens_{EA_{res}}$ is the electrical-to-acoustical sensitivity at resonance and can be experimentally determined by applying a voltage signal to the device at the resonant frequency while the diaphragm deflection is measured via a laser Doppler velocimeter (LDV). $Sens_{AE_{res}}$ is the acoustical-to-electrical sensitivity at resonance and can be found experimentally by acoustically exciting the diaphragm at resonance via the PWT while measuring the voltage produced by the device. Both of these resonant sensitivities can then be compared to theory which is computed directly from the lumped element models for R_{rad} , C_{aD} , M_{aD} , R_s and ϕ' .

The static electrical to acoustical sensitivity, $Sens_{EA_{low}}$, is approximated using the LDV at low frequencies. The LDV requires a finite velocity, and so a low frequency approximation is necessary for estimation of the static value. Similarly, the static acoustical to electrical sensitivity, $Sens_{AE_{low}}$, is measured in the PWT using an acoustic input signal at low frequencies. The same limitation to the static case occurs in this measurement as well. Both of these values can then be compared to theoretical values computed directly from the lumped element model using the equations for C_{aD} , R_{ef} , C_{ef} and ϕ .

The initial deflection of the diaphragm that results from residual stress in the composite can be measured using a Wyko optical profilometer without any excitation to the device. Theoretical values are obtained by numerical calculations accounting for the residual stress.

The coupling factor, k , is measured in two different ways. First it may be obtained from the difference between the open and short circuit resonant frequencies, or it can be found via $k = \sqrt{\phi\phi'}$. Theoretical values are obtained from ϕ and ϕ' or from d_A , C_{aD} and C_{ef} .

Finally, the electroacoustic, ϕ , and acoustoelectric, ϕ' , transduction factors are extracted from a combination of $Sens_{EA_{low}}$ and C_{aD} and a combination of $Sens_{AE_{low}}$ and C_{ef} , respectively. The theoretical values can be found directly from the numerical model.

Experimental Setup Details

Ferroelectric Measurements

The ferroelectric properties of the devices were measured by attaching the two electrodes to a Precision LC, Precision Materials Analyzer manufactured by Radiant Technologies. This ferroelectric tester applies a bipolar triangular waveform, while it measures the resulting charge, from which it can calculate the polarization of the material as a function of applied voltage. The bipolar waveform excitation to the ferroelectric material leads to the familiar hysteresis loop. For these measurements, the voltage was swept first between -0.5 V and 0.5 V . Subsequent loops swept to higher voltages in steps of 0.25 V up to a maximum of 5 V . For each loop, 101 points were measured and the total loop time was set to 10 ms . In addition, for each loop, a pre-loop was performed, where the same sweep was performed without measurements taken. Then the loop was repeated with the actual measurements taken. This process is designed to preset the conditions for the measurement. A delay of 1 ms was used between the preloop and the measurement loop.

Electrically Actuated Response—Laser Scanning Vibrometer

In order to determine the voltage actuated mode shapes and frequency response, laser scanning vibrometry was performed. The packaged energy harvesters were mounted under an Olympus BX60 Microscope, [154] with a 5x objective lens. The composite diaphragms were excited using either an HP 33120A Arbitrary Waveform Generator [155] or a Stanford Research Systems SRS-785 Dynamic Signal Analyzer. Displacement data were obtained over the surface of the composite diaphragms using a Polytec OFV 3001S laser scanning vibrometer, with a Polytec OFV-074 Microscope Adapter. [156] The laser vibrometer was equipped with a velocity decoder, from which the displacement was calculated.

To determine the frequency response, a white noise input was applied. The center deflection was then measured as a function of frequency, while the reference voltage was simultaneously recorded. From this measurement, the resonant frequencies were determined. A Hanning window was applied to all incoming data and 6400 FFT lines, with 100 averages were taken. Depending on the particular device, the measurement bandwidth was adjusted as was the laser sensitivity and range in order to optimize the signal level and resulting data quality. A slow tracking filter was applied to all incoming laser measurements. Additionally, due to an inherent time delay in the laser vibrometry channel, there is a fixed linear phase trend in any measured frequency response data. All resulting plots were detrended by taking this time delay into account. The amount of the delay varies, depending on the gain setting, however for a given setting it is fixed and defined by the manufacturer.

The input was then changed to a sine wave at the primary resonant frequency and the laser was scanned over the surface to measure the primary mode shape. Higher order

modes were also measured, although primarily to identify the nature of the higher resonances, and will not be presented in much detail.

Acoustic Characterization – Plane Wave Tube

The packaged energy harvesters were mounted, one at a time, to the end of the 1” x 1” cross section plane wave tube (PWT). Figure 4-2 shows this experimental setup for obtaining acoustical input impedance and power to the energy harvester. A Bruel and Kjaer (B&K) microphone type 4138 [157] was mounted on the wall of the PWT near the end of the tube to record the incident sound pressure level (SPL). Additionally, two B&K microphones were mounted in a rotating plug at 3.19 *cm* and 5.26 *cm* from the end of the tube. These two microphones were used to record the acoustic field in the tube, extract the standing wave component, and determine the corresponding impedance of the energy harvester. The data was recorded by a B&K PULSE Acoustic Characterization System that also supplied the periodic random source signal through a Techron 7540 Power Supply Amplifier [158] to the BMS 50.8 *mm* coaxial compression driver (Model 4590P) mounted at the far end of the PWT. The tests were then repeated with a 1 *kΩ* load shunted across the electrodes of the piezoelectric composite diaphragm. For all of the tests, the equipment was setup to measure 6400 FFT lines from 0 *kHz* to 12.8 *kHz* with uniform windowing, no overlap, and 500 averages.

To determine the normal incidence acoustic impedance, frequency response measurements (later defined as H_{12}) were taken using the two microphones in the rotating plug. [159, 160] The plug was then rotated and the measurement repeated. The two measurements were then averaged to remove any differences due to the individual

microphone calibrations. This averaged frequency response was then used with the two-microphone method (TMM) to determine the acoustic impedance [159, 161-163].

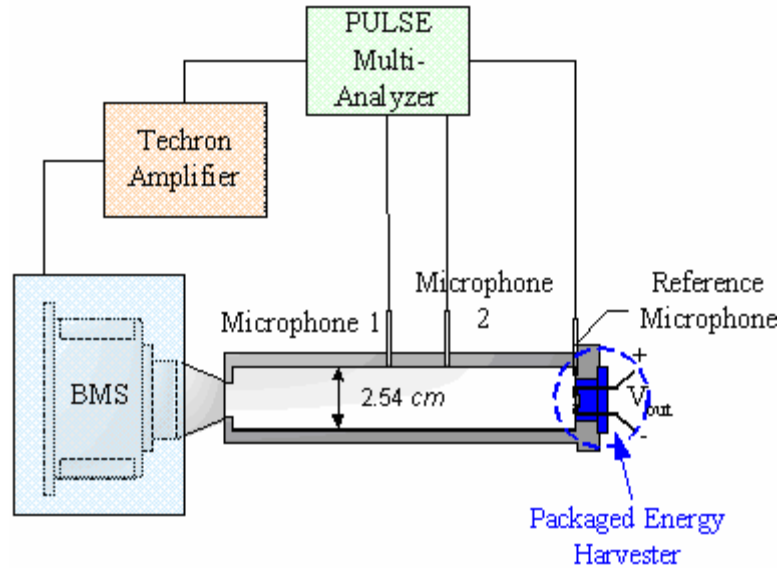


Figure 4-2: Experimental setup for impedance and power measurements.

The TMM is a method for estimating the reflection coefficient of an object or material mounted at the end of an acoustic wave guide. The TMM requires less than a half-wavelength spacing between the two microphone locations [159-161, 163, 164]. Although the waveguide used is physically capable of supporting plane waves up to 6.7 kHz , testing was limited to 6.4 kHz because of this microphone spacing constraint. An alternative, single-microphone method [157] exists but was not used due to greater errors associated with the technique. Additionally, the uncertainties were estimated for the acoustic impedance measurements using a technique presented by Schultz et al [165].

Under the assumption of planar waves in the waveguide, the sound field inside the waveguide can be described by

$$p' = \text{Re} \left[p_i \left(e^{j(\omega t + kd)} + R e^{j(\omega t - kd)} \right) \right], \quad (3.6)$$

where the $e^{j(\omega t+kd)}$ term represents the right-propagating waves, the $e^{j(\omega t-kd)}$ term represents the left-propagating waves, and d is the axial distance from the specimen surface. From Eq. (3.6), an expression for the reflection coefficient is found by taking the ratio of two pressure measurements at different axial locations,

$$R = \frac{H_{12}e^{jkd_1} - e^{jkd_2}}{-e^{jkd_2} - H_{12}e^{-jkd_1}}, \quad (3.7)$$

where d_1 and d_2 are the distances from the specimen test surface to the measurement locations, ω is the radian frequency, k is the wavenumber, R is the complex reflection coefficient, and H_{12} is an estimate of the frequency response function between the two microphones. The frequency response function is defined as [166]

$$H_{12} = |H_{12}|e^{j\phi_{12}} = \frac{G_{12}}{G_{11}}, \quad (3.8)$$

where G_{12} is the cross-spectral density function and G_{11} is the autospectral density function. After calculation of the reflection coefficient from the measured data, the normalized acoustic impedance is then found to be a function of the reflection coefficient and is given by

$$\xi = \frac{Z_1}{Z_0} = \frac{1+R}{1-R} = \theta + j\chi, \quad (3.9)$$

where Z_0 and Z_1 are the specific acoustic impedance of the acoustic medium and the test specimen, respectively and θ and χ are the normalized resistance and reactance, respectively.

Using the same test setup as described above, the input acoustic power, Π_{input} , can also be found. A schematic showing the incident and input power is given in Figure 4-3.

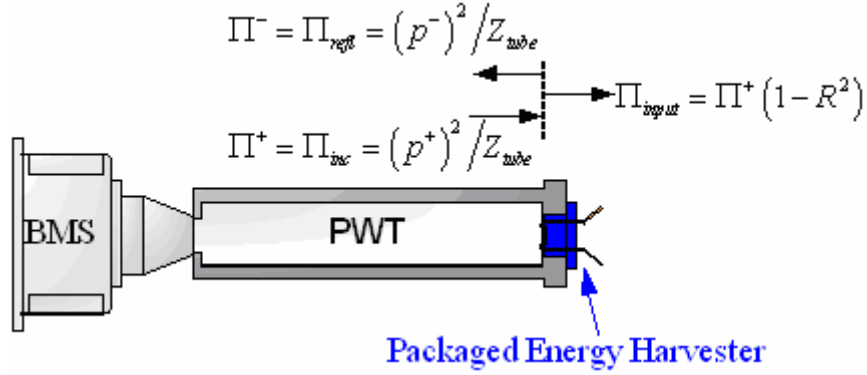


Figure 4-3: Schematic of incident, reflected and input power.

There are two main methods for obtaining the input acoustic power. First it can be calculated from the power reflection coefficient, $r = R^2$, and the incident acoustic power, $\Pi^+ = (p^+)^2 / Z_{tube}$, as

$$\Pi_{input} = \Pi^+ (1 - r) = \frac{(p^+)^2}{Z_{tube}} (1 - R^2), \quad (3.10)$$

where Z_{tube} is the acoustic impedance of the plane-wave tube, and p^+ is the acoustic pressure of the right-propagating (incident) waves. The second method for obtaining the input acoustic power is to utilize the input impedance, Z_{in} , that was also calculated from the two-microphone measurements via R . Using this method yields

$$\Pi_{input} = \frac{P_{tr}^2}{Z_{in}} \quad (3.11)$$

where $P_{tr} = P^+ + P^-$ is the transmitted acoustic pressure. Under ideal conditions, both methods yield equivalent answers; however, when R approaches 1, the value for R is known with significantly greater certainty than the value for Z_{in} .

In addition to measuring the input impedance and power, the frequency response function of the devices can be measured. The resonant frequency of the diaphragm can

be found from the frequency response function, as can the maximum output voltage and power. As the input power is also known, the efficiency can be calculated. Additionally, a load can be placed across the electrical terminals of the energy harvester and the effects monitored. The resistance of the load can be varied to experimentally determine the optimal loads for maximum power and maximum efficiency.

Electrical Impedance Characterization

The electrical impedance was measured using a HP 4294A Impedance Analyzer [155] after first poling the devices. Measurements of the parallel capacitance and resistance were obtained at 1 *kHz* for each of the packaged devices. Additionally, the impedance was measured over a sufficient spectral bandwidth to capture the first resonance that varied from device to device.

Initial Deflection Measurements – Wyko Optical Profilometer

Due to residual stresses in the composite diaphragms and compliant boundary conditions, the devices exhibited an initial static deflection. This deflection was measured by mounting the devices under a Wyko Optical Profilometer [131] with a 5x optical lens and a 0.5x reducer, yielding a total magnification of 2.5x.

CHAPTER 5 EXPERIMENTAL RESULTS AND DISCUSSION

This chapter discusses the experimental results that were obtained from the various measurements. First, the electrical impedance results are shown and explained. This is followed by the electrically actuated frequency response measurements. Following this, the acoustically actuated frequency response and impedance results are discussed for both package configurations. Finally, the initial deflection measurements are presented for several devices. A graphical overview of this chapter is provided by the roadmap of Figure 5-1.

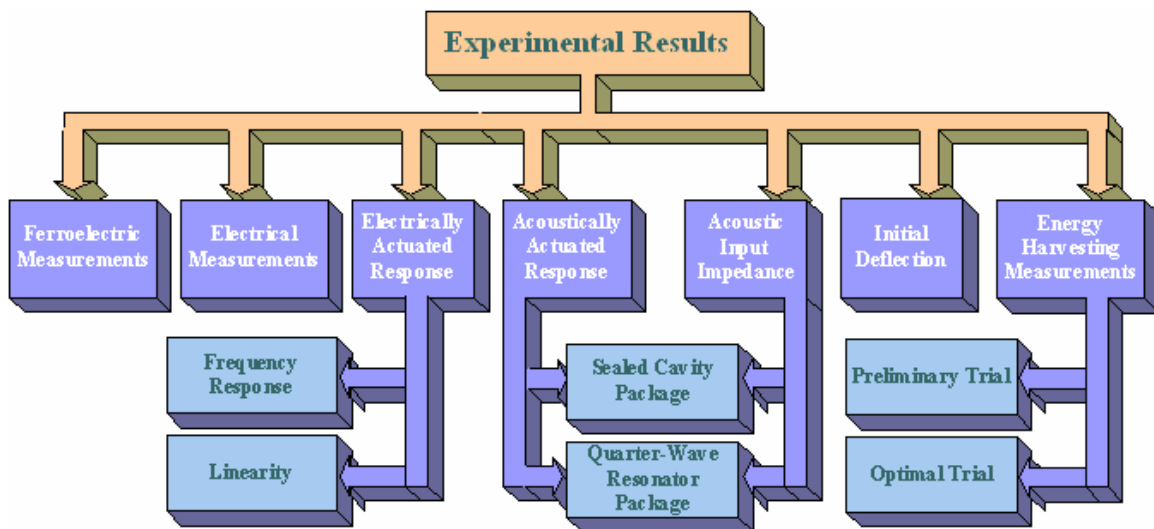


Figure 5-1: Roadmap for Chapter 5.

Ferroelectric Measurements

The ferroelectric properties of several devices were measured using the Radiant Technologies, Precision LC Analyzer. Shown in Figure 5-2, is a graph of the polarization versus applied voltage over several loops of steadily increasing voltage. For

this measurement, the voltage maxima were swept from 1 V to 5 V in 0.25 V increments, corresponding to a maximum applied electric field of 187.95 [kV/cm]..

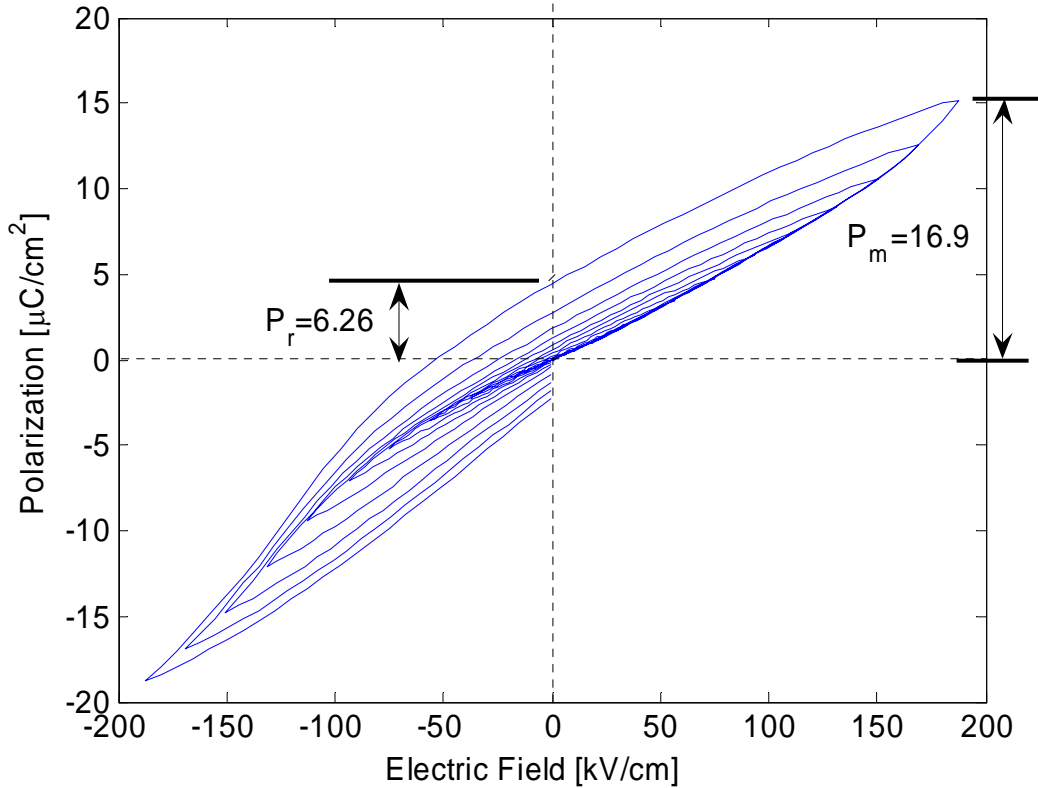


Figure 5-2: Hysteresis loop for Device 1A-5-4 in a sealed cavity package. The device has a radius of 1200 μm and a central mass.

The resulting polarization reached a maximum of 16.9 $\mu\text{C}/\text{cm}^2$ with a remanent polarization of 6.26 $\mu\text{C}/\text{cm}^2$ for the 5 V sweep. A typical hysteresis curve shows flattened regions near the upper and lower ends of the sweep, where the response becomes saturated. It was not possible to extend the measured hysteresis curve into those regions as the maximum voltage that could place across the piezoelectric was approximately 5 V. Beyond this voltage, unexpected effects occurred in the material that produced a short circuit between the two electrodes. The nature of this short circuit was

not resolutely identified, but it is believed to be related to the overhanging top electrode resulting from problems in the fabrication.

Electrical Measurements

Electrical Output Impedance

Electrical measurements were taken using a HP 4294A Impedance Analyzer. Data was generally recorded from 1 kHz to 50 kHz, however, the results shown below were extracted from the 1 kHz values. The parallel capacitance and parallel resistance were measured in this manner, and the corresponding relative dielectric constants and loss tangents were extracted, by taking into account the respective geometries of each device. Shown in Figure 5-3 is the measured parallel capacitance as a function of the outer radius, R_2 . All eight device configurations, as given in Table 2-5, were measured, resulting in two data points for each outer radius. The capacitance was found to vary between 8.65 nF and 27.4 nF, and increases with increasing radius as expected.

The individual corresponding relative dielectric constants were calculated using,

$$\epsilon_r = \frac{t_p \cdot C_p}{\pi (R_2^2 - R_1^2) \epsilon_o}, \quad (5.1)$$

where t_p is the piezoelectric thickness, R_2 and R_1 are the outer and inner radii respectively, and ϵ_o is the permittivity in a vacuum. The relative dielectric constant was found to have an average value of 483.47 with a standard deviation of 23.48. Others have reported dielectric constants for PZT from 125 [16] to 1400 [32], although the average value in the literature is approximately 839.

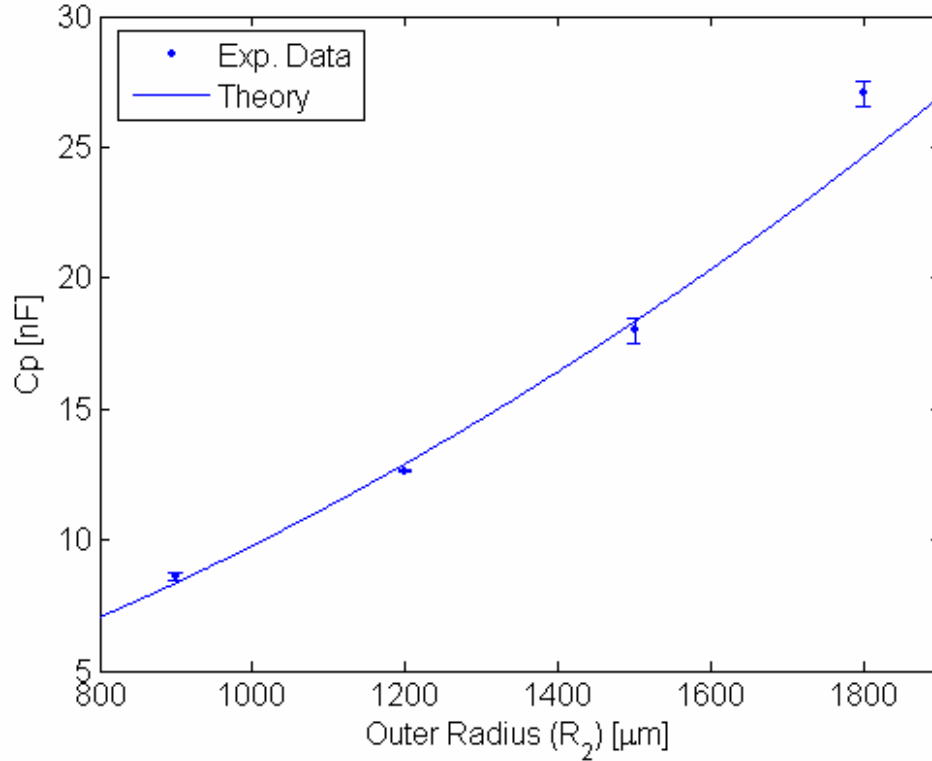


Figure 5-3: Measured parallel output capacitance, C_p vs. outer radius, R_2 overlaid with a theoretical capacitance curve based on the average extracted dielectric constant. The error bars indicate the 95% confidence intervals based on the variance across multiple devices.

In a manner similar to the capacitance measurements, the parallel output resistance was measured at 1 kHz for each of the devices and is shown in Figure 5-4. As can be seen from the figure, it was found to decrease with increasing radius. This effect was investigated further by looking at the conductance per unit area of each of the devices, given by

$$\Gamma = \frac{G}{\pi(R_2^2 - R_1^2)} = \frac{1}{R_p \pi(R_2^2 - R_1^2)}, \quad (5.2)$$

where G is the conductance. It was found that the conductance per unit area was relatively constant with respect to radius, with the exception of one outlier point measured for the device with an 1800 μm outer radius. The average value was found to

be $2.40 \text{ Siemens}/\mu\text{m}^2$, with a standard deviation of $0.46 \text{ Siemens}/\mu\text{m}^2$, when excluding the outlier point.

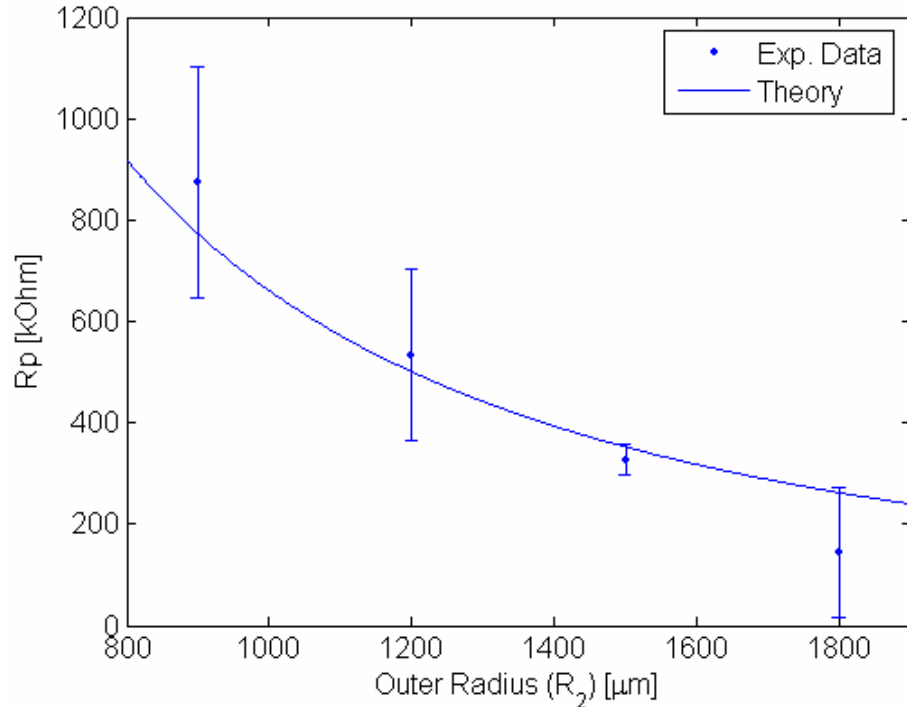


Figure 5-4: Parallel output resistance, R_p , vs. outer radius, R_2 , overlaid with a theoretical resistance curve based on the average measured conductivity. The error bars indicate the 95% confidence intervals of the variance across multiple devices.

The loss tangent was then calculated based on the measured electrical reactance, X_p and resistance, R_p , and is given by,

$$\tan \delta = \frac{|X_p|}{R_p}. \quad (5.3)$$

The average loss tangent, as measured at 1 kHz , and once again ignoring the outlier, was found to be approximately 0.024, which matches well with previously published values ranging from 0.02 to 0.05 for thin film PZT [12, 26, 34, 35, 37]. A summary of all the electrical impedance measurements is provided by Table 5-1. The average values are given at the bottom of the table and were computed without the outlier points that are marked in the dotted box.

Table 5-1: Summary of electrical impedance measurements.

Device #	$R_1 [\mu m]$	$R_2 [\mu m]$	$R_{mass} [\mu m]$	$C_p [nF]$	$R_p [k\Omega]$	ϵ_r	$\tan \delta$	$G/\mu m^2$
1A-5-1	830	900	0	8.72	665.89	507.91	0.027	2.867
1A-6-1	830	900	0	8.65	837.09	503.77	0.022	2.281
1A-6-2	830	900	180	8.45	1120.20	492.42	0.017	1.704
1A-10-2	830	900	180	7.76	900.73	451.84	0.023	2.120
1A-11-3	1115	1200	0	12.68	652.73	478.21	0.019	1.895
1A-5-4	1115	1200	240	12.14	730.94	458.04	0.018	1.692
1A-10-4	1115	1200	240	12.59	414.63	474.99	0.030	2.983
1A-6-5	1400	1500	0	18.33	348.04	486.75	0.025	2.501
1A-6-6	1400	1500	300	17.64	306.31	468.60	0.029	2.842
1A-10-6	1400	1500	300	18.32	367.91	486.67	0.024	2.366
1A-3-7	1685	1800	0	26.70	52.60	527.59	0.113	12.314
1A-6-7	1685	1800	0	22.82	237.78	450.94	0.029	2.724
1A-3-8	1685	1800	360	27.40	233.55	541.54	0.025	2.773
Average	n/a	n/a	n/a	n/a	n/a	483.47	0.024	2.40

The devices are numbered according to the device type and location on the wafer, in the form of WW-BB-DD, where WW is the wafer number, BB is the block number as defined in Figure 3-8 and DD is the device number as defined in Figure 3-7. Note that all the devices that were tested came from the same wafer, referred to here as wafer 1A.

Shown in Table 5-2 is a comparison of the properties of the PZT presented in this dissertation along with the properties of thin-film PZT as reported in the literature. Upon comparison, the relative permittivity and loss tangent are within range of previously reported values, however the remanent polarization is lower. This is most likely a direct result of the room temperature poling process, and future work will seek to understand the precise nature of this result.

Table 5-2: Comparison of ferroelectric and dielectric properties of thin film PZT.

Author	$P_r [\mu C/cm^2]$	ϵ_r	$\tan \delta$
Tuttle and Schwartz [167]	27	1000	--
Morita et al. [169]	9.2	--	--
Nunes et al. [160]	20	436	0.07
Xia et al. [135]	25	860	0.03
Kueppers et al. [161]	22	480	--
Horowitz	6.3	500	0.03

Electrically Actuated Response—Laser Scanning Vibrometer

Frequency response

The results of the electrically actuated frequency response in terms of magnitude and phase are shown in Figure 5-5 to Figure 5-12 for a number of devices. Along with each frequency response plot is the corresponding uncertainty for each measurement, based on the measured coherence. A minimum of one resonance was detected for each device. Some of the larger devices also show a second resonance within the measured frequency range. Note that the phase shifts by 180° at the resonance, close to the observed peak in the magnitude response. At low frequencies, well below resonance, the devices exhibit a relatively flat response, although more significant scatter is evident in the data resulting from poor coherence due to signal levels close to the noise floor. Also note that the frequency range varies from graph to graph to focus in on the features of interest. All of the devices tested below have the same materials and layer thicknesses, and only vary with respect to the radius as well as the presence or absence of a central mass.

The electrically actuated frequency response that is defined here to be the frequency dependent center deflection, $w(0)$, that results from an applied voltage, can be found from the circuit of Figure 2-15 to be

$$\frac{w(0)}{V} = \frac{\phi}{sA_{eff} (Z_{ad} + Z_{adrad})} \quad (5.4)$$

where $Z_{ad} = sM_{ad} + 1/sC_{ad}$, Z_{adrad} is defined in Eq. (2.95), and A_{eff} is the effective area of transduction.

Shown in Figure 5-5 is the electrically actuated frequency response for the smallest device, with a radius of $900 \mu m$, and without a central mass. Note the resonant peak occurring around $50 kHz$ with a peak response of $0.71 \mu m/V$.

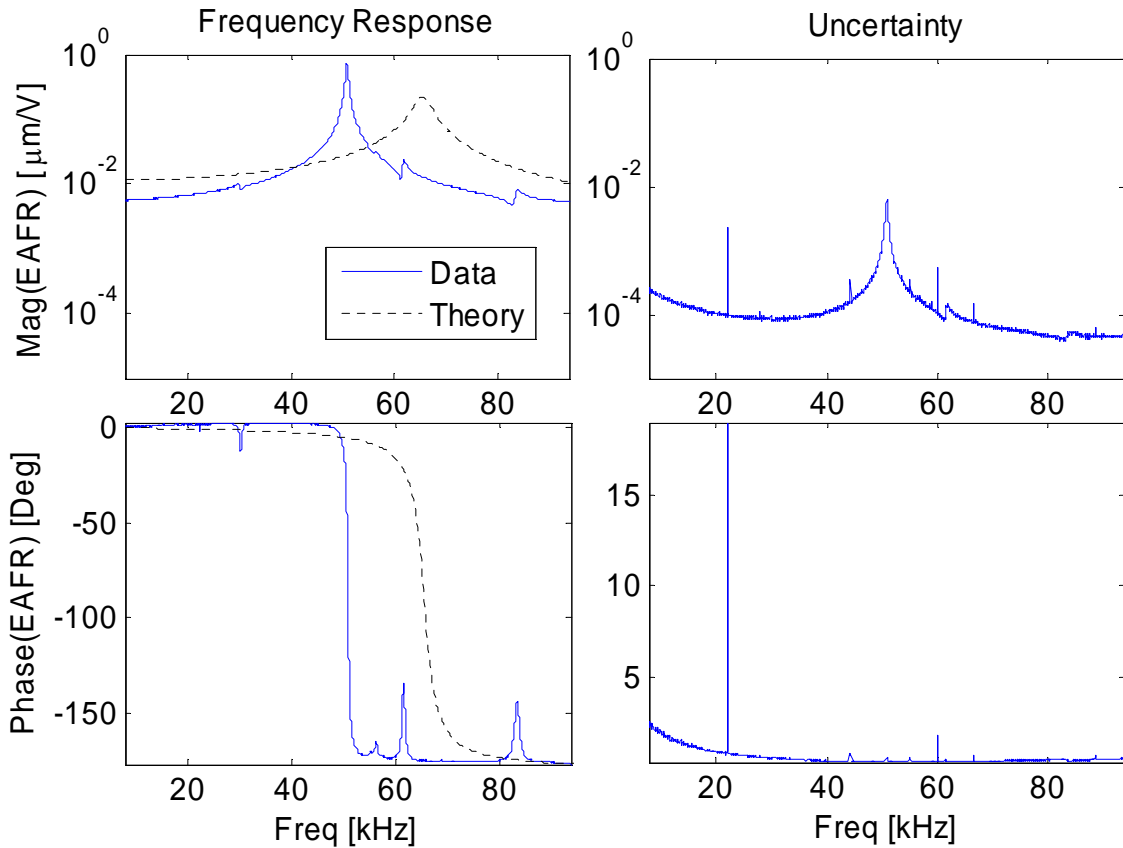


Figure 5-5: Device 1A-6-1, electrically actuated center deflection for the device with a radius of $900 \mu m$ and no central mass, packaged in the quarter-wave resonator package. Frequency response is shown in the left column with the corresponding uncertainty given in the right column.

For an identical size device, except with the addition of a central mass, the electrically actuated frequency response is shown in Figure 5-6. With the addition of the central mass, the resonant frequency drops from $50 kHz$ down to roughly $23 kHz$, while the peak response increases to $6.66 \mu m/V$. This demonstrates that the central mass works as intended. Namely, it increases the overall effective mass without a

correspondingly large decrease in effective compliance, thereby leading to an overall decrease in the resonant frequency. There had been some apprehension prior to testing as to the net effect of the central mass, mainly because significant modeling of the effect of the mass had not been performed prior to fabrication.

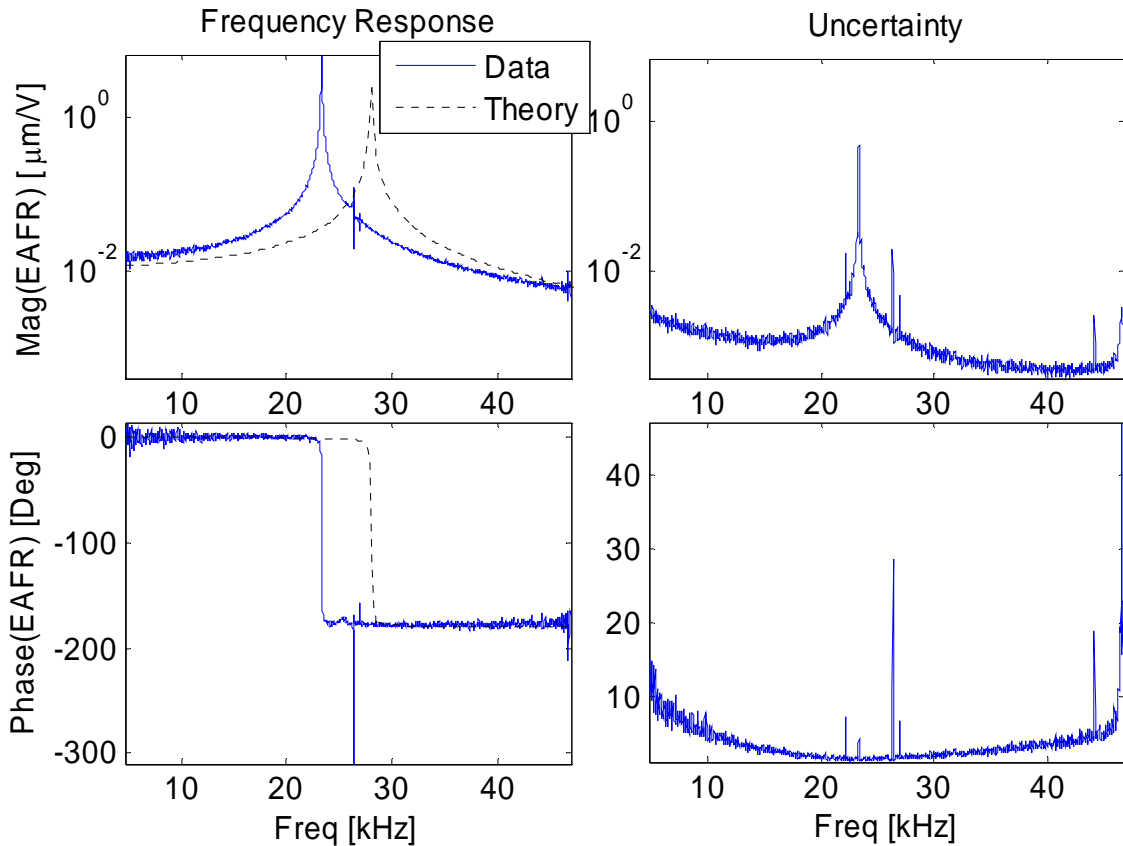


Figure 5-6: Device 1A-6-2, electrically actuated center deflection for the device with a radius of $900 \mu\text{m}$ and a central mass, packaged in the quarter-wave resonator package. Frequency response is shown in the left column with the corresponding uncertainty given in the right column.

Shown in Figure 5-7 is the frequency response for the second smallest device, with an outer radius of $1200 \mu\text{m}$. Similar to Figure 5-5, it does not have a central mass. Note two resonant frequencies are visible. The first resonance occurs near 34 kHz with peak value of $0.44 \mu\text{m}/\text{V}$ and represents the fundamental mode of the device, as were the resonances in the previous graphs. The second resonance occurs near 120 kHz and

corresponds to a higher order mode, with a peak value of $0.98 \mu\text{m}/\text{V}$. This was verified through use of the scanning feature on the laser vibrometer, and is shown in Figure 5-8.

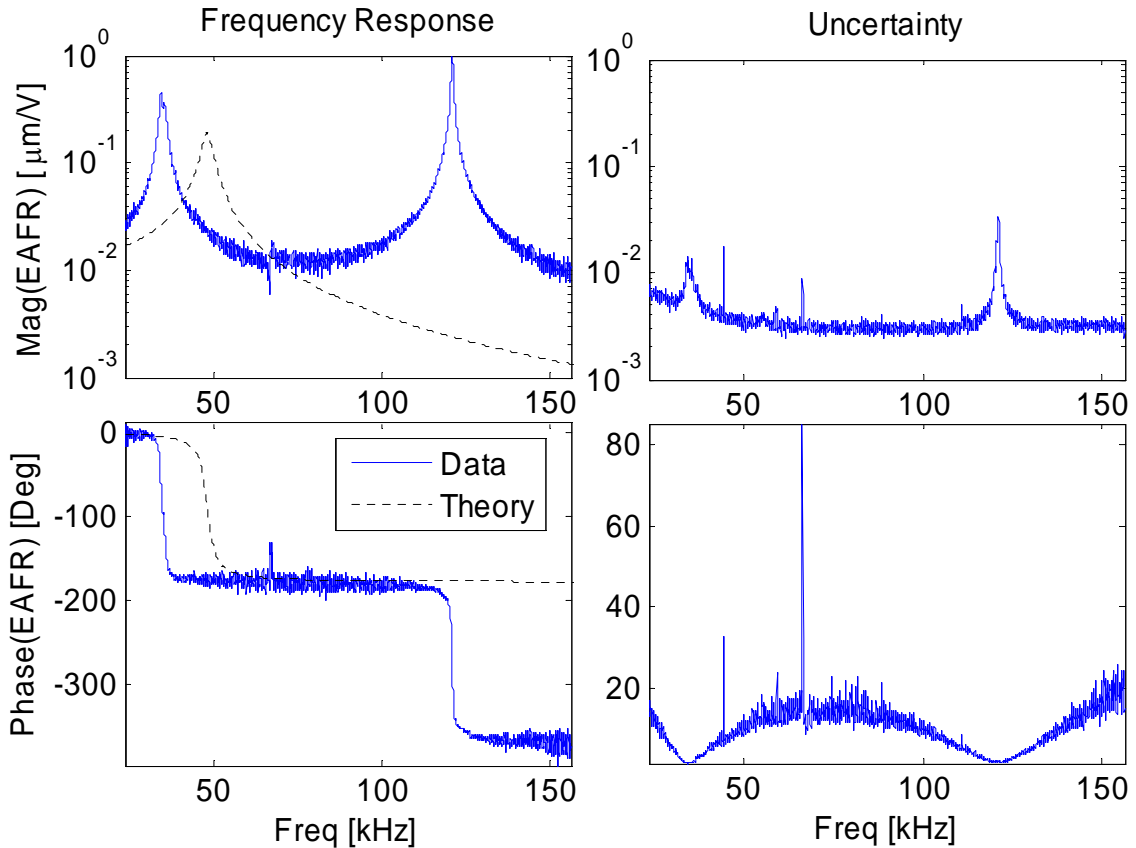


Figure 5-7: Device 1A-11-3, electrically actuated center deflection for the device with a radius of $1200 \mu\text{m}$ and no central mass, packaged in the quarter-wave resonator package. Frequency response is shown in the left column with the corresponding uncertainty given in the right column.

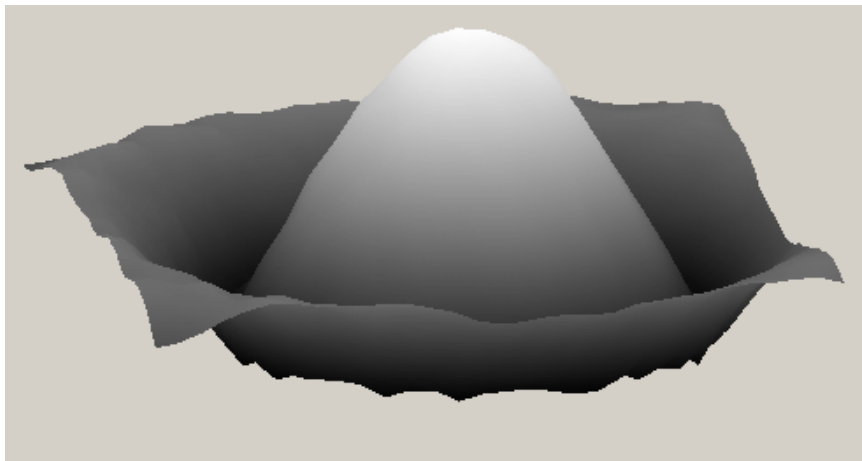


Figure 5-8: Higher order mode image of Device 1A-11-3, taken using scanning laser vibrometer at 120.9 kHz .

Once again, the addition of a central mass lowers the resonant frequency, as illustrated in Figure 5-9. In this instance, the resonant frequency drops from 34 kHz as measured above to 14 kHz as shown below. It should be noted here that these are physically different devices and the use of the phrase “addition of a central mass” is not meant to convey that the same physical structure was modified, but simply that the central mass is the main distinguishing feature between the two devices.

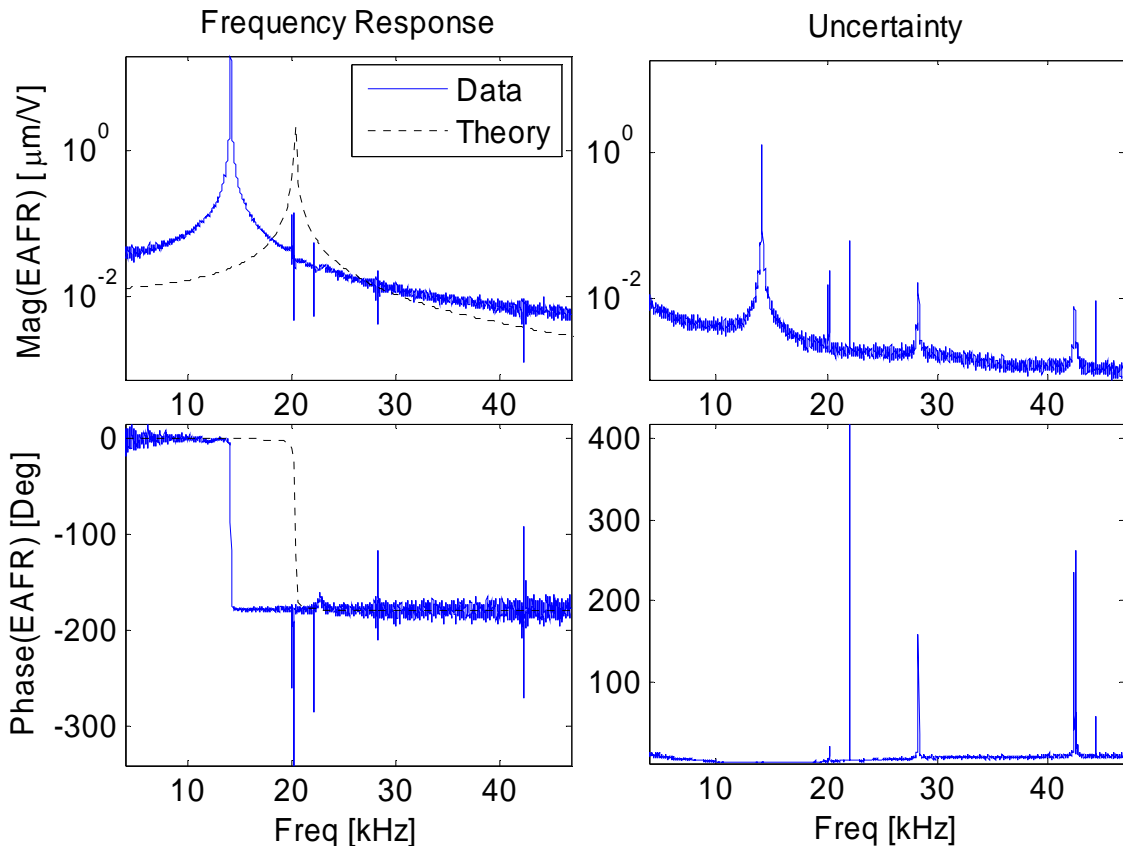


Figure 5-9: Device 1A-10-4, electrically actuated center deflection for the device with a radius of 1200 μm and a central mass, packaged in the quarter-wave resonator package. Frequency response is shown in the left column with the corresponding uncertainty given in the right column.

Shown in Figure 5-10 is the frequency response for the second largest radius device without a central mass. This device has an outer radius of 1500 μm . It exhibits a resonant frequency of around 25 kHz, compared to 34 kHz for the next smaller device.

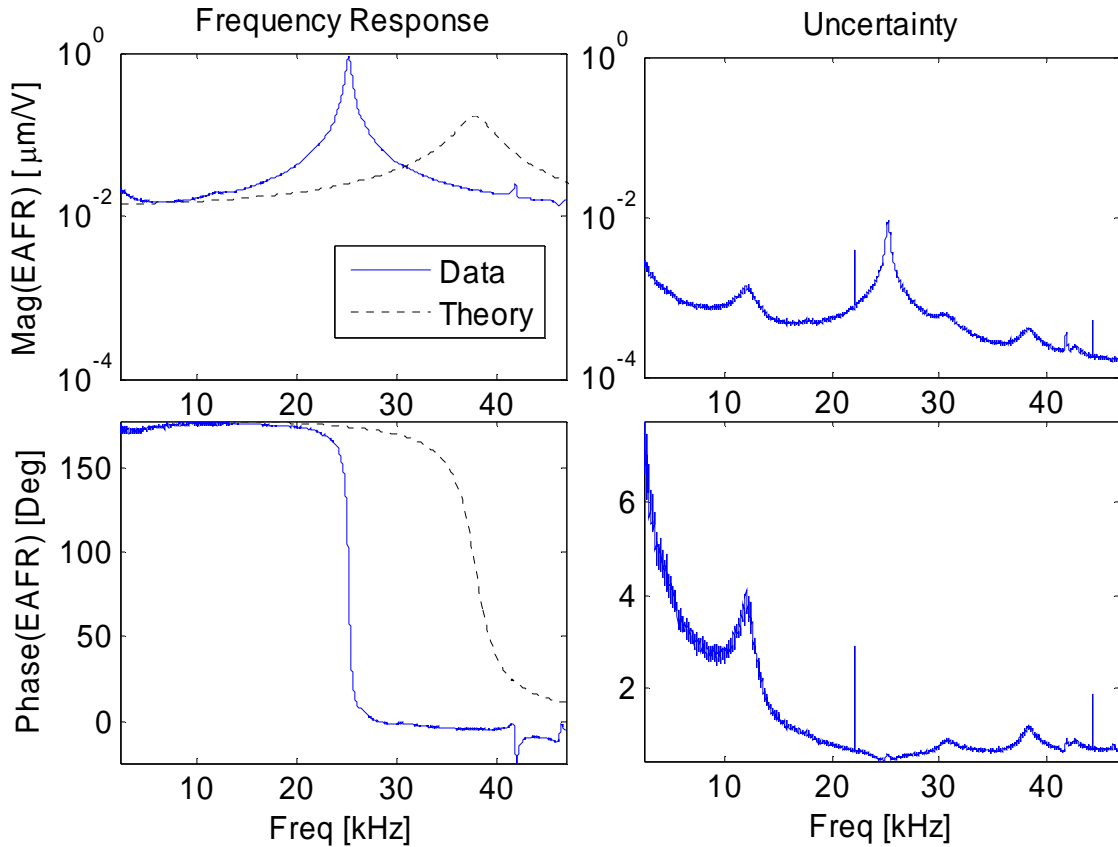


Figure 5-10: Device 1A-6-5, electrically actuated center deflection for the device with a radius of $1500 \mu m$ and no central mass, packaged in the quarter-wave resonator package. Frequency response is shown in the left column with the corresponding uncertainty given in the right column.

With the addition of a central mass to this size device, with outer radius of $1500 \mu m$, the resonant frequency drops from $25 kHz$ to $10.5 kHz$. This is shown in Figure 5-11 for Device 1A-10-6 and corroborates that the addition of the mass does not increase the stiffness enough to cancel out the lowering effect on the resonance frequency.

The largest device is shown in Figure 5-12, with a radius of $1800 \mu m$ without a central mass. A resonant frequency of around $20 kHz$ was measured for this device, as compared to $23.5 kHz$ for the next smaller device. Also note the smaller resonances at around $26 kHz$ and $45 kHz$ that are most likely effects from higher order modes.

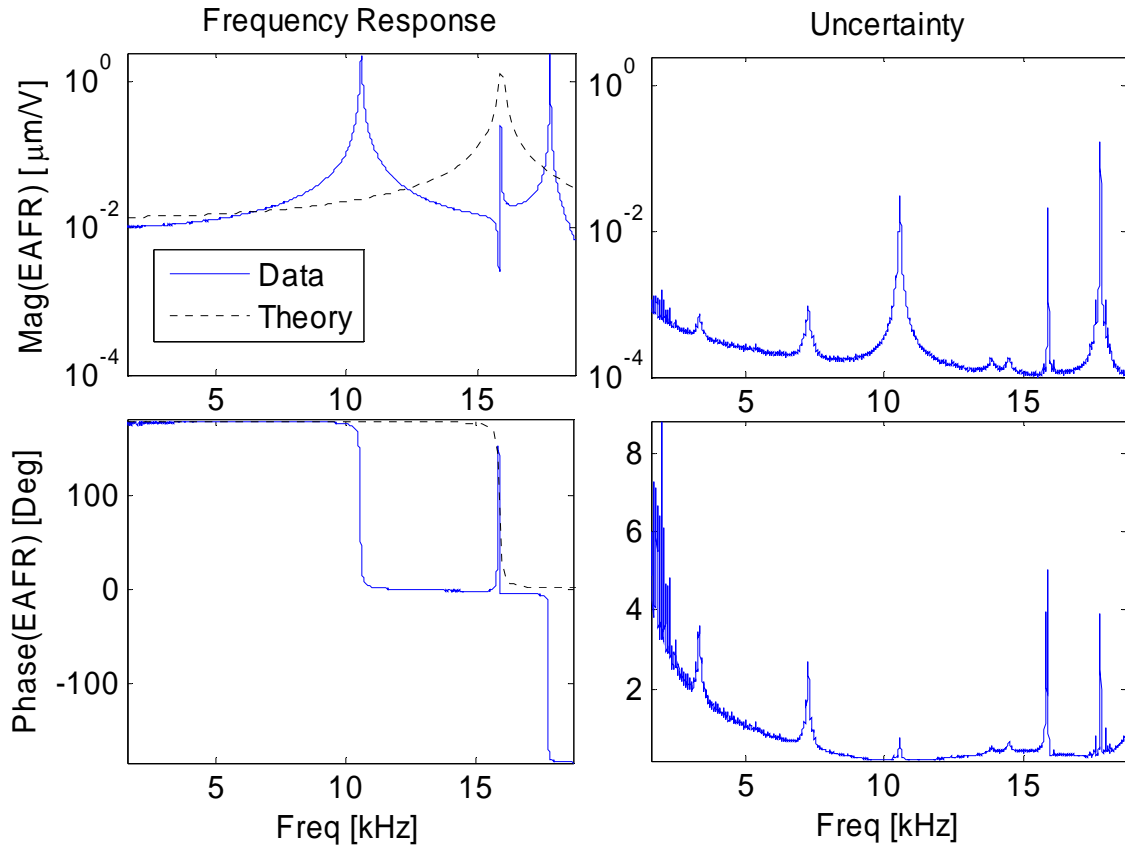


Figure 5-11: Device 1A-10-6, electrically actuated center deflection for a device with a radius of $1500 \mu\text{m}$ and a central mass, packaged in the quarter-wave resonator package. Frequency response is shown in the left column with the corresponding uncertainty given in the right column.

Overall, the electrically actuated frequency response tests demonstrated the general trends that were expected, namely that of a decrease in resonant frequency with each increase in outer radius, as well as a decrease in resonant frequency due to the addition of central pillar in the center of the diaphragm that acts like a point mass.

Shown in Figure 5-13 is a summary graph of the low frequency sensitivity as measured well below each individual resonance. Note the general trend towards increasing sensitivity with increasing radius, as expected from a physical standpoint, although the variation in sensitivity among identical devices is on the same order of

magnitude. These results as well as the measured resonant frequencies and sensitivities at resonance are summarized in Table 5-3.

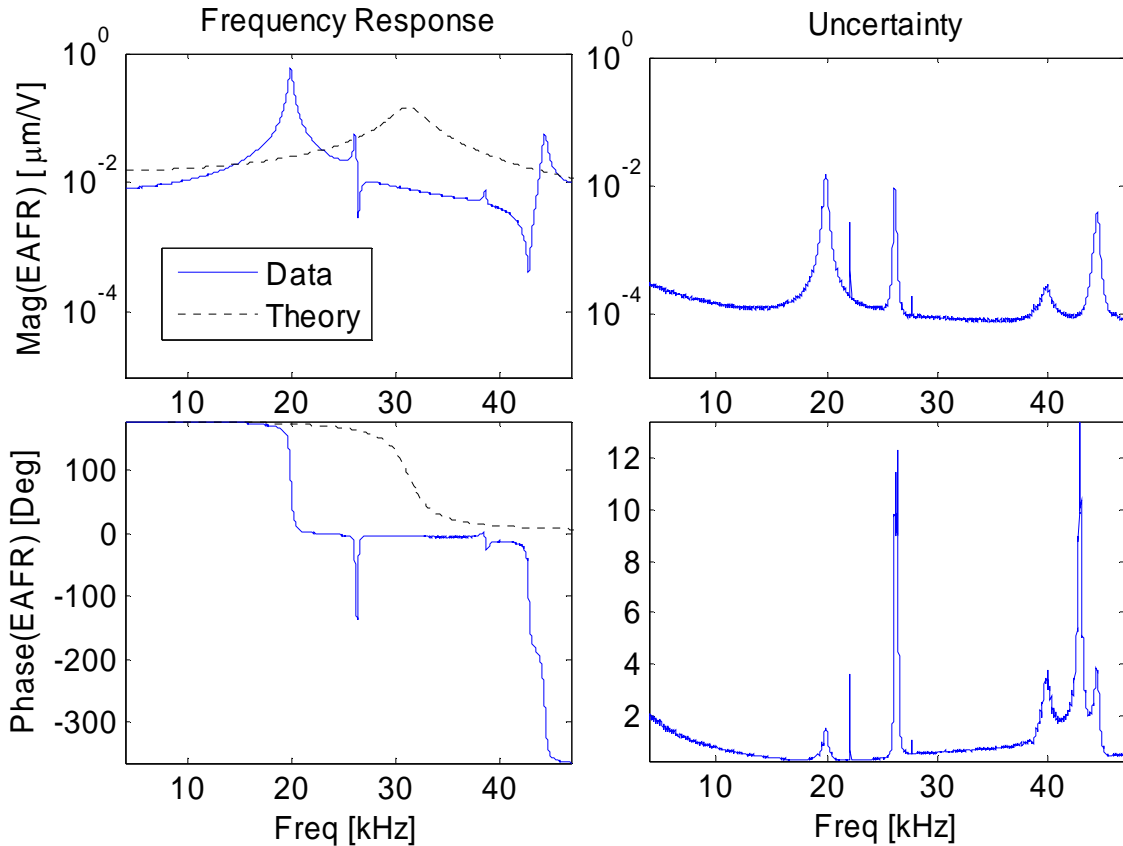


Figure 5-12: Device 1A-3-7, electrically actuated center deflection for the device with a radius of $1800 \mu\text{m}$ and no central mass, packaged in the sealed-cavity package. Frequency response is shown in the left column with the corresponding uncertainty given in the right column.

A graph of the measured resonant frequencies under electrical excitation is shown in Figure 5-14. Two series of data are shown, both with and without a central mass. The central mass was measured to have the effect of reducing the resonant frequency as was expected. These results show that, as desired, the effect of the addition of mass due to the central pillar was dominant over any decrease in compliance that resulted from the presence of the pillar. Also, as the radius is increased, the resonance frequency decreases. Overall, the range of resonant frequencies varies from 6.73 kHz to 60.34 kHz .

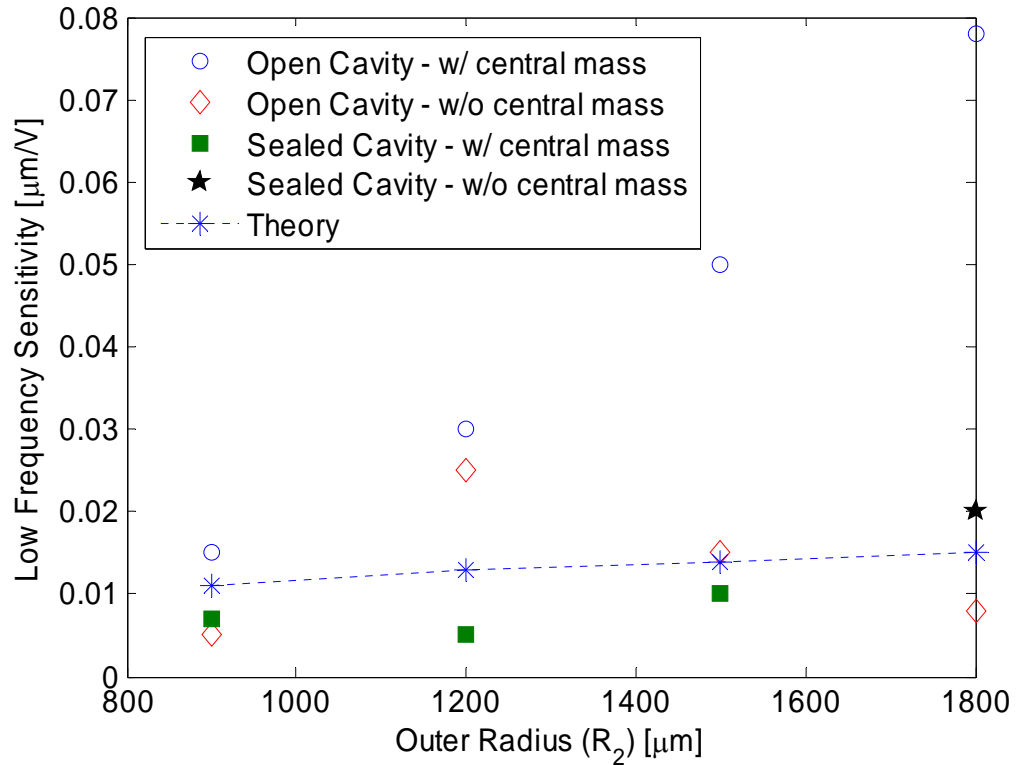


Figure 5-13: Electrically actuated sensitivity at low frequency (well below resonance) ($R_1/R_2 = 0.95$).

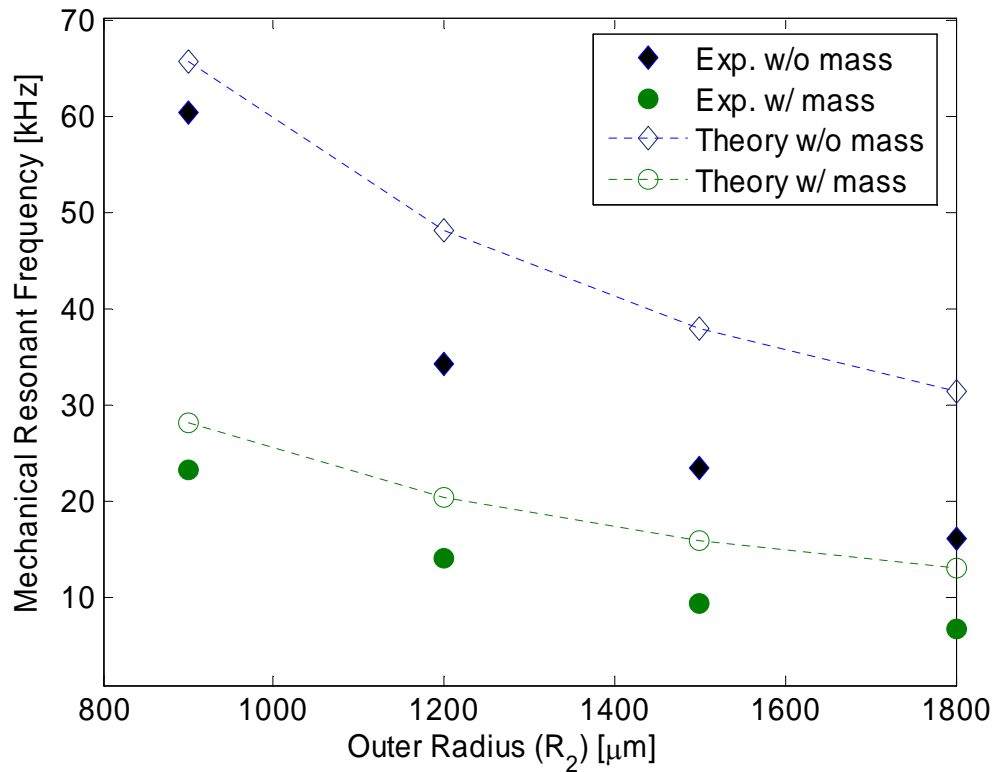


Figure 5-14: Summary of electrically actuated resonant frequencies.

The effect of the central mass is illustrated more explicitly in Figure 5-15, where the negative shift in resonant frequency due to the additional mass is plotted versus the original resonant frequency. The values are expressed in percentage change from the original values, where a positive number indicates a drop in resonant frequency. The mean percentage change was experimentally found to be 58.93 %, as compared to a predicted shift of 57.76 %. Also the shift was found to be more prominent for the larger devices with the lower resonant frequencies

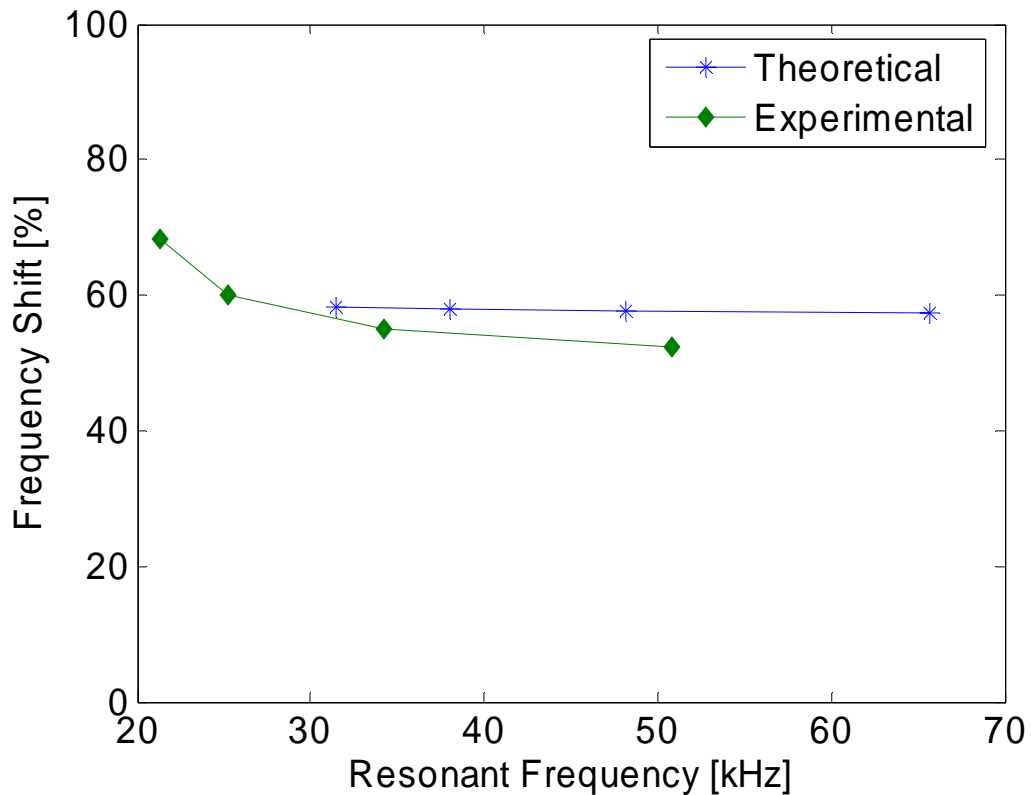


Figure 5-15: Drop in resonant frequency due to the addition of the central mass.

Overall, significant numerical differences were seen between theory and experiment, as evidenced in Table 5-3. Qualitatively, however the device behavior did generally follow the expected trends, particularly for the resonant frequencies, as seen in Figure 5-14 and Figure 5-15. On the other hand, while the low frequency sensitivity did generally increase with radius, as expected, the experimental behavior was not as

predictable and varied greatly in response to packaging and the presence of the central mass. The measured behavior was most consistent with the theory in the sealed cavity packages, suggesting that unwanted acoustical interactions related to the package geometry, may be altering the low frequency sensitivity of the open cavity packaged devices.

Table 5-3: Summary of electrically actuated frequency response measurements.

Device #			Experimental			Theoretical		%Difference	
	R_2 [μm]	R_m [μm]	f_{res_m} [kHz]	$Sens_{EA_{low}}$ [$\mu m/V$]	$Sens_{EA_{res}}$ [$\mu m/V$]	f_{res_m} [kHz]	$Sens_{EA_{low}}$ [$\mu m/V$]	f_{res_m} [%]	$Sens_{EA_{low}}$ [%]
1A-5-1	900	0	n/a	n/a	n/a	65.68	0.011	n/a	n/a
1A-6-1	900	0	50.8	0.005	0.30	65.68	0.011	22.54	54.55
1A-6-2	900	180	23.30	0.015	6.66	28.08	0.011	17.02	-36.36
1A-10-2	900	180	25.20	0.007	0.47	28.08	0.011	10.26	36.36
1A-11-3	1200	0	34.25	0.025	0.45	48.14	0.013	28.85	-92.31
1A-5-4	1200	240	16.69	0.005	1.54	20.37	0.013	18.07	61.54
1A-10-4	1200	240	14.12	0.030	19.70	20.37	0.013	30.68	-130.7
1A-6-5	1500	0	25.2	0.015	0.88	38.01	0.014	33.70	-7.143
1A-6-6	1500	300	9.53	0.050	8.18	15.98	0.014	40.36	-257.1
1A-10-6	1500	300	10.56	0.010	6.60	15.98	0.014	33.92	28.57
1A-3-7	1800	0	19.84	0.008	4.20	31.41	0.015	36.84	46.67
1A-6-7	1800	0	22.72	0.020	0.62	31.41	0.015	27.67	-33.33
1A-3-8	1800	360	6.74	0.078	12.20	13.15	0.015	48.75	-420.0

Linearity

Once the frequency response was measured for each device, experiments to characterize the linearity of the response were performed. The measurements were made at the resonant frequency of each device, in order to maximize deflection. A zero DC offset sinusoidal voltage signal was used to drive the diaphragm while the velocity at the center of the diaphragm was measured using the laser vibrometer. The center deflection was then derived from this measurement and plotted versus the driving voltage. The resulting plot is shown in Figure 5-16 for all of the tested devices. In the figure, most of the measured devices exhibited a linear response up to about 50 mV of input voltage.

Increasing the voltage beyond that did not lead to a corresponding increase in deflection for these devices. From these results, the maximum input voltage for a linear response appears to be independent of the device radius. This suggests that it is not due to a mechanical factor that would increase when the device is scaled. Instead, it is most likely due to a depoling of the piezoelectric material, leading to a reduction in piezoelectric properties and the resulting deflection.

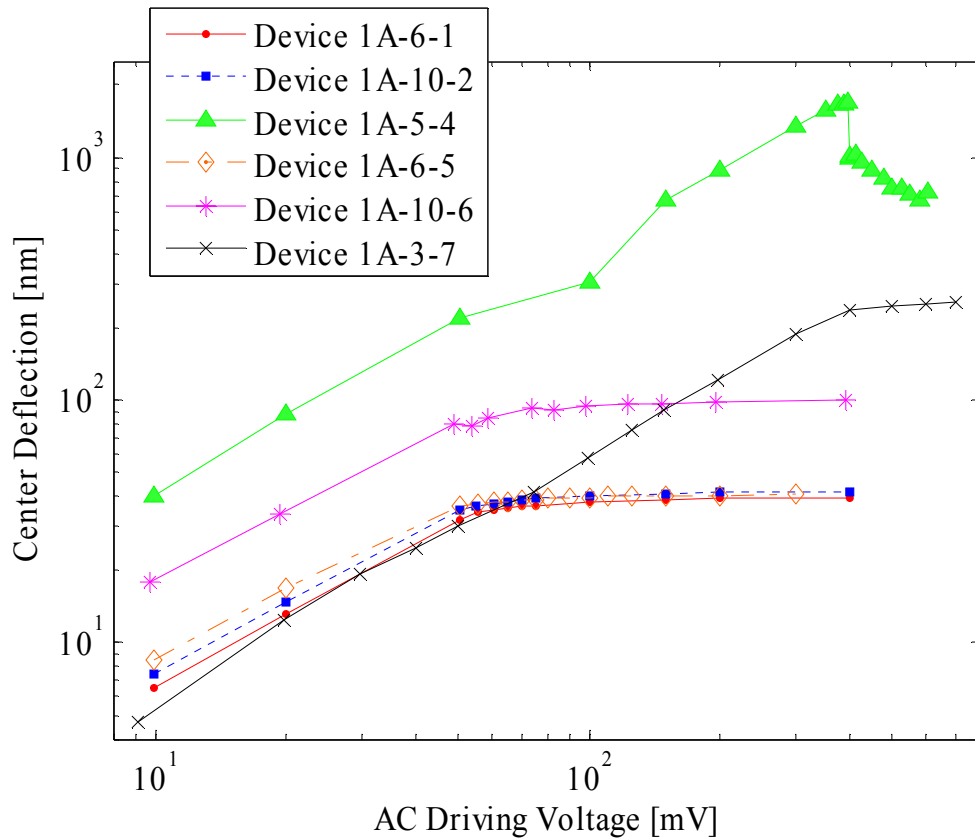


Figure 5-16: Magnitude of the resonant center deflection versus driving voltage.

Another convenient way of looking at the nonlinear behavior is by calculating the mechanical sensitivity to voltage inputs as the driving voltage is varied. The resulting plot is shown in Figure 5-17. From this plot it is easy to see where the sensitivity starts to drop for most of the devices, indicating the onset of nonlinear behavior.

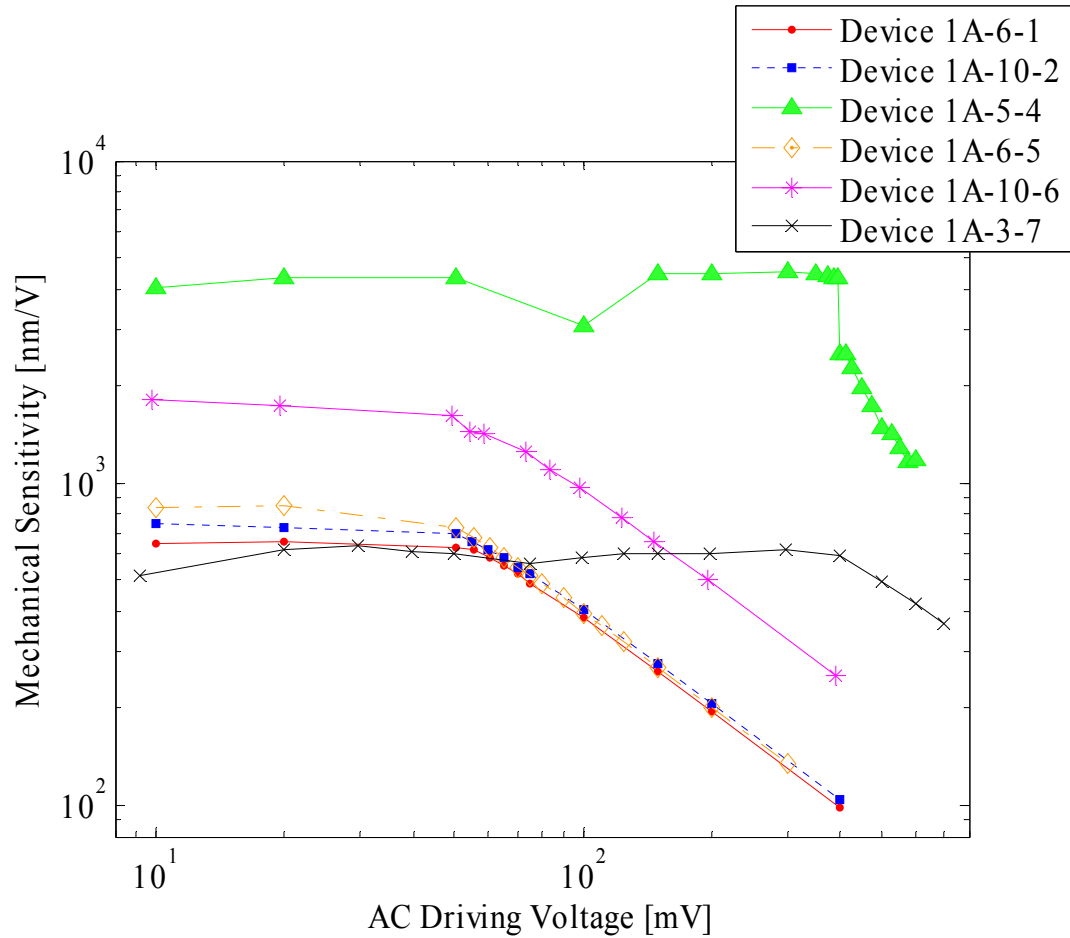


Figure 5-17: Mechanical sensitivity at resonance versus driving voltage.

Acoustical Measurements

Acoustically Actuated Frequency Response – Plane-Wave Tube

Sealed cavity package

The devices that were packaged in the sealed cavity packages (Device 1A-10-2, Device 1A-5-4 and Device 1A-3-7) were tested in the plane-wave tube, with a nominally average incident acoustic pressure of 92.6 dB. The frequency response results shown below in terms of magnitude and phase are plotted in Figure 5-18 over the frequency range of 250 Hz to 6700 Hz for Device 1A-5-4, which has a radius of 1200 μm and a central mass. The plots for the other devices were not shown to avoid needless repetition,

as they are all highly similar in behavior. The lower frequency limit was set to avoid speaker inefficiencies while the upper limit was due to the onset of higher order modes in the tube. The important thing to note from all of these results is the relatively flat magnitude over the frequency range, which is to be expected well below resonance. A slight dip in the low frequency region is most likely due to a vent resistance arising from a small leakage in the packaging. The other factor that will lead to a low-frequency rolloff is due to the $R_p C_{eB}$ time constant of the piezoelectric. For the device shown in Figure 5-18, $R_p C_{eB} = 0.0089$, and therefore the related corner frequency, given by $1/R_p C_{eB}$, was found to be 112.7 Hz . As can be seen in Figure 5-18, the corner is closer to 1792 Hz and therefore unrelated to the dielectric losses.

Among all of the tested devices, a relatively flat magnitude of the response was seen, with the numerical value of the magnitude as the only significant difference between devices. This value was found to increase with increasing radius and occurs because the testable frequency range was well below all of the resonant frequencies, leading to a compliance dominated testing regime. Once again, this frequency range was limited by the cut-on conditions for higher order modes in the plane wave tube.

Quarter-wave resonator package

The same experiment was then performed on the devices that were packaged in the quarter wave resonator package (Device 1A-5-1, Device 1A-11-3, Device 1A-10-4, Device 1A-6-5, Device 1A-10-6, Device 1A-3-7 and Device 1A-3-8). The results for Device 1A-10-4 with a radius of $1200 \mu\text{m}$ and a central mass and Device 1A-6-5 with a radius of $1500 \mu\text{m}$ and no central mass are shown in Figure 5-19 and Figure 5-20 in terms of magnitude and phase. Note that a dip occurs in the magnitude at around 3.694

kHz , instead of the flat responses of the sealed cavity packages. The dip arises due to a quarter wave anti-resonance that causes a maximum in the acoustic impedance of the vent channel, as seen by the diaphragm. At this frequency, the diaphragm sees a significantly higher impedance, and the resulting load acts to reduce the deflection, thereby leading to a stiffening effect on the diaphragm.

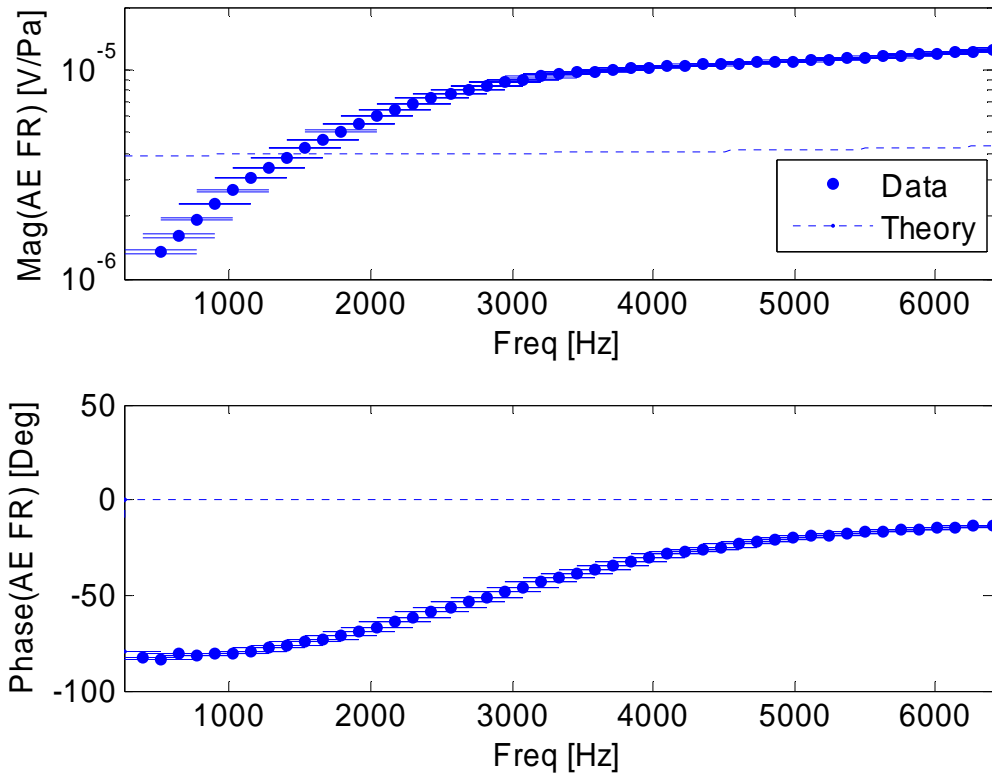


Figure 5-18: Device 1A-5-4, magnitude and phase of the acoustically actuated frequency response in a sealed cavity package for the device with a radius of $1200 \mu m$ and a central mass.

Using an analytical approach to calculate the impedance of a tube with an open end yields a theoretical maximum in impedance (and hence minimum in sensitivity) occurring at $3.882 kHz$, leading to a difference of 4.84% between the experimental and theoretical values. The radiation impedance from the open end of the tube was also considered, however it was found to have only a small impact on the response, by

extending the effective length of the tube to $l_{eff} = l + l'$, where l' is the effect due to the radiation mass.

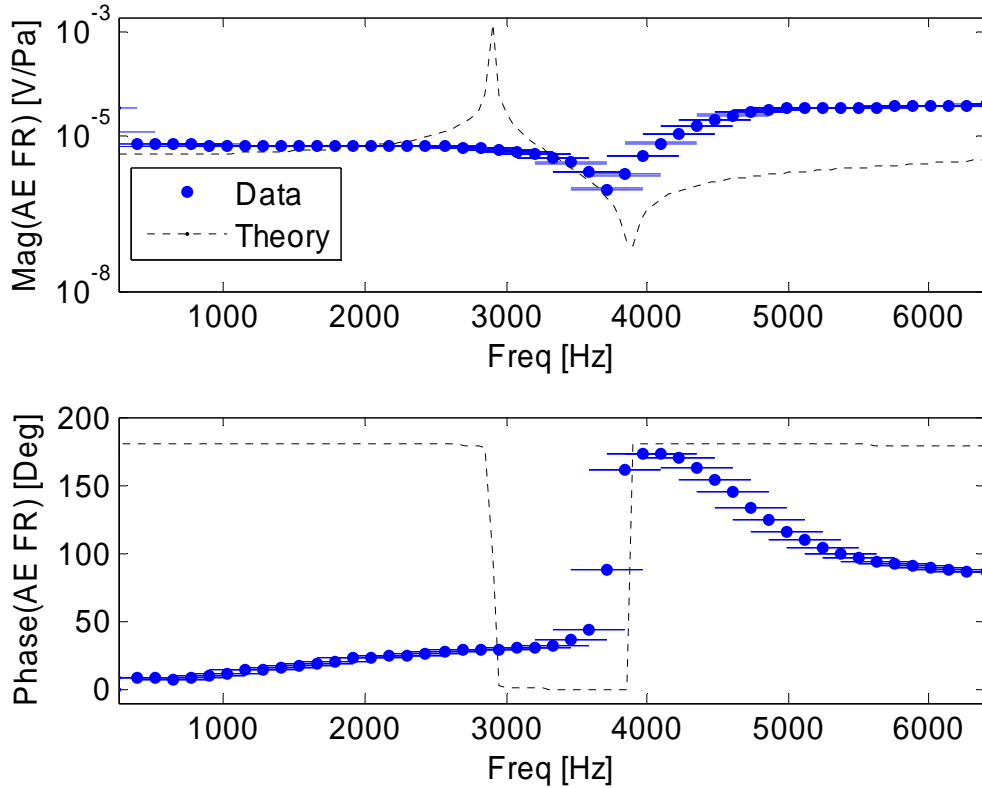


Figure 5-19: Device 1A-10-4 in a quarter-wave resonator package. Magnitude and phase of the acoustically actuated frequency response for the device with a radius of $1200 \mu m$ and a central mass.

For all of these devices, the antiresonant frequency is the same while the overall magnitude increases with each larger device. The constant antiresonant frequency is indicative of this packaging dominated effect, rather than a device dominated effect. The packaging is identical for all of these devices, meanwhile the geometry of the device itself varies. Furthermore, the antiresonant frequency has a quarter wavelength that corresponds closely to the length of the backside hole in the resonator package. This quarter-wave resonator behavior was not initially intended, but became obvious in retrospect, considering the geometry of the package.

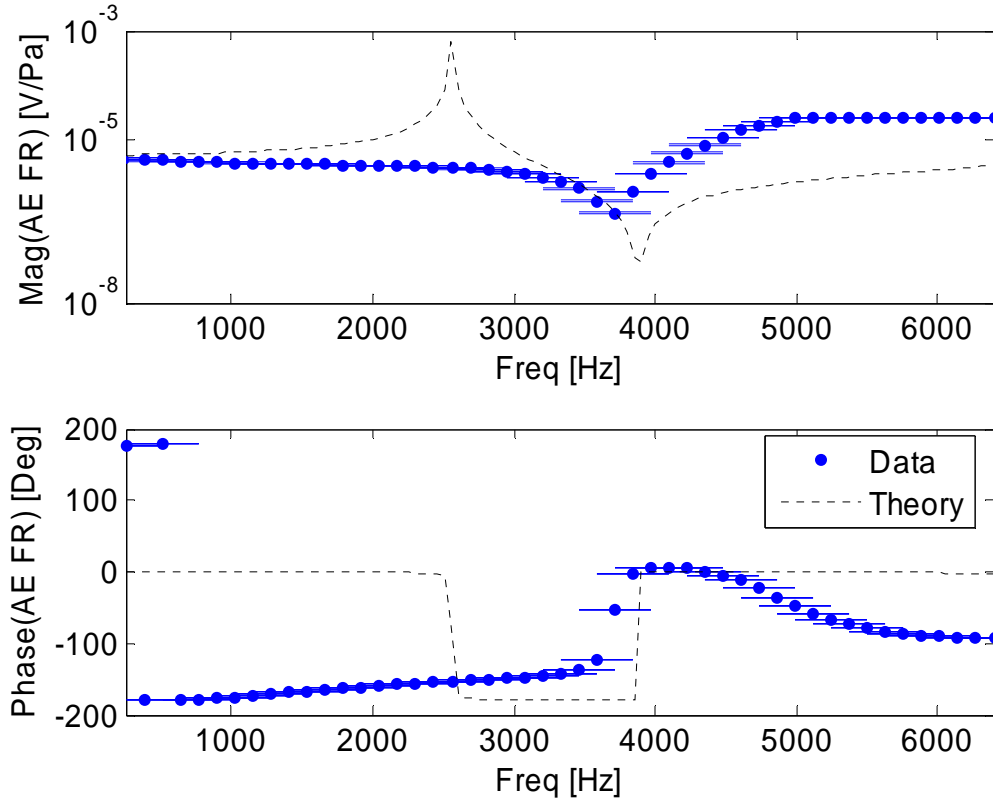


Figure 5-20: Device 1A-6-5 in a quarter-wave resonator package. Magnitude and phase of the acoustically actuated frequency response for the device with a radius of $1500 \mu m$ and no central mass.

Acoustic Input Impedance Measurements – Plane-Wave Tube

The results of the acoustical input impedance measurements on the devices in the sealed cavity packages are shown in Figure 5-21 to Figure 5-23 in terms of normalized resistance and reactance. The normalization was performed with respect to the acoustic impedance of the plane wave tube, and can be found as

$$\xi = \frac{Z_{in}}{Z_{tube}} = \frac{Z_{in}}{\frac{\rho_o c_o}{A_{tube}}} = \theta + j\chi, \quad (5.5)$$

where A_{tube} is the cross-sectional area of the tube.

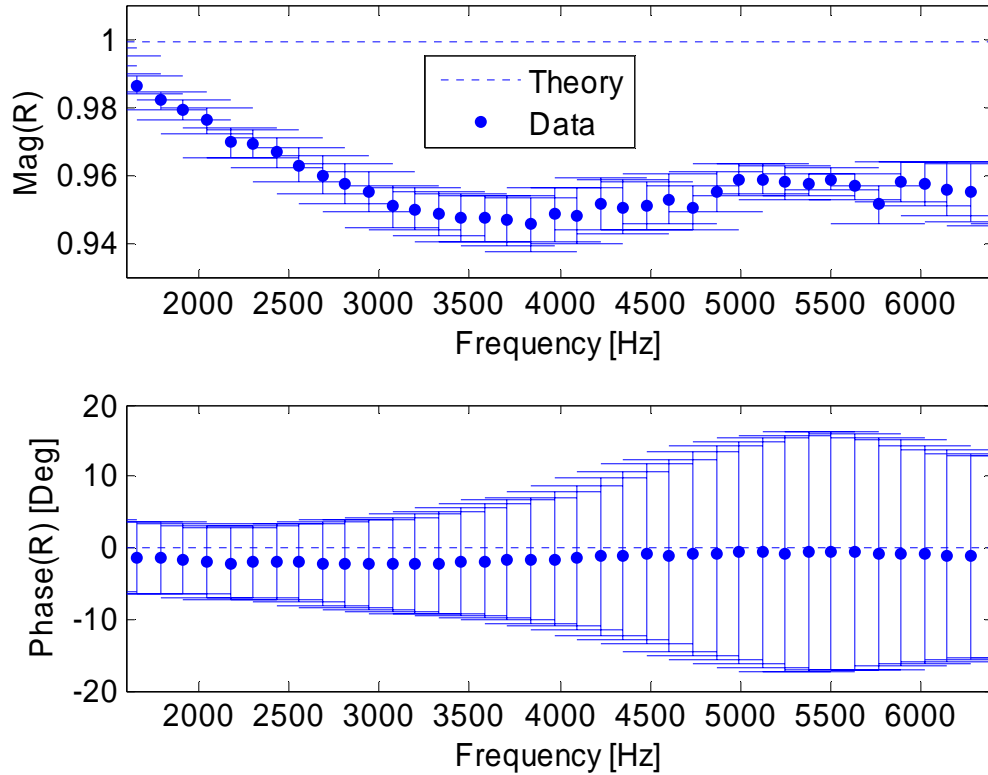


Figure 5-21: Device 1A-10-2, Normalized acoustic impedance in a sealed cavity package for the device with a radius of $900 \mu\text{m}$ and a central mass.

The impedances were shown over the same range of 250 Hz to 6700 Hz . The reactance of these devices was generally negative, as would be expected below resonance, where the behavior is dominated by the compliance of the diaphragm. Additionally, the resistance shows some unusual and inconsistent features below 2 kHz ; however, due to the close proximity to unity of the reflection coefficient at these frequencies, small measurement errors and uncertainties are magnified when calculating the acoustic impedance.

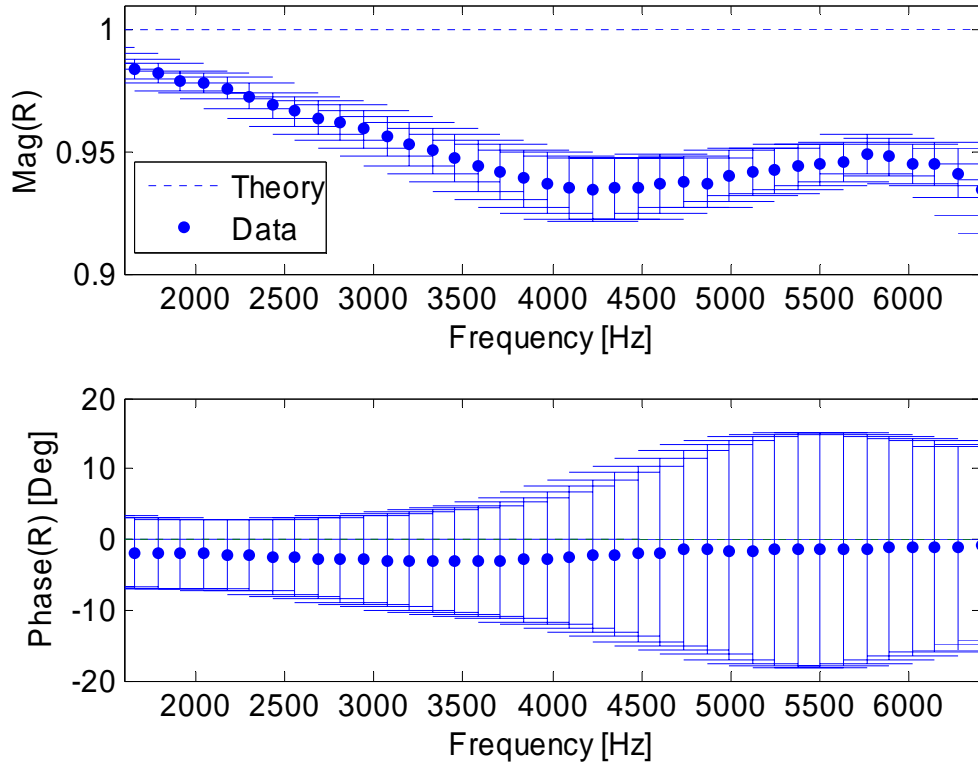


Figure 5-22: Device 1A-5-4, Normalized acoustic impedance in a sealed cavity package for the device with a radius of $1200 \mu m$ and a central mass.

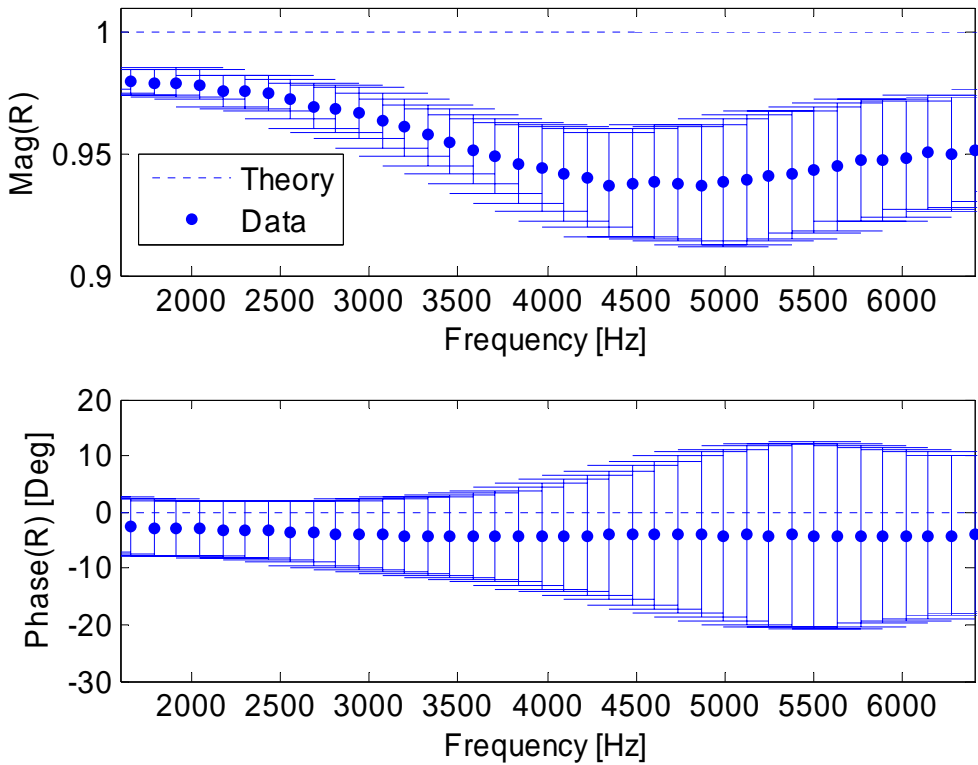


Figure 5-23: Device 1A-3-7, Normalized acoustic impedance in a sealed cavity package for the device with a radius of $1800 \mu m$ and no central mass.

Quarter-Wave Resonator Package

The same measurements were then performed on the devices that were packaged in the quarter-wave resonator package (Device 1A-6-1, Device 1A-11-3, Device 1A-10-4, Device 1A-6-5, Device 1A-10-6, Device 1A-3-7 and Device 1A-3-8). The results of some of these measurements are shown in Figure 5-24 and Figure 5-25, for Device 1A-6-1 with a radius of $900 \mu\text{m}$ and no central mass and Device 1A-11-3 with a radius of $1200 \mu\text{m}$ and also no central mass, respectively. The plots for the other devices were not shown to avoid needless repetition, as they are all highly similar in behavior. Note how the reactance is no longer solely negative, due to the presence of the quarter wave resonator. Furthermore, a peak was consistently observed in the resistance near 1500 Hz .

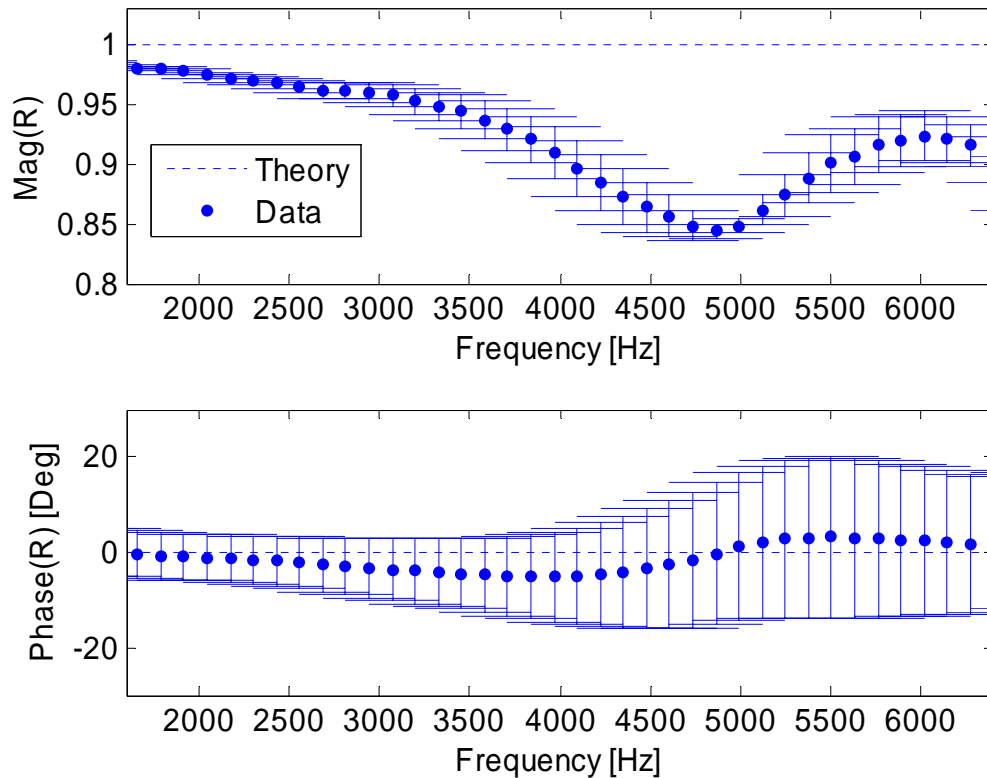


Figure 5-24: Device 1A-6-1, Normalized acoustic impedance in a quarter-wave resonator package for the device with a radius of $900 \mu\text{m}$ and no central mass.

The important thing to note from Figure 5-24 and Figure 5-25 is the decidedly different character of the impedance as compared to the previous experiments with sealed cavity devices. With the sealed cavity devices, the reactance was primarily negative and increased more or less monotonically with frequency, however the introduction of the quarter-wave resonator package alters the impedance such that positive reactances occur more frequently and the reactance in general has a more variable nature. The significant changes in the impedance highlight the role of the packaging in the overall behavior.

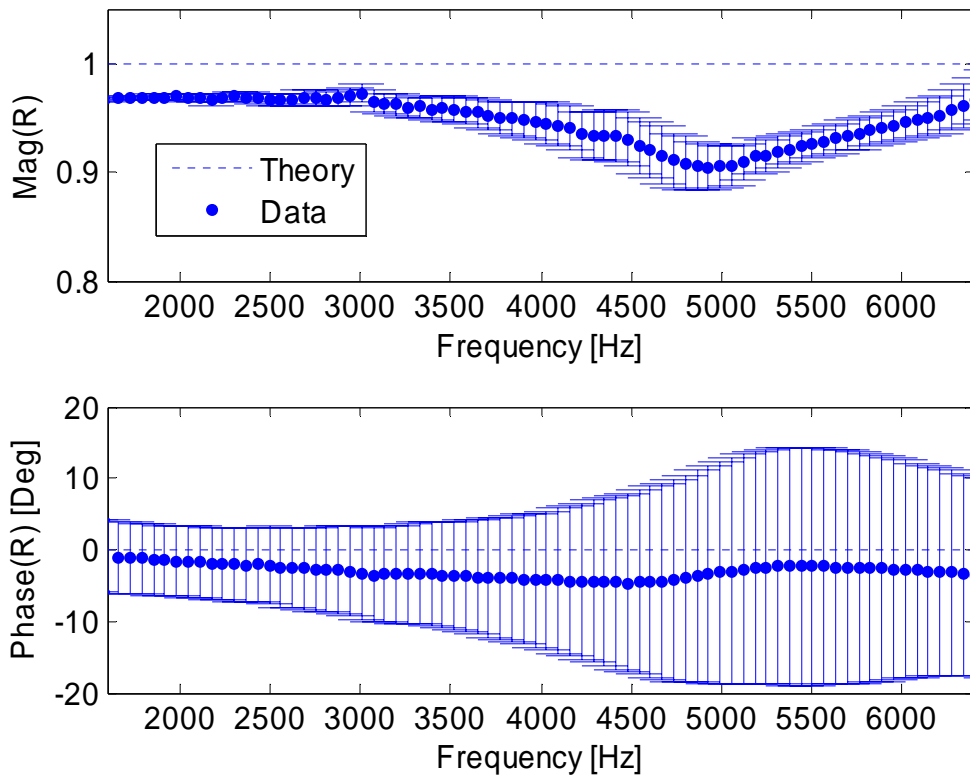


Figure 5-25: Device 1A-11-3, Normalized acoustic impedance in a quarter-wave resonator package for the device with a radius of $1200 \mu m$ and no central mass.

Initial Deflection Measurements – Wyko Optical Profilometer

Using the Wyko Optical Profilometer, the initial static deflection was measured for four devices. The initial deflection that arises due to residual stresses in the composite

structure is plotted versus radius in Figure 5-26 to Figure 5-29. Note that a small step is evident in the region near the clamped edge, resulting from the height difference between the piezoelectric ring and diaphragm surface. Also note that the two even numbered devices, Figure 5-27 and Figure 5-29, have a flatter central region due to the presence of the central pillar.

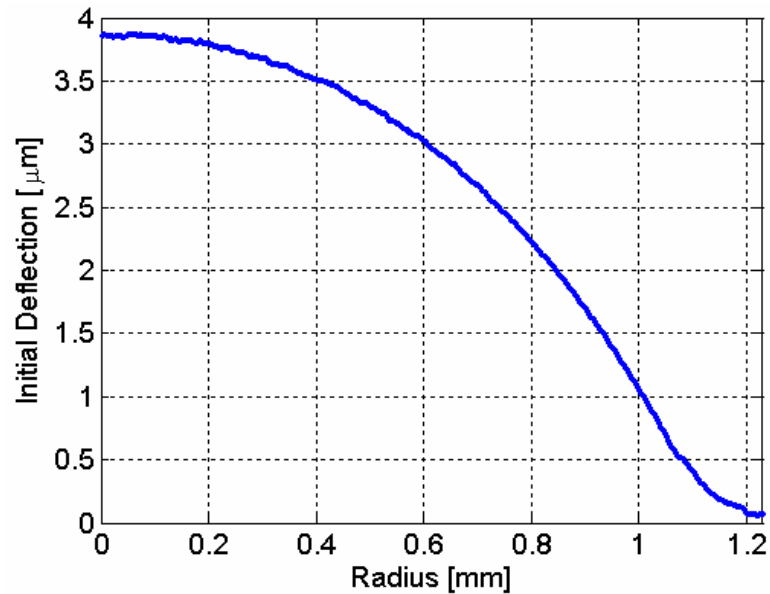


Figure 5-26: Device 1A-11-3, Initial static deflection resulting from residual stresses for a device with a radius of 1200 μm and no central mass.

There are several key points of note from the initial static deflection plots. First of all, the static deflection was found to be significant and on the same order of magnitude as the diaphragm thickness. The models that were used to predict the device behavior are linear models that depend on the assumption of small deflections. The large initial deflections violate this assumption and leads to a device that behaves differently than predicted using a linear theory.

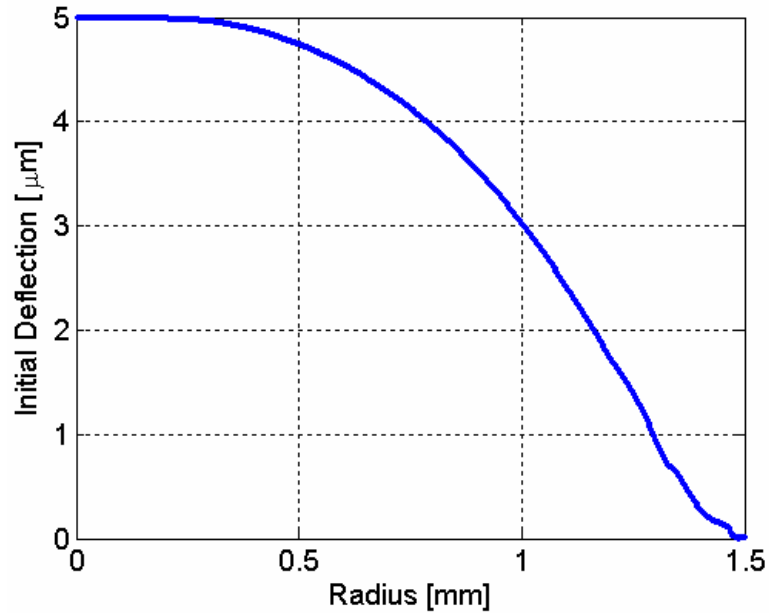


Figure 5-27: Device 1A-6-6, Initial static deflection resulting from residual stresses for a device with a radius of $1500 \mu\text{m}$ and a central mass.

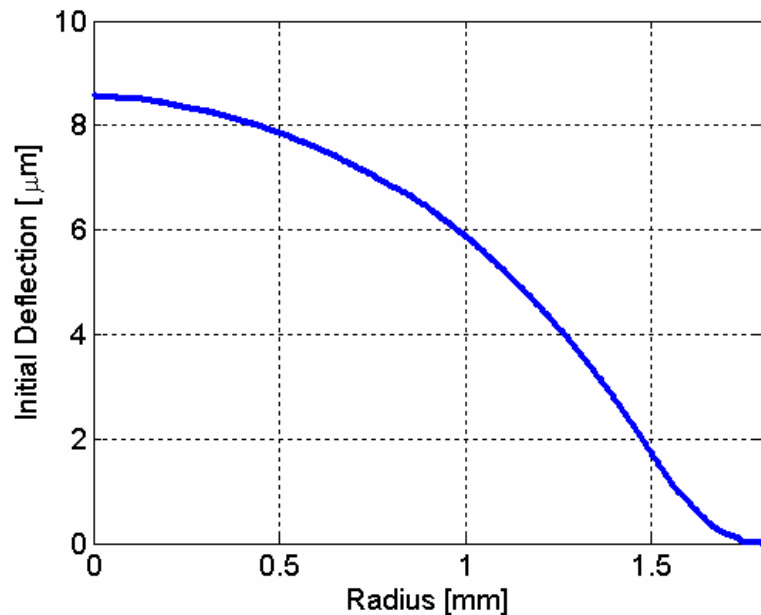


Figure 5-28: Device 1A-3-7, Initial static deflection resulting from residual stresses for a device with a radius of $1800 \mu\text{m}$ and no central mass.

Knowledge of the deflection curve is critical to accurate prediction of the device, as many of the lumped element parameters, such as the piezoelectric coefficient, d_A , are fundamentally derived from the curve. Because of the nonlinear nature of the deflection, the models cannot accurately predict the device behavior. Therefore, in order to compare

the experimental data against a more reasonable theoretical prediction, measured deflection curves were used to compute new values for the piezoelectric coefficient, d_A . Additionally, the measured dielectric loss resistance, R_p , and damping factor, R_m , were included into the model, are shown in Table 5-4. In the theoretical curves, previously shown in Chapter 2, these were not included. The energy harvesting measurement section utilizes these new predictions for comparison to the measurements. Notice from Table 5-4 that the measured d_A values are much lower than the predicted values of $1.93(10)^{-13}$ and $2.42(10)^{-12}$ for Device 1A-4-4 and Device 1A-3-8 respectively. The explanation behind this phenomenon will be discussed later in this chapter.

Table 5-4: Revised lumped element parameters used for comparing experimental data to theory. New and revised columns are marked with an asterisk.

Device	ϕ $\left[\frac{Pa}{V}\right]$	ϕ' $\left[\frac{V}{Pa}\right]$	k	d_A^* $\left[\frac{m^3}{V}\right]$	C_{ad} $\left[\frac{m^3}{Pa}\right]$	M_{ad} $\left[\frac{kg}{m^4}\right]$	M_{admass} $\left[\frac{kg}{m^4}\right]$	C_{eb} [nF]	R_p^* [kΩ]	R_m^* $\left[\frac{kg}{m^4s}\right]$
1A-4-4	-9.29	-7.16E-6	0.008	3.08E-14	2.07E-14	2602.5	11052	26.9	414.6	3.24E7
1A-3-8	-16.92	-4.71E-5	0.028	2.15E-14	1.43E-13	1009.8	4912.2	51.3	233.5	5.09E7

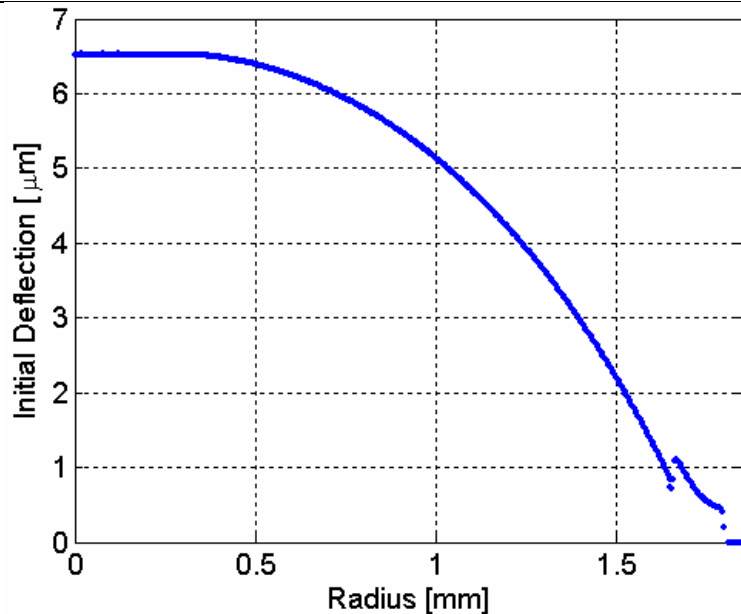


Figure 5-29: Device 1A-3-8, Initial static deflection resulting from residual stresses for a device with a radius of $1800 \mu m$ and a central mass.

Energy Harvesting Measurements

The primary application of the work presented in this dissertation is as a harvester of acoustic energy. For this application, it is useful to look at the device performance at resonance as a function of the applied acoustic pressure. In order to accomplish this, a load is placed across the output of the resonator and the voltage is measured across that load as the pressure is varied. Before varying the pressure, however, it is useful to optimize the load in order to maximize the energy transfer. Recall from Eq. (2.12), that under the constraint of a purely resistive load, the power transfer to the load is maximized when the load resistance is equal to the magnitude of the output impedance. This optimal value was determined experimentally by measuring the power while the load is varied. The resulting value was then compared against the measured output impedance of the device, in order to check for consistency with Eq. (2.12).

Optimal Resistance

Using a Stanford Research Systems SRS785 Dynamic Signal Analyzer, the optimal resistance for maximum power transfer was determined. First however, the exact resonant frequency values had to be determined, therefore the SRS785 was first set to record 500 averages of 800 frequency bins over a frequency span of 25.6 kHz. For Device 1A-4-4, no window was needed as a chirp input was used, while for Device 1A-3-8, a Hanning window was used in conjunction with a band-limited white noise signal input. This measurement resulted in measured resonant frequencies of 13.568 kHz and 5.232 kHz for Device 1A-4-4 and Device 1A-3-8, respectively.

Once the resonant frequencies were determined, the source was changed to a sinusoidal signal at each of these frequencies for the respective devices. The output voltage was then measured while the load resistance was varied from 46.4 Ω to 1.003

$M\Omega$. The output power was then calculated according to Eq. (2.117) and the results were then plotted as shown in Figure 5-30. The figure is overlaid with the theoretical values for comparison. As can be seen, there is less than one order of magnitude between data and theory, which overpredicted the power for Device 1A-4-4 and underpredicted the power for Device 1A-3-8. The experimentally determined, optimal resistance for both of these devices was found to be 982.9Ω .

Optimal Energy Harvesting

Using the optimal frequency and load resistance measured previously, the input signal was steadily increased in amplitude while the output voltage was measured. The power was then calculated based on the voltage and resistance measurements, again according to Eq. (2.117). The resulting output voltage for each device is shown in Figure 5-31 and is overlaid with the theoretical predictions for the output voltage.

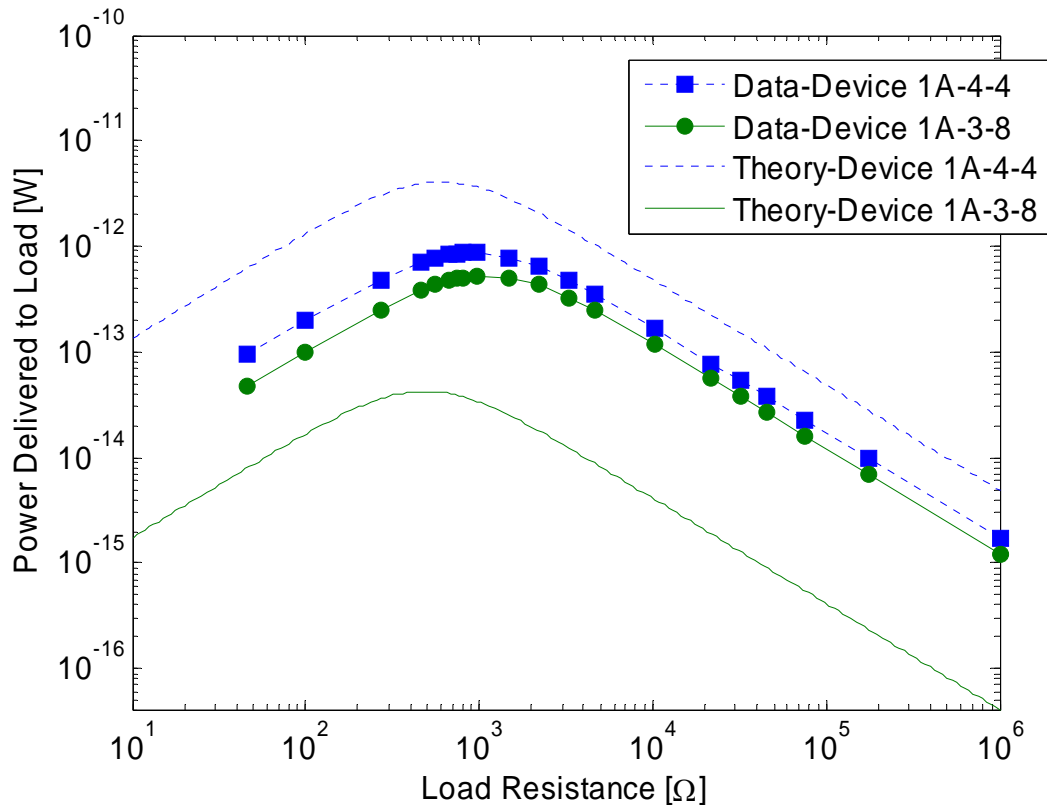


Figure 5-30: Measured power delivered to a load as function of the load resistance for Device 1A-4-4 and Device 1A-3-8 as compared against theoretical values. The input acoustic pressure was 92 dB for these measurements.

As can be seen in the figure, the output voltage was linear up to 125 dB for Device 1A-4-4 and up to 133 dB for Device 1A-3-8. The output voltage was seen to range between 22 μV and 4.6 mV. Using the voltage data, the output power was then calculated and is shown in Figure 5-32.

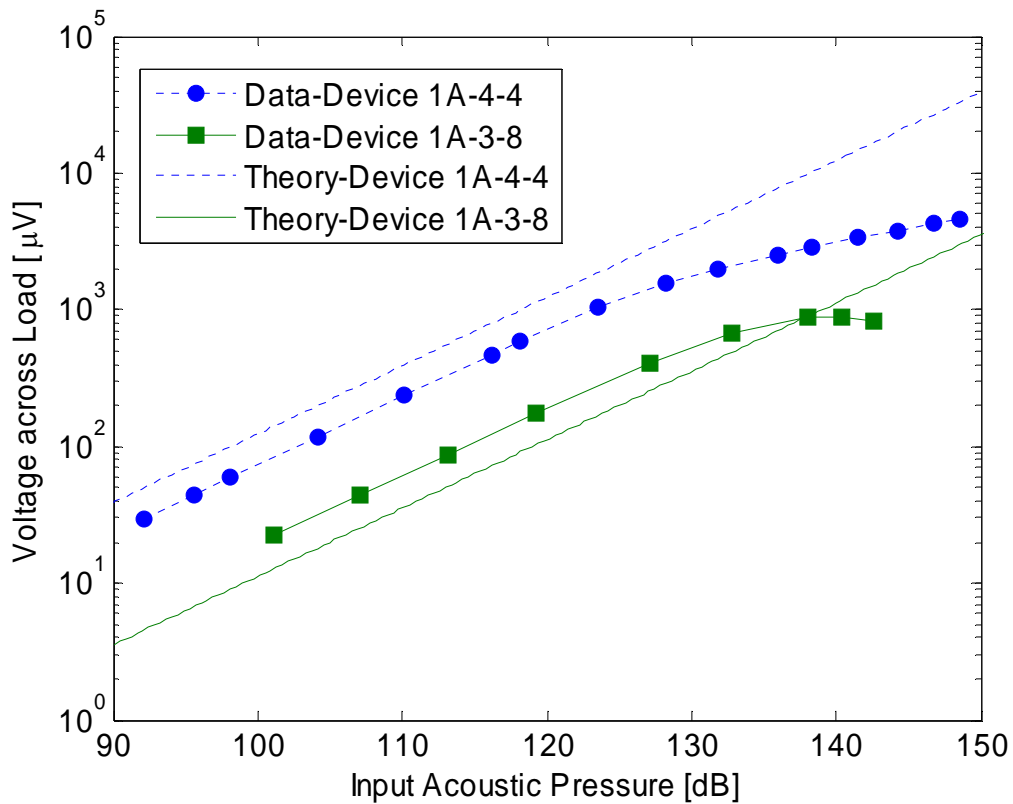


Figure 5-31: Measured output voltage across the load as a function of applied acoustic pressure and compared to theoretical values. The load resistance was fixed at the optimal value of 982.9 Ω . ($f = 13.568$ kHz and 5.232 kHz for Device 1A-4-4 and Device 1A-3-8, respectively)

The power density was then calculated based on a square unit cell with lateral dimensions equal to the diameter of the diaphragm. The resulting values are shown in Figure 5-33 and are again overlaid with theoretical values. Note from the graph that the maximum power density measured was around 1 $\mu W/cm^2$ at around 150 dB, which is

considerably lower than the available acoustic power density of $100 \text{ mW}/\text{cm}^2$ at the acoustic pressure of 150 dB .

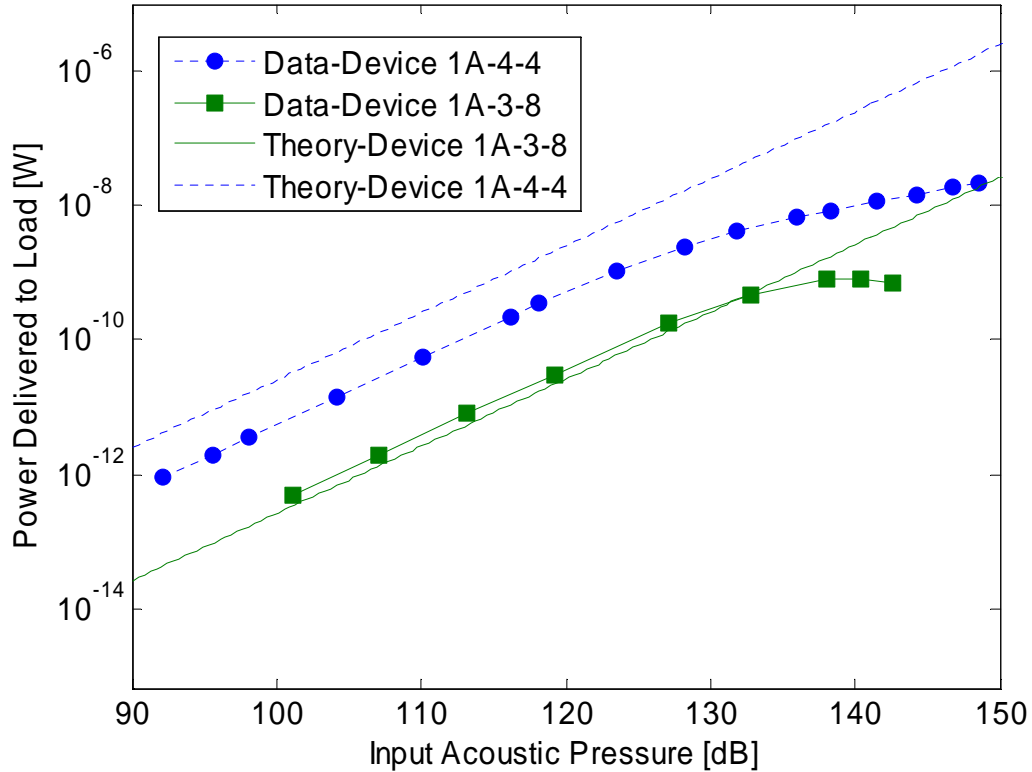


Figure 5-32: Measured power delivered to load as a function of applied acoustic pressure and compared to theoretical values. The load resistance was fixed at the optimal value of 982.9Ω . ($f = 13.568 \text{ kHz}$ and 5.232 kHz for Device 1A-4-4 and Device 1A-3-8, respectively)

This can be seen more clearly by looking at the efficiency, Γ . The efficiency was calculated according to Eq. (2.118) for each of the devices, and is shown in Figure 5-34. As can be seen, the efficiency was fairly constant near 0.012% for Device 1A-4-4 in the linear regime and $4 \times 10^{-4} \%$ for Device 1A-3-8 in the linear regime. For comparison, the theoretical model predicts efficiencies of 0.056% and $3 \times 10^{-4} \%$, respectively.

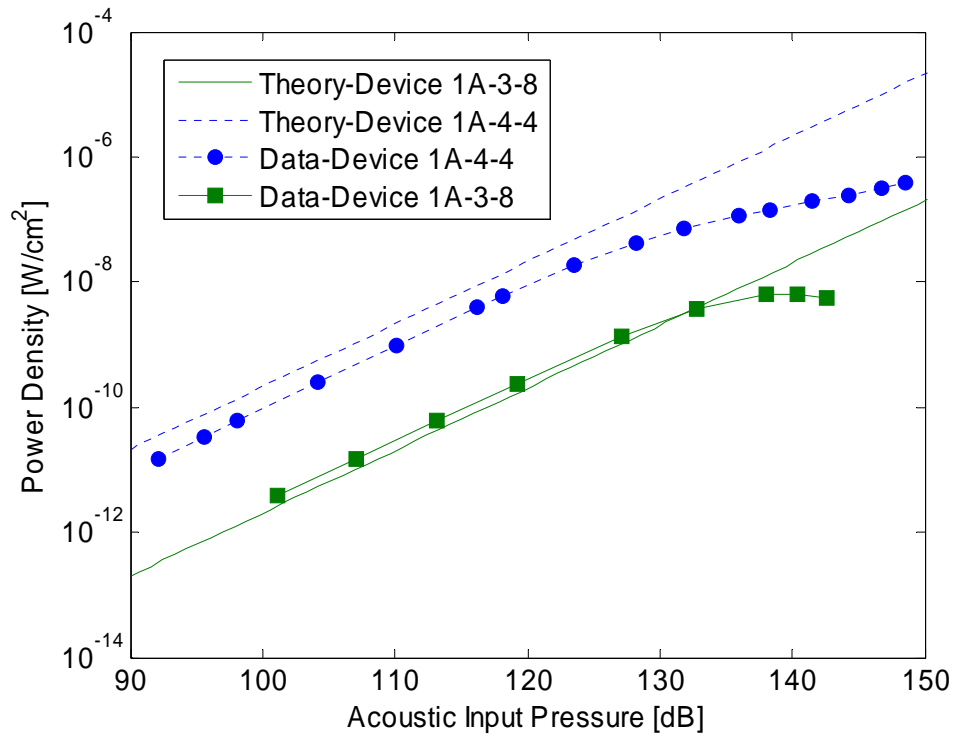


Figure 5-33: Measured power density delivered to load as a function of applied acoustic pressure and compared to theoretical values. ($f = 13.568 \text{ kHz}$ and 5.232 kHz for Device 1A-4-4 and Device 1A-3-8, respectively)

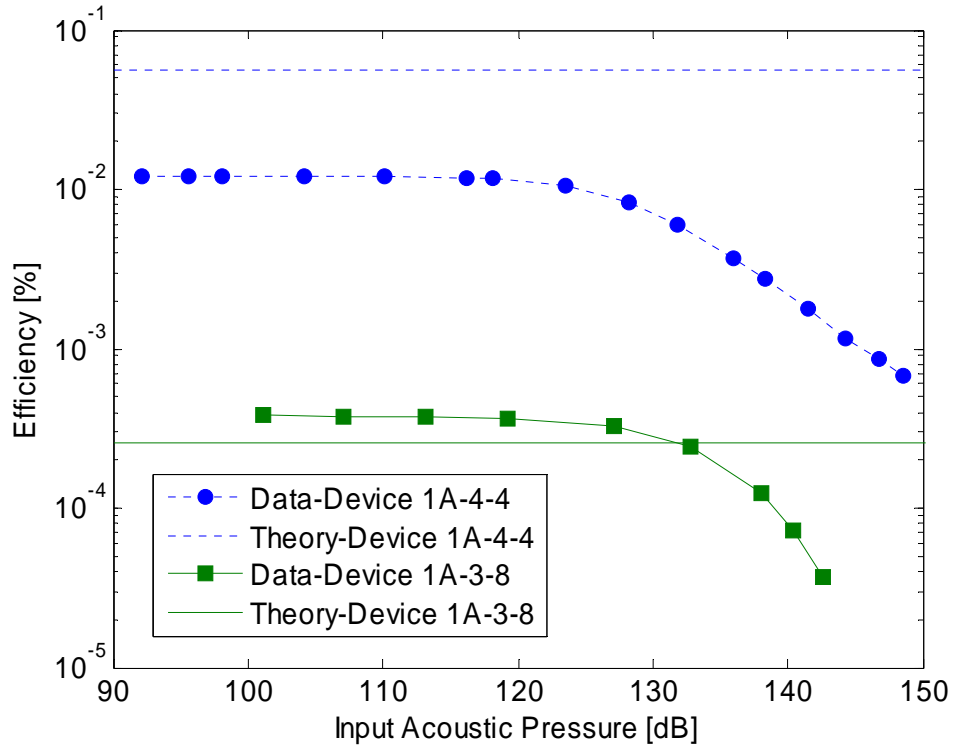


Figure 5-34: Measured overall efficiency of each device overlaid with theoretical values for comparison. ($f = 13.568 \text{ kHz}$ and 5.232 kHz for Device 1A-4-4 and Device 1A-3-8, respectively).

A question then arises regarding the origin of the low efficiency and whether improvements in either the manufacturing or design of the devices could improve the efficiency, and thereby the output power. Several issues were faced during the fabrication process that limited the efficiency of the devices. First, the materials and processes led to a large residual stress in several layers of the device, most notably the titanium dioxide. The effect of this large tensile stress, σ_{TiO_2} , is twofold: (1) it alters the deflection mode shape of the devices and (2) it leads to a large, non-linear, initial deflection of the diaphragm. The end result is a modification to the piezoelectric coefficient, d_A and ultimately the coupling coefficient, k . It is difficult to ascertain the exact magnitude of this effect since the deflection lies in the nonlinear regime and the analytical model is only linear. Nevertheless, a 1st order estimate of the effect can be made by using the linear model and comparing the results for the existing high-stress case to an ideal zero-stress case. Using this method, the power density decreased by a factor of 4.3 over the ideal zero-stress case.

A second issue arising from the fabrication is the overhanging metal on the electrodes that created short circuits under high electric fields. The field limitation imposes a maximum poling voltage that can be applied. As the piezoelectric coefficient, d_A , is proportional to the polarization, the full potential poling was not realized. The effects of this issue, along with the unmodeled (non-linear) portion of the stress induced effects, lead to a reduction in power density by a factor of 24.6 below the ideal case.

The final fabrication issue concerns the choice of the starting piezoelectric material and the process by which it is deposited on the wafer. The particular sol-gel technique that was employed in this research produces a typical d_{31} of -50 pC/N , whereas other

variations of the sol-gel process as well as techniques such as sputtering can produce a film with a d_{31} of -120 pC/N . The output power density is smaller by a factor of 2.8 as a result of the lower value of d_{31} as compared to other reported PZT thin films.

The final issue that reduces the output power density concerns the quality factor, Q , of the device. The measured quality factor for Device 1A-3-8 is approximately 10, leading to a damping factor of 0.05. This damping accounts for radiation resistance and internal damping, as well as radiation to the supports. This damping factor is much higher than a more typical 0.02, leading to a reduction in power density by a factor of 2.5

Through improvements in the fabrication and design, leading to a reduction in the damping factor, the output power density would increase by a factor of 2.5. Additionally, provided that all of the other sources of inefficiency are addressed, including the PZT material quality, the poling capability, and the residual stress, the overall power density would increase by a factor of 740. The resulting power density curve is shown in Figure 5-35, overlaid with the currently achievable results. With these improvements, at 150 dB , the output power density would be on the order $500 \mu\text{W}/\text{cm}^2$. Additionally, the individual contributions to this improvement are illustrated in Figure 5-36, clearly showing the prominent role of improving d_A to the overall results.

Nonlinear behavior is evident in Figure 5-31 through Figure 5-34. Physically, there are several possible sources for the nonlinear behavior. The overall response may be affected by one or all of these sources. First of all, a mechanical nonlinearity arises, when the deflection of a plate is on the order of the thickness of that plate. Under large deflections, the neutral axis of the plate stretches by a finite amount, requiring energy in addition to the energy required for bending of the plate. The resulting effect is an

increase in stiffness above that predicted by linear, small-deflection plate theory. The increase in stiffness leads to a lower sensitivity and an increased resonant frequency.

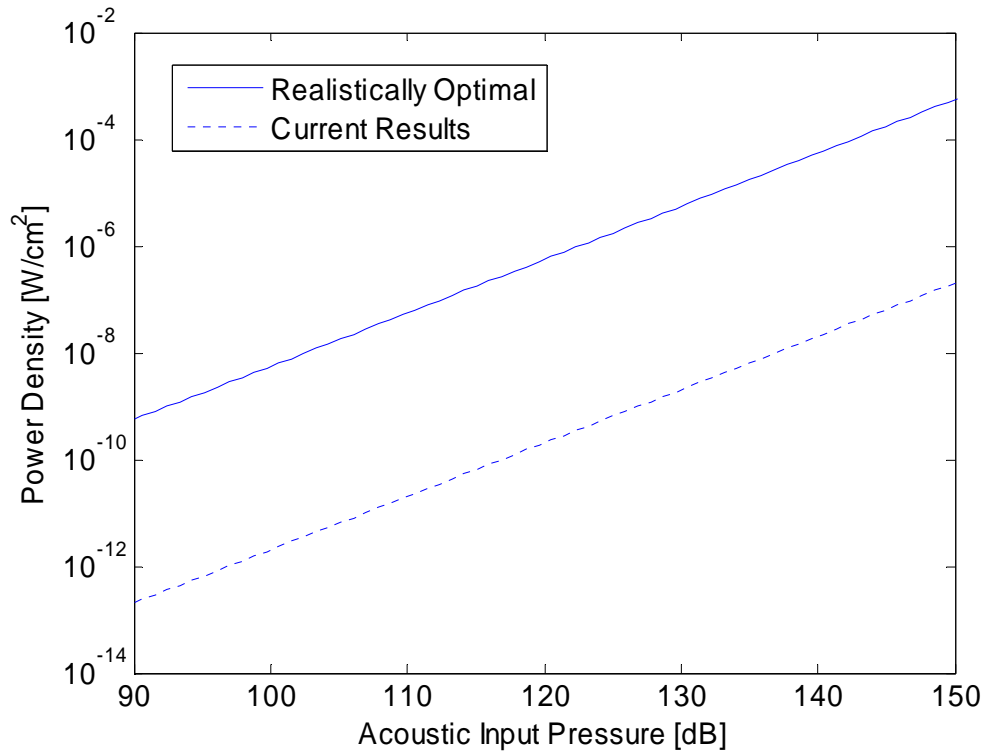


Figure 5-35: Currently achievable power density for Device 8 and potentially achievable power density using an improved fabrication process.

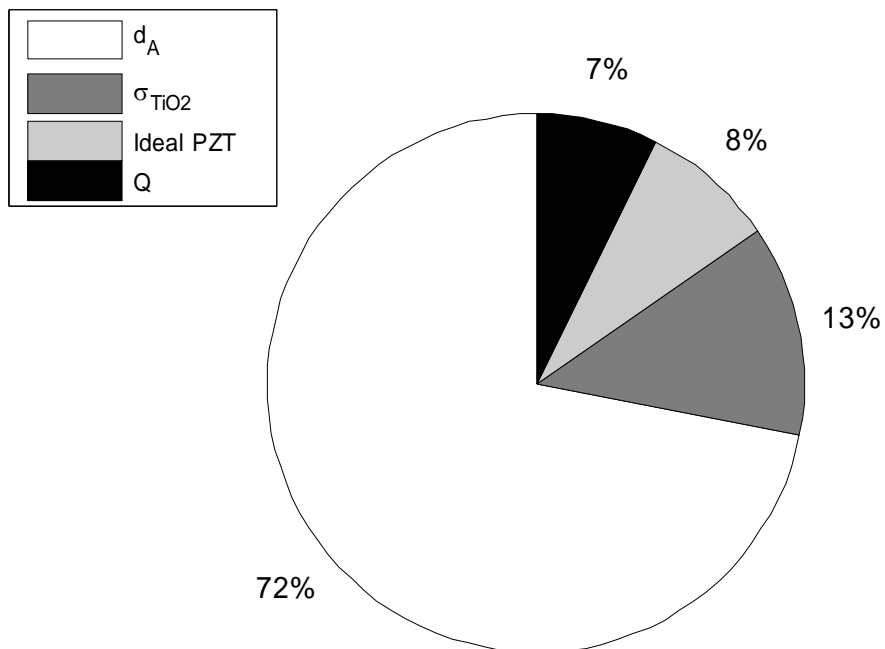


Figure 5-36: Breakdown of the individual contributions to the overall improvement in power that is achievable under better fabrication conditions.

The effect on the resonant frequency was measured for one particular device that exhibited strong nonlinear behavior and is shown in Figure 5-37. The resonant frequency was seen to approximately shift linearly as the acoustic pressure was increased. Additionally, in the frequency domain, the nonlinearity generates harmonics at integer multiples of the fundamental signal frequency, thereby dumping some of the energy that would have otherwise resided at the fundamental frequency.

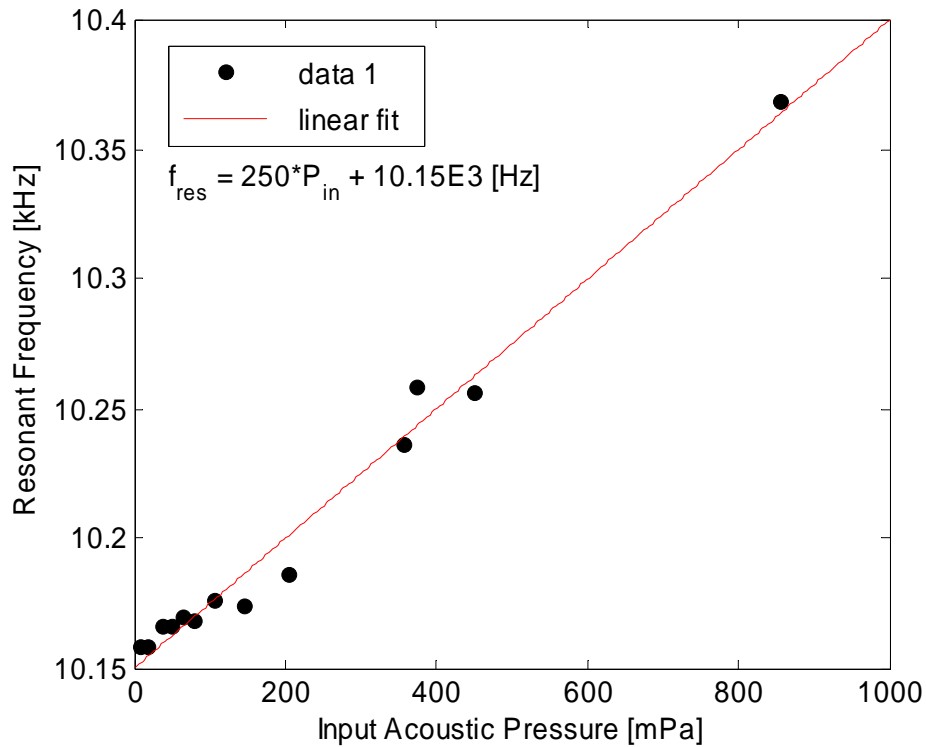


Figure 5-37: Resonant frequency vs. acoustic pressure, arising from nonlinear response.

CHAPTER 6 ALTERNATIVE APPLICATION—PIEZOELECTRIC MICROPHONE

The previous chapter on experimental characterization measured the overall characteristics of the device in terms of impedance, acoustical response, and electrical response in a general sense, as well as an evaluation of the performance of the device as an energy harvester. The goal was to understand the actual behavior and to try and explain the difference between the actual behavior and the predicted behavior.

This chapter serves to enhance our understanding of the device performance by looking at an alternative application of the piezoelectric composite diaphragm, by using it as a piezoelectric microphone. For the energy harvester devices, we are using the piezoelectrically generated charge as an energy source, whereas in a microphone application, this charge (or corresponding voltage) is a signal for transmitting information about the acoustical environment. For this set of experiments, a piezoelectric diaphragm with 1.8 *mm* diameter and no central mass was used.

Experiments were performed both as a sensor (acoustically actuated) and as an actuator (electrically actuated) in order to obtain the performance specifications. The packaged device was mounted to the end of a 1" x 1" cross section plane wave tube (PWT) for obtaining the frequency response and linearity. A Bruel and Kjaer (B&K) 1/8" Type 4138 microphone was mounted on the wall of the PWT near the end of the tube to record the incident sound pressure level (SPL). The signal was provided by a PULSE Multi-Analyzer system to a BMS 2" coaxial compression driver, via a Techron amplifier.

The PULSE analyzer was also used to record the signals from the B&K microphone and the piezoelectric microphone.

First, the linearity was tested using a sinusoidal signal at 1 kHz. Measurements were taken with a binwidth of 1 Hz and the signal falling directly on the center of a bin to avoid leakage. Additionally, 100 averages were taken at each point. The measured linearity of the sensor at 1 kHz is shown in Figure 6-1. The device was experimentally found to be linear up to (at least) the maximum testable sound pressure level of 169 dB.

The sensitivity was measured over this range to be approximately 11.0 $\mu V/Pa$.

Furthermore, the response flattens out below 45 dB as the signal level approaches the noise floor. The maximum testable level is limited here by the output capacity of the compression driver. The measured sensitivity was found to be 0.75 $\mu V/Pa$.

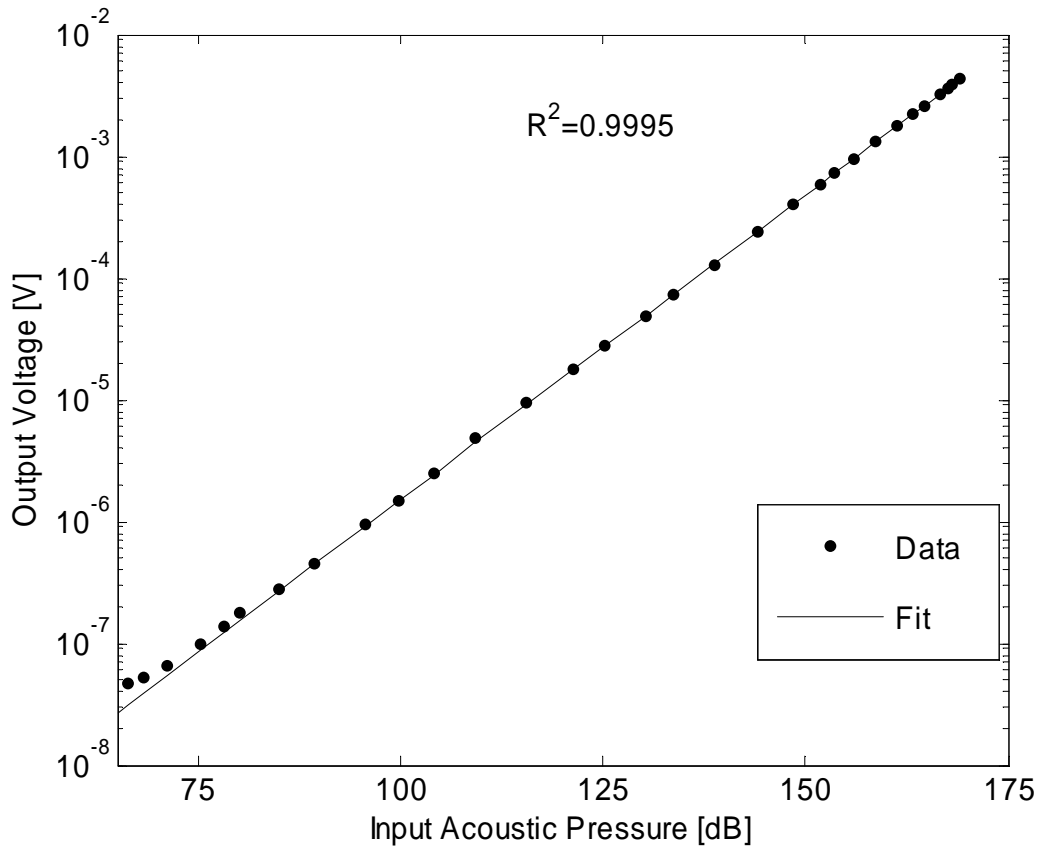


Figure 6-1: Linearity of the microphone device at 1 kHz.

The frequency response was measured using a periodic random noise acoustic signal of 94 dB and 1000 spectral averages over a bandwidth from 0 to 6.4 kHz with a 1 Hz bin width. Once again, the testable frequency range was limited on the upper end by the onset of higher order modes. The resulting frequency response of the sensor is shown in Figure 6-2 in terms of magnitude and phase.

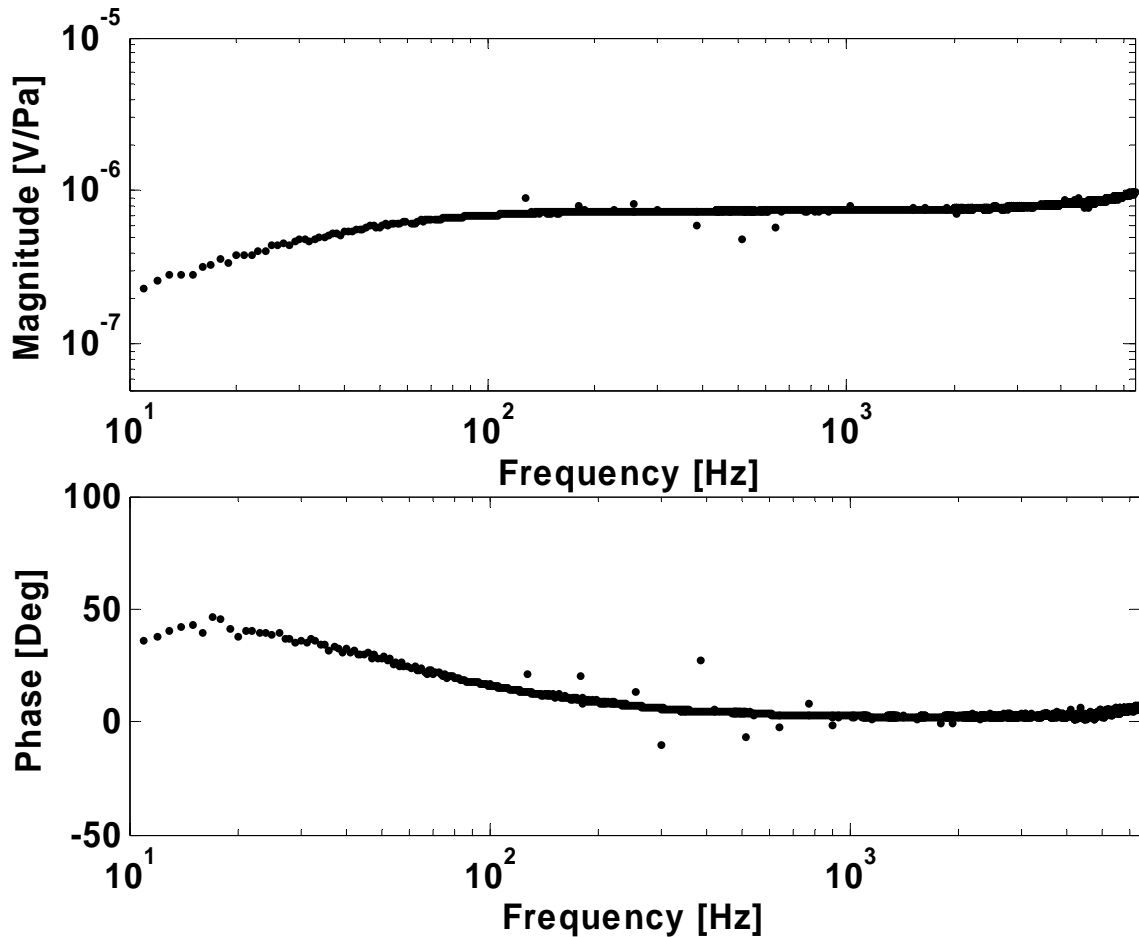


Figure 6-2: Frequency response spectrum in terms of magnitude and phase.

The response is flat over the testable frequency range up to 6.7 kHz, except for a low frequency rolloff at approximately 100 Hz. This is most likely due to the vent resistance; however, the magnitude of this contribution is unknown, as the value for the vent resistance due to packaging leaks has not been measured. Additionally, there is a low-frequency rolloff due to the parallel combination of the capacitance and resistance in

the piezoelectric material, however the corner frequency due to this combination is 6.7 Hz, well below that of the measurable corner frequency of 100 Hz .

The noise floor spectrum of the sensor is shown in Figure 6-3 from 0 Hz to 12.8 kHz, along with the noise floor due to the experimental setup alone. The noise floor was found to generally decrease with increasing frequency. The noise spectrum of the experimental setup alone was obtained by shorting the inputs to the preamplifier and recording the resulting output voltage signal, using the same conditions and setup as the sensor noise floor measurement. This noise spectrum is characteristic of a resistance shunted by a capacitance. The resistance in this case is the sensor dielectric resistance, R_p , and the capacitance is the blocked electrical capacitance, C_{eb} . The resistance and capacitance form a low-pass transfer function that spectrally shapes the thermal noise. When integrated over an infinite bandwidth, the resulting mean square noise voltage is given by kT/C_{eb} , where k is Boltzmann's constant and T is the ambient temperature. For this device, the low pass filter has a cutoff frequency of 6.7 Hz, determined by $1/2\pi R_p C_{eb}$. There are three characteristic regions in this spectrum. Below 6.7 Hz, there exists a relatively flat region where the noise is dominated by the resistance of the sensor. Then, from 6.7 Hz up to approximately 2 kHz a $1/f$ rolloff in the noise is observed that is consistent with a capacitive dominated noise source. Above 2 kHz, the noise spectrum flattens out again as the sensor noise approaches the setup noise. For a 1 Hz bin width centered at 1 kHz, the output voltage with no acoustic signal applied is 3.69 nV that corresponds to an equivalent acoustic pressure of 4.93 mPa or 47.8 dB .

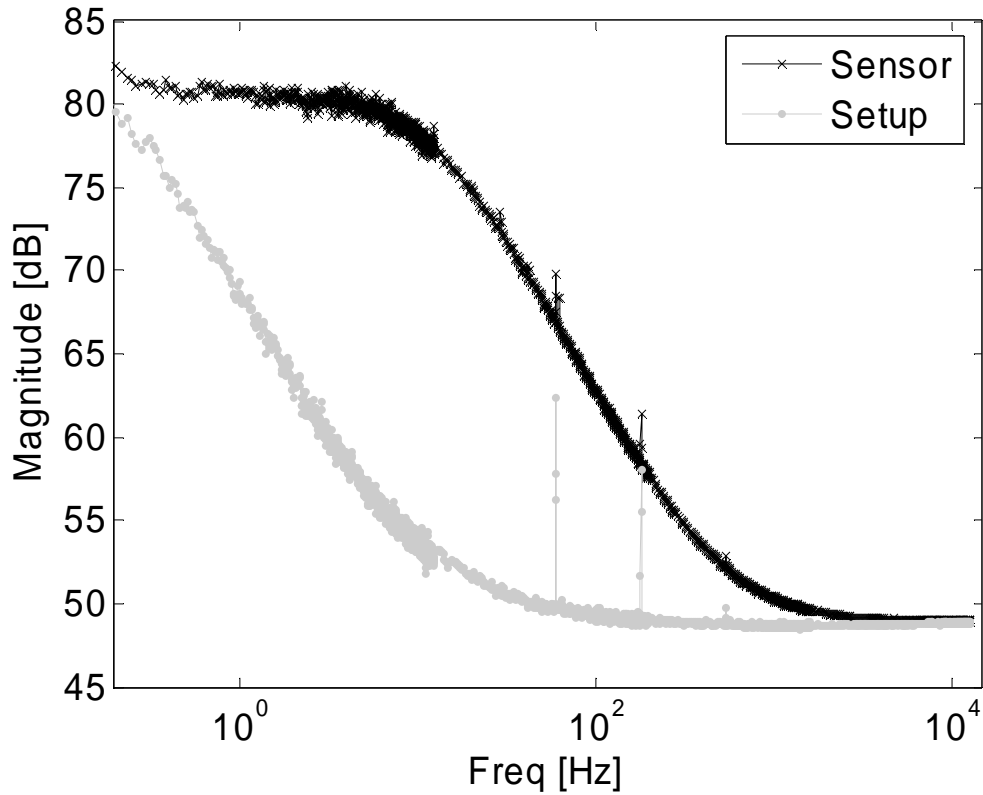


Figure 6-3: Noise floor spectrum of output voltage when no acoustic signal is applied, as well as noise floor due to measurement setup alone.

Because the device is a linear, reciprocal electromechanical transducer, it can operate in both an electrically driven and acoustically driven modes and the electrically driven frequency response can be used to gain additional information about the sensor, such as the bandwidth. In particular, as the acoustically actuated frequency response could only be measured up to 6700 Hz due to testing limitations of the plane wave tube, the bandwidth can be approximated via use of the electrically actuated frequency response.

The electrically actuated frequency response is shown in Figure 6-4 in terms of magnitude and phase. The resonant frequency was found to be 50.8 kHz and provides an estimate of the usable bandwidth as a microphone, as the electrically and acoustically

actuated resonance frequencies are related. A summary of the overall performance specifications of the microphone is given in Table 6-1.

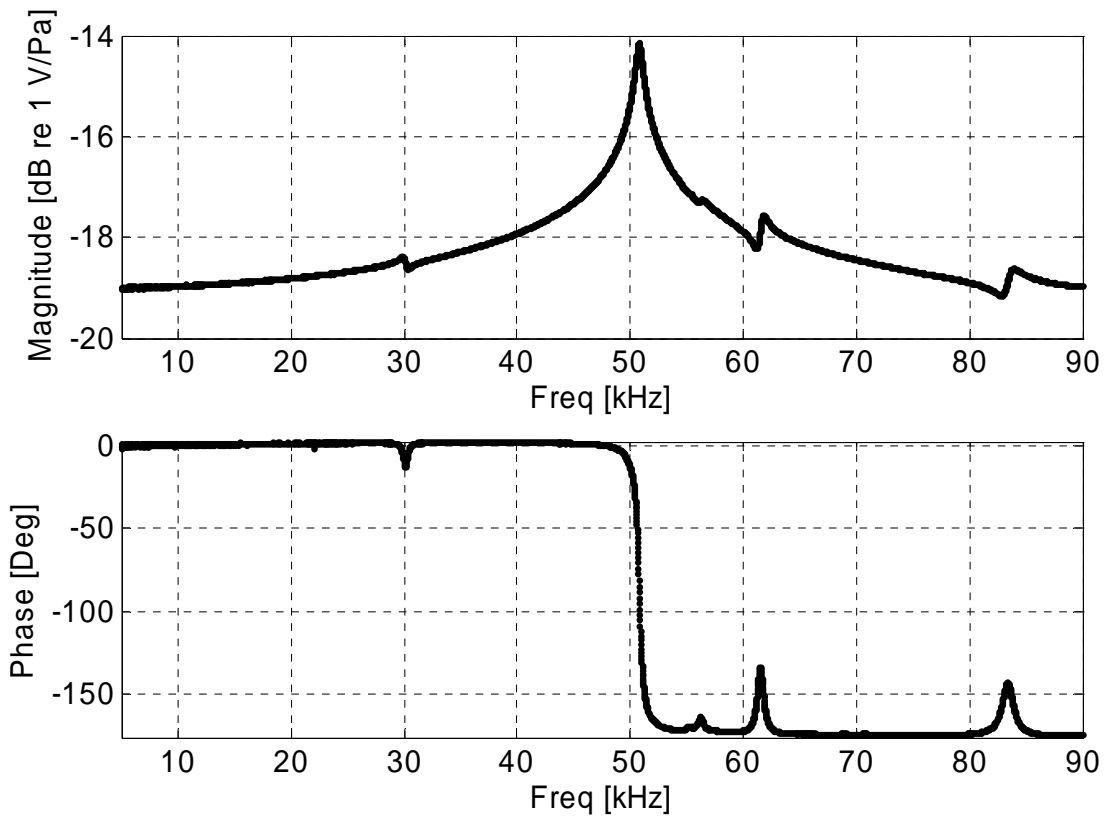


Figure 6-4: Electrically actuated frequency response of microphone device.

Table 6-1: Summary of experimental results of microphone.

Specification	Measured Value
Diaphragm Size	1.8 mm diameter, 3 μm thick
Die Size	5 mm × 5 mm
Measured Resonant Frequency	50.8 kHz
Sensitivity	0.75 μV/Pa
Dynamic Range	47.8–169 dB

CHAPTER 7 CONCLUSION AND FUTURE WORK

The acoustic energy harvesting technique that was developed in this dissertation provides a unique and innovative method for extracting energy from an otherwise inaccessible source. For the development of acoustic energy harvesters, piezoelectric composite diaphragms were designed based on analytical models of circular piezo-composite structures. Lumped element modeling was then used to further understand the dynamics of the system. The modeling served as a basis around which the geometry and dimensions of numerous diaphragms were determined. The lumped element model developed in this dissertation serves as a design basis for other types of piezoelectric composite structures as well as energy harvesting devices employing other transduction methods. Furthermore, it is directly applicable to those interested in the scaling and design of piezoelectric composite diaphragms.

Following the design stage, a fabrication process flow and mask set was developed to synthesize the devices. Fabrication was then performed as prescribed in the process flow. Following this, the devices were packaged into two different packages for testing purposes. Finally, a number of experiments were set up and performed on the devices to better understand the real behavior as compared to the theory. A graphical overview of this chapter is provided by the roadmap of Figure 7-1.

The main contributions of this dissertation included the development of the acoustic energy harvesting concept. While previous researchers had looked at harvesting

energy from vibration, solar, chemical and thermal energy among others, a thorough investigation into the harvesting of acoustic energy had not been performed.

Additionally, in order to develop the concept, a comprehensive lumped element model (LEM) of the acoustic energy harvester was utilized. This model allowed for a single representation for the dynamics of the system as a whole, as well as the individual components.

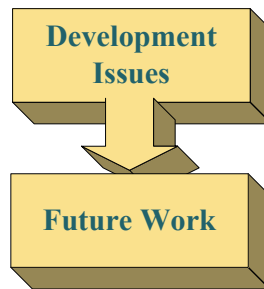


Figure 7-1: Roadmap to Chapter 7.

The implementation of the acoustic energy harvester led to the first reported integration of thin-film PZT with SOI-based MEMS. While numerous researchers had previously looked at thin-film PZT, or MEMS using SOI wafers, none had sought to combine them. The high transduction coefficient of PZT along with a simpler fabrication route to a diaphragm via SOI wafers led to the decision to combine these technologies.

Finally, although the circular piezoelectric membrane was initially intended as a harvester of acoustic energy, it was discovered that it also served as fairly capable microphone. This is the first reported instance of an aeroacoustic capable piezoelectric microphone.

Development Issues

Several issues arose during the development of these devices. First of all, the initial process flow that was developed contained more steps and masks than the process

flow that was presented here. Initially, gold bond pads and an insulating oxide were incorporated to enable on-chip arrays of devices; however, this process flow was later simplified prior to fabrication to reduce cost, time and fabrication complexity.

The next issue arose during fabrication of the devices, but was not discovered until packaging of the devices was attempted. The problem involved a thin strip of platinum that overhung the piezoelectric ring from the top electrode. Normally, for a metal liftoff step, a image reversal mask is used on positive photoresist to obtain a negative sloping sidewall prior to metal deposition. The negative slope permits a clean break in the metal for improved liftoff results. However, due to processing constraints, we had to use a negative photoresist for this pattern, resulting in a positive sloping sidewall. Then during the metal liftoff, a clean break was not achieved, resulting in a few microns of overhanging metal around the edges of the ring. This was not noticed until electrical testing was performed on the devices after fabrication was completed. The testing showed that four of the six wafers had electrical short circuits between the top and bottom electrodes. Furthermore, the resistance of the short circuits was proportional to the perimeter of the ring, indicating it was due to an edge effect rather than a surface effect. The two remaining wafers still functioned correctly, though, despite the same overlapping metal issues, and were solely used for the experiments presented here.

Another fabrication issue that arose concerned the residual stress in the devices. It was discovered that the measured residual stress of the titanium dioxide (TiO_2), at 1800 *GPa* was significantly higher than anticipated. This led to a large initial static deflection of the diaphragms. Additionally, the buried oxide layer on the backside of the

diaphragms proved difficult to remove. This residual stress of this layer further exacerbated the initial static deflection.

Unfortunately, the large initial static deflection placed the devices into a nonlinear regime of plate mechanics and led to a stiffer device than was anticipated. Furthermore, the models that were developed for the design of the diaphragms were no longer applicable under this nonlinear condition. This caused numerous difficulties in fully understanding the overall behavior of the devices from a quantitative standpoint. Qualitatively, however, the devices did behave as expected, following anticipated trends and dependencies.

Ultimately, however, the increased stiffening opened up a new application for the devices as a microphone. Because the stiffer devices had a higher resonance frequency, the usable bandwidth was extended beyond our expectations. Experimental characterization indicates a sensitivity of $11.0 \mu V/Pa$ with a dynamic range from $44.1 dB$ to $153 dB re 20 \mu Pa$ and a resonant frequency of $22.72 kHz$, suggesting a potential suitability as a microphone.

Future Work

A number of improvements can be made in the design of these devices. The fabrication process flow needs to be modified to avoid the platinum liftoff issue and resulting short circuits. Furthermore, more analysis and optimization of the residual stress in the various layers is needed, in particular for the TiO_2 . A reduction in this residual stress would improve performance by reducing the diaphragm stiffness, lowering the resonant frequency to a more testable range and ultimately allowing for comparison to a well understood linear model. Alternatively, a modified process allowing for the

removal of most of the TiO_2 would achieve the same results. Additional work is also needed on developing a nonlinear extension to the model to facilitate the analysis of the existing structures.

Other future work involves a more thorough investigation of this device as a microphone, including a rigorous microphone calibration. Additionally, other applications need to be explored further, including the use of the devices as a piezoelectric actuator and speaker, as well as the potential for active acoustic impedance control.

APPENDIX A MATLAB CODE

lem.m

```
clear all;
close all;

eh_setup;

%Helmholtz Resonator
Ma=(rho*Leff)/(pi*r_neck^2);    %acoustic mass of neck
Ca=volume/(rho*c^2);          %acoustic compliance of cavity
Ra=(40*8*mu*L)/(pi*r_neck^4);  %acoustic resistance of neck

% Readinput;
silicon_sweep;                %Reading shim properties
platinum;                     %Reading platinum properties
tio2;                          %Reading silicon dioxide properties
piezo_sweep;                  %Reading piezo props from console

R21= R1/R2;

% Give the values
PP          = 1;
VV          = 1;
h_ca       = 2e-4;
density_air = 1.165;
sound_velocity = 344;

initialise;                    %Initialising sampling etc.

N_in = .001;                   %Initial in-plane stresses in the inner
region
N_out = sigma02*t02+sigmap*tp; %Initial in-plane stresses in
the outer region

% Calculate the total deflection for the pressure loading
totaldeflection_forP;

% Calculate the total deflection for the voltage loading
totaldeflection_forV;
```

```

% Calculate the initial deflection
initialdeflection;

% Incremental deflection for pressure loading
Wi = Wlp - W0vp;
formmatrix_CMFa;

% Voltage loading only
Wiv = Wlv - W0vp;
frommatrix_dA;

k = sqrt((dA^2)/(Cefp*CaD)); %Calculate the value
of 1-k^2
PHI = -dA/CaD; %Electro-acoustic Xduction
coefficient
PHIprime = -dA/Cefp;
Ceb = Cefp*(1-k^2);

Rrad_RES=(FREQ*2*pi*R2/c)^2*rho*c/(2*Area); %rad resistance at
resonance
RloadA=Rrad_RES;

%Equivalent Circuit
Zrad=tf([0 Rrad_RES],1); %radiation impedance
ZaD=tf([MaD 0],1)+tf(1,[CaD 0]); %impedance of diaphragm
Zeb=tf(1,[Ceb 0]); %blocked electrical impedance
Zload1=tf(RloadA+Ra,1);
ZL=tf([0 0],1);
ZRopen=tf(10^9,1);
ZRshort=tf(1,1);
Zload2=tf(RloadA,1);
Zneck=tf([Ma Ra],1); %impedance of neck
Zcav=tf(1,[Ca 0]); %impedance of cavity
Ztube=rho*c/Atube;

wnHR=1/sqrt(Ma*Ca);
fHR=wnHR/(2*pi);
wnD=1/sqrt(MaD*CaD);
fD=wnD/(2*pi);%
alpha=Ma/MaD;

Pmax=2.3*Esi/(R2/tsi)^4
PmaxdBSPL=20*log10(Pmax/20e-6)

P=1;

Zel=Zeb*Zload1/(Zeb+Zload1);
Zelshort=Zeb*ZRshort/(Zeb+ZRshort);

```

```

Ze2=Zeb*Zload2/(Zeb+Zload2);

Zin1=Zneck+Zcav*(ZaD+Zrad+PHI^2*Ze1)/(Zcav+ZaD+Zrad+PHI^2*Ze1);
Zin2=ZaD+Zrad+PHI^2*Ze2;
Zin2short=ZaD+Zrad+PHI^2*Ze1short;
Zout1=Zeb*((ZaD+Zrad+Zcav*Zneck)/(Zcav+Zneck))/PHI^2/(Zeb+(ZaD+Zrad+Zcav*Zneck)/(Zcav+Zneck))/PHI^2);
Zout2=Zeb*((ZaD+Zrad)/PHI^2)/(Zeb+(ZaD+Zrad)/PHI^2);
Powin1=P^2/Zin1;
Powin2=P^2/Zin2;

%Frequency response
Vout1=PHI*Ze1*P/(((Zneck/Zcav)+1)*(ZaD+Zrad+PHI^2*Ze1)+Zneck);
%voltage generated by diaphragm on HR
Vout2=PHI*Ze2*P/(ZaD+Zrad+PHI^2*Ze2);
%voltage generated by diaphragm alone
Voutmax1=PHI*Ze1*Pmax/(((Zneck/Zcav)+1)*(ZaD+Zrad+PHI^2*Ze1)+Zneck);
%max voltage generated by diaphragm on HR
Voutmax2=PHI*Ze2*Pmax/(ZaD+Zrad+PHI^2*Ze2);
%max voltage generated by diaphragm alone

Sens1Open=PHI*Ze1/(((Zneck/Zcav)+1)*(ZaD+Zrad+PHI^2*Ze1)+Zneck);
%sensitivity of diaphragm on HR
Sens2Open=PHI*Ze1/(ZaD+Zrad+PHI^2*Ze1); %sensitivity of diaphragm alone
Sens1Short=PHI*Ze1short/(((Zneck/Zcav)+1)*(ZaD+Zrad+PHI^2*Ze1short)+Zneck);
%sensitivity of diaphragm on HR
Sens2Short=PHI*Ze1short/(ZaD+Zrad+PHI^2*Ze1short); %sensitivity of diaphragm alone

PA1=Zcav/(Zneck+Zcav);
Pow1=Vout1^2/Ze1;
Pow2=Vout2^2/Ze2;
PowAvail=P^2/Ztube;

Eff1=Pow1/Powin1;
Eff2=Pow2/Powin2;
PowMax1=Voutmax1^2/Ze1;
PowMax2=Voutmax2^2/Ze1;

bode(Vout1,Vout2);

F=linspace(0,7000,100);
W=2*pi*F;

V1=freqresp(Vout1,W);
V2=freqresp(Vout2,W);
VMAX1=freqresp(Voutmax1,W);
VMAX2=freqresp(Voutmax2,W);
P1=freqresp(Pow1,W);
P2=freqresp(Pow2,W);
POWMAX1=freqresp(PowMax1,W);
POWMAX2=freqresp(PowMax2,W);
PowIn1=freqresp(Powin1,W);
PowIn2=freqresp(Powin2,W);

```

```

ZIn1=freqresp(Zin1,W);
ZIn2=freqresp(Zin2,W);
ZIn2short=freqresp(Zin2short,W);
PAmp1=freqresp(PA1,W);
SENS1OPEN=freqresp(Sens1Open,W);
SENS2OPEN=freqresp(Sens2Open,W);
SENS1SHORT=freqresp(Sens1Short,W);
SENS2SHORT=freqresp(Sens2Short,W);
EFF1=freqresp(Eff1,W);
EFF2=freqresp(Eff2,W);
PHIarray=ones(length(F),1)*PHI;
PHIprimearray=ones(length(F),1)*PHIprime;
ZOUT1=freqresp(Zout1,W);
ZOUT2=freqresp(Zout2,W);

figure(2);
subplot(2,1,1)
semilogy(F,abs(V1(1,:)),F,abs(V2(1,:)));
axis tight;
xlabel('Frequency [Hz]');
ylabel('Mag(V_o_u_t) [V]');
subplot(2,1,2);
plot(F,angle(V1(1,:))*180/pi,F,angle(V2(1,:))*180/pi);
xlabel('Frequency [Hz]');
ylabel('Phase(V_o_u_t) [Deg]');
legend('with Helmholtz resonator','without Helmholtz resonator');

figure(3);
subplot(2,1,1)
semilogy(F,abs(P1(1,:)),F,abs(P2(1,:)));
axis tight;
xlabel('Frequency [Hz]');
ylabel('Mag(\pi_o_u_t) [W]');
subplot(2,1,2);
plot(F,angle(P1(1,:))*180/pi,F,angle(P2(1,:))*180/pi);
xlabel('Frequency [Hz]');
ylabel('Phase(\pi_o_u_t) [Deg]');
legend('with Helmholtz resonator','without Helmholtz resonator');

hold on;
figure(4);

subplot(2,1,1);
semilogy(F,real(ZOUT1(1,:)),F,real(ZOUT2(1,:)));
axis tight;
xlabel('Frequency [Hz]');
ylabel('Re(Z_o_u_t) [Ohms]');
subplot(2,1,2);
plot(F,imag(ZOUT1(1,:)),F,imag(ZOUT2(1,:)));
axis tight;
xlabel('Frequency [Hz]');
ylabel('Im(Z_o_u_t) [Ohms]');
legend('with Helmholtz resonator','without Helmholtz resonator');

figure(5)
subplot(2,1,1);
semilogy(F,abs(PowIn1(1,:)),F,abs(PowIn2(1,:)));

```

```

axis tight;
xlabel('Frequency [Hz]');
ylabel('Mag(\pi_i_n) [W]');
subplot(2,1,2);
plot(F,angle(PowIn1(1,:))*180/pi,F,angle(PowIn2(1,:))*180/pi);
axis tight;
xlabel('Frequency [Hz]');
ylabel('Phase(\pi_i_n) [Deg]');
legend('with Helmholtz resonator','without Helmholtz resonator');

figure(6);
subplot(2,1,1);
semilogy(F,abs(EFF1(1,:)),F,abs(EFF2(1,:)));
axis tight;
xlabel('Frequency [Hz]');
ylabel('Mag(Efficiency)');
subplot(2,1,2);
plot(F,angle(EFF1(1,:))*180/pi,F,angle(EFF2(1,:))*180/pi);
axis tight;
xlabel('Frequency [Hz]');
ylabel('Phase(Efficiency) [Deg]');
legend('with Helmholtz resonator','without Helmholtz resonator');

figure(7)
subplot(2,1,1)
semilogy(F,real(ZIn1(1,:)),F,real(ZIn2(1,:)));
axis tight;
xlabel('Frequency [Hz]')
ylabel('Input Impedance Real [kg/m^4*s]')
legend('with Helmholtz resonator','without Helmholtz resonator')
subplot(2,1,2);
plot(F,imag(ZIn1(1,:)),F,imag(ZIn2(1,:)));
axis tight;
xlabel('Frequency [Hz]')
ylabel('Input Impedance imag [kg/m^4*s]')
legend('with Helmholtz resonator','without Helmholtz resonator')

figure(8)
subplot(2,1,1);
semilogy(F,abs(PAmp1(1,:)));
xlabel('Frequency [Hz]');
ylabel('Magnitude [dB]');
subplot(2,1,2);
plot(F,angle(PAmp1(1,:))*180/pi);
xlabel('Frequency [Hz]');
ylabel('Phase [deg]');

figure(9);
semilogy(F,abs(SENS2OPEN(1,:)),F,abs(SENS2SHORT(1,:)),F,1./abs(PHIarray),F,abs(PHIprimearray));

figure(10)
semilogy(F,imag(ZOUT1(1,:)),F,imag(ZOUT2(1,:)));
axis tight;
xlabel('Frequency [Hz]')

```

```
ylabel('Output Impedance [kg/m^4*s]')
legend('with Helmholtz resonator','without Helmholtz resonator')
```

eh_setup.m

```
clear all;
%Constants

rho=1.165;      %density of air
mu=1.789E-5;   %viscosity of air
c=344;         %speed of sound in air
eps0=8.85E-12; %free-space permittivity

%Vent/Neck
L=3.18e-3;
r_neck=(4.72E-3)/2;
Leff=L+1.6*r_neck; %effective neck/vent length

%Resonator Cavity
r_cav=5E-3;
depth=2E-3;
area_cav=pi*r_cav^2;
volume=1950E-9;

%Piezo-Diaphragm
tsi = 3E-6; %thickness of silicon
R2 = 1.95E-3; % radius of silicon
%R2=3e-3;
tp = 0.6E-6; %thickness of piezo
%tp = 10e-6;
R1 = .95*R2; %inner radius of piezo

%Impedance tube
Atube=(1*2.54e-2)^2;
```

silicon_sweep.m

```
Esi = 169e9; %youngs modulus of shim
vsi = 0.3; %poissons ratio of shim
mu = 1; %const of proportionality of shear stress
vs shear strain
densitysi = 2500; %Density of the shim
```

platinum.m

```
%all distances in um
%http://www.webelements.com/webelements/elements/text/Ag/phys.html
Epl=170E9;
vpl=0.38;
tpl=170e-9;

densitypl=21440;
```

tio2.m

```
% tio2
%all distances in um
```

```

%http://www.webelements.com/webelements/elements/text/Ag/phys.html
E02=283E9;
v02=0.28;
t02=.1e-6;

```

```

density02=2150;
sigma02=1200e6;

```

piezo_sweep.m

```

%Material Properties of the piezo
%all distances in um
Ep          = 30e9;          %Youngs modulus of the piezo
vp          = 0.3;          %Poissons ratio of the piezo
material

d31         = -50e-12;      %electromechanical transduction
const of the piezo
densityp    = 7600;        %Density of the piezo
epsilon0    = 8.85E-12;    %permittivity of free space in F/m
dielectricconstant = 1000; %relative permittivity of the
piezo
epsilon=dielectricconstant*epsilon0; %absolute permittivity of the
piezo
sigmap      = 100E6;

```

initialise.m

```

num1 = 125;
r     = linspace(0,1,num1+1);
deltar= r(2)-r(1);
sr=size(r);
theta=zeros(sr);

```

totaldeflection_forP.m

```

%%% totaldeflection_forP.m %%%%%%%%%%%

P      = -PP;
V      = 0;
Ef     = V/tp;

%pressure loading only
abdpiezo; %Calculate the stiffness matrix A B
D
constants1234; %Obtain the constants c1 c2 c3 c5
solver1;
Wlp = w;

```

totaldeflection_forV.m

```

%%%%%%%% totaldeflection_forV.m %%%%%%%%%

V      = VV; %electric field in V
applied in direction 3(Z)

```

```

Ef    = V/tp;
P     = 0;

    %voltage loading only
    abdpiezo;                                %Calculate the stiffness
matrix A B D
    constants1234;                            %Obtain the constants c1
c2 c3 c5
    solver1;
    Wlv = w;

```

initialdeflection.m

```

P     = 0;
V     = 0;
Ef    = V/tp;

    %no pressure and voltage
    abdpiezo;                                %Calculate the stiffness matrix A B
D
    constants1234;                            %Obtain the constants c1 c2 c3 c5
    solver1;
    W0vp = w;

```

formmatrix_CMFa.m

```

%%%%%% formmatrix_CMFa.m %%%%%%%%%%%

% Intergrate the deflection to obtain energy, WW and total deflection
jj=floor(R21*num1)+1;
for i=1:num1+1
    rad1=r(i)*R2;
    if (i<jj+1)
        w_area(i)= Wi(i)*2*pi*rad1*R2/num1;
        ww(i)     = (tsi*densitysi +
t02*density02)*(Wi(i)^2)*rad1*R2/num1;
    else
        w_area(i)= Wi(i)*2*pi*rad1*R2/num1;
        ww(i)     =
(tp*densityp+densitysi*tsi+2*tpl*densitypl+t02*density02)*(Wi(i)^2)*rad
1*R2/num1;
    end;
end;

wwtot    = sum(ww);                            %Total w^2 over the radius
wtotal   = sum(w_area);                        %Total deflection area
weff     = wtotal/(pi*(R2^2));                 %Effective deflection

% Calculate the acoustical compliance, mass and frequency

Area     = pi*R2^2;                            % area of the
diaphragm
RlbyR2   = R1/R2;
CaD      = abs(wtotal/PP);                     % acoustical
compliance

```

```

MaD          = 2*pi*wwtot/(wtotal^2);           % acoustical
mass
FREQUENCY    = sqrt(1/(CaD*MaD))/2/pi;         % resonant
frequency

%R1byR2(index) = R21;                          % for the
graphs
Areap        = pi*(R2^2-R1^2);                 % area of the pzt layer
Cefp        = epsilon*pi*(R2^2-R1^2)/tp;

```

frommatrix_dA.m

```

%%%%%%%%% frommatrix_dA.m %%%%%%%%%%%%%%

% Intergrate the deflection to obtain energy, WW and total deflection
jj=floor(R21*num1)+1;
for i=1:num1+1
    rad1=r(i)*R2;
    if (i<jj+1)
        wv_area(i) = Wiv(i)*2*pi*rad1*R2/num1;
    else
        wv_area(i) = Wiv(i)*2*pi*rad1*R2/num1;
    end;
end;

Wvtotal      = sum(wv_area);                   %Total deflection area for voltage
loading

% Calculate the acoustical compliance, mass and frequency
dA = abs(Wvtotal/VV);                         %Effective deflection

```

abdpiezo.m

```

% Computing A,B,D for the central and annular paltres

% Constitutive Relations for isotropic circular plates
Qsi          = [1 vsi; vsi 1].*(Esi/(1-(vsi^2)));
Q02          = [1 v02; v02 1].*(E02/(1-(v02^2)));
Qp           = [1 vp; vp 1].*(Ep/(1-(vp^2)));
Qp1          = [1 vpl; vpl 1].*(Epl/(1-(vpl^2)));

% Taking the original zxis as centre of the shim layer for

zin1 = -tsi/2 ;                               %distance of bottom of shim layer
from reference
zin2 = tsi/2 ;                                 %distance of interface from
reference
zin3 = t02 + tsi/2;

zout1 = -tsi/2 ;                              %distance of top of the piezo
layer from reference
zout2 = tsi/2;
zout3 = t02 + tsi/2;
zout4 = t02 + tpl + tsi/2;
zout5 = t02 + tpl + tp + tsi/2;

```

```

zout6 = t02 + tpl + tp + tpl + tsi/2;

% A B D Matrixs for inner and outer
A_in = Qsi.*(zin2-zin1) + Q02.*(zin3-zin2);
B_in = Qsi.*((zin2^2-zin1^2)/2) + Q02.*((zin3^2-zin2^2)/2);
D_in = Qsi.*((zin2^3-zin1^3)/3) + Q02.*((zin3^3-zin2^3)/3);

A_out = Qsi.*(zout2-zout1) + Q02.*(zout3-zout2) +
Qpl.*(zout4-zout3) + Qp.*(zout5-zout4) + Qpl.*(zout6-
zout5);
B_out = Qsi.*((zout2^2-zout1^2)/2) + Q02.*((zout3^2-zout2^2)/2) +
Qpl.*((zout4^2-zout3^2)/2)+ Qp.*((zout5^2-zout4^2)/2)+Qpl.*((zout6^2-
zout5^2)/2);
D_out = Qsi.*((zout2^3-zout1^3)/3) + Q02.*((zout3^3-zout2^3)/3) +
Qpl.*((zout4^3-zout3^3)/3)+ Qp.*((zout5^3-zout4^3)/3)+Qpl.*((zout6^3-
zout5^3)/3);

% Computing D Mark(determinant of matrix mapping defined variables
y1,y2 to U0 theta
Dstar_in = D_in(1,1)-(B_in(1,1)^2)/A_in(1,1);
Dstar_out = D_out(1,1)-(B_out(1,1)^2)/A_out(1,1);

% Computing fictitious forces due to piezo
Mp_in = 0;
Np_in = 0;
Mp_out = -Ef* (Ep/(1-vp)) * d31 * (zout5^2-zout4^2)/2;
Np_out = -Ef* (Ep/(1-vp)) * d31 * (zout5-zout4);

constants1234.m

%%%% constants1235.m %%%%%%%%%%

k_in = sqrt(N_in*(R1^2)/Dstar_in);
k_out = sqrt(N_out*(R2^2)/Dstar_out);
a_R = R1/R2;
b_jy = besseli(1,k_out)/besselk(1,k_out);
Gamma_out = B_out(1,1)/A_out(1,1);
Gamma_in = B_in(1,1)/A_in(1,1);

AB11_in = -(Gamma_in*A_in(1,1)-B_in(1,1))*k_in/2/R1;
AB11_out = -(Gamma_out*A_out(1,1)-B_out(1,1))*k_out/2/R2;
AB12_in = -(Gamma_in*A_in(1,2)-B_in(1,2))/R1;
AB12_out = -(Gamma_out*A_out(1,2)-B_out(1,2))/R1;
BD11_in = -(Gamma_in*B_in(1,1)-D_in(1,1))*k_in/2/R1;
BD11_out = -(Gamma_out*B_out(1,1)-D_out(1,1))*k_out/2/R2;
BD12_in = -(Gamma_in*B_in(1,2)-D_in(1,2))/R1;
BD12_out = -(Gamma_out*B_out(1,2)-D_out(1,2))/R1;

x_p = P*R2/2/N_out/besselk(1,k_out);

% Compute the matrix
A11 = besselj(1,k_in);
A12 = 0;
A13 = b_jy*besselk(1,k_out*a_R) - besseli(1,k_out*a_R);
A14 = 0;

```

```

A21 = -Gamma_in*besselj(1,k_in) ;
A22 = R1;
A23 = (-b_jy*besselk(1,k_out*a_R) + besseli(1,k_out*a_R))*Gamma_out;
A24 = R1*(1/(a_R^2)-1);
A31 = AB11_in*(besselj(0,k_in) - besselj(2,k_in)) +
AB12_in*besselj(1,k_in);
A32 = A_in(1,1)+A_in(1,2);
A33 = -
AB11_out*((besseli(0,k_out*a_R)+besseli(2,k_out*a_R))+b_jy*(besselk(0,k
_out*a_R)+besselk(2,k_out*a_R))) - ...
    AB12_out*(besseli(1,k_out*a_R)-b_jy*besselk(1,k_out*a_R)) ;
A34 = A_out(1,2)*(1/(a_R^2)-1) - A_out(1,1)*(1+1/(a_R^2));
A41 = BD11_in*(besselj(0,k_in)-besselj(2,k_in)) +
BD12_in*besselj(1,k_in);
A42 = B_in(1,1) + B_in(1,2) ;
A43 = -
BD11_out*((besseli(0,k_out*a_R)+besseli(2,k_out*a_R))+b_jy*(besselk(0,k
_out*a_R)+besselk(2,k_out*a_R))) - ...
    BD12_out*(besseli(1,k_out*a_R)-b_jy*besselk(1,k_out*a_R)) ;
A44 = B_out(1,2)*(1/(a_R^2)-1) - B_out(1,1)*(1/(a_R^2) + 1);

b1 = -P*R2*besselk(1,k_out*a_R)/2/N_out/besselk(1,k_out) + P*R1/N_out/2
+ P*R1/2/N_in;
b2 = (P*R2*Gamma_out/2/N_out)*(besselk(1,k_out*a_R)/besselk(1,k_out)-
1/a_R);
b3 = x_p*AB11_out*(besselk(0,k_out*a_R)+besselk(2,k_out*a_R)) -
x_p*AB12_out*besselk(1,k_out*a_R) + (P/2/N_out)*(B_out(1,2)+ B_out(1,1)
...
+ (Gamma_out/(a_R^2))*(A_out(1,1)-A_out(1,2))) +
(P/2/N_in)*(B_in(1,1)+B_in(1,2)) - Np_out + Np_in + (N_out);
b4 = x_p*BD11_out*(besselk(0,k_out*a_R)+besselk(2,k_out*a_R)) -
x_p*BD12_out*besselk(1,k_out*a_R) + (P/2/N_out)*(D_out(1,2)+D_out(1,1)
+ ...
(Gamma_out/(a_R^2))*(B_out(1,1)-B_out(1,2)))
+(P/2/N_in)*(D_in(1,1)+D_in(1,2)) - Mp_out + Mp_in +
(N_out)*(tp+tsi)/2;

A = [A11 A12 A13 A14; A21 A22 A23 A24; A31 A32 A33 A34; A41 A42 A43
A44];
b = [b1 b2 b3 b4]';

c1234 = inv(A)*b;

c1=c1234(1);
c2=c1234(2);
c3=c1234(3);
c4=c1234(4);

```

solver1.m

```

% Composite plates;

% Computing deflections and Forces at the interface by superposition
% Finding Deflection in the central region and the annular region

sr=size(r);

```

```

w=zeros(sr);

jj=floor(R21*num1)+1;
for i=1:num1+1
    rad1=r(i)*R2;
    if (i<jj+1)
        w(i) = c1*R1*(besselj(0,k_in*rad1/R1)-besselj(0,k_in))/k_in +
P*((rad1^2)-(R1^2))/4/N_in - P*((R1^2)-(R2^2))/4/N_out - ...
        c3*R2*(besseli(0,k_out*a_R) - besseli(0,k_out) +
b_jy*(besselk(0,k_out*a_R)-besselk(0,k_out)))/k_out -...
        P*(R2^2)*(besselk(0,k_out*a_R)-
besselk(0,k_out))/2/k_out/N_out/besselk(1,k_out);
        u0(i) = c2*rad1 - Gamma_in*c1*besselj(1,k_in*rad1/R1);
    else
        w(i) = -c3*R2*(b_jy*besselk(0,k_out*rad1/R2) +
besseli(0,k_out*rad1/R2) - b_jy*besselk(0,k_out) -
besseli(0,k_out))/k_out - ...
        P*((rad1^2)-(R2^2))/4/N_out - P*(R2^2)*(besselk(0,
k_out*rad1/R2)-besselk(0,k_out))/k_out/2/N_out/besselk(1,k_out) ;
        u0(i) = c4*(rad1-(R2^2)/rad1) -
Gamma_out*(besseli(1,k_out*rad1/R2) - b_jy*besselk(1,k_out*rad1/R2))*c3
        + ...

(P*Gamma_out*R2/2/N_out)*(besselk(1,k_out*rad1/R2)/besselk(1,k_out)-
R2/rad1);
    end;
end;

```

APPENDIX B
DETAILED PROCESS FLOW

Energy Harvester - Process Traveler

Table B-1: Process Traveler

Wafer	4" n-type <100> SOI	6	wafers
<u>Step #</u>	<u>Lab/Equip</u>	<u>Process Description</u>	
0	-	Start with SOI wafer with 4000 Å oxide + 12 μm of silicon overlayer.	
1.1	Sandia National Labs (SNL)	Reduce silicon overlayer using KOH (~1.7 μm/min) and HNA (~2.6 μm/min) etches. KOH: (Temp ~ 85 °C) 3 wafers → 320 s etch → expected thickness of Si = 2.933 μm 2 wafers → 270 s etch → expected thickness of Si = 4.350 μm 3 wafers → 212 s etch → expected thickness of Si = 5.993 μm HNA: Recipe → 160 ml acetic acid, 60 ml nitric acid, 20 ml hydrofluoric acid 1 wafer → 211 s etch → expected thickness of Si = 2.86 μm 1 wafer → 176 s etch → expected thickness of Si = 4.37 μm	
1.3	SNL	Deposit 100 nm Ti Temescal BJD-1800 Evaporator (modified) Conditions: $P_{am} = 2.1(10)^7 - 2.3(10)^7 \text{ Torr}$ Ti deposition rate = 3 Å/sec Total thickness = 1000Å	
1.4	SNL	Oxidize in tube furnace at 650 C for 30 mins with dry O ₂ ambient to form TiO ₂	
2.1	SNL	spin positive photoresist (Clariant AZP4330-RS) on back surface (1μm) - positive resist and pattern backside alignment marks, (BS_Metal) Mask - DARK FIELD - evaporated HMDS onto wafer for adhesion - spin @ 4000 RPM for 30 s - baked @ 90 °C for 90 s on hot plate yields 3.75 μm thick resist	
2.2	SNL	Sputter deposit 15 nm of Cr on backside followed by 40 nm of Pt Conditions: $P_{am} = 6.3(10)^{-7} \text{ Torr}$ Deposition rate = 3 Å/sec	

- 2.3 SNL Strip resist in Acetone for 2 min to liftoff Cr
Ash resist residue in Oxygen plasma stripper
- 2.4 SNL spin negative photoresist (JSR) on front surface (1 μ m) - **negative resist**
and pattern bottom electrode, (ElectrodeBot) Mask - **DARK FIELD**
- spin @ **3000 RPM** for **30 s**
 - bake @ **120°C** for 1 min
 - pattern and expose (**Front to back alignment**) using Karl Suss MA6/BA6 Backside Aligner
 - develop in AZ400K for **90 s**
 - bake @ **100°C** for **45 s**
 - descum in Oxygen plasma (PDS/PDE-301) for **5 min**
- 2.5 SNL Evaporate **30 nm** of Ti in Temescal BJD-1800 Evaporator for adhesion of Pt to TiO₂ @ 3 Å/sec for 100 s.
- 2.6 SNL Evaporate **170 nm** of Pt in Temescal BJD-1800 @ 2.5 Å/sec for 680 s.
- 2.7 SNL Strip resist to liftoff Ti/Pt in acetone
- 3.1 SNL Spin coat 52/48 PZT solution @ **3000 RPM** for **30 sec**
- 3.2 SNL Pyrolize @ **300 C** for **5 min** on a hot-plate in an air ambient
- 3.3 SNL Repeat spin/pyrolize **4 times** to achieve **400 nm** thick PZT
- 3.4 SNL Furnace anneal at **650 C** for **30 min**
- 4.1 SNL spin negative photoresist (JSR) on front surface (1 μ m) - **negative resist**
and pattern top electrode, (ElectrodeTop) Mask - **DARK FIELD**
- spin @ **3000 RPM** for **30 s**
 - bake @ **120°C** for 1 min
 - pattern and expose (**Front to back alignment**) using Karl Suss MA6/BA6 Backside Aligner
 - develop in AZ400K for **90 s**
 - bake @ **100°C** for **45 s**
 - descum in Oxygen plasma (PDS/PDE-301) for **5 min**
- 4.2 SNL Deposit **180 nm** Pt in Temescal BJD-1800
@ 2.5 Å/sec for 720 s.
- 4.3 SNL Strip resist to liftoff Pt in acetone
- 5.1 *Army Research Lab (ARL)* Etch PZT in 3:1:1 ammonium bifluoride/hydrochloric acid/DI water
uses Pt top electrode as etch mask
- 5.2 *ARL* Etch PZT residues left behind by previous etch
dilute nitric acid/hydrogen peroxide etchant
- 6.1 *UF* Spin thick photoresist on backside - **positive resist**
and pattern cavity, (Cavity) Mask - **DARK FIELD**
- 6.2 *UF* Plasma etch (DRIE) **500 um** of silicon from backside

stops on BOX layer (STS MESC Multiplex ICP)

- 6.3 UF Strip resist in acetone.
- 6.4 UF Etch oxide (BOE) on backside to remove oxide mask and BOX

Graphical Representation of Process Flow

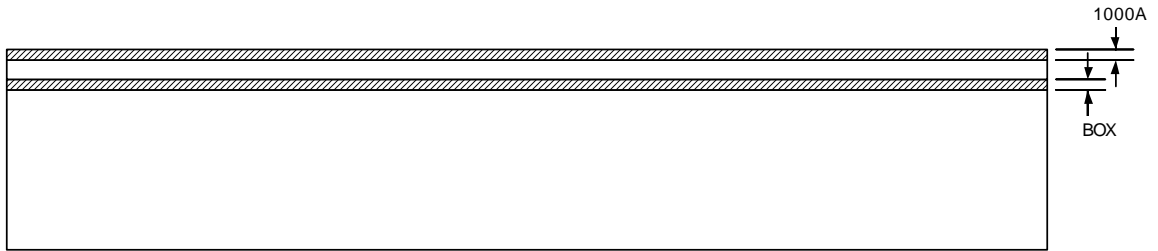


Figure B-1: Step 1: Deposit Ti on SOI Wafer and oxidize to TiO₂.

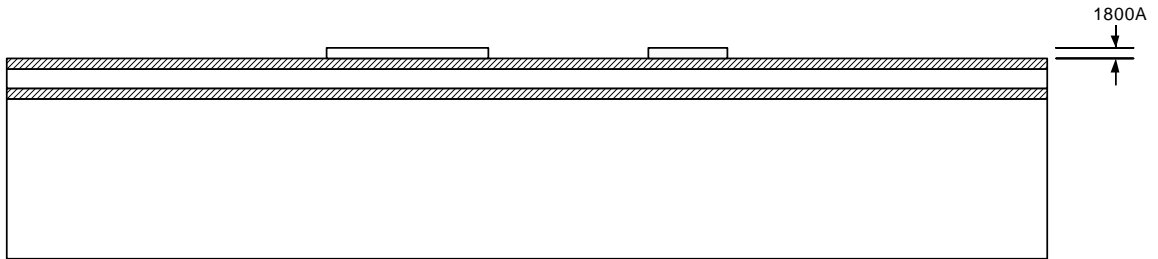


Figure B-2: Step 2: Deposit Ti/Platinum(30nm/170nm) -Lift-Off w/ Mask (ElectrodeBot).

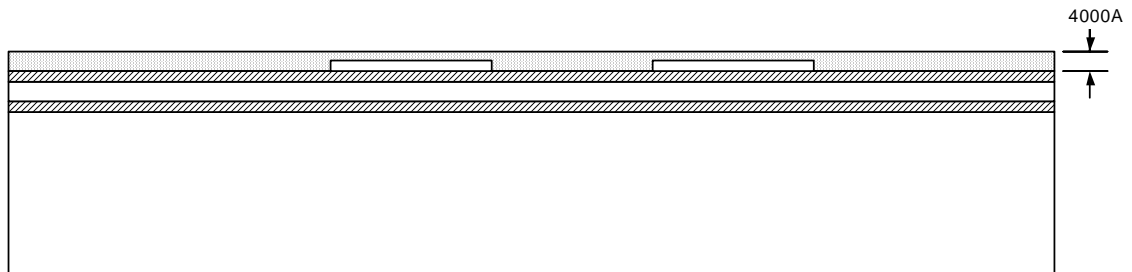


Figure B-3: Step 3: Spin PZT - 6 times to achieve desired thickness.

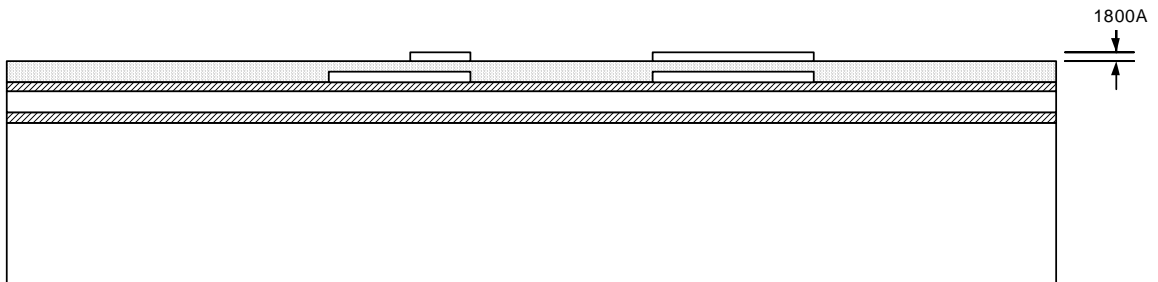


Figure B-4: Step 4: Deposit Platinum(180nm)-Lift-off w/ Mask (ElectrodeTop).

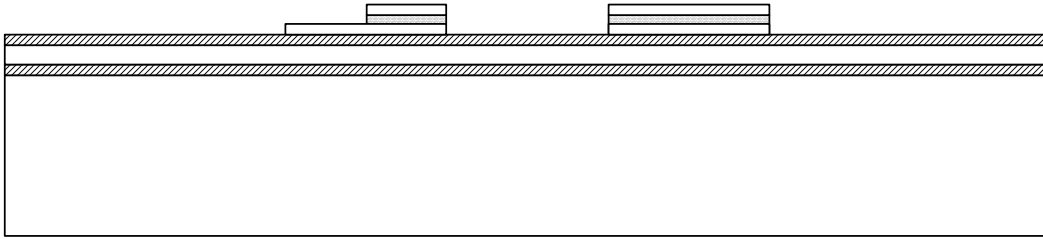


Figure B-5: Step 5: Wet Etch PZT using Pt as etch mask.

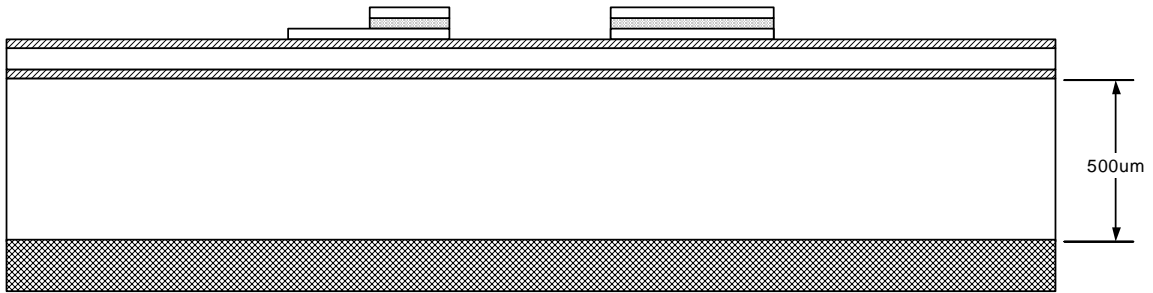


Figure B-6: Step 6.1: Spin thick photo resist on bottom (7um).

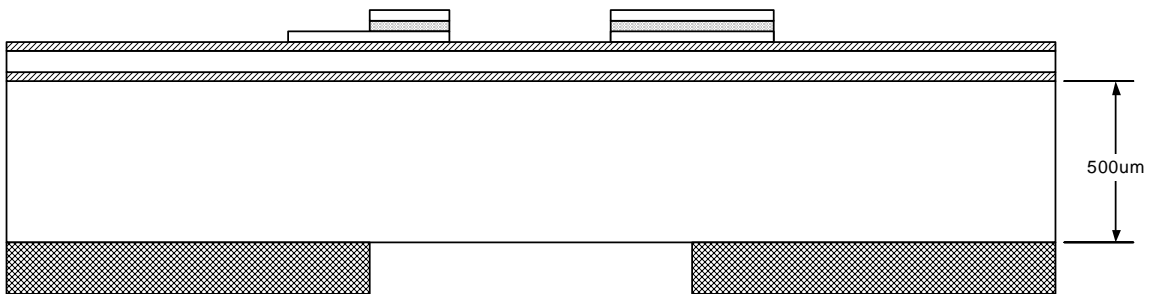


Figure B-7: Step 6.2: Pattern using mask (Cavity).

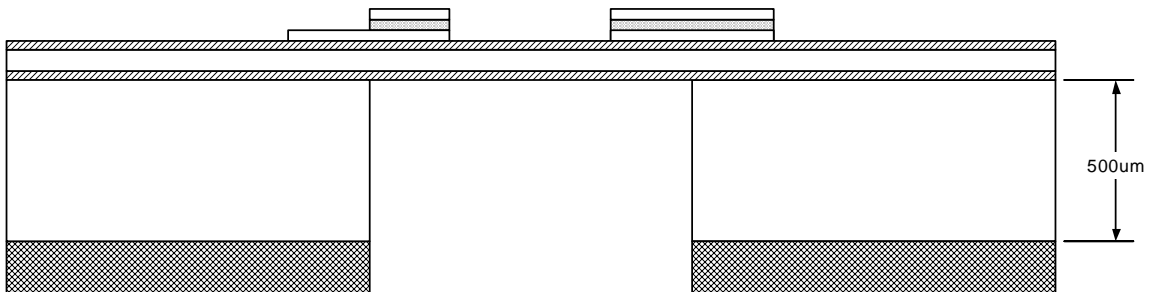


Figure B-8: Step 6.3: DRIE to BOX

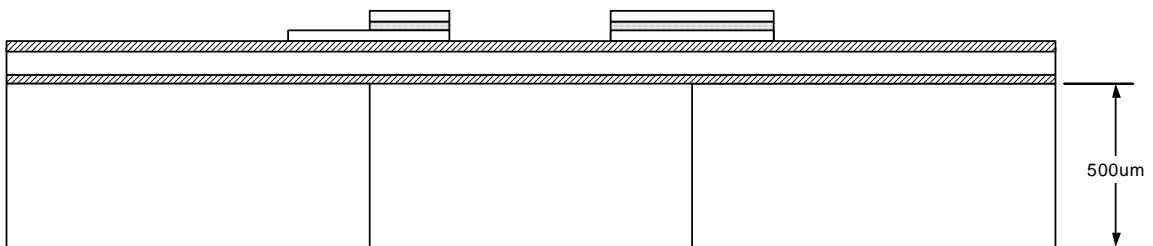


Figure B-9: Step 6.4: Ash Resist.

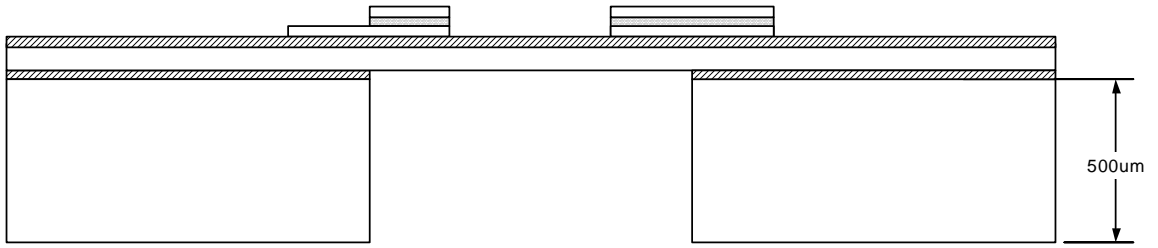


Figure B-10: Step 6.5: BOE backside to remove oxide.

Mask Layouts

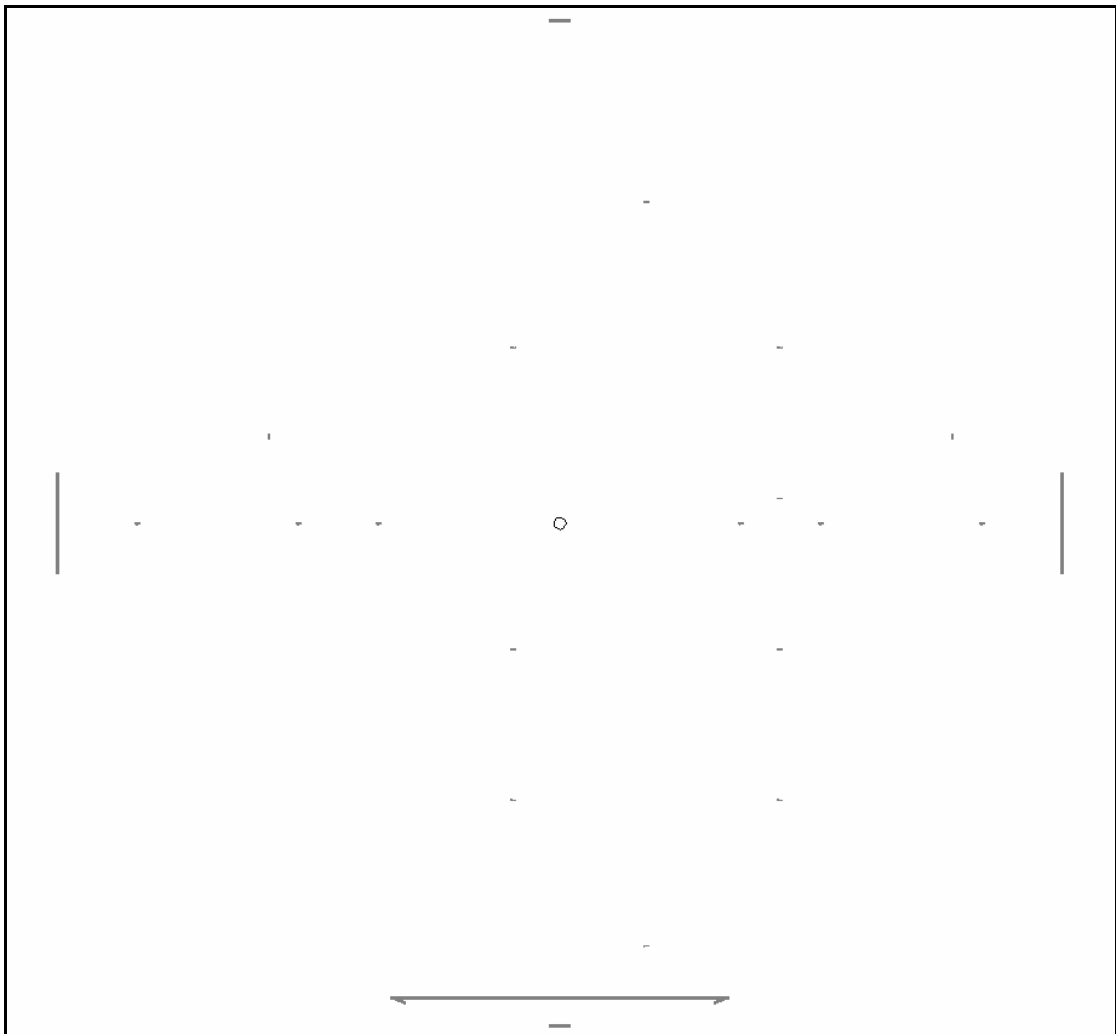


Figure B-11: Backside metal mask

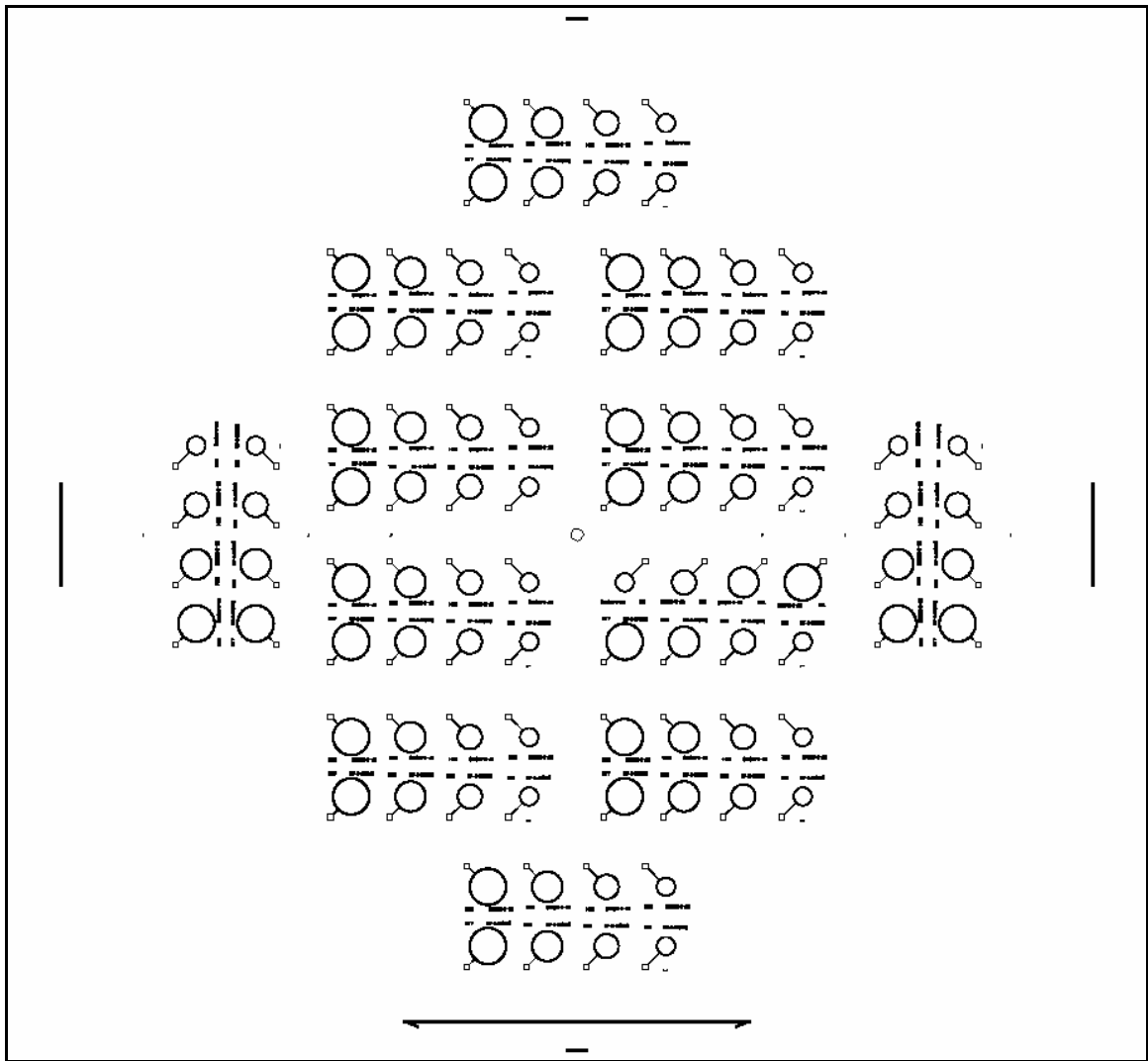


Figure B-12: Bottom electrode mask

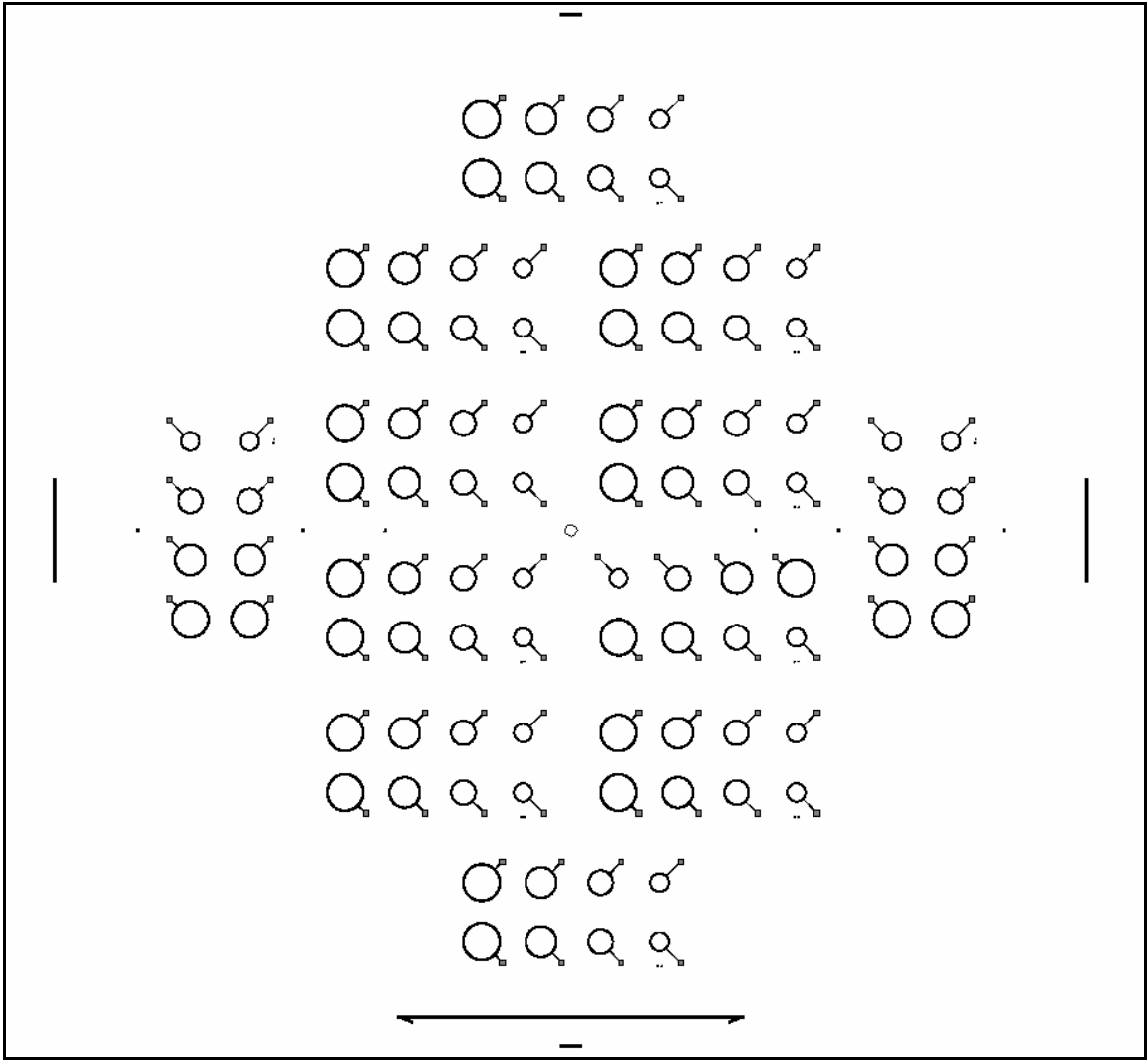


Figure B-13: Top electrode mask

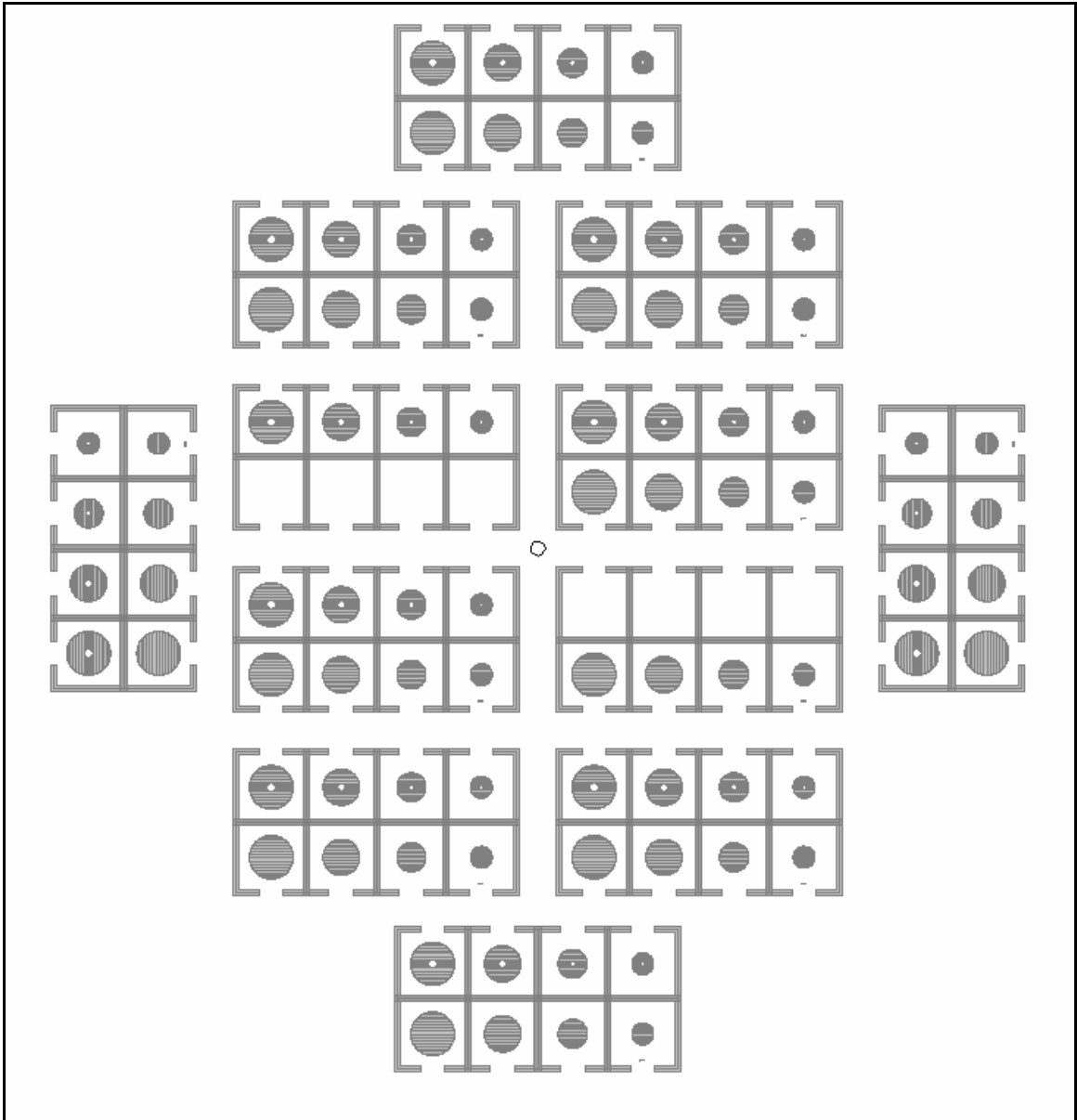
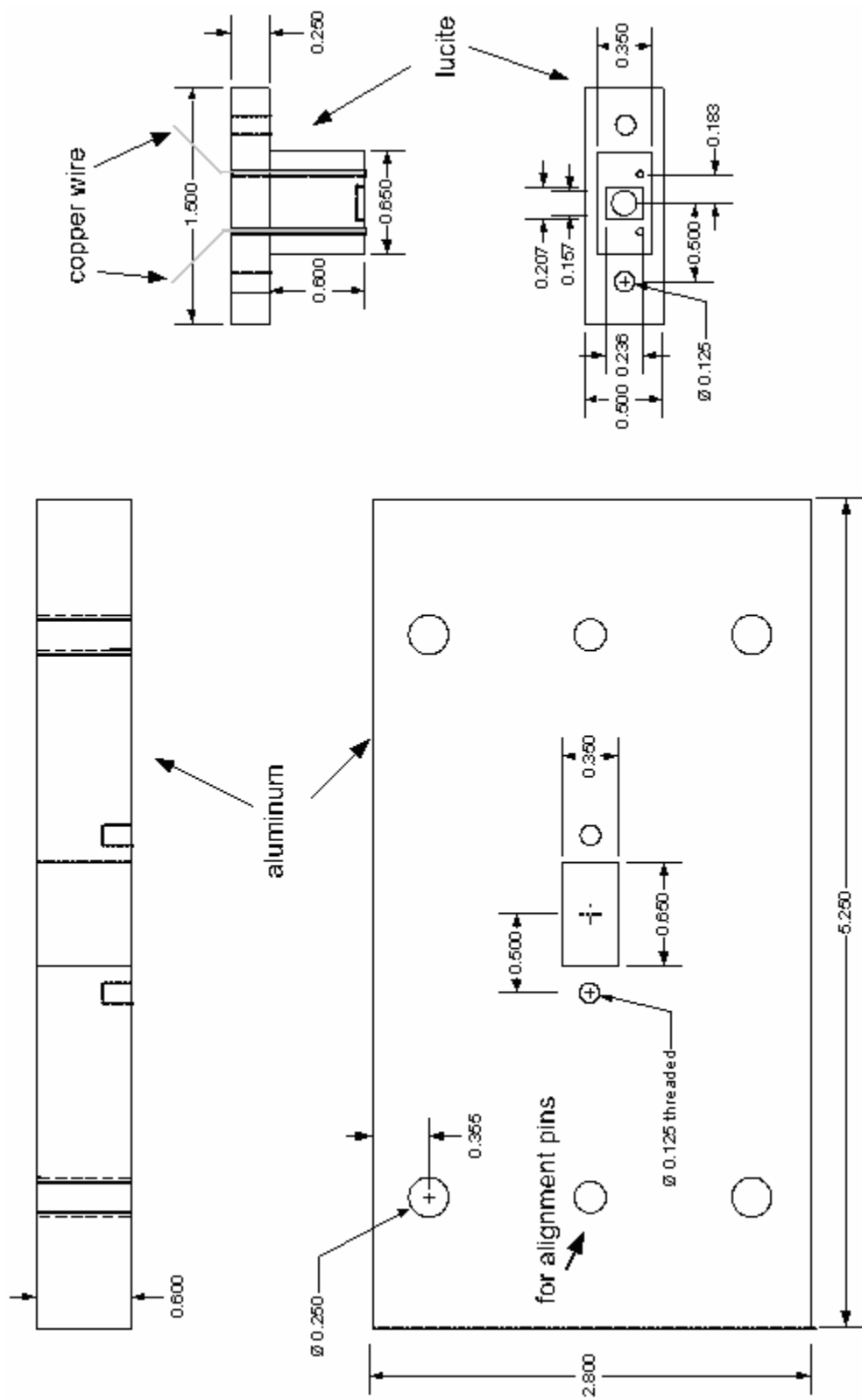


Figure B-14: Cavity mask



EH Package #2

all dimensions are inches

Figure B-16: Detailed schematic of sealed cavity package and mounting plate.

LIST OF REFERENCES

1. M. Rossi, *Acoustics and Electroacoustics*, Artech House: Norwood, MA, p. 245-308. 1988.
2. D.T. Blackstock, *Fundamentals of Physical Acoustics*, John Wiley & Sons, Inc.: New York, p. 153-156. 2000.
3. P. Smalser, *Power Transfer of Piezoelectric Generated Energy*, USA: Ocean Power Technologies, West Trenton, NJ, 1997, #5,703,474.
4. J. Kymissis, C. Kendall, J. Paradiso, and N. Gershenfeld. "Parasitic Power Harvesting in Shoes." in *2nd International Symposium on Wearable Computers*, Pittsburgh, Pennsylvania p. 132-139, 1998.
5. W.G. Cady, *Piezoelectricity*, Dover Publications, Inc.: New York, p. 1-8. 1964.
6. N. Setter, ed. *Piezoelectric Materials in Devices*. N. Setter, EPFL Swiss Federal Institute of Technology: Lausanne. 2002.
7. J. Baborowski, "Microfabrication of Piezoelectric MEMS." *Journal of Electroceramics*. **12**: p. 33-51, 2004.
8. M.-A. Dubois and P. Muralt, "Measurement of the Effective Transverse Piezoelectric Coefficient e_{31} of AlN and Pb(Zr,Ti)O₃ Thin Films." *Sensors and Actuators, A: Physical*. **77**(2): p. 106-112, 1999.
9. D.L. DeVoe, "Piezoelectric Thin Film Micromechanical Beam Resonators." *Sensors and Actuators, A: Physical*. **88**(3): p. 263-272, 2001.
10. D.L. DeVoe and A.P. Pisano, "Surface Micromachined Piezoelectric Accelerometers (Pixls)." *Journal of Microelectromechanical Systems*. **10**(2): p. 180-186, 2001.
11. C.H. Han and E.S. Kim. "Micromachined Piezoelectric Ultrasonic Transducers Based on Parylene Diaphragm in Silicon Substrate." in *IEEE International Ultrasonic Symposium*, San Juan, Puerto Rico p. 919-923, 2000.

12. B.L. Lee, K.H. Lee, and B.K. Ju, "Compositional Dependence of the Properties of Ferroelectric Pb(Zr,Ti)O₃ Thin Film Capacitors Deposited on Single-Layered Pt-Rh Electrode Barriers." *Ceramics International*. **30**(7): p. 1543-1546, 2004.
13. K.T. Kim, C.I. Kim, and S.G. Lee, "Ferroelectric Properties of Pb(Zr,Ti)O₃ Heterolayered Thin Films for FRAM Applications." *Microelectronic Engineering*. **66**(1-4): p. 662-669, 2003.
14. G.R. Fox, F. Chu, and T. Davenport, "Current and Future Ferroelectric Nonvolatile Memory Technology." *Journal of Vacuum Science and Technology, Part B: Microelectronics and Nanometer Structures*. **19**(5): p. 1967-1971, 2001.
15. P. Verardi, M. Dinescu, and F. Craciun, "Pulsed Laser Deposition and Characterization of PZT Thin Films." *Applied Surface Science*. **154-155**: p. 514-518, 2000.
16. R.N. Castellano and L.G. Feinstein, "Ion-Beam Deposition of Thin Films of Ferroelectric Lead Zirconate Titanate (PZT)." *Journal of Applied Physics*. **50**(6): p. 4406-11, 1979.
17. K. Sreenivas, M. Sayer, and P. Garrett, "Properties of D.C. Magnetron-Sputtered Lead Zirconate Titanate Thin Films." *Thin Solid Films*. **172**: p. 251-67, 1989.
18. L. Blossfeld, W.L. Larson, L. Kammerdiner, B.T. Banko, and C.E. Wickersham, "Ferroelectric Pb(Zr,Ti)O₃ Thin Films by Reactive Sputtering from a Metallic Target." *Vacuum*. **41**(4-6): p. 1428-30, 1990.
19. M. Huffman, J.P. Goral, M.M. Al-Jassim, A.R. Mason, and K.M. Jones, "Compositional and Microstructural Characterization of Thin Film Lead Zirconate Titanate Ferroelectrics." *Thin Solid Films*. **193-4**(1): p. 1017-22, 1990.
20. Z. Surowiak, M. Lopuszko, I.N. Zakharchenko, A.A. Bakirov, E.A. Marchenko, E.V. Sviridov, V.M. Mukhortov, and V.P. Dudkevich, "Thin Ferroelectric Films of the Lead Zirconate-Titanate Type Obtained by R.F. Sputtering." *Thin Solid Films*. **205**: p. 76-84, 1991.
21. Z. Surowiak, D. Czekaj, A.M. Margolin, E.V. Sviridov, V.A. Aleshin, and V.P. Dudkevich, "The Structure and the Piezoelectric Properties of Thin Pb(Zr,Ti)O₃ Films." *Thin Solid Films*. **214**: p. 78-83, 1992.
22. S. Trolier-McKinstry, H. Hu, S.B. Krupanidhi, P. Chindaudom, K. Vedam, and R.E. Newnham, "Spectroscopic Ellipsometry Studies on Ion Beam Sputter Deposited Pb(Zr, Ti)O₃ Films on Sapphire and Pt-Coated Silicon Substrates." *Thin Solid Films*. **230**: p. 15-27, 1993.

23. S.-G. Yoon, H.-Y. Lee, and H.-G. Kim, "Compositional Analysis of Lead Titanate Thin Films by Auger Electron Spectroscopy and Their Electrical Properties." *Thin Solid Films*. **171**(2): p. 251-62, 1989.
24. T. Kawabata, M. Ikeda, H. Goto, M. Matsumoto, and T. Yada, "2-Dimensional Micro Scanner Integrated with PZT Thin Film Actuator." *International Conference on Solid-State Sensors and Actuators, Proceedings*. **1**: p. 339-342, 1997.
25. X.S. Li, K. Yamashita, T. Tanaka, Y. Suzuki, and M. Okuyama, "Structural and Electrical Properties of Highly Oriented Pb(Zr,Ti)O₃ Thin Films Deposited by Facing Target Sputtering." *Sensors and Actuators, A: Physical*. **82**(1): p. 265-269, 2000.
26. T. Kanda, T. Morita, M.K. Kurosawa, and T. Higuchi, "Flat Type Touch Probe Sensor Using PZT Thin Film Vibrator." *Sensors and Actuators, A: Physical*. **83**(1): p. 67-75, 2000.
27. T. Morita, M.K. Kurosawa, and T. Higuchi, "A Cylindrical Shaped Micro Ultrasonic Motor Utilizing PZT Thin Film (1.4 Mm in Diameter and 5.0 Mm Long Stator Transducer)." *Sensors and Actuators, A: Physical*. **83**: p. 225-230, 2000.
28. T. Morita, Y. Wagatsuma, H. Morioka, and H. Funakubo, "Ferroelectric Property of an Epitaxial Lead Zirconate Titanate Thin Film Deposited by a Hydrothermal Method." *Journal of the Material Research Society*. **19**(6): p. 1862-1868, 2004.
29. T. Morita and Y. Cho, "A Hydrothermally Deposited Epitaxial Lead Titanate Thin Film on Strontium Ruthenium Oxide Bottom Electrode." *Applied Physics Letters*. **85**(12): p. 2331-2333, 2004.
30. T. Morita, M. Kurosawa, and T. Higuchi, "Cylindrical Micro Ultrasonic Motor Fabricated by Improved Hydrothermal Method." *International Conference on Solid-State Sensors and Actuators, Proceedings*. **1**: p. 49-52, 1997.
31. D.F. Bahr, J.C. Merlino, P. Banerjee, C.M. Yip, and A. Bandyopadhyay, "Reliability and Properties of PZT Thin Films for MEMS Applications." *Materials Research Society Symposium - Proceedings*. **546**: p. 153-158, 1999.
32. J. Bernstein, K. Houston, L. Niles, S. Finberg, H. Chen, L.E. Cross, K. Li, and K. Udayakumar, "Micromachined Ferroelectric Transducers for Acoustic Imaging." *International Conference on Solid-State Sensors and Actuators, Proceedings*. **1**: p. 421-424, 1997.
33. B. Xu, L.E. Cross, and J. Bernstein, "Ferroelectric and Antiferroelectric Films for Microelectromechanical Systems Applications." *Thin Solid Films*. **377-378**: p. 712-718, 2000.

34. T. Itoh, J. Chu, I. Misumi, K. Kataoka, and T. Suga, "New Dynamic Scanning Force Microscopes Using Piezoelectric PZT Microcantilevers." *International Conference on Solid-State Sensors and Actuators, Proceedings*. **1**: p. 459-462, 1997.
35. C. Lee, T. Itoh, R. Maeda, and T. Suga, "Characterization of Micromachined Piezoelectric PZT Force Sensors for Dynamic Scanning Force Microscopy." *Review of Scientific Instruments*. **68**(5): p. 2091-2100, 1997.
36. J.M. Jungk, B.T. Crozier, A. Bandyopadhyay, N.R. Moody, and D.F. Bahr, "Mechanical Properties and Adhesion of PZT Thin Films for MEMS." *Materials Research Society Symposium - Proceedings*. **594**: p. 225-230, 2000.
37. K. Kunz, P. Enoksson, and G. Stemme, "Highly Sensitive Triaxial Silicon Accelerometer with Integrated PZT Thin Film Detectors." *Sensors and Actuators, A: Physical*. **92**(1-3): p. 156-160, 2001.
38. B. Piekarski, D.L. Devoe, R. Kaul, and M. Dubey. "Design, Modeling, and Testing of Micromachined Piezoelectric Clamped-Clamped Beam Resonators." in *Microelectromechanical Systems (MEMS) - ASME 2000*, 2000.
39. B. Piekarski, D. DeVoe, M. Dubey, R. Kaul, and J. Conrad, "Surface Micromachined Piezoelectric Resonant Beam Filters." *Sensors and Actuators, A: Physical*. **90**(3): p. 313-320, 2001.
40. J.S. Pulskamp, A. Wickenden, R. Polcawich, B. Piekarski, and M. Dubey, "Mitigation of Residual Film Stress Deformation in Multilayer Microelectromechanical Systems Cantilever Devices." *Journal of Vacuum Science and Technology, Part B: Microelectronics and Nanometer Structures*. **21**(6): p. 2482-2486, 2003.
41. A.T. Ferguson, L. Li, V.T. Nagaraj, B. Balachandran, B. Piekarski, and D.L. DeVoe, "Modeling and Design of Composite Free-Free Beam Piezoelectric Resonators." *Sensors and Actuators, A: Physical*. **118**: p. 63-69, 2005.
42. Y. Yee, H.-J. Nam, S.-H. Lee, J.U. Bu, and J.-W. Lee, "PZT Actuated Micromirror for Fine-Tracking Mechanism of High-Density Optical Data Storage." *Sensors and Actuators, A: Physical*. **89**(1-2): p. 166-173, 2001.
43. J.-C. Yu and C.-B. Lan, "System Modeling of Microaccelerometer Using Piezoelectric Thin Films." *Sensors and Actuators, A: Physical*. **88**(2): p. 178-186, 2001.
44. E. Zakar, M. Dubey, B. Piekarski, J. Conrad, R. Piekarz, and R. Widuta, "Process and Fabrication of a Lead Zirconate Titanate Thin Film Pressure Sensor." *Journal*

- of Vacuum Science and Technology, Part A: Vacuum, Surfaces and Films.* **19**(1): p. 345-348, 2001.
45. E. Zakar, M. Dubey, R. Polcawich, B. Piekarski, R. Piekarz, J. Conrad, and R. Widuta, "Study of PZT Film Stress in Multilayer Structures for MEMS Devices." *Materials Research Society Symposium - Proceedings.* **605**: p. 287-292, 2000.
 46. L.M.R. Eakins, B.W. Olson, C.D. Richards, R.F. Richards, and D.F. Bahr, "Influence of Structure and Chemistry on Piezoelectric Properties of Lead Zirconate Titanate in a Microelectromechanical Systems Power Generation Application." *Journal of the Material Research Society.* **18**(9): p. 2079-2086, 2003.
 47. S. Whalen, M. Thompson, D.F. Bahr, C.D. Richards, and R.F. Richards, "Design, Fabrication and Testing of the P3 Micro Heat Engine." *2003.* **104**: p. 290-298, 2003.
 48. S. Zurn, M. Hsieh, G. Smith, D. Markus, M. Zang, G. Hughes, Y. Nam, M. Arik, and D. Polla, "Fabrication and Structural Characterization of a Resonant Frequency PZT Microcantilever." *Smart Materials and Structures.* **10**(2): p. 252-263, 2001.
 49. T. Shiosaki and A. Kawabata, "Piezoelectric Thin Films for Saw Applications." *Ferroelectrics.* **42**(1-4): p. 219-232, 1982.
 50. M. Royer, J.O. Holmen, M.A. Wurm, and O.S. Aadland, "Zno on Si Integrated Acoustic Sensor." *Sensors and Actuators, A: Physical.* **4**: p. 357-362, 1983.
 51. H.N. Al-Shareef, K.R. Bellur, O. Auciello, X. Chen, and A.I. Kingon, "Effect of Composition and Annealing Conditions on the Electrical Properties of Pb(ZrTi)O₃ Thin Films Deposited by the Sol-Gel Process." *Thin Solid Films.* **252**: p. 38-43, 1994.
 52. P.F. Indermuhle, G. Schurmann, G.A. Racine, and N.F. de Rooij, "Tip Integration on Arrays of Silicon Micro Cantilevers with Self Exciting Piezoelectric Sensor for Parallel Atomic Force Microscopy Applications." *International Conference on Solid-State Sensors and Actuators, Proceedings.* **v 1**: p. 451-453, 1997.
 53. S. Butterworth, *Proceedings of the Physical Society.* **27**: p. 410-24, 1915.
 54. K.S. Van Dyke, "The Electrical Network Equivalent of a Piezoelectric Resonator." *Physical Review.* **40**: p. 1026, 1932.
 55. K.S. Van Dyke, "The Electric Network Equivalent of a Piezoelectric Resonator." *Physical Review.* **25**: p. 895, 1925.

56. K.S. Van Dyke, "The Piezoelectric Resonator and Its Equivalent Network." *Institute of Radio Engineers (IRE) Proc.* **16**: p. 742-64, 1928.
57. D.W. Dye, "Piezoelectric Quartz Resonator and Equivalent Electrical Circuit." *Proceedings of the Physical Society.* **38**: p. 399-458, 1926.
58. W.P. Mason, "An Electromechanical Representation of Piezoelectric Crystal Used as a Transducer." *Institute of Radio Engineers (IRE) Proc.* **23**: p. 1252-1263, 1935.
59. W.P. Mason, *Piezoelectric Crystals and Their Application to Ultrasonics*. The Bell Telephone Laboratories Series, D. Van Nostrand Company, Inc.: New York. 1950.
60. F.A. Fischer, *Fundamentals of Electroacoustics*, Interscience Publishers, Inc.: New York, p. 21-22. 1955.
61. Y.S. Cho, Y.E. Pak, H.M. Jeong, and S.K. Ha, "Five-Port Equivalent Electric Circuit of Piezoelectric Bimorph Beam." *Proceedings of SPIE - The International Society for Optical Engineering.* **3673**: p. 261-277, 1999.
62. G. Wang, *Modeling and Design of a MEMS-Based Piezoelectric Microphone*, in *Mechanical and Aerospace Engineering*. 2003, University of Florida: Gainesville, FL. Last accessed
63. G. Wang, B.V. Sankar, L. Cattafesta, and M. Sheplak. "Analysis of a Composite Piezoelectric Circular Plate with Initial Stresses for MEMS,." in *International Mechanical Engineering Congress & Exposition*, New Orleans, LA: ASME Paper IMECE2002-39337, 2002.
64. S.A.N. Prasad, B.V. Sankar, L.N. Cattafesta, S.B. Horowitz, Q. Gallas, and M. Sheplak. "Two-Port Electroacoustic Model of an Axisymmetric Piezoelectric Composite Plate." in *43rd AIAA/ASME/ASCE/AHS/ASC Structures, Structural Dynamics, and Materials Conference*, Denver, CO, 2002.
65. Y.S. Cho, Y.E. Pak, C.S. Han, and S.K. Ha, "Five-Port Equivalent Electric Circuit of Piezoelectric Bimorph Beam." *Sensors and Actuators, A: Physical.* **84**(1): p. 140-148, 2000.
66. C. Liang, Sun, Fanping, Rogers, Craig A., "Electro-Mechanical Impedance Modeling of Active Material Systems." *Smart Materials and Structures.* **5**: p. 171-186, 1996.
67. C. Liang, Sun, F.P., Rogers, C.A., "An Impedance Method for Dynamic Analysis of Active Material Systems." *Journal of Vibration and Acoustics.* **116**: p. 120-128, 1994.

68. G.E. Martin, "Determination of Equivalent-Circuit Constants of Piezoelectric Resonators of Moderately Low Q by Absolute-Admittance Measurements." *The Journal of the Acoustical Society of America*. **26**(3): p. 413-420, 1954.
69. S. Sherrit, H.D. Wiederick, B.K. Mukherjee, and M. Sayer, "Accurate Equivalent Circuit for the Unloaded Piezoelectric Vibrator in the Thickness Mode." *Journal of Physics D: Applied Physics*. **30**(16): p. 2354-2363, 1997.
70. S. Sherrit, Wiederick, H.D., Mukherjee, B.K. "Accurate Equivalent Circuits for Unloaded Piezoelectric Resonators." in *IEEE Ultrasonics Symposium*, Toronto, Can.: IEEE p. 931-935, 1997.
71. S. Lin, "Analysis of the Equivalent Circuit of Piezoelectric Ceramic Disk Resonators in Coupled Vibration." *Journal of Sound and Vibration*. **231**(2): p. 277-290, 2000.
72. D.P. Chen, S. Jen, and C.S. Hartmann, "Resonant Modes in Coupled Resonator Filters and the Unique Equivalent Circuit Representation." *Proceedings of the IEEE Ultrasonics Symposium*. **1**: p. 59-62, 1995.
73. Q. Meng, M. Mehregany, and K. Deng, "Modeling of the Electromechanical Performance of Piezoelectric Laminated Microactuators." *Journal of Micromechanics and Microengineering*. **3**(1): p. 18-23, 1993.
74. P. Seshu and N.G. Naganathan, "Analysis of Strain Induced in Piezoelectric Actuated Beams." *Proceedings of SPIE - The International Society for Optical Engineering*. **2715**: p. 658-669, 1996.
75. H.T. Banks, Smith, R.C., Wang, Yun, "The Modeling of Piezoceramic Patch Interactions with Shells, Plates, and Beams." *Quarterly of Applied Mathematics*. **53**(2): p. 353-381, 1995.
76. S.H. Chang and B.C. Du, "Optimization of Asymmetric Bimorphic Disk Transducers." *The Journal of the Acoustical Society of America*. **109**(1): p. 194-202, 2001.
77. C.C. Cheng and P.W. Wang, "Applications of the Impedance Method on Multiple Piezoelectric Actuators Driven Structures." *Journal of Vibration and Acoustics*. **123**: p. 262-268, 2001.
78. J.L. Delany, "Bender Transducer Design and Operation." *The Journal of the Acoustical Society of America*. **109**(2): p. 554-562, 2000.
79. E.M. Flint, Rogers, Craig A., Liang, Chen, "Electro-Dynamic Transduction Equations for Piezoelectric Stack Actuators." *Adaptive Structures and Composite*

Materials: Analysis and Application American Society of Mechanical Engineers, Proceedings of the 1994 International Mechanical Engineering Congress and Exposition Chicago, IL. AD-45: p. 201-210, 1994.

80. V. Giurgiutiu, Rogers, Craig A. "New Results in the Application of E/M Impedance Method to Machinery Health Monitoring and Failure Prevention." in *53rd Meeting of the Society for Machinery Failure Prevention Technology*, Virginia Beach, VA, 1999.
81. M. Goldfarb, Celanovic, Nikola, "A Lumped Parameter Electromechanical Model for Describing the Nonlinear Behavior of Piezoelectric Actuators." *ASME Journal of Dynamic Systems, Measurement, and Control*. **119**(3): p. 478-485, 1997.
82. C. Hu, Kawiecki, Grzegorz, Chandra, Ramesh, Chopra, Inderjit. "Structural Modeling of Beams with Skewed Piezoactuators." in *36th AIAA/ASME/ASCE/AHS/ASC Structures, Structural Dynamics, and Materials Conference and AIAA/ASME Adaptive Structures Forum*, New Orleans, LA: AIAA p. 3423-3430, 1995.
83. F. Lalande, Chaudhry Zaffir, Rogers, Craig A., "Impedance Modeling of in-Phase Actuation of Actuators Bonded on Ring Structures." *Adaptive Structures and Composite Materials: Analysis and Application American Society of Mechanical Engineers, Proceedings of the 1994 International Mechanical Engineering Congress and Exposition Chicago, IL. AD-45: p. 193-200, 1994.*
84. F. Lalande, C. Zaffir, and C.A. Rogers, "Impedance-Based Modeling of Induced Strain Actuators Bonded on Ring Structures." *Journal of Sound and Vibration*. **201**(2): p. 169-187, 1997.
85. C.K. Lee, "Theory of Laminated Piezoelectric Plates for the Design of Distributed Sensors/Actuators. Part I: Governing Equations and Reciprocal Relationships." *Journal of the Acoustical Society of America*. **87**(3): p. 1144-1158, 1990.
86. M. Leibowitz, Vinson, Jack R. "The Use of Hamilton's Principle in Laminated Piezoelectric and Composite Structures." in *ASME Winter Annual Meeting*, New Orleans, LA: ASME p. 257-267, 1993.
87. G.A. Lesieutre and C.L. Davis, "Can a Coupling Coefficient of a Piezoelectric Device Be Higher Than Those of Its Active Material?" *Proceedings of SPIE - The International Society for Optical Engineering*. **3041**: p. 281-292, 1997.
88. S.E. Miller and H. Abramovich, "Self-Sensing Piezolaminated Actuator Model for Shells Using a First Order Shear Deformation Theory." *Journal of Intelligent Material Systems and Structures*. **6**(5): p. 624-638, 1995.

89. A. Sermoneta, Liang, C., Rogers, C.A. "Investigation of the Electro-Mechanical Coupling in Active Structures with Multiple Actuators Determination of Optimal Actuator Locations." in *36th AIAA/ASME/ASCE/AHS/ASC Structures, Structural Dynamics, and Materials Conference and AIAA/ASME Adaptive Structures Forum*, New Orleans, LA: AIAA p. 3524-3528, 1995.
90. H.A.C. Tilmans, "Equivalent Circuit Representation of Electromechanical Transducers: I Lumped-Parameter Systems." *Journal of Micromechanics and Microengineering*. **6**: p. 157-176, 1996.
91. R.H.M. van de Leur, "Critical Consideration on the Interpretation of Impedance Plots." *Journal of Physics D: Applied Physics*. **24**(8): p. 1430-1435, 1991.
92. K. Yao and K. Uchino, "Analysis on a Composite Cantilever Beam Coupling a Piezoelectric Bimorph to an Elastic Blade." *Sensors and Actuators, A: Physical*. **89**(3): p. 215-221, 2001.
93. S. Zhou, Liang, C., Rogers, Craig A. "Impedance Modeling of Two-Dimensional Piezoelectric Actuators Bonded on a Cylinder." in *ASME Winter Annual Meeting*, New Orleans, LA: ASME p. 247-255, 1993.
94. S.-W. Zhou, Liang, Chen, Rogers, Craig A., "Modeling of Distributed Piezoelectric Actuators Integrated with Thin Cylindrical Shells." *Journal of the Acoustical Society of America*. **96**(3): p. 1605-1612, 1994.
95. S.Y. Lin, "Coupled Vibration Analysis of Piezoelectric Ceramic Disk Resonators." *Journal of Sound and Vibration*. **218**(2): p. 205-217, 1998.
96. X. Li, R. Lin, and K.W. Leow, "Performance-Enhanced Micro-Machined Resonant Systems with Two-Degrees-of-Freedom Resonators." *Journal of Micromechanics and Microengineering*. **10**(4): p. 534-539, 2000.
97. N.W. Hagood, von Flotow, A., "Damping of Structural Vibrations with Piezoelectric Materials and Passive Electrical Networks." *Journal of Sound and Vibration*. **146**(2): p. 243-268, 1991.
98. J.J. Hollkamp, "Multimodal Passive Vibration Suppression with Piezoelectric Materials and Resonant Shunts." *Journal of Intelligent Material Systems and Structures*. **5**(1): p. 49-57, 1994.
99. K.W. Wang, Lai, J.S., Yu, W.K., "Structural Vibration Control Via Piezoelectric Materials with Real-Time Semi-Active Electrical Networks." *Adaptive Structures and Composite Materials: Analysis and Application American Society of Mechanical Engineers, Proceedings of the 1994 International Mechanical Engineering Congress and Exposition Chicago, IL*. **AD-45**: p. 219-226, 1994.

100. D.J. Leo, Inman, Daniel J., "Pointing Control and Vibration Suppression of a Slewing Flexible Frame." *Journal of Guidance, Control, and Dynamics*. **17**(3): p. 529-536, 1994.
101. D. Sciulli and D.J. Inman, "Comparison of Single- and Two-Degree-of-Freedom Models for Passive and Active Vibration Isolation Design." *Proceedings of SPIE - The International Society for Optical Engineering*. **2720**: p. 293-304, 1996.
102. C.L. Davis, Lesieutre, George A., Dosch, Jeffrey. "A Tunable Electrically Shunted Piezoceramic Vibration Absorber." in *SPIE Smart Structures and Materials Conference* p. 51-59, 1997.
103. J. Hwang, T. Ueno, Y. Tomabechi, and K. Matsumara, "Variation of Resonant Frequency of Disk Resonator Coupled with External Circuit." *Electronics & Communications in Japan, Part II: Electronics (English translation of Denshi Tsushin Gakkai Ronbunshi)*. **80**(11): p. 48-57, 1997.
104. G.A. Lesieutre, "Vibration Damping and Control Using Shunted Piezoelectric Materials." *The Shock and Vibration Digest*. **30**(3): p. 187-195, 1998.
105. C.J. Cross, Fleeter, Sanford, "Passive Control of Flow Induced Vibrations Using Shunted Piezoelectrics." *AIAA-98-1952/A98-25205*: p. 2021-2033, 1998.
106. A. Curtis, *Piezoelectric Materials for Energy Transfer Vibration Control*, Materials Systems Inc. 1-19. 1999, ONR BAA 99-023
107. C.L. Davis, Lesieutre, George A., "An Actively Tuned Solid State Piezoelectric Vibration Absorber." *Proceedings of SPIE - The International Society for Optical Engineering*. **3327**: p. 169-182, 1998.
108. J. Kim, Y.-H. Ryu, and S.-B. Choi, "New Shunting Parameter Tuning Method for Piezoelectric Damping Based on Measured Electrical Impedance." *Smart Materials and Structures*. **9**(6): p. 868-877, 2000.
109. G. Caruso, "A Critical Analysis of Electric Shunt Circuits Employed in Piezoelectric Passive Vibration Damping." *Smart Materials and Structures*. **10**: p. 1059-1068, 2001.
110. S.-y. Wu, T.L. Turner, and S.A. Rizzi, "Piezoelectric Shunt Vibration Damping of F-15 Panel under High Acoustic Excitation." *Proceedings of SPIE - The International Society for Optical Engineering*. **3989**: p. 276-287, 2000.
111. M. Goldfarb and L.D. Jones, "On the Efficiency of Electric Power Generation with Piezoelectric Ceramic." *ASME Journal of Dynamic Systems, Measurement, and Control*. **121**(3): p. 566-571, 1999.

112. V. Giurgiutiu, Rogers, Craig A., "Dynamic Power and Energy Capabilities of Commercially-Available Electro-Active Induced-Strain Actuators." *Journal of Intelligent Material Systems and Structures*. **7**(November): p. 656-667, 1996.
113. V. Giurgiutiu, Rogers, Craig A., "Power and Energy Characteristics of Solid-State Induced-Strain Actuators for Static and Dynamic Applications." *Journal of Intelligent Material Systems and Structures*. **8**(September): p. 738-750, 1997.
114. R.A. Lomenzo, Sumali, Hartono, Cudney, Harley H. "Maximizing Mechanical Power Transfer from Piezoceramic Stacked Actuators to Structures." in *ASME Winter Annual Meeting*, New Orleans, LA: ASME p. 229-235, 1993.
115. S. Meninger, Mur-Miranda, Jose Oscar, Amirtharajah, Rajeevan, Chandrakasan, Anantha, Lang, Jeffrey, *Vibration-to-Electric Energy Conversion*, MIT
116. S.C. Stein, Liang, Chen, Rogers, Craig A., "Power Consumption of Piezoelectric Actuators Driving a Simply Supported Beam Considering Fluid Coupling." *Journal of the Acoustical Society of America*. **96**(3): p. 1598-1604, 1994.
117. S.-W. Zhou, Rogers, Craig A., "Power Flow and Consumption in Piezoelectrically Actuated Structures." *AIAA Journal*. **33**(7): p. 1305-1311, 1995.
118. R. Taylor, F. Liu, S.B. Horowitz, K. Ngo, T. Nishida, L. Cattafesta, and M. Sheplak. "Technology Development for Electromechanical Acoustic Liners." in *Active 04*, Williamsburg, VA, Paper #A04-093, 2004.
119. A. Kasyap, S.B. Horowitz, J.-S. Lim, K. Ngo, A. Kurdila, T. Nishida, M. Sheplak, and L.N. Cattafesta. "Energy Reclamation from a Vibrating Piezoceramic Composite Beam." in *9th International Congress on Sound and Vibration (ICSV9)*, Orlando, FL, 2002.
120. S.B. Horowitz, A. Kasyap, F. Liu, D. Johnson, T. Nishida, K. Ngo, M. Sheplak, and L.N. Cattafesta. "Technology Development for Self-Powered Sensors." in *1st AIAA Flow Control Conference*, St. Louis, MO, 2002.
121. S. Roundy, P.K. Wright, and J. Rabaey, "A Study of Low Level Vibrations as a Power Source for Wireless Sensor Nodes." *Computer Communications*. **26**: p. 1131-1144, 2003.
122. A. Mehra, X. Zhang, A.A. Ayon, I.A. Waitz, M.A. Schmidt, and C.M. Spadaccini, "A Six-Wafer Combustion System for a Silicon Micro Gas Turbine Engine." *Journal of Microelectromechanical Systems*. **9**(4): p. 517-526, 2000.
123. R.K. Wangsness, *Electromagnetic Fields*. 2nd ed, John Wiley & Sons, Inc.: Hoboken, NJ. 587. 1986.

124. J.D. Irwin. "Basic Engineering Circuit Analysis." in, Upper Saddle River, NJ: Prentice-Hall, Inc. p. 466-7, 1996.
125. F.V. Hunt, *Electroacoustics: The Analysis of Transduction, and Its Historical Background*, Acoustical Society of America: New York. 1982.
126. J.F. Lindsay and S. Katz, *Dynamics of Physical Circuits and Systems*, Matrix Publishers, Inc.: Champaign, Illinois. 1978.
127. H.A.C. Tilmans, "Equivalent Circuit Representation of Electromechanical Transducers: Ii Distributed-Parameter Systems." *Journal of Micromechanics and Microengineering*: p. 285-309, 1997.
128. S.D. Senturia, *Microsystem Design*, Kluwer Academic Publishers: Boston, MA. 689. 2001.
129. A.P. Dowling and J.E. Ffowcs Williams, *Sound and Sources of Sound*. Ellis Horwood Series in Engineering Science, Ellis Horwood Limited: Chichester, Eng. 1983.
130. A.W. Nolle, "Small-Signal Impedance of Short Tubes." *The Journal of the Acoustical Society of America*. **25**(1): p. 32-39, 1953.
131. A.S. Hersh and B. Walker, *Fluid Mechanical Model of the Helmholtz Resonator*, NASA Contractor Report. 1977, NASA CR-2904
132. R.C. Rosenberg and D.C. Karnopp, *Introduction to Physical System Dynamics*, McGraw-Hill Book Company: New York, N.Y. 1983.
133. IEEE, *IEEE Standard on Piezoelectricity*, IEEE. 1987, ANSI/IEEE Std 176-1987
134. Y. Xu, *Ferroelectric Materials and Their Applications*, North-Holland: Amsterdam. 391. 1991.
135. J.F. Shackelford and W. Alexander, eds. *Crc Materials Science and Engineering Handbook*. 3 ed. CRC Press: Boca Raton, FL. 2001.
136. P. Hess, "Laser Diagnostics of Mechanical and Elastic Propertis of Silicon and Carbon Films." *Applied Surface Science*. **106**: p. 429-437, 1996.
137. J.B. Price. "Anisotropic Etching of Silicon with Koh -H20-Isopropyl Alcohol." in *Semicond Silicon 1973, 2nd Int Symp on Silicon Material Sci and Technology*, Chicago, IL p. 339-353, 1973.

138. D. Resnik, D. Vrtacnik, U. Aljancic, M. Mozek, and S. Amon, "Different Aspect Ratio Pyramidal Tips Obtained by Wet Etching of (100) and (111) Silicon." *Microelectronics Journal*. **34**: p. 591-593, 2003.
139. B. Tuttle, J.A. Voigt, T.J. Headley, B.G. Potter, D. Dimos, R.W. Schwartz, M.T. Dugger, J. Michael, R.D. Nasby, T.J. Garino, and D.C. Goodnow, "Ferroelectric Thin Film Microstructure Development and Related Property Enhancement." *Ferroelectrics*. **151**: p. 11-20, 1994.
140. L.I. Vergara, M.C.G. Passeggi Jr., and J. Ferron, "The Role of Passivation in Titanium Oxidation: Thin Film and Temperature Effects." *Applied Surface Science*. **187**: p. 199-206, 2002.
141. M. Harting and G. Fritsch, "Structural Analysis and Residual Stress Measurements in a Natural Titanium Oxide Layer." *Materials Science Forum*. **166-169**: p. 343-348, 1994.
142. S. Norasetthekul, P.Y. Park, K.H. Baik, K.P. Lee, J.H. Shin, B.S. Jeong, V. Shishodia, L. E.S., D.P. Norton, and S.J. Pearton, "Dry Etch Chemistries for Tio₂ Thin Films." *Applied Surface Science*. **185**: p. 27-33, 2001.
143. K. Yao, S. Yu, and F. Eng-Hock Tay, "Residual Stress Analysis in Ferroelectric Pb(ZrTi)O₃ Thin Films Fabricated by a Sol-Gel Process." *Applied Physics Letters*. **82**(25): p. 4540-4542, 2003.
144. D. Xia, M. Liu, Y. Zeng, and C. Li, "Fabrication and Electrical Properties of Lead Zirconate Titanate Thick Films by the New Sol-Gel Method." *Materials Science and Engineering*. **B87**: p. 160-163, 2001.
145. G.G. Stoney, "The Tension of Thin Metallic Films Deposited by Electrolysis." *Proceedings of the Royal Society of London*. **A 82**: p. 172, 1909.
146. X. Zhang, K.S. Chen, R. Ghodssi, A.A. Ayon, and S.M. Spearing, "Residual Stress and Fracture in Thick Tetraethylorthosilicate (Teos) and Silane-Based Pecvd Oxide Films." *Sensors and Actuators, A: Physical*. **91**: p. 373-380, 2001.
147. J.S. Kim and K.W. Paik, "The Multilayer-Modified Stoney's Formula for Laminated Polymer Composites on a Silicon Substrate." *Journal of Applied Physics*. **86**(10): p. 5474-5479, 1999.
148. L. Fu, J.M. Miao, X.X. Li, and R.M. Lin, "Study of Deep Silicon Etching for Micro-Gyroscope Fabrication." *Applied Surface Science*. **177**: p. 78-84, 2001.
149. K.S. Chen and A.A. Ayon, "Effect of Process Parameters on the Surface Morphology and Mechanical Performance of Silicon Structures after Deep

- Reactive Ion Etching (Drie)." *Journal of Microelectromechanical Systems*. **11**(3): p. 264-275, 2002.
150. A.A. Ayon, S. Nagle, L. Frechette, A. Epstein, and M.A. Schmidt, "Tailoring Etch Directionality in a Deep Reactive Ion Etching Tool." *Journal of Vacuum Science and Technology, Part B: Microelectronics and Nanometer Structures*. **18**(3): p. 1412-1416, 2000.
 151. F. Laermer and A. Urban, "Challenges, Development and Applications of Silicon Deep Reactive Ion Etching." *Microelectronic Engineering*. **67-68**: p. 349-355, 2003.
 152. A.M. Hynes, H. Ashraf, J.K. Bhardwaj, J. Hopkins, I. Johnston, and J.N. Shepherd, "Recent Advances in Silicon Etching for MEMS Using the Ase Process." *Sensors and Actuators, A: Physical*. **74**: p. 13-17, 1999.
 153. H. Jansen, M. de Boer, J. Burger, R. Legtenberg, and M. Elwenspoek, "The Black Silicon Method II: The Effect of Mask Material and Loading on the Reactive Ion Etching of Deep Silicon Trenches." *Microelectronic Engineering*. **27**: p. 475-480, 1995.
 154. Olympus America Inc., www.Olympusamerica.com. Microscopes & Imaging Systems, 1-800-446-5967. Last accessed June 2005
 155. Agilent Technologies Inc., www.Agilent.com. Test & Measurement Center, 1 (800) 829-4444. Last accessed December 2004
 156. Polytec PI Inc., www.Polytecpicom.com. (508)832-3456. Last accessed August 2005
 157. Bruel and Kjaer Inc., www.Bkhome.com. (800) 332-2040. Last accessed May 2005
 158. AE Techron Inc., www.Aetechron.com. (574)295-9495. Last accessed December 2004
 159. M.G. Jones and P.E. Stiede, "Comparison of Methods for Determining Specific Acoustic Impedance." *Journal of the Acoustical Society of America*. **101**(5 Pt. 1): p. 2694-2704, 1997.
 160. M.G. Jones and T.L. Parrott, "Evaluation of a Multi-Point Method for Determining Acoustic Impedance." *Mechanical Systems and Signal Processing*. **3**(1): p. 15-35, 1989.
 161. W.T. Chu, "Extension of the Two-Microphone Transfer Function Method for Impedance Tube Measurements." *Journal of the Acoustical Society of America*. **80**(1): p. 347-349, 1986.

162. J.Y. Chung and D.A. Blaser, "Transfer Function Method of Measuring in-Duct Acoustic Properties. I. Theory." *Journal of the Acoustical Society of America*. **68**(3): p. 907-921, 1980.
163. ASTM, *Standard Test Method for Impedance and Absorption of Acoustical Materials Using a Tube, Two Microphones, and a Digital Frequency Analysis System*, ASTM. 871-876. 1990, E 1050-90
164. ASTM, *Standard Test Method for Impedance and Absorption of Acoustical Materials by the Impedance Tube Method*, ASTM. 113-121. 1995, C 384-95
165. T. Schultz, L. Cattafesta, T. Nishida, and M. Sheplak. "Uncertainty Analysis of the Two-Microphone Method." in *8th AIAA/CEAS Aeroacoustics Conference*, Breckenridge, CO, 2002.
166. J.S. Bendat and A.G. Piersol, *Random Data: Analysis and Measurement Procedures*. 3 ed, John Wiley & Sons, Inc.: New York. 594. 2000.
167. B. Tuttle and R.W. Schwartz, "Solution Deposition of Ferroelectric Thin Films." *MRS Bulletin*. **21**(6)1996.

BIOGRAPHICAL SKETCH

Stephen Brian Horowitz was born on August 3, 1977, in Pompton Plains, N.J. He attended Marjory Stoneman Douglas High School in Parkland, FL, graduating in 1995. He received his bachelor's degree in electrical engineering from the University of Florida in 1999 and his Master of Science degree in electrical engineering in 2001. He is completing his doctoral degree at the University of Florida, concentrating his research efforts in the area of microelectromechanical systems (MEMS) and energy harvesting.